Long Period Grating Optical Fibre Sensors for Human Immunoglobulin Measurement

Peizhou Wu

20197425

Thesis submitted to the University of Nottingham for the degree of Doctor of Philosophy

Aug/2024

Abstract

This research focuses on the development of human antibody sensors based on long period gratings (LPG). The detection of human antibodies plays an important role in the diagnosis and monitoring of diseases. For example, the detections of immunoglobulin (Ig) G, IgA, and IgM have been used in the diagnosis of the infection of Dengue virus and COVID-19. The detection of monoclonal antibody is considered the gold standard to monitor plasma cell dyscrasias. Therefore, having access to fast and accurate antibody detection methods can improve the efficiency of disease diagnosis and monitoring. Traditional detection methods, including enzyme-linked immunosorbent assay (ELISA), surface plasmon resonance (SPR), and western blotting (WB), require complex sample processing and bulky equipment and can take up to a few hours to get results. Optical fibre sensors (OFS) have been applied in various area such as structural monitoring, biomedical measurements, and environmental monitoring due to their advantages such as light weight, small size, and being immune to electromagnetic interference. They measure the change of either intensity or wavelength caused by the measurand. The long period grating is a widely used OFS configuration. It is fabricated by periodically modulating the refractive index (RI) of the core of an optical fibre. The change of an external RI causes a wavelength shift of the attenuation bands in an LPG's transmission spectrum. Comparing with other OFS configurations, sensors based on an LPG are not affected by the fluctuation of intensity of light source; they also don't require complex signal processing.

A set of developed MATLAB codes is used for the simulation of LPGs. By manipulating different parameters, the properties of LPGs are demonstrated. The simulations show that an LPG works near phase matching condition (PMC) when the grating period line intersects the resonance curve at its local maxima. This is characterized by a U-shape band in the transmission spectrum. The resonance curves of an LPG move to longer wavelengths in five scenarios: i) the cladding diameter gets larger; ii) the RI of the cladding increases; iii) the core diameter gets narrower; iv) the RI of the core decreases; v) the external RI increases. An LPG has higher sensitivity to the change of external RI in terms of the wavelength shifts of attenuation bands if it works closer to the PMC. In this work an LPG is tested in external RIs ranging from 1.3326 to 1.3734 with different functional materials deposited on the surface. A bare LPG respond to the change of external RI with sensitivity of 332.8nm/RIU. The LPG with bovine serum albumin (BSA) immobilized on the surface with Glutaraldehyde has sensitivity of 335.1nm/RIU. The LPG with poly(allylamine hydrochloride, PAH) and 100nm silica nanoparticles (SiNPs) deposited on the surface has sensitivity of 370.7nm/RIU. The LPG coated with PAH/SiNPs and sub-5nm gold nanoparticles (AuNPs) has sensitivity of 464.9nm/RIU.

Human IgA, IgG, and IgM sensors are fabricated based on LPGs. Dual layers of PAH/SiNPs are deposited on the surface of LPGs by a mean of layer-by-layer (LbL) deposition. The PAH/SiNPs layers are then decorated with sub-5nm AuNPs. The bio-receptors are immobilized with 11-Mercaptoundecanoic acid (11-MUA), 3-Dimethylaminopropyl-N'-ethylcarbodiimide hydrochloride (EDC), and N-hydroxysuccinimide (NHS). The IgA sensor has a limit of detection (LoD) of 8.59μg/ml, a linear range between 0 and 30μg/ml, a Relative Standard Deviation (RSD) of 17.9%, and selectivity of 30.67. The IgG sensor has an LoD of 7.38μg/ml, a linear range between 0 and 90μg/ml, and RSD of 30.3%, and selectivity of 18.45. The IgM sensor has an LoD of 7.02μg/ml, a linear range between 0 and 80μg/ml, an RSD of 62.4%, and selectivity of 15.25.

A set of sensors to detect IgG-type monoclonal proteins are then developed based on LPGs by immobilizing bio-receptors on the surface of LPGs with Glutaraldehyde: an IgG$_{\kappa}$ sensor, an IgG$_{\lambda}$ sensor, and a IgG sensor. The IgG$_{\kappa}$ sensor has an LoD of 3.8μg/ml, a linear range between 0 and 20μg/ml, an RSD of 46.1%, and selectivity of 9.73. The IgG$_{\lambda}$ sensor has an LoD of 3.77μg/ml, a linear range between 0 and 20μg/ml, an RSD of 40.3%, and selectivity of 29.7. The whole IgG sensor can detect IgG$_{\kappa}$ and IgG$_{\lambda}$ with LoDs of 3.63μg/ml and 3.73μg/ml respectively. The RSDs are 35.4% and 42% for IgG$_{\kappa}$ measurement and IgG$_{\lambda}$ measurement respectively. The linear range is between 0 and 20μg/ml for both analytes.

A long period grating Mach-Zehnder interferometer (LPGMZI) is fabricated by making two identical LPGs in a single fibre. Cladding modes interfere with the core mode and form an interference pattern in the transmission spectrum. Both the envelope and fringes of the interference pattern are investigated. An LPGMZI responds to external RI in the range between 1.3326 and 1.3734 in two different ways: i) when the external RI changes over the whole LPGMZI, the envelope and fringes shift with external RI at the same rate of 94.6nm/RIU; ii) if only the external RI over the connecting section changes, the fringes shift at a rate of 75.4nm/RIU, while the envelope doesn't shift. If temperature changes over the whole LPGMZI homogeneously between 25°C and 40°C, the fringe and envelope shift at the same rate of 0.4nm/°C. An IgM sensor is fabricated by immobilizing bio-receptors on the connecting section with Glutaraldehyde. It has an LoD of 15μg/ml, a linear range between 0 and 80μg/ml, an RSD of 27.33% and selectivity of 18.48.

From the reviewing of literatures, the first optical-fibre IgA sensor and the first IgG-type M protein sensors are implemented in this project. An LPGMZI's responses to external RI and temperature in terms of the wavelength shifts of both envelope and fringes are investigated, which demonstrates the feasibility of implementing compensation for cross-sensitivity to fluctuations of external RI and temperature.

Chapter 5 and Chapter 7 of this thesis have been reported in 2 peer-reviewed papers:

1. P. Wu, L. Liu, S. P. Morgan, R. Correia, and S. Korposh, "Label-Free Detection of Antibodies Using Functionalised Long Period Grating Optical Fibre Sensors," *Results in Optics,* vol. 5, p. 100172, 2021.

2. P. Wu, L. Liu, S. P. Morgan, R. Correia, and S. Korposh, "Long Period Grating Mach–Zehnder Interferometer Based Immunosensor with Temperature and Bulk Refractive Index Compensation," *Biosensors,* vol. 12, no. 12, p. 1099, 2022.

Table of Contents

Acknowledgements

Firstly, I need to express my great gratitude to my supervisors Prof Sergiy Korposh, Prof Stephen P Morgan, and Dr Ricardo Correia for supporting me during the past 4 years. I would also like to thank Dr Liangliang Liu, who supervised me from Feb/2020 to Aug/2022. He left the university afterwards. I had valuable discussions with Prof Patrick Tighe and Dr Alexander Tarr from the School of Life Sciences, who taught me lots of immunological knowledge. I also can't forget my parents, who covered all the costs during my PhD study.

Secondly, I would like to thank my Judo coaches Dr Paul J Robinson and Mrs Anna Maria Carbone. I kept practicing Judo in the past two years, which makes my PhD life more colourful. My coaches help me improve myself in this great sport.

Thirdly, I would like to state that the MATLAB codes I used for LPG simulations were mainly created by Sumeth Sutharak in 2015 at the University of Nottingham. I had communications with Mr Mark East from the Centre of Additive Manufacturing, University of Nottingham to discuss the manufacturing of amplitude masks, and shared pictures of amplitude mask with him.

Finally, I would like to thank all my colleagues, who make the lab a lovely place to do research!

List of Figures

List of Tables

List of Abbreviations

Immunoglobulin	Ig
Enzyme-linked immunosorbent assay	ELISA
Western blotting	WB
Surface plasmon resonance	SPR
Lateral flow assay	LFA
Point-of-care	PoC
Optical fibre sensor	OFS
Goat anti-human IgG	GaHIgG
Refractive index	RI
Long period grating	LPG
Localized surface plasmon resonance	LSPR
Long period grating Mach-Zehnder interferometer	LPGMZI
Limit of detection	LoD
Layer-by-layer	LbL
11-Mercaptoundecanoic acid	11-MUA
3-Dimethylaminopropyl-N' -ethylcarbodiimide hydrochloride	EDC
N-hydroxysuccinimide	NHS
Phase matching condition	PMC
Bovine serum albumin	BSA
Poly(allylamine hydrochloride, PAH)	PAH
Silica nanoparticles	SiNPs
Gold nanoparticles	AuNPs
Refractive index unit	RIU

Multiple myeloma	MM
Smouldering multiple myeloma	SMM
Monoclonal gammopathy of uncertain significance	MGUS
Numerical Aperture	NA
Linear polarized	LP
Light emitting diode	LED
Carbon dioxide	CO_2
Ammonia	NH_3
Relative humidity	RH
Lossy mode resonance	LMR
Nitrogen dioxide	NO_2
Volatile organic compounds	VOC
Hydrogen	H_2
Fibre Bragg Grating	FBG
Tilted Fibre Bragg Grating	TFBG
In-fibre Fabry-Perot Interferometer	FFPI
Optical spectral analyser	OSA
in-fibre Mach-Zehnder interferometer	FMZI
Thinner fibre	TF
Single-mode fibres	SMF
Polyacrylamide gel electrophoresis	PAGE
Polyvinylidene difluoride	PVDF
Polyacrylamide gel	PAG
Surface plasmon	SP

Surface-enhanced Raman scattering	SERS
Silver nanoparticles	SNP
Human IgG	HIgG
Graphene oxide	GO
Silver	Ag
C-reactive protein	CRP
Gold nanorods	AuNR
Goat anti-rabbit IgG	GaRIgG
Alpha-fetoprotein	AFP
Streptavidin	SV
Rabbit anti-human IgG	RaHIgG
Carboxyl group	-COOH
Goat anti-human IgM	GaHIgM
Cytokeratin	CK
N-terminal B-type natriuretic peptide	NT-proBNP
Hydroxyl group	-OH
Human IgM	HIgM
Goat anti-mouse IgG	GaMIgG
6-maleimidohexanoic acid *n*-hydroxysuccinimide ester	EMCS
Indium tin oxide	ITO
Tin dioxide	SnO_2
Monoclonal protein	M protein
(3-Aminopropyl)triethoxysilane	APTES
Scanning electron microscope	SEM

poly (ethylene glycol)	PEG
Relative standard deviation	RSD
Quartz Crystal Microbalance	QCM
Detection accuracy	DA

Chapter 1. Introduction

The detection of biomolecules plays important roles in healthcare such as the diagnosis of diseases like plasma cell dyscrasia and the infection by pathogens [1], [2]. Human immunoglobulins (Ig), also known as antibodies, are generated by human B cells and protect body against the invasion of pathogens [3]. The concentrations of antibodies in secretion can reflect human's health condition [3].

There are five types of antibodies, IgA, IgG, IgM, IgD, and IgE [4] which are different in molecular structure [4]. The detections of IgA, IgG, and IgM have been used in the diagnosis of diseases such as the infection of Dengue virus and the infection of COVID-19 [5]-[9]. They can also be used for the investigations of immunodeficiency [10]. The concentration of monoclonal antibodies can be used as a criterion to monitor plasma cell dyscrasias [11], [12]. Therefore, to further improve the efficiency of diseases diagnosis, it is important to have access to fast and accurate technologies to detect antibodies.

Enzyme-linked immunosorbent assay (ELISA) [13], western blotting (WB) [14], and surface plasmon resonance (SPR) are traditional technologies to detect antibodies [15]. They should be conducted by experienced technicians and require bulky equipment. ELISA includes multiple incubation and washing steps and can take up to a few hours to get results [13]. Although having multiple testing wells on a single ELISA plate can improve the throughput, the time required for going through one ELISA test isn't reduced. The plate reader is bulky [17]. A modified ELISA strategy exploits smartphone-based computer vision technology to analyse the plate, which is more compact and portable than traditional plate readers [17]. However, the multiple incubation and washing steps is still complex. An ELISA can also be implemented based on particles such as magnetic beads functionalized with bio-receptors [18]. The protocol should be assisted by a particle manipulation machine, which saves manual labour and reaction time [18]. It pushes ELISA on step further to Point-of-Care (PoC) applications. However, the particle manipulation machine is complex and the reagent loading need to be carried out manually before ELISA analysis [18]. WB includes electrophoresis, blotting transfer, and visualisation processes. It takes several hours to complete a WB analysis, requires bulky equipment with high voltage (60V to 140V), and should be conducted by trained technicians like ELISA [14], [19]-[21]. A fast WB can be implemented with microfluidic chips and automatic translation stage [22]. The time is reduced from around 20 hours to one hour. However, a much higher voltage is required (>1kV) [22]. SPR technologies implement fast antibody detection. Traditional SPR instruments are bulky and include an open-space optical system, which requires a precise alignment [23]. Some newly developed SPR sensors are based on optical fibres, which are more miniaturised and flexible than traditional SPR instruments [24]. Lateral Flow Assay (LFA) is easy-to-use and can give results within 15 to 30 minutes [25]. It is suitable for PoC applications. End-users can use LFA without any training. Traditional LFAs are qualitative assays. Quantitative LFAs can be implement by using a colourimeter to analyse the LFA stripes [26]. Due to the basic principles of them, ELISA, WB, traditional SPR, and LFA can’t implement ultra-miniaturised and flexible assays.

Optical fibres employ total internal reflection to transmit light [27]. An optical fibre sensor (OFS) transduces the measurand into the change of optical signals such as intensity, phase and wavelengths [28]. Sensors to detect biomolecules have been developed based on different OFS configurations [29], [30]. The sensors are usually made by immobilizing bio-receptors on the sensing part of OFS configurations. When target biomolecules bind to the bio-receptors, either the light absorbance or the refractive index (RI) near the sensing part is modulated [29], [31]. For example, a sensor based on cladding-removed fibre can detect the intensity change of transmitted light caused by goat anti-human IgG (GaHIgG) [29]; A cladding-removed fibre with silver film and graphene oxide coated on the surface can detect the change of surface RI caused by human IgG [31]. Comparing with traditional assays, OFS is more miniaturized, flexible, and simple to use due to their light weight and compact sizes [28]. Comparing with other newly developed assays such as sensors based on planer optical waveguides and electronic platforms, OFS is easier to be fabricated [32]-[34]. Various types of optical fibres are commercially available. Sensors can be fabricated directly based on the optical-fibre platforms, while planer optical waveguides and electronic platforms are usually homemade. Comparing with sensors based on Quartz Crystal Microbalance (QCM) measurements [35], OFS is more reliable in complex electromagnetic environments as it is immune to electromagnetic interference [28].

A long period grating (LPG) is fabricated by modulating the RI of the fibre core periodically [36]. Light is coupled from core mode into cladding mode when propagating through the grating area and is attenuated, which forms attenuation bands in the transmission spectrum. An LPG is a platform to detect the RI of an external medium [36]. The attenuation bands shift in wavelength when external RI changes [36]. Many biomolecular sensors have been designed based on LPGs such as human IgM sensor and GaHIgG sensor [30], [37]. As the wavelengths of attenuation bands are measured and analysed, an LPG sensor is not affected by the intensity fluctuations of light source. Comparing with the attenuation bands caused by SPR or localized surface plasmon resonance (LSPR), the attenuation bands of an LPG are narrower, sharper and easier to be tracked [38]. LPGs are fabricated with an automatic UV laser system and amplitude masks in this work. Comparing with interferometric optical fibre sensor configurations such as fibre Fabry-Perot interferometer (FFPI) and in-fibre Mach-Zehnder interferometer (FMZI) [39], [40], the fabrication process of an LPG is more automatic, and the fabrication results are more controllable.

1.1 Aim and Objectives

Having access to fast and accurate human antibody detection technologies can improve the efficiency of disease diagnoses. IgA, IgG, and IgM have been proven to be of high diagnostic significance. An LPG is an OFS configuration with reliable response to the change of external RI and simple signal processing requirements. The aim of this project is to design sensors to detect human antibodies based on LPGs.

There are many variables when fabricating an LPG such as the grating period and the diameters and RIs of core and cladding. It is important to understand how an LPG is affected by these parameters.

An LPG detects the change of external RI. It is functionalized with different materials to fabricate sensors. It is important to understand how these coatings affect an LPG's response to the change of external RI.

New OFS configuration such as LPG Mach-Zehnder interferometer (LPGMZI) can be developed based on LPGs. The properties of an LPGMZI and the feasibility to develop antibody sensors based on it are investigated.

To achieve the aim of this research, the objectives listed below need to be completed:

1. Conduct a comprehensive literature review to acquire the background knowledge. It helps understand how optical fibre and LPGs work and different optical fibre sensing technologies:

    a. The theories about antibodies and their relationship with health conditions.
    b. The theories of optical fibre and LPG.
    c. OFS (Different configurations and their applications).
    d. The current biosensing technologies (traditional and newly developed methods), especially OFS and their fabrication methods.
2. Conduct simulations on LPGs to understand better how the transmission spectrum changes with parameters (length and period of grating, diameters and RIs of core and cladding, and external RIs).
3. Conduct the characterisations of LPGs. The properties of LPGs that is too complex to be simulated can be demonstrated experimentally:
    a. The LPG's responses to external RI with different functional coatings on the surface.
    b. The LPG's response to the change of temperature.
4. Fabricate LPGs with the developed amplitude mask method. The deviations of the fabrication of LPGs can be demonstrated experimentally and analysed.
5. Fabricate and characterize IgA, IgG, and IgM sensors based on LPGs (the limit of detection (LoD), selectivity, linear range, and Relative Standard Deviation (RSD) of each sensor). It can demonstrate the feasibility of designing antibody sensors based on LPGs.
6. Fabricate and characterize sensors to detect monoclonal antibodies. It demonstrates the feasibility of designing monoclonal antibody sensors based on LPGs.
7. Fabricate and characterize an LPGMZI. It helps understand the properties of LPGMZIs.
    a. The LPGMZI's response to the change of external RI
    b. The LPGMZI's response to the change of temperature.
8. Fabricate an antibody sensor based on the LPGMZI and characterize it.

1.2 Structure of the thesis

Chapter 1 (Introduction): Aim and objectives of this project have been introduced in this chapter.

Chapter 2 (Background): This chapter explains background knowledge required to understand this thesis, including the knowledge of human immune systems and antibodies, optical fibre, LPG, OFS, and current biosensing technologies.

Chapter 3 (Sensor fabrication methodologies): This chapter explains the fabrication of LPGs and their functionalization, including a comparison of two different LPG fabrication methods (point-by-point and amplitude mask), the fabrication set-ups and results of amplitude mask method, and two surface functionalization protocols (LbL-aided crosslinking with 11-MUA/EDC/NHS and crosslinking with Glutaraldehyde).

Chapter 4 (LPG Simulations and Characterizations): The simulations show how an LPG's transmission spectrum changes with optical properties (length and period of grating, diameter and RIs of core and cladding, and external RI). The characterizations show how an LPG with different functional coatings responds to the change of external RI, and how a bare LPG responds to the change of temperature.

Chapter 5 (Immunoglobulin A, G, and M Sensors): This chapter shows the processes of fabricating IgA, IgG, and IgM sensors using LbL-aided crosslinking with 11-MUA/EDC/NHS. Sensors' LoD, selectivity, linear range, and RSD are evaluated.

Chapter 6 (Measurements of IgG-type Monoclonal Proteins): This chapter shows how to design IgG$_\kappa$, IgG$_\lambda$, and whole IgG sensors based on LPGs using the method of crosslinking with Glutaraldehyde. Sensors' LoD, selectivity, linear range, and RSD are evaluated.

Chapter 7 (Immunoglobulin M Sensor Based on Long Period Grating Mach-Zehnder Interferometer with the Compensation for Fluctuations of Temperature and Bulk Refractive Index): An LPGMZI is fabricated. It is characterized with different external RI in two scenarios: i) the external RI over the whole LPGMZI changes; ii) only the external RI over the connecting section changes. The LPGMZI's response to the change of temperature is also evaluated with the temperature over the whole LPGMZI changing homogeneously. An IgM sensor is fabricated based on the LPGMZI. Sensors' LoD, selectivity, linear range, and RSD are evaluated. Both the envelope and fringes of the interference pattern in the transmission spectrum are analysed.

Chapter 8 (Conclusion and Future Work): The main results are concluded in this chapter. The future development directions are provided.

Chapter 2. Background

The detection of biomolecules plays an important role in healthcare, for example, the diagnosis of many diseases such as plasma cell dyscrasia and the infection by pathogens [1], [2]. Biosensors based on optical fibre sensors have great potential for improving healthcare. This chapter covers the background knowledge that is needed to understand the development of LPG-based biosensors which are the focus of this research. There are four main subsections in this chapter: The essentials of human immunology, the essentials of Long Period Gratings (LPGs) and optical fibre sensors, the state of the art of optical-fibre biosensors, and a discussion on different optical fibre antibody sensors.

2.1 A review of human immune system and antibodies

Humans are living in a complex environment. Many factors can influence the normal functions of the human body such as the infections of microbes (e.g. bacteria, viruses, and fungi) and the growth of cancer cells [41]. The human immune system provides protections to the body against these factors [41].

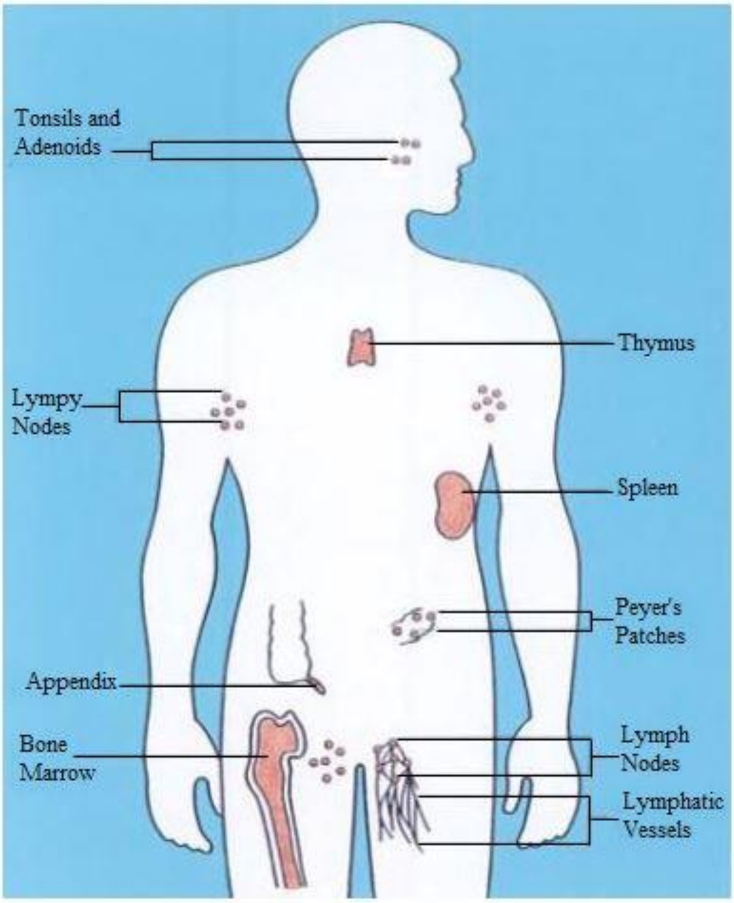

Figure 2- 1. The human immune organs, sourced from [42]

As shown in Figure 2-1, immune organs, also called lymphoid organs [42], are distributed over the whole body. They implement the production, maturation, and transportation of lymphocytes and provide places for them to encounter and eliminate the pathogens or unhealthy cells [42]. There are two types of lymphocytes—T cells and B cells. They both originate in bone marrow and can travel over the whole body through blood vessels and lymphatic vessels [42]. T cells mature in the thymus and B cells mature in bone marrow. They are the cells directly working on the unhealthy cells [42]. Spleen, lymph nodes, tonsils, and adenoids are the main places where lymphocytes encounter and eliminate their enemies [42]. There are two main types of T cells. Killer T cells directly attack the unhealthy cells when recognizing specific fragments on their surfaces. Helper T cells coordinate the whole immune system by stimulating other lymphocytes [42]. The main function of B cells is to secrete different chemicals and antibodies which coordinate the whole immune system [3], [42].

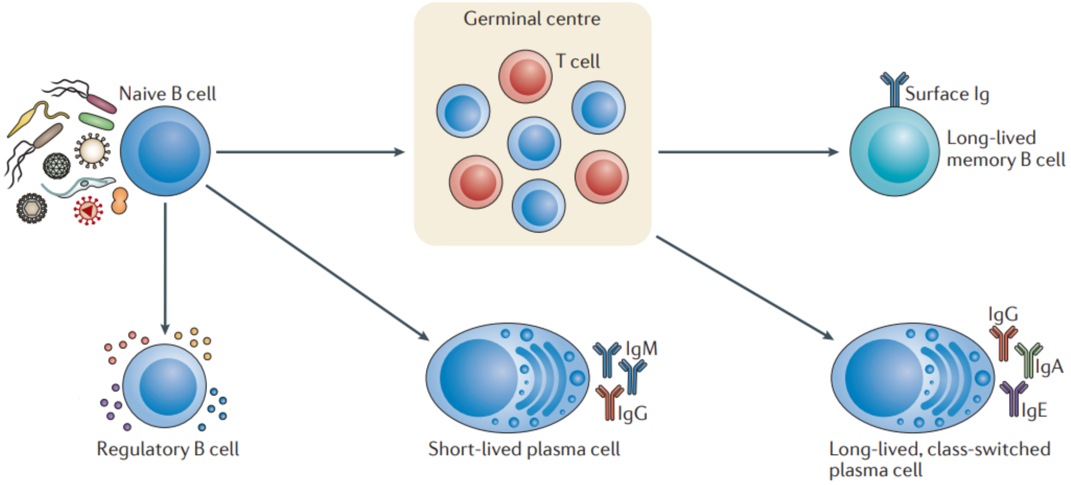

Figure 2-2. The response of B cells to pathogens sourced from [3].

As shown in Figure 2-2, in response to the invasion of pathogens, native B cells start to differentiate [3]. Some of them develop into regulatory B cells. Regulatory B cells secrete chemicals to coordinate T cell responses [3]. Some of them develop into short-lived plasma cells [3]. They participate in the immune system by secreting Immunoglobulin (Ig) M and a small amount of IgG [3]. If the pathogens' invasion lasts for long time, some of the native B cells will go to the germinal centre to differentiate further into long-lived memory B cells or long-lived, class-switched plasma cells [3]. The long-lived, class-switched plasma cells continuously produce antibodies (mainly IgG, IgA, and IgE) to protect the body against infection [3]. The long-lived memory B cells are activated if the same pathogen invades for the second time (secondary infection) [3], [41]. They differentiate into plasma cells to secrete the pathogen-specific antibodies [3], [41]. Long-lived memory B cells and long-lived, class-switched plasma cells constitutes a human's life-long adaptive immunity [3].

There are five types of antibodies, IgM, IgG, IgA, IgE, and IgD [4]. They have different molecular structures and dominate in different positions of the body or different stages of the progression during an infection [4].

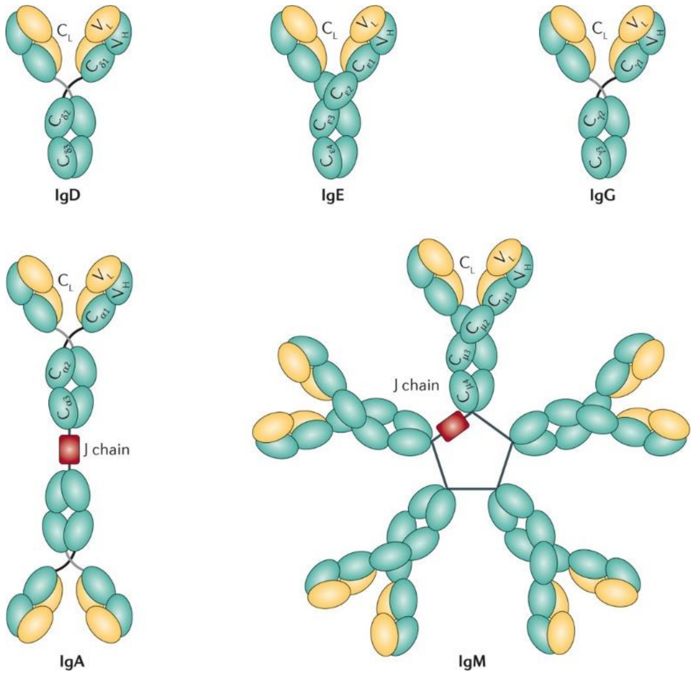

Figure 2-3. The structures of five types of antibodies sourced from [43].

As shown in Figure 2-3, IgD, IgE, and IgG have a Y-shaped structure. IgA is a complex of two Y-shaped structures and IgM has the structure of a pentagon, which consists of 5 Y-shaped structures. The detailed components in a Y-shaped structure are shown in Figure 2-4.

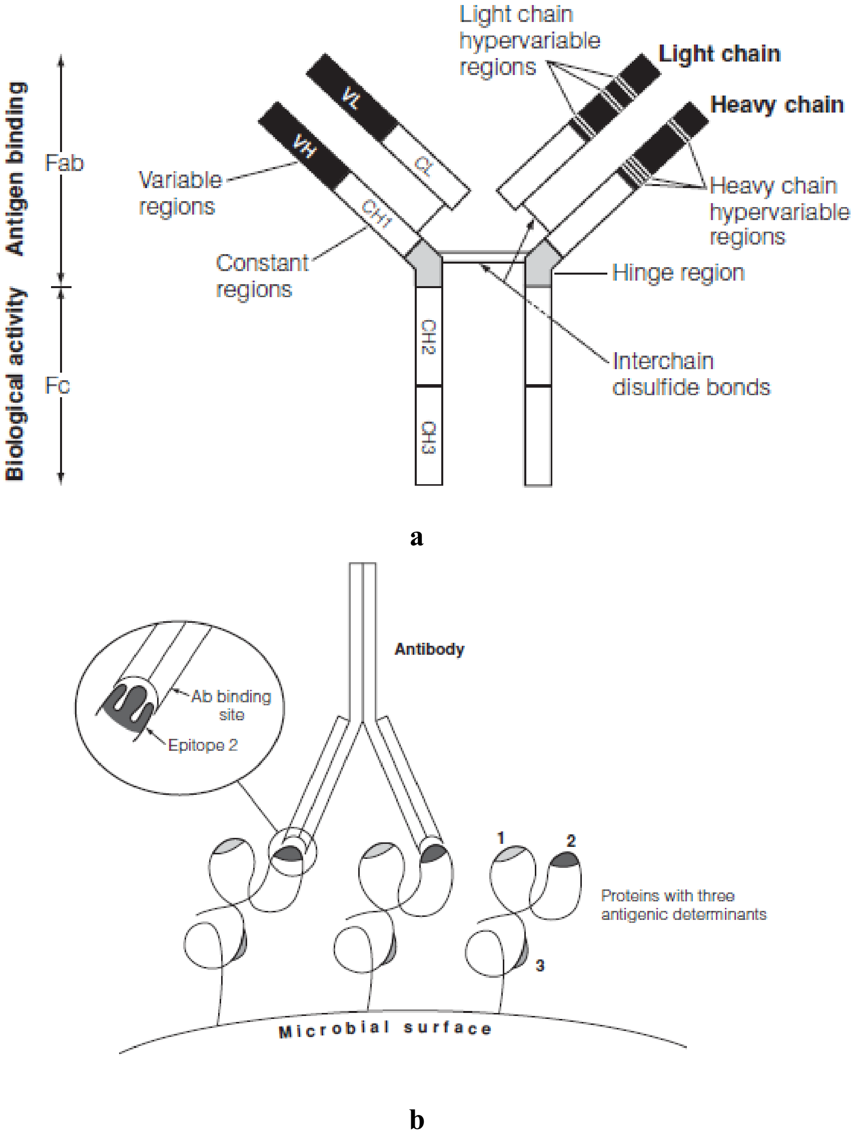

Figure 2-4. (a) The components in an antibody sourced from [41];
(b) An antibody binds to a pathogen sourced from [41].

An antibody consists of variable regions (VH & VL in Figure 2-4(a)) and constant regions (CHs & CL in Figure 2-4(a)) [41]. The same type of antibodies has the same constant region. IgD, IgE, IgA, IgG, and IgM have δ chain, ε chain, α chain, γ chain, and μ chain as their constant regions respectively [41]. Different variable regions can be grafted onto the constant region, which makes antibodies specific to different antigens [41]. The fragment crystallizable region (Fc in Figure 2-4(a)) coordinates with other functions [41]. For example, it combines with complementary proteins to trigger the complement cascade, which involves the reactions among a series of molecules and finally destroys and eliminates the pathogens and unhealthy cells [41]. The fragment antigen-binding region (Fab in Figure 2-4(a)) binds to specific antigens which appear on the surface of pathogen [41]. A Y-shaped molecule can also be divided into light chain (VL & CL in Figure 2-4(a)) and heavy chain (VH & CHs in Figure 2-4(a)). There are two types of light chains – λ chain and κ chain [41]. Each antibody molecule has only one type of light chain. Light chains are made by plasma cells. One plasma cell only produces one type of light chain for its whole life [41]. The plasma cells of healthy people produce polyclonal immunoglobulins, which contains all subtypes of immunoglobulins such as IgG with κ chain ($IgG_{κ}$), $IgG_{λ}$, $IgM_{κ}$, and $IgM_{λ}$ [41]. The plasma cells of people with plasma cell dyscrasias only produce a subtype of immunoglobulin (monoclonal immunoglobulin, M protein) [41].

The concentrations of different antibodies vary during the progression of an infection as shown in Figure 2-5.

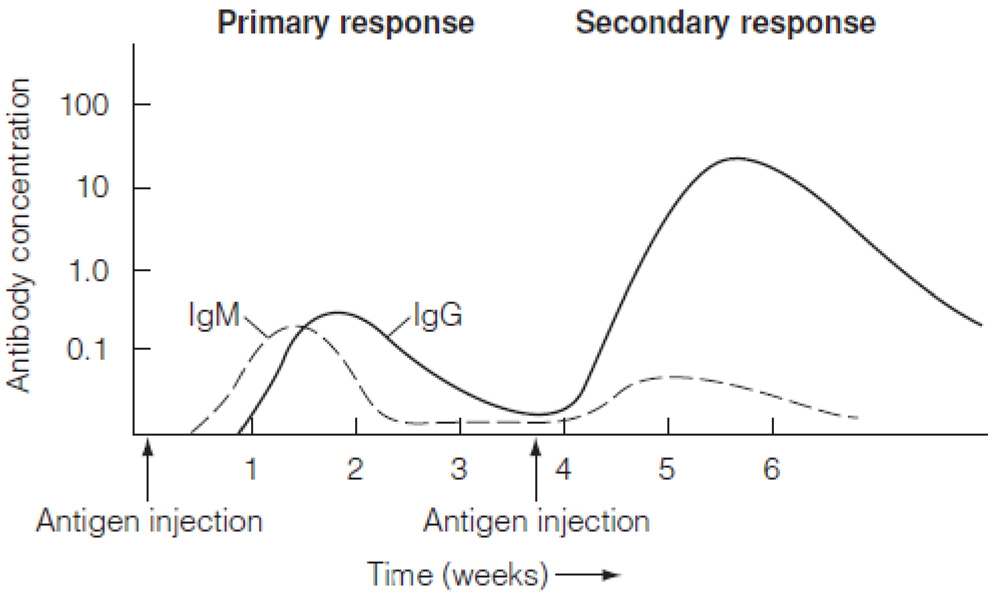

Figure 2- 5. The kinetics of immune response sourced from [26]

In a primary immune response, when the body is invaded by a pathogen for the first time, plenty of IgM and a little IgG is secreted to plasma [4], [41]. The concentration of IgM is higher than the concentration of IgG at the beginning of an infection and reaches the peak in around 1.5 weeks [4], [41], then, it is exceeded. Some of the native B cells develop into long-lived memory B cells and long-lived, class-switched plasma cells. Long-lived, class-switched plasma cells continuously produce antibodies to protect the body, while long-lived memory B cells are activated to secret plenty of IgG during the secondary immune response, when the body is infected by the same pathogen again [4], [41]. The concentrations of IgG and IgM both increase in secondary immune response, but the concentration of IgG is much higher and stays at a high level for longer time [4], [41].

The detection of IgA, IgG, and IgM has been used in the diagnosis of many diseases such as dengue virus infection and COVID-19 infection [5]. For example, in the primary immune response to dengue virus infection, the IgM becomes detectable within 3-5 days after the symptoms occur [6]. The IgG concentration starts to increase after around 14 days [6]. In the secondary immune response, the concentrations of IgG and IgM start to increase within 1-2 days after the symptoms occur [6]. In the diagnosis of COVID-19 infection, the COVID-specific IgA test shows a diagnostic sensitivity of 98.6%, which means 98.6% of the patients can be screened by a positive IgA test [9]. Both IgG and IgM tests show diagnostic sensitivity of 96.8% [9]. IgA, IgG, and IgM all become detectable within 4-10 days after the onset of symptoms [8], [9]. The concentrations of IgG and IgM reach the peak within 16-20 days, while the concentration of IgG reaches the peak within 21-25 days [9].

Apart from being used to diagnose specific infectious diseases, antibody tests are identified as necessary in the investigations of immunodeficiency states by National Health Service (NHS) in the UK [10]. For example, an increased level in IgM might be related to biliary cirrhosis [10]. IgG and IgA increase in viral hepatitis [10]. A prolonged and unusual infection without known cause might be related to IgG deficiency [10]. Furthermore, people with coeliac disease tend to have a lower IgA level, but don't have visible symptoms [10]. The detection of M protein plays an important role in the diagnosis and monitoring of plasma cell dyscrasias such as multiple myeloma (MM), smouldering multiple myeloma (SMM), and monoclonal gammopathy of uncertain significance (MGUS) [1], [11], [12]. Patients of plasma cell dyscrasias have sera M protein concentration of higher than 30mg/ml [1], [11].

2.2 The essentials of long period gratings and optical fibre sensors

Optical fibres employ total internal reflection to transmit light [27]. They have been applied in optical fibre communications, medical instruments, and optical fibre sensing [44]. The history of optical fibre sensors dates to the early 20th century [44]. In 1927, fibres of silica were designed to transfer images [44]. In 1930s, a plastic fibre was used in medical inspection to illuminate the inspection area [44]. The first optical fibre constituted by core and cladding with distinct refractive indices was designed in 1950s, which is the forerunner of modern optical fibres [44].

2.2.1 Optical fibre

An optical fibre is constituted by core and cladding with refractive indices (RIs) n_1 and n_2 ($n_2<n_1$) as shown in Figure 2-6.

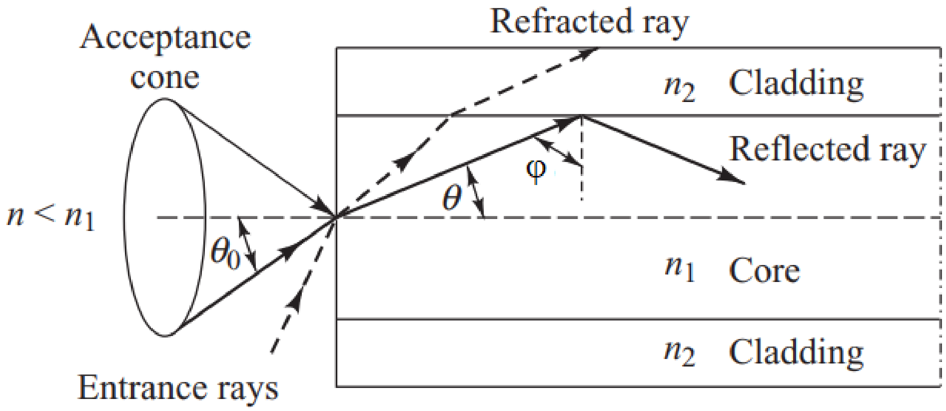

Figure 2- 6. The structure of an optical fibre sourced from [27]

The entrance rays transmitting from an external medium to the core are refracted due to the distinction between their RIs n and n_1 [27].

$$\theta = \arcsin\left(\frac{n}{n_1}\sin(\theta_0)\right) \tag{2-1}$$

Where θ_0 is the incident angle of light; θ is the refractive angle. The light rays striking the core-cladding interface are totally reflected if the incident angle φ is greater than the critical angle φ_c such that the light can transmit in the core with low energy loss.

$$\varphi_c = \arcsin\left(\frac{n_2}{n_1}\right) \tag{2-2}$$

As $\theta + \varphi = \frac{\pi}{2}$, the maximum incident angle of entrance rays is:

$$\theta_{0,max} = \arcsin\left(\frac{\sqrt{{n_1}^2-{n_2}^2}}{n}\right) \tag{2-3}$$

Where $\theta_{0,\,max}$ is also known as acceptance angle θ_A. θ_A is related to the RIs of the external medium (n), core (n_1), and cladding (n_2). n_1 and n_2 define the Numerical Aperture (NA) of an optical fibre.

$$NA = \sqrt{{n_1}^2 - {n_2}^2} \tag{2-4}$$

The transmission of light in optical fibres can be analysed and described by Maxwell's equations.

$$\nabla \times \boldsymbol{E} = -\mu \frac{\partial \boldsymbol{H}}{\partial t} \tag{2-5a}$$

$$\nabla \times \boldsymbol{H} = \varepsilon \frac{\partial \boldsymbol{E}}{\partial t} \tag{2-5b}$$

$$\nabla \cdot \boldsymbol{E} = 0 \tag{2-5c}$$

$$\nabla \cdot \boldsymbol{H} = 0 \tag{2-5d}$$

Equations (2-5 a-d) are the Maxwell's equations for linear, isotropic dielectric mediums. Where $\boldsymbol{E}$ is electric field intensity; $\boldsymbol{H}$ is the magnetic field intensity; μ is the permeability of medium; ε is permittivity of medium. ∇ is Del operator.

Light transmits in an optical fibre as different transmission modes, which can be described by waveguide equations [27]:

$$\boldsymbol{E} = \begin{bmatrix} E_z(r) \\ E_\phi(r) \\ E_r(r) \end{bmatrix} e^{jl\phi} e^{j(\omega t - \beta z)} \tag{2-6a}$$

$$\boldsymbol{H} = \begin{bmatrix} H_z(r) \\ H_\phi(r) \\ H_r(r) \end{bmatrix} e^{jl\phi} e^{j(\omega t - \beta z)} \tag{2-6b}$$

Equation (2-6a & b) are the waveguide equations of a cylindrical optical fibre. $\begin{bmatrix} E_z(r) \\ E_\phi(r) \\ E_r(r) \end{bmatrix}$ and $\begin{bmatrix} H_z(r) \\ H_\phi(r) \\ H_r(r) \end{bmatrix}$ are the field distribution over the cross-section of the optical fibre. Where r is the distance from a point to the centre of circle; ϕ is the angular displacement from the vertical axis to the position vector of the point as shown in Figure 2-7. l is an integer, ω is the angular frequency of light and β is the propagation constant of the mode which is related to the geometric shape of optical fibre and RIs of core and cladding. For light with a certain frequency, each β refers to one transmission mode [27].

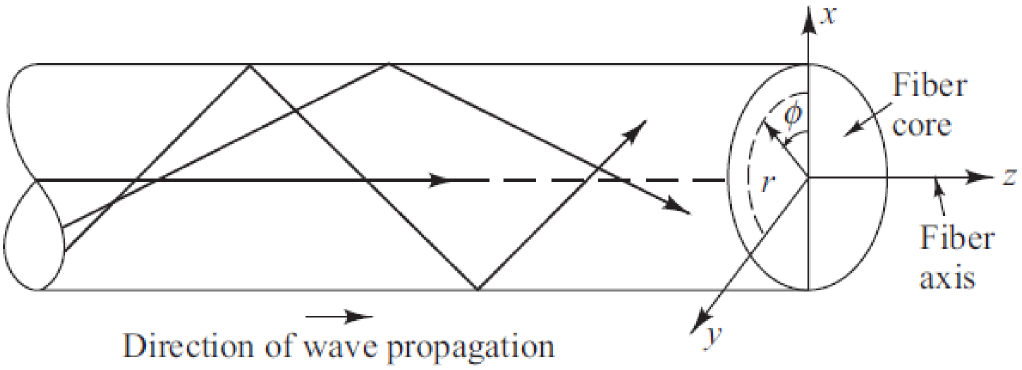

Figure 2- 7. The axis on the cross-section of a cylindrical optical fibre sourced from [27]

$\begin{bmatrix} E_z(r) \\ E_\phi(r) \\ E_r(r) \end{bmatrix}$ and $\begin{bmatrix} H_z(r) \\ H_\phi(r) \\ H_r(r) \end{bmatrix}$ obey the following relationships [27]:

$$E_z(r) = AJ_l\left(\sqrt{{k_1}^2 - \beta^2 r}\right), r < a \tag{2-7a}$$

$$H_z(r) = BJ_l\left(\sqrt{{k_1}^2 - \beta^2 r}\right), r < a \tag{2-7b}$$

$$E_z(r) = CK_l\left(\sqrt{\beta^2 - {k_2}^2 r}\right), r > a \tag{2-7c}$$

$$H_z(r) = DK_l\left(\sqrt{\beta^2 - {k_2}^2 r}\right), r > a \tag{2-7d}$$

$$E_r(r) = -\frac{j}{k^2-\beta^2}(\beta\frac{\partial E_z(r)}{\partial r} + \frac{\mu\omega}{r}\frac{\partial H_z(r)}{\partial \phi}) \tag{2-7e}$$

$$H_r(r) = -\frac{j}{k^2-\beta^2}(\beta\frac{\partial H_z(r)}{\partial r} - \frac{\varepsilon\omega}{r}\frac{\partial E_z(r)}{\partial \phi}) \tag{2-7f}$$

$$E_\phi(r) = -\frac{j}{k^2-\beta^2}(\frac{\beta}{r}\frac{\partial E_z(r)}{\partial \phi} - \mu\omega\frac{\partial H_z(r)}{\partial r}) \tag{2-7g}$$

$$H_\phi(r) = -\frac{j}{k^2-\beta^2}(\frac{\beta}{r}\frac{\partial H_z(r)}{\partial \phi} + \varepsilon\omega\frac{\partial E_z(r)}{\partial r}) \tag{2-7h}$$

Where J_l is the l^{th} order Bessel function of the first kind; K_l is the l^{th} order Bessel function of the second kind; $k_1 = \frac{2\pi n_1}{\lambda}$; $k_2 = \frac{2\pi n_2}{\lambda}$. k_1, k_2, and β obey the relationship $k_2 < \beta < k_1$. The propagation constant β is determined by the following equation [27]:

$$\left(\frac{J_l'\left(\sqrt{{k_1}^2-\beta^2}a\right)}{\sqrt{{k_1}^2-\beta^2}J_l\left(\sqrt{{k_1}^2-\beta^2}a\right)}+\frac{K_l'\left(\sqrt{\beta^2-{k_2}^2}a\right)}{\sqrt{\beta^2-{k_2}^2}K_l\left(\sqrt{\beta^2-{k_2}^2}a\right)}\right)\left({k_1}^2\frac{J_l'\left(\sqrt{{k_1}^2-\beta^2}a\right)}{\sqrt{{k_1}^2-\beta^2}J_l\left(\sqrt{{k_1}^2-\beta^2}a\right)}\right.$$
$$\left.+{k_1}^2\frac{K_l'\left(\sqrt{\beta^2-{k_2}^2}a\right)}{\sqrt{\beta^2-{k_2}^2}K_l\left(\sqrt{\beta^2-{k_2}^2}a\right)}\right)=\left(\frac{\beta l}{a}\right)^2\left(\frac{1}{{k_1}^2-\beta^2}+\frac{1}{\beta^2-{k_2}^2}\right)^2 \tag{2-8}$$

For a weakly-guiding optical fibre, the difference between the RIs of cladding and core is very small $n_1 \approx n_2$ [27]. Equation (8) can be simplified as [27]

$$\left(\frac{J_l'\left(\sqrt{{k_1}^2-\beta^2}a\right)}{\sqrt{{k_1}^2-\beta^2}J_l\left(\sqrt{{k_1}^2-\beta^2}a\right)}+\frac{K_l'\left(\sqrt{\beta^2-{k_2}^2}a\right)}{\sqrt{\beta^2-{k_2}^2}K_l\left(\sqrt{\beta^2-{k_2}^2}a\right)}\right)=\pm\left(\frac{l}{a}\right)\left(\frac{1}{{k_1}^2-\beta^2}+\frac{1}{\beta^2-{k_2}^2}\right) \tag{2-9}$$

Each solution of Equation (2-9) corresponds to a transmission mode's propagation constant. All the transmission modes in a weakly-guiding fibre are linear polarized (LP) [27]. Equation (2-9) is equivalent to [27]:

$$LP_{0m}(l=0)\colon \frac{J_1(\sqrt{{k_1}^2-\beta^2}a)}{J_0(\sqrt{{k_1}^2-\beta^2}a)\sqrt{{k_1}^2-\beta^2}}=\frac{K_1(\sqrt{\beta^2-{k_2}^2}a)}{K_0(\sqrt{\beta^2-{k_2}^2}a)\sqrt{\beta^2-{k_2}^2}} \tag{2-10a}$$

$$LP_{1m}(l=1)\colon \frac{J_0(\sqrt{{k_1}^2-\beta^2}a)}{J_1(\sqrt{{k_1}^2-\beta^2}a)\sqrt{{k_1}^2-\beta^2}}=-\frac{K_0(\sqrt{\beta^2-{k_2}^2}a)}{K_1(\sqrt{\beta^2-{k_2}^2}a)\sqrt{\beta^2-{k_2}^2}} \tag{2-10b}$$

$$LP_{lm}(l>1)\colon \frac{J_{l-1}(\sqrt{{k_1}^2-\beta^2}a)}{J_l(\sqrt{{k_1}^2-\beta^2}a)\sqrt{{k_1}^2-\beta^2}}=-\frac{K_{l-1}(\sqrt{\beta^2-{k_2}^2}a)}{K_l(\sqrt{\beta^2-{k_2}^2}a)\sqrt{\beta^2-{k_2}^2}} \tag{2-10c}$$

Where m corresponds to the m^{th} root of each equation.

Depending on the number of modes that optical fibres can support, they can be classified into single mode fibres and multimode fibres. It can be judged from the normalised frequency of [27].

$$V=\frac{2\pi a}{\lambda}NA \tag{2-11}$$

Where V is the normalised frequency of an optical fibre; NA is the numerical aperture (equation (2-4)); λ is the light wavelength in free space. The number of transmission modes can be estimated by V [27].

$$M \approx \frac{V^2}{2} \tag{2-12}$$

If $V<2.405$, the optical fibre is a single mode fibre, otherwise, it is a multimode fibre. The first four modes that an optical fibre can support are LP_{01}, LP_{11}, LP_{21}, and LP_{22}

[27]. The intensity distribution over the cross-section of an optical fibre is different according to different modes as shown in Figure 2-8.

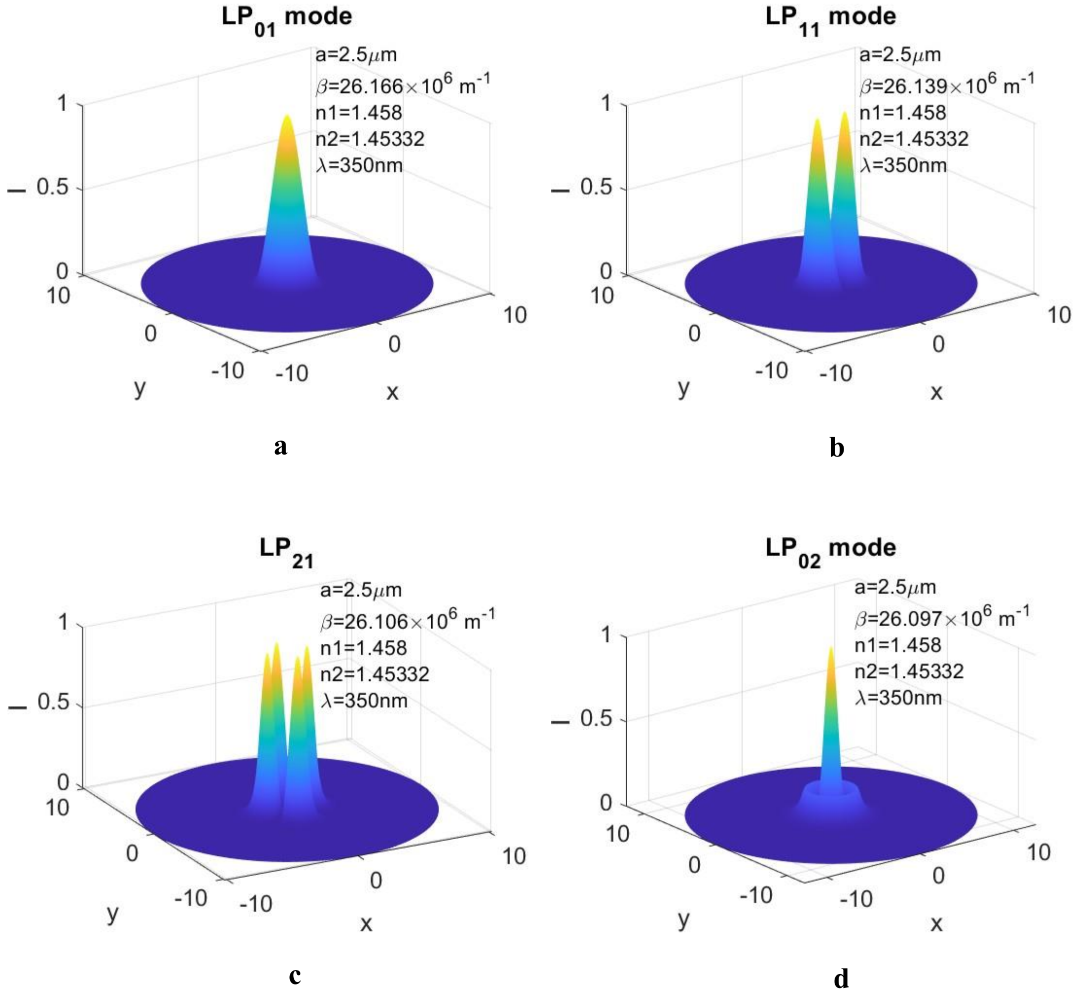

Figure 2- 8. The intensity distribution of different transmission modes of a multimode fibre, a=2.05µm, n1=1.458, n2=1.45332, λ=350nm. (a) LP$_{01}$ mode; (b) LP$_{11}$ mode; (c) LP$_{21}$ mode; (d) LP$_{02}$ mode.

The LP$_{01}$ mode shown in Figure 2-8(a) is the fundamental mode of an optical fibre. It has the greatest propagation constants. LP$_{11}$, LP$_{21}$, and LP$_{02}$ are 2nd-order, 3rd-order, and 4th-order mode respectively. The propagation constant decreases with the order of mode.

2.2.2 Long period grating

A long period grating (LPG) is usually fabricated in a single mode optical fibre by periodically modulating the RI of the core as shown in Figure 2-9 [36].

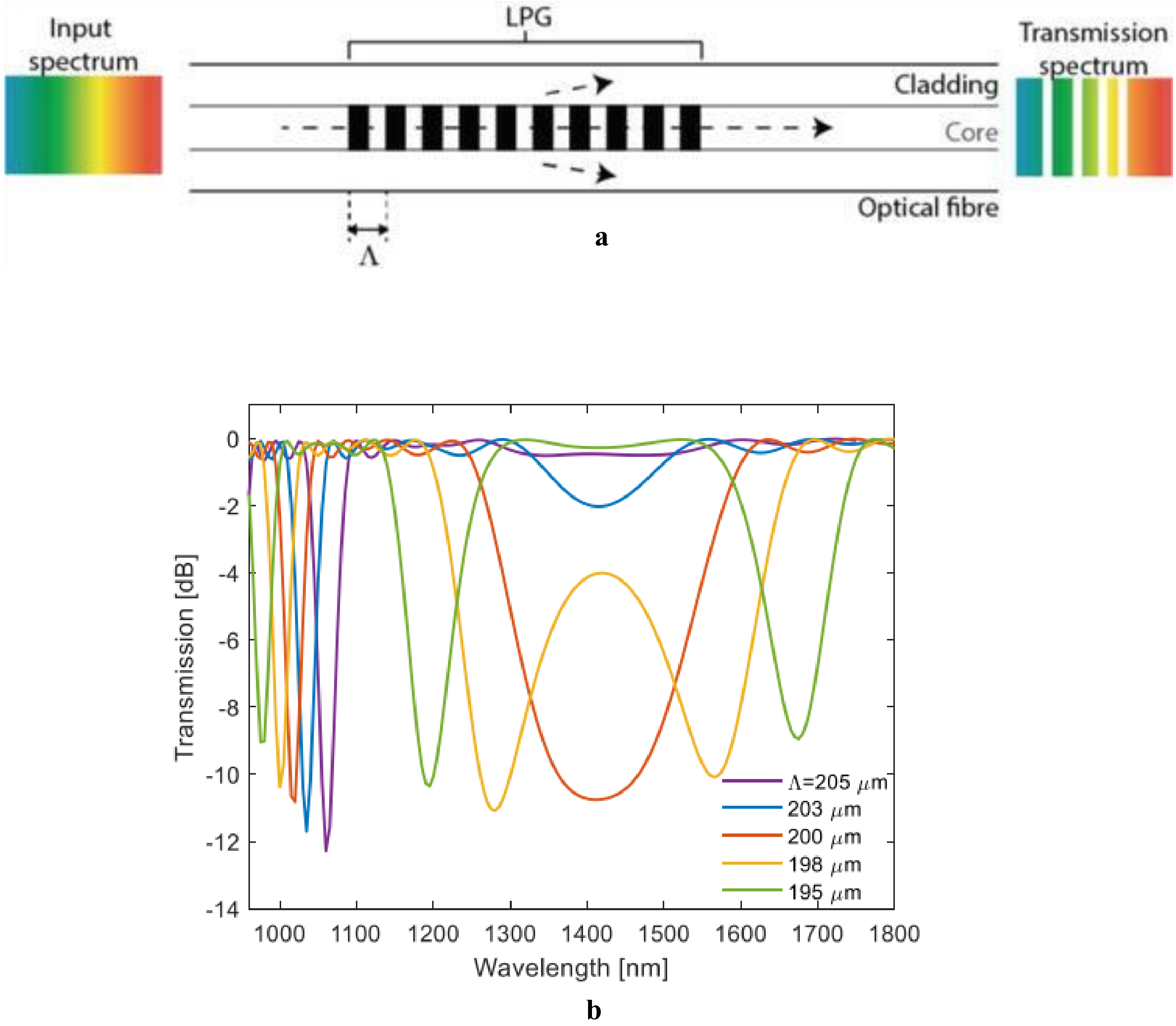

Figure 2- 9. (a) The structure of an LPG sourced from [45]; (b) The transmission spectra of LPGs with different grating periods sourced from [46].

In Figure 2-9(a), the black bars in the core indicate that the RI of those positions are modulated to a higher value. The black bars are distributed uniformly in a certain area, which is called grating region. Λ is the period of the grating region which ranges from 50μm to 500μm. Due to the mismatch in the RI over the grating region, the light propagating in the core can be coupled into cladding modes [36]. The cladding modes are attenuated during transmission [36] which induces attenuation bands in the transmission spectrum (Figure 2-9(b)). Different attenuation bands in a spectrum refers to the coupling to different cladding modes [47]. The gratings might have different profiles which can be described by a function [47], [48]:

$$\Delta n_1(z) = \overline{\Delta n_1}(z)\{\xi + \rho cos\left(\frac{2\pi}{\Lambda}z + \varsigma(z)\right)\} \tag{2-13}$$

Where $\Delta n_1(z)$ is the RI difference at a longitudinal position z; $\overline{\Delta n_1}(z)$ is the envelope of grating; ξ is 'dc' part of the grating; $\rho cos\left(\frac{2\pi}{\Lambda}z+\varsigma(z)\right)$ is the 'ac' part of the grating; ρ is the amplitude; Λ is period; $\varsigma(z)$ is the phase offset at a longitudinal position z. A few examples of gratings are shown in Figure 2-10.

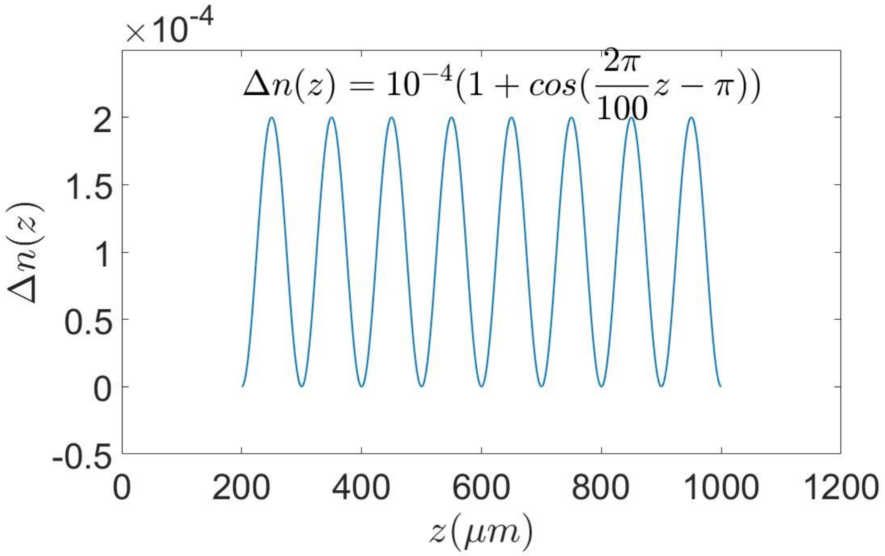

a

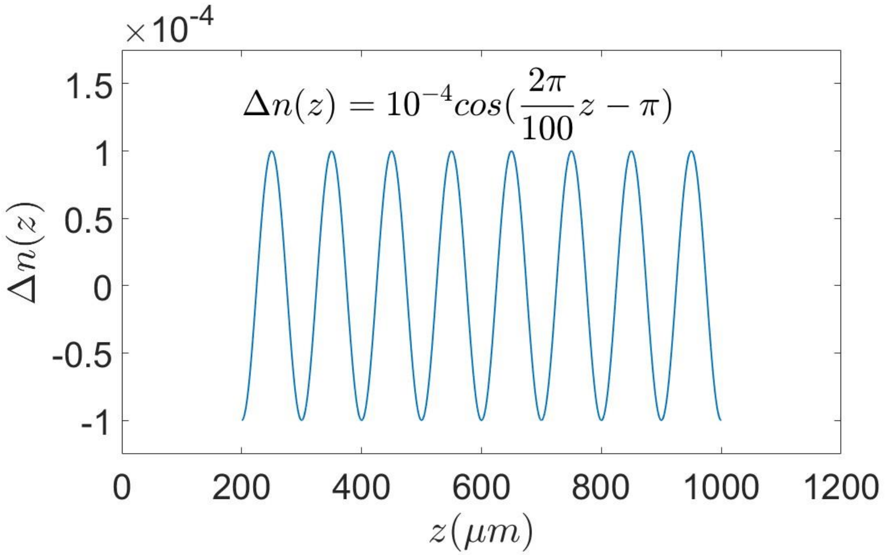

b

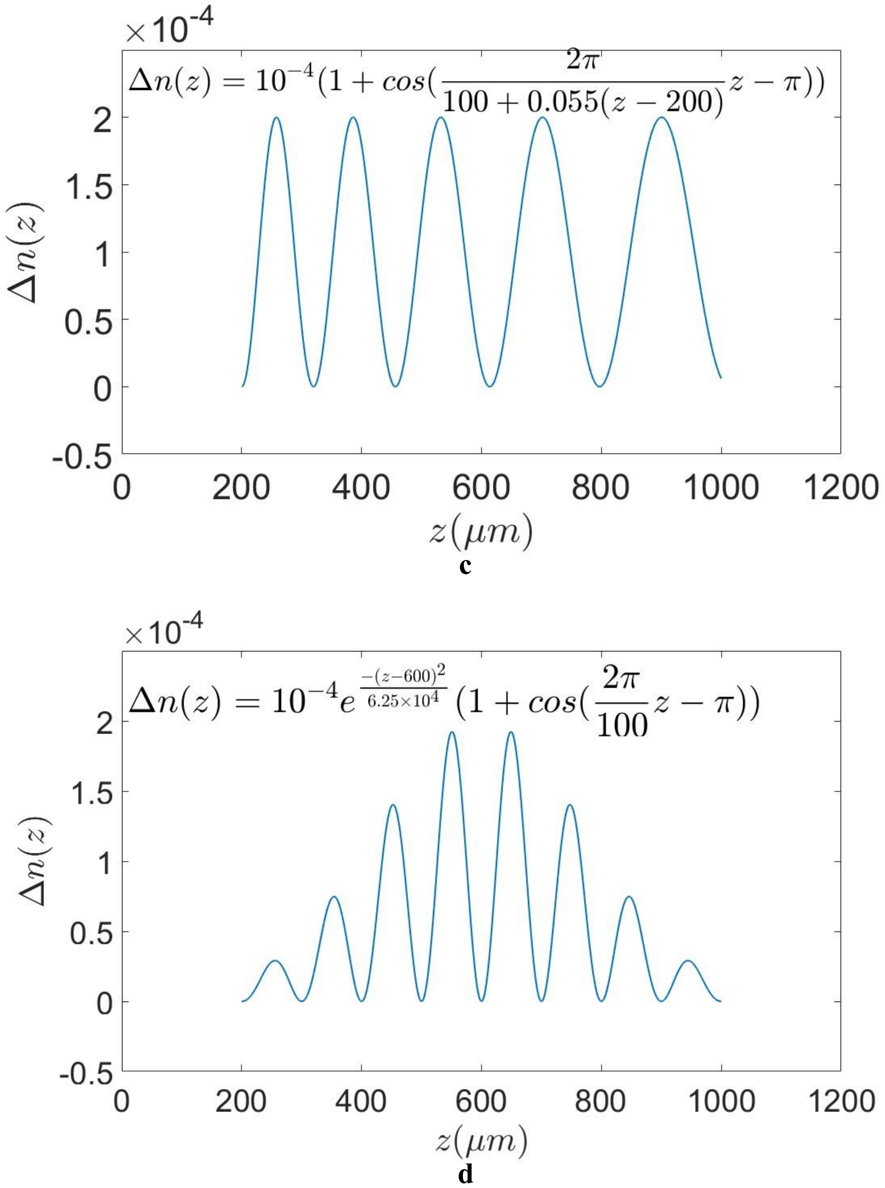

Figure 2- 10. Examples of grating profiles. (a) Uniform grating; (b) Uniform grating without 'dc' part; (c) Chirped grating; (d) Uniform grating with Gaussian envelope.

Figure 2-10(a) shows the profile of a uniform LPG. It has a constant envelope of 10^{-4} refractive index units (RIU) and a grating period of 100μm. The 'dc' part of the grating is 1. Figure 2-10(b) also shows a uniform LPG, but the 'dc' part is zero. This profile is widely used in the simulation of LPGs. Figure 2-10(c) shows an example of a chirped grating whose grating period changes with longitudinal position *z*. It starts from 100μm and increases linearly by 5.5μm every 100μm. Figure 2-10(d) shows a grating with a Gaussian envelope.

An approximated analysis of an LPG can be conducted by coupled mode theory [49], [50].

$$\psi(r,\phi,z,t) = R(z)\psi_R(r,\phi)e^{j(\omega t-\beta_R Z)} + S(z)\psi_S(r,\phi)e^{j(\omega t-\beta_S Z)} \tag{2-14}$$

In equation (2-14), ψ is the electrical or magnetic field at time t and position (r, ϕ, z); ψ_R and ψ_s are the normalised core-mode filed distribution and cladding-mode field distribution over the cross-section respectively. Since core-mode wave and cladding-mode wave are coupled into each other during transmission, $R(z)$ and $S(z)$ are the amplitudes of core-mode wave and cladding-mode wave respectively at longitude position z. β_R and β_S are the propagation constants of core-mode wave and cladding-mode wave respectively. ω is the angular frequency of light. The aim of the analysis of an LPG is to find the solutions of $R(z)$ and $S(z)$. It can be done by solving the Equations 2-15a-g) [49], [50].

$$\frac{dR(z)}{dz} = j\hat{\sigma}R(z) + jvS(z) \tag{2-15a}$$

$$\frac{dS(z)}{dz} = -j\hat{\sigma}S(z) + jv^*R(z) \tag{2-15b}$$

$$\hat{\sigma} = \delta + \frac{\sigma_{SS} - \sigma_{RR}}{2} \tag{2-15c}$$

$$\delta = \frac{1}{2}(\beta_R - \beta_S) - \frac{\pi}{\Lambda} \tag{2-15d}$$

$$\sigma_{SS} = \frac{\omega n_1 \overline{\Delta n_1}(z)}{2} \iint r dr d\phi (\boldsymbol{e_S} \cdot \boldsymbol{e_S^*}) \tag{2-15e}$$

$$\sigma_{RR} = \frac{\omega n_1 \overline{\Delta n_1}(z)}{2} \iint r dr d\phi (\boldsymbol{e_R} \cdot \boldsymbol{e_R^*}) \tag{2-15f}$$

$$v = \frac{\omega n_1 \overline{\Delta n_1}(z)\rho}{4} \iint r dr d\phi (\boldsymbol{e_R} \cdot \boldsymbol{e_S^*}) \tag{2-15g}$$

Where σ_{SS} and σ_{RR} are the ‘dc’ self-coupling constants of cladding mode and core mode respectively; $\boldsymbol{e_S}$ and $\boldsymbol{e_R}$ are the normalised electrical field of cladding mode and core mode respectively; v is the ‘ac’ cross-coupling constant between core mode and cladding mode. The analytical solutions of $R(z)$ and $S(z)$ are [50]:

$$R(z) = \left[\cos\left(vz\sqrt{1+\left(\frac{\hat{\sigma}}{v}\right)^2}\right) + j\frac{\hat{\sigma}}{v\sqrt{1+\left(\frac{\hat{\sigma}}{v}\right)^2}} sin\left(vz\sqrt{1+\left(\frac{\hat{\sigma}}{v}\right)^2}\right)\right] R(0) + j\frac{v}{\sqrt{\hat{\sigma}^2+v^2}} sin\left(vz\sqrt{1+\left(\frac{\hat{\sigma}}{v}\right)^2}\right) S(0) \tag{2-16a}$$

$$S(z) = \left[\cos\left(vz\sqrt{1+\left(\frac{\hat{\sigma}}{v}\right)^2}\right) - j\frac{\hat{\sigma}}{v\sqrt{1+\left(\frac{\hat{\sigma}}{v}\right)^2}} sin\left(vz\sqrt{1+\left(\frac{\hat{\sigma}}{v}\right)^2}\right)\right] S(0) + j\frac{v}{\sqrt{\hat{\sigma}^2+v^2}} sin\left(vz\sqrt{1+\left(\frac{\hat{\sigma}}{v}\right)^2}\right) R(0) \tag{2-16b}$$

Where $R(0)$ and $S(0)$ are the amplitudes of core mode and cladding mode at longitudinal position z respectively. Say $R(0) = 1$ and $S(0) = 0$, the transmission of an LPG is derived [49]:

$$T_{LPG} = cos^2\left(vz\sqrt{1+\left(\frac{\hat{\sigma}}{v}\right)^2}\right) + \left(\frac{\hat{\sigma}}{v}\right)^2 sin^2\left(vz\sqrt{1+\left(\frac{\hat{\sigma}}{v}\right)^2}\right) \tag{2-17}$$

The transmission reaches the local minimal if $\delta = 0$. The resonance wavelengths of an LPG are [36]:

$$\lambda_x = (n_{eff}^{co} - n_{eff}^{cl,x})\Lambda \tag{2-18a}$$

$$n_{eff}^{co} = \frac{\lambda_{co}\beta_R}{2\pi} \tag{2-18b}$$

$$n_{eff}^{cl,x} = \frac{\lambda_{cl,x}\beta_S}{2\pi} \tag{2-18c}$$

Where λ_x is the wavelength of the x^{th} attenuation band; n_{eff}^{co} is the effective RI of the core mode; $n_{eff}^{cl,x}$ is the effective RI of the x^{th} cladding mode; λ_{co} is the wavelength of core-mode light; $\lambda_{cl,x}$ is the wavelength of the x^{th}-cladding-mode light. The wavelengths of an LPG's attenuation bands are sensitive to the RI of the external medium. It is mainly because the effective RIs of cladding modes change with external RI [51]:

$$\left(\frac{2\pi}{\lambda_p}\right) D_{clad}\sqrt{(n_{clad})^2 - \left(n_{eff}^{cl,p}\right)^2} - \left(p - \frac{3}{4}\right)\frac{\pi}{2} = 2arccos\sqrt{\frac{(n_{clad})^2 - \left(n_{eff}^{cl,p}\right)^2}{(n_{clad})^2 - (n_{ext})^2}} \tag{2-19}$$

Where λ_p is the wavelength of the p^{th} attenuation band; D_{clad} is the diameter of the cladding; n_{clad} is the RI of the cladding; $n_{eff}^{cl,p}$ is the effective RI of the p^{th} cladding mode; n_{ext} is the RI of external medium. The designing of bio-/chemical sensors based on an LPG exploits its response to external RI. The wavelengths also change with other physical parameters such as temperature and strain [36].

2.2.3 Optical fibre sensors

Optical fibre sensors are extensively used in structural monitoring, biomedical sensing, and point-of-care instruments due to their advantages such as light weight, small size, and immunity to electromagnetic interference [28], [52], [53]. A sensor is a device that can respond to a stimulus [54]. It usually transduces a stimulus to other more processible signals, typically electronic signals [54]. A schematic to generally describe an optical fibre sensor is shown in Figure 2-11.

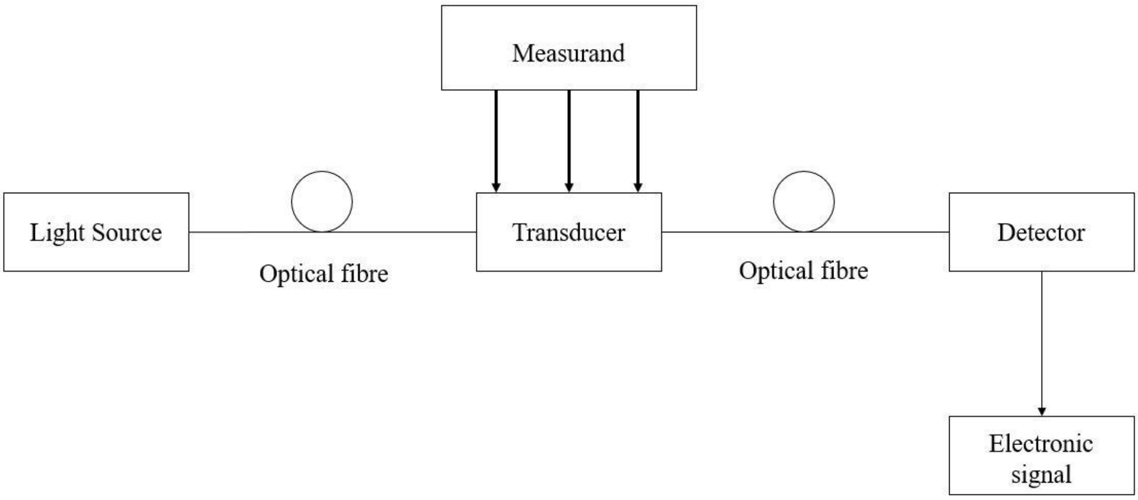

Figure 2- 11. The schematic of an optical fibre sensor

As shown in Figure 2-11, an optical fibre sensor consists of a light source, a transducer, and a detector that are all connected by optical fibres. The incident light is modulated by a transducer and finally goes to a detector. When a stimulus is applied to the transducer, the modulation on the transmitted light is changed, which can be observed by a detector. Depending on the applications, different light sources and detectors can be selected. For example, a halogen tungsten light source can cover a broad spectrum; a light emitting diode (LED) has low power consumption, small size, and is convenient to modulate; a spectrometer can detect a broad spectrum with high accuracy and resolution; a photodiode has small size and is easy to be integrated in circuits. There are several configurations on which optical fibre sensors can be developed.

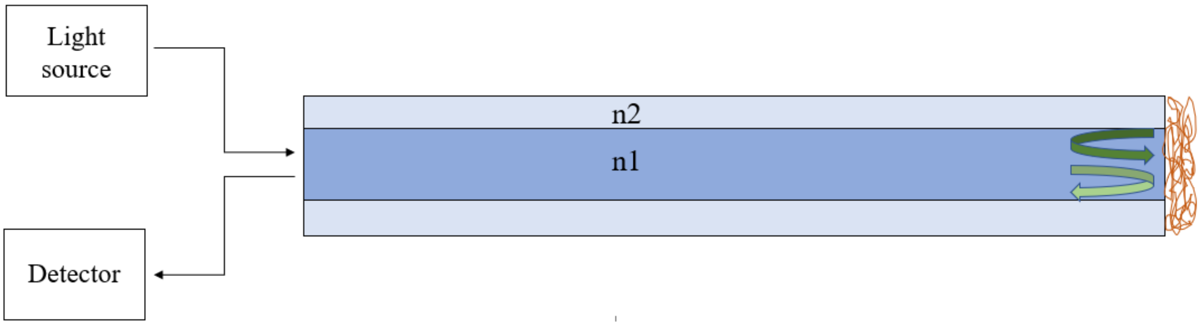

Figure 2- 12. Optical fibre sensor based on the tip of a fibre.

A sensor can be fabricated based on the tip of an optical fibre by depositing measurand-sensitive materials. Light is transmitted to the tip and is then reflected and changes in the measurand modulate the light. Some parameters such as light absorbance and the wavelength of the absorbance peak change with external environment [55], [56]. Many sensors have been fabricated based on the tip of optical fibre such as carbon dioxide (CO_2) concentration sensor [55], ammonia (NH_3) concentration sensor [57], relative humidity (RH) sensor [58], temperature sensor [59], and a biomolecule concentration sensor [55], [56], [60]. The optical fibre is not modulated by the measurand directly and it only works as a waveguide. Therefore, it is classified as an extrinsic optical fibre sensor.

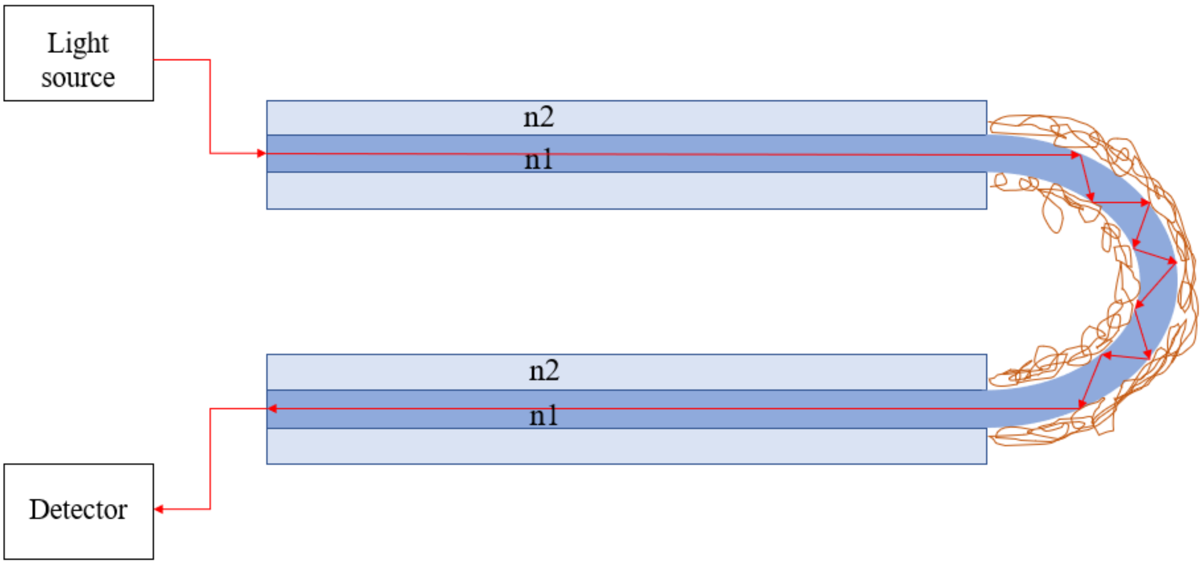

Figure 2- 13. Optical fibre sensor based on a U-shaped fibre.

As shown in Figure 2-13, a U-shape is fabricated on a fibre. Due to the large curvature of the U-shaped region, light propagating in the fibre penetrates fibre-medium interface and gets modulated [61], [62]. The changes of the geometric properties of U-shape region or the optical properties of external medium (such as RI and spectral absorbance) can modulate the transmitted light [61], [62]. By depositing different sensitive materials on the U-shape region, different sensors such as a biomolecular concentration sensor [60], pH sensor [63], propofol concentration sensor [64], and NH_3 concentration sensor have been designed [60], [65]. They are extrinsic optical fibre sensors as a U-shape fibre only transmits light and is not changed by the measurand. Light transmitted through the U-shape region is modulated by the RI or light absorbance change of sensitive coatings.

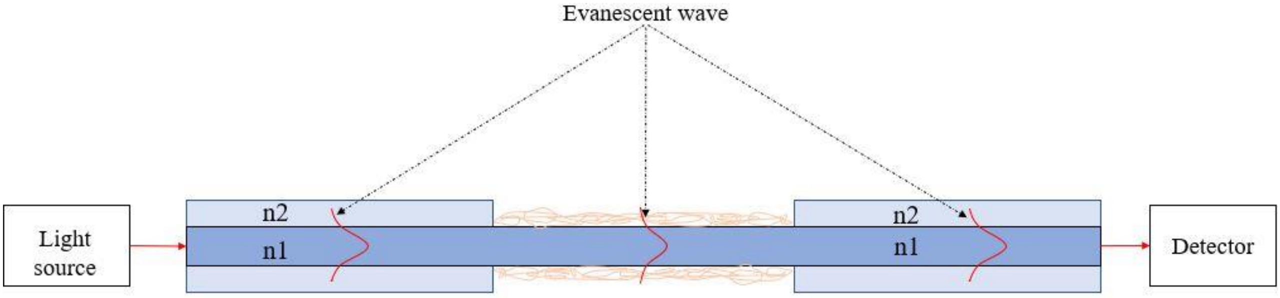

Figure 2- 14. Optical fibre sensor based on cladding-removed fibre.

As shown in Figure 2-14, a sensor can be fabricated based on a cladding-removed optical fibre. When the light goes through the cladding-removed region, the evanescent wave probes into external medium thus the light gets modulated. The penetration depth of the evanescent wave is [28]:

$$d_p = \frac{\lambda}{2\pi\sqrt{(n_{eff})^2 - (n_s)^2}} \tag{2-20}$$

Where λ is the light wavelength in free space; n_{eff} is the effective RI of the transmission mode; n_s is the RI of surrounding medium. The evanescent wave can be absorbed by external medium. The intensity of transmitted light obeys the Lambert-Beer law [28]:

$$\frac{I_1}{I_0} = c \cdot \alpha \cdot L \tag{2-21}$$

Where I_1 is the transmitted intensity; I_0 is the incident intensity; c is the concentration of the light absorbing substance; α is the molar extinction coefficient of a substance; L

is the optical path length. A cladding-removed fibre is also a platform to achieve Lossy Mode Resonance (LMR) and Surface Plasmon Resonance (SPR) based sensing [66]-[69]. Nitrogen dioxide (NO_2) sensor [70], Volatile Organic Compounds (VOC) sensor (such as Ethanol, Methanol and Ammonia) [71], pH sensor [72], and biomolecule sensor are designed based on cladding-removed fibre [60]. The cladding-removed fibre usually works as extrinsic sensor as the fibre doesn't transduce the measurand.

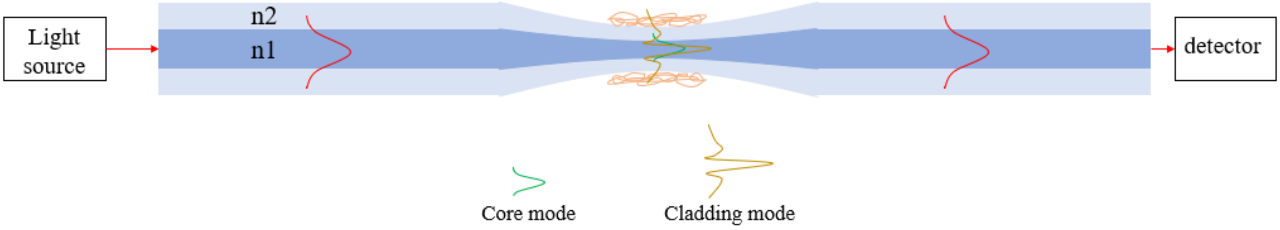

Figure 2- 15. Optical fibre sensor based on tapered optical fibre.

A tapered optical fibre is shown in Figure 2-15. The tapered region is much thinner than the normal region. Tapered optical fibres possess two properties: i) the core-mode light is coupled into cladding-modes when it propagates through the tapered region, and they interfere with each other when they re-enter the normal region, forming interference fringes in the transmission spectrum; ii) the cladding-mode light penetrates the external medium and becomes modulated [73]. The transmission spectrum responds to the changes of optical properties of external medium such as RI and optical absorbance [73]. When a sensitive material is deposited on the tapered region, the cladding-mode light is therefore modulated by the measurand. A biomolecule sensor [60], an hydrogen (H_2) concentration sensor [74], and an NH_3 concentration sensor are examples of numerous sensors that have been developed based on tapered optical fibres [75].

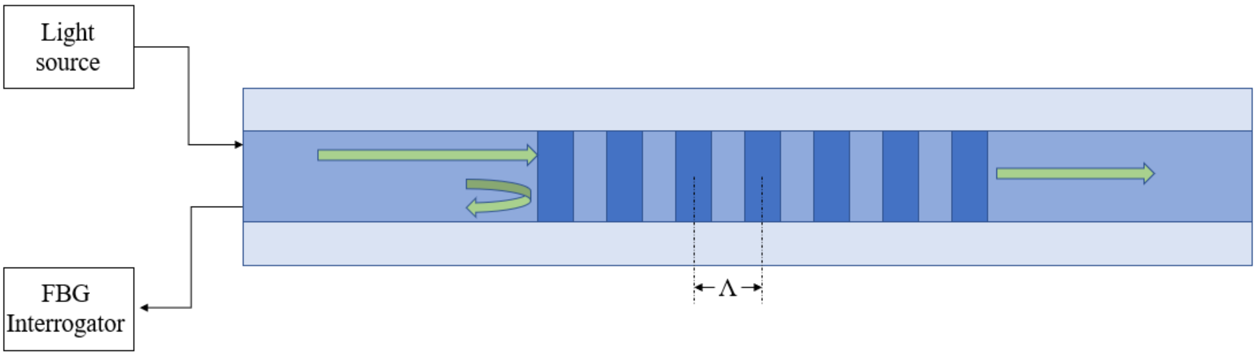

Figure 2- 16. A fibre Bragg grating.

Like an LPG, a Fibre Bragg Grating (FBG) is fabricated by periodically modulating the RI of the core of a single mode fibre. The grating period Λ is around 1µm. When light propagates through the grating region, light of a specific wavelength is reflected [28]:

$$\lambda_{Bragg} = 2n_{eff}\Lambda \tag{2-22}$$

Where λ_{Bragg} is the wavelength of the reflected light, also called the Bragg wavelength; n_{eff} is the effective RI of the transmission mode. λ_{Bragg} is typically affected by temperature and strain. The wavelength shift is approximately [28]:

$$\Delta\lambda = \lambda_{Bragg}[(1 - P_e)\acute{\varepsilon} + ((1 - P_e)\alpha - \xi)\Delta T] \tag{2-23}$$

Where P_e is the photo-elastic coefficient of the optical fibre, ξ is the thermo-optic coefficient of the optical fibre; $\acute{\varepsilon}$ is the strain; α is the thermal expansion coefficient; ΔT is the temperature change. Applications of FBGs exploit their responses to temperature and strain. FBG-based sensors have been used in many areas such as structural health monitoring [76], wearable devices to measure respiratory and cardiac rates and joints' movement [77], [78], and pH sensing [79]. FBG-based sensors are mostly intrinsic as the measurand affects the FBG directly. Strain or temperature can change the geometric shape or optical properties of an FBG, which modulate the reflected spectrum.

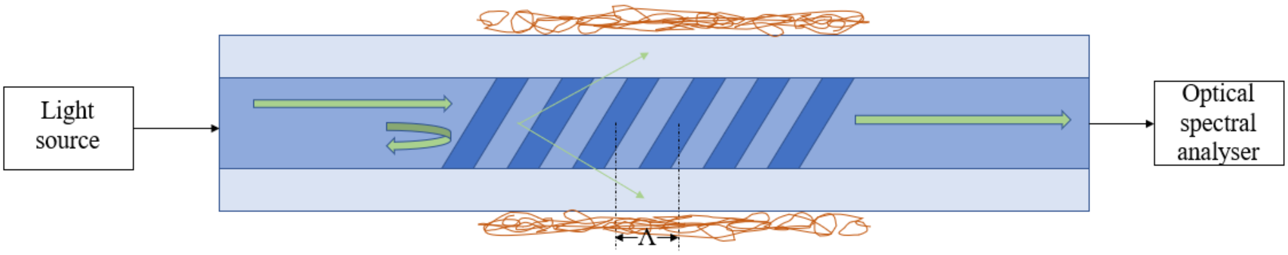

Figure 2- 17. Sensor based on tilted fibre Bragg grating.

A Tilted Fibre Bragg Grating (TFBG) has a grating period Λ of around 1µm. However, the RI modulated region is not orthogonal to the fibre core as shown in Figure 2-17. When the incident light propagates through the grating, light at the Bragg wavelength is reflected. In the meantime, some light is coupled into cladding modes from the core mode. The cladding modes are attenuated during transmission, which leads to the attenuation bands in the transmission spectrum. Like an FBG, the reflection wavelength of a TFBG responds to temperature and strain [80], [81]. The cladding modes of a

TFBG are sensitive to temperature, strain, and the RI of the external medium [80], [81]. A TFBG can be directly used to measure temperature, strain, and curvature [80], [81]. Its responsivity to external RI can be exploited by coating sensitive materials on the surface. A H_2 concentration sensor [82], [83], RH sensor [84], and pH sensor are fabricated with a TFBG using this method [85]. A TFBG can work either as an extrinsic sensor or an intrinsic sensor. When detecting temperature, strain, and curvature, the optical fibre is directly affected by measurand to change the geometric shape. It is an intrinsic sensor. However, it is an extrinsic sensor when designed as a bio-/chemical sensor.

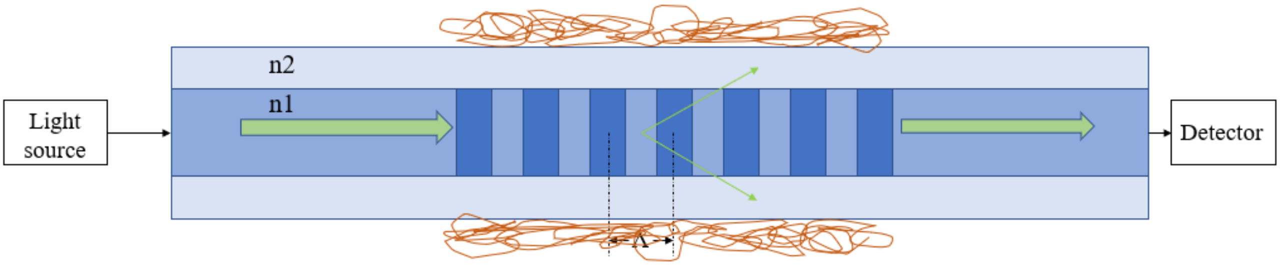

Figure 2- 18. Sensor based on an LPG.

Designing sensors based on an LPG exploits its response to the change of external RI. An LPG is usually used along with functional coatings. The change of measurand affects the RI of functional coatings, which further affect the transmission spectrum of the LPG. Therefore, an LPG can work as an extrinsic sensor. For example it has been used in CO_2 sensing [86], RH sensing [87], and biomolecule sensing [60]. LPGs are also designed as intrinsic sensors to measure parameters such as curvature and temperature [88], [89]. The geometric shape of the LPG is changed by the measurand and transmission spectrum is affected.

Figure 2- 19. A Fabry-Perot interferometer based in an optical fibre.

Figure 2-19 shows the structure of an in-fibre Fabry-Perot Interferometer (FFPI) in which a cavity is fabricated at the distal end of an optical fibre. The incident light is reflected at both fibre-cavity interface and external reflector. An interference pattern is therefore formed in the reflected light and observed by the detector (usually an Optical Spectral Analyser (OSA)). The reflected light can be described as [90]:

$$I(\lambda) = I_1(\lambda) + I_2(\lambda) + \sqrt{I_1(\lambda) I_2(\lambda)} \cos\left(\frac{4\pi n_m L}{\lambda} + \Theta_0\right) \qquad (2\text{-}24)$$

Where λ is the wavelength of reflected light; $I(\lambda)$ is the observed light intensity; $I_1(\lambda)$ and $I_2(\lambda)$ are the reflected light intensities at the fibre-cavity interface and external reflector respectively; L is cavity length; n_m is the RI of the cavity medium; Θ_0 is the phase shift introduced by the reflection. In practice, the FFPI can have different structures as shown in Figure 2-20 [90].

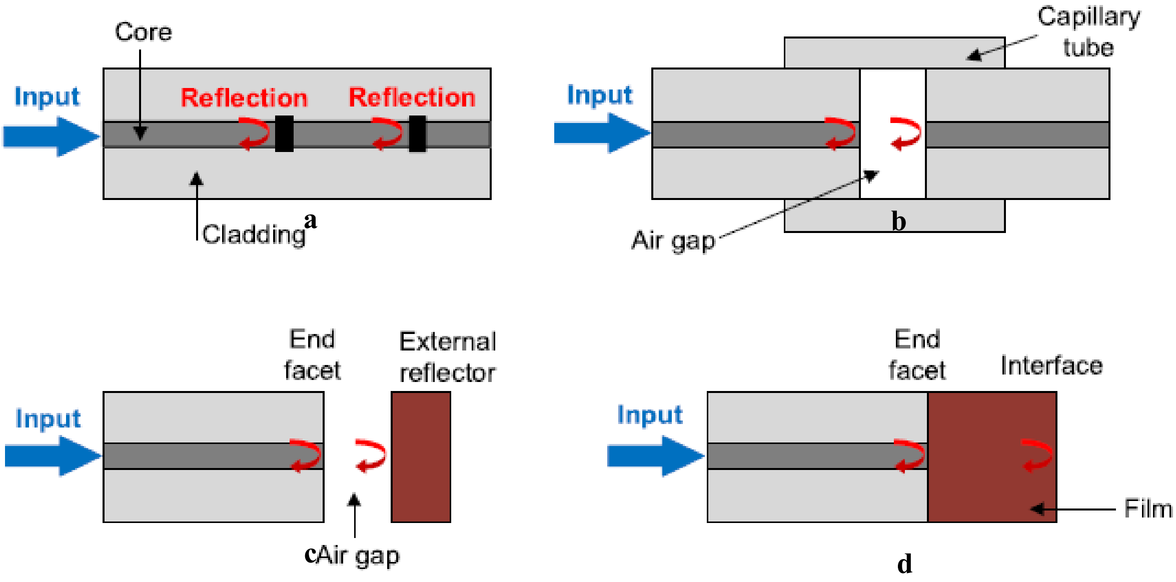

Figure 2- 20. 4 types of in-fibre Fabry-Perot interferometers sourced from [75]. (a) intrinsic FFPI; (b) FFPI fabricated by cascading two fibres; (c) FFPI with an external reflector; (d) FFPI fabricated by depositing a film at the end of fibre.

Figure 2-20(a) shows an FPI fabricated in-fibre. Two RI-discontinuity points are made inside an optical fibre by femtosecond laser machining or fusion-splicing. Since the FPI is fabricated in fibre, it can be small in size, but fragile. Strain sensor and curvature sensor are made based on this configuration [91], [92]. Figure 2-20(b) shows an FFPI fabricated by cascading two optical fibres. A section of capillary tube is fused between two optical fibres and light is reflected at the two fibre-cavity interfaces. Strain sensors based on this configuration are stronger and have a larger measurement range than sensors based on in-fibre configuration [93]. Figure 2-20(c) shows the structure of an FFPI with an external reflector. The reflector is positioned away from the optical fibre by a certain distance. This configuration is typically suitable for displacement sensors and contact force sensors [94], [95]. By attaching a free external reflector to an objective, displacement sensors can be fabricated [94]. In another aspect, if an external reflector is fixed by mechanical components, contact pressure sensors or force sensors can be fabricated [95]. Figure 2-20(d) shows the structure of an FFPI fabricated by depositing a film on the tip of an optical fibre. The film works as the cavity and light is reflected at the fibre-film interface and film-external-medium interface. This configuration is typically suitable for chemical sensors. Humidity and CO_2 sensors have been developed based on it [96], [97]. An FFPI-based sensor can be intrinsic or extrinsic. Figure 2-20(a) is a typical intrinsic FFPI-based sensor structure in which changes happen to the fibre between the two RI-discontinuity points during the sensing process. Figures 2-20(b-d) are extrinsic FFPI-based sensor structures as the optical fibre doesn't change during sensing process.

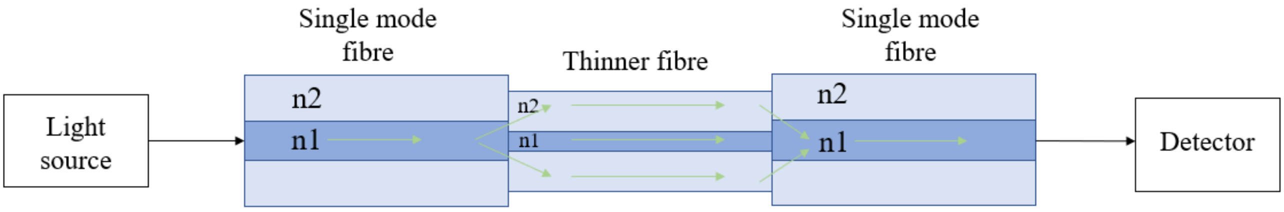

Figure 2- 21. An in-fibre Mach-Zehnder interferometer

Another type of optical interferometer based on an optical fibre is the in-fibre Mach-Zehnder interferometer (FMZI). The interference between different transmission modes will cause interference fringes in the transmission spectrum. Optical-property mismatches along an optical fibre can make an in-fibre Mach-Zehnder interferometer. As shown in Figure 2-21, a thinner fibre (TF) is spliced between two identical single-mode fibres (SMF) [98]. When the incident light arrived at the first SMF-TF interface, part of the energy is coupled into cladding modes from the core mode. The cladding modes and core mode then propagate in parallel in the TF. When the light arrives at the second TF-SMF interface, the cladding modes that couple back interfere with the core mode. Apart from splicing a different fibre between two identical fibres, an FMZI can be fabricated with many other methods such as cascading two tapered fibres, splicing a fibre with core offset between two fibres, and cascading two LPGs [84]. The transmission light of an in-fibre interferometer is [98]:

$$I(\lambda) = I_{core}(\lambda) + I_{clad}(\lambda) + 2\sqrt{I_{core}(\lambda) I_{clad}(\lambda)} \cos\left(\frac{2\pi \Delta n_{eff} L}{\lambda}\right) \tag{2-25}$$

Where λ is the wavelength of light; I_{core} is the intensity of core mode; I_{clad} is the intensity of cladding mode; Δn_{eff} is the difference between the effective RIs of core and cladding modes; L is the distance that the core mode and cladding mode propagate in parallel. The effective RI of cladding-mode light changes with external RI, which causes a wavelength shift of the interference pattern [99]. In another aspect, changes of geometric shape of the FMZI can also cause the wavelength shift of the interference pattern [100]. Examples of designs based on an FMZI are biosensor [101], strain sensor [102], temperature sensor [102], [103], and liquid level sensor [104], [105].

A brief review of the working principles and applications of several optical fibre sensor configurations is conducted in this section. These sensor configurations respond to either a change of optical properties such as RI and absorbance or the parameters causing a change to the optical fibre such as strain and temperature. Sensors can be developed by functionalizing these configurations such as coating functional films to fabricate bio-/chemical sensors based on LPGs, tapered fibres, and U-shaped fibres, or using these prototypes directly without functionalization such as measuring pressure with FBG arrays and measuring liquid level with FMZI. The sensor configurations in which the light intensity is measured suffer from the power fluctuation of light source such as U-shaped fibre and cladding-removed fibre, while the configurations in which wavelength is measured don't. U-shape fibre, FBG, and sensors based on the tip can operate as probes. They can be put into a small and remote space easily and are more flexible than transmission-mode configurations such as LPG, TFBG, tapered fibre, and cladding-removed fibre.

2.3 Current biosensing technologies

Biosensors usually detect analytes which are of biological origin such as DNA, bacteria, antibodies, or any compounds generated by organisms [106]. Biosensors have been used extensively in disease diagnosis, food safety, environmental monitoring, and in the pharmaceutical industry [106], [107]. The detection of human antibodies plays an important role in disease diagnosis [108]-[110]. Biosensing technologies can be based in the lab relying on skilled technicians and bulky equipment such as Enzyme-Linked Immunosorbent Essay (ELISA) and Surface Plasmon Resonance (SPR) [111], [112]. They can also be made user-friendly and Point-of-Care (PoC) such as paper-based immunoassay, optical fibre biosensors, and electronic biosensors. These are promising technologies to make PoC, rapidly responding, and low-cost biosensors.

2.3.1 Enzyme-Linked Immunosorbent Assay

Enzyme-Linked Immunosorbent Essay (ELISA) is currently the most widely used technique to detect biomolecules [13], [113], [114]. An example of ELISA is illustrated in Figure 2-22. The bio-receptor to the target analyte is immobilized on a solid support. It then takes several incubation and washing steps to immobilize the analytes and enzyme-linked secondary bio-receptor on the solid support. Finally, a substrate to the enzyme is added, which results in a colorimetric readout. The intensity of the colour indicates the concentration of analyte in the sample. ELISA possesses a high specificity to the target analytes. However, it is time consuming, and it can’t provide real-time readout [115]-[118]. Although including multiple testing wells in one ELISA plate can improve the throughput, the time required for completing each ELISA process isn’t reduced. Based on the same principle, fluorescent ELISA (FELISA) can be implemented. FELISA uses bio-receptors conjugated to fluorescent dye [119]-[121]. It has a larger dynamic range [122]. Fluorescence is excited by light with specific wavelength [123]. The fluorophore suffers from photobleaching, which is an irreversible process that hinders the fluorophore ability to emit fluorescence permanently [123]. The photobleaching rate depends on the type of fluorophore and the power excitation light [123]. Quantitative information can be acquired by analysing the ELISA plate with a plate reader, which is an optical system to detect the colorimetric change of on the plate [16]. The plate reader is bulky. Research activities have been taken to miniaturizing the plate reader and fastening ELISA process. For example, a smartphone-based computer vision technology is developed to replace the plate reader [17]. It has compacted size and portable. However, the multiple incubation and washing steps is still carried out manually. An ELISA has been implemented based on magnetic beads functionalized with bio-receptors [18]. The protocol is assisted with a particle manipulation machine. It can save labour and reaction time. The time required for running the protocol is less than 10 minutes. It pushes ELISA one step forward to PoC use. However, the particle manipulation machine is complex. The reagent loading should be done manually at the beginning of the protocol. The working principle of ELISA determines it's hard to implement in-vivo and continuous monitoring of analytes as there are multiple reagents exchanging steps.

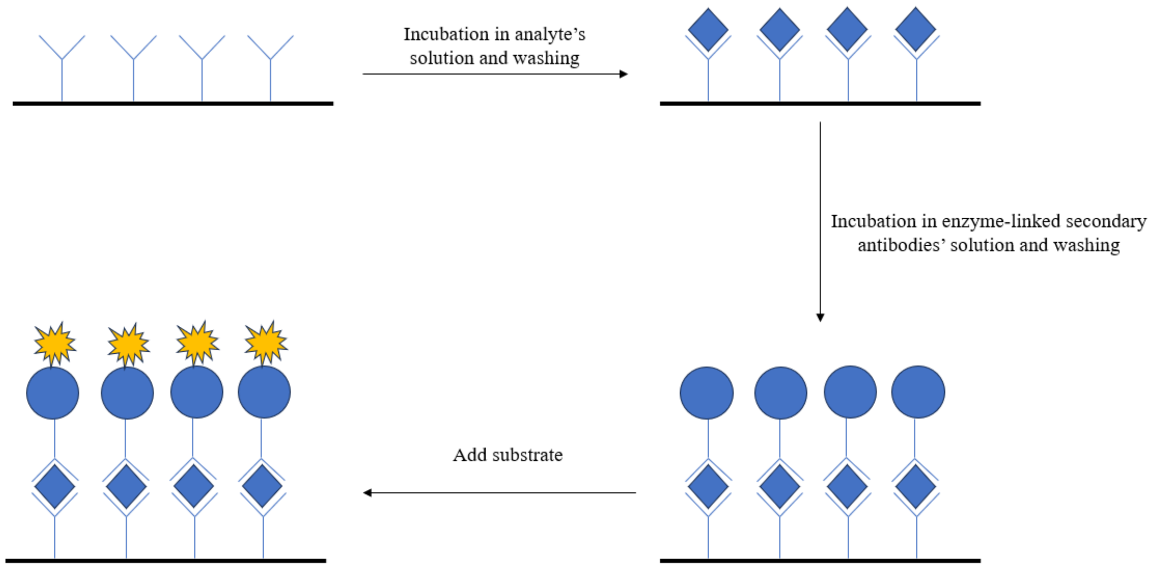

Figure 2- 22. The ELISA technique.

2.3.2 Western Blotting

Traditional western blotting (WB) technology is used to detect a wide range of proteins. It makes use of polyacrylamide gel electrophoresis (PAGE). The proteins experience separation, blotting transfer, and the visualization of target analyte in a traditional WB analysis [14], [19], [20]. The processes are illustrated in Figure 2-23(a). The wells at a side of a polyacrylamide gel (PAG) are filled with sample to be analysed. Different proteins travel with different velocities in PAG when voltage is applied due to the difference in molecular weight and electrical properties. Protein bands are formed in the PAG which are then transferred to a polyvinylidene difluoride (PVDF) membrane. Like ELISA, after several incubation and washing steps, the primary bio-receptor and enzyme-linked secondary bio-receptors are immobilized on the PVDF membrane. The substrate is then added to visualize the analyte with high specificity. However, a traditional WB analysis takes even longer time than ELISA. The first separation typically takes hours to be completed under 60V to 140V voltage [21], the blotting transfer typically takes 1.5 hours [19] and visualization of analyte takes another several hours [19], [21]. There is high requirement for the quality control of PAG and PVDF membrane during the handling process. It involves lots of manual work operated by experienced technicians, therefore, traditional WB can't satisfy PoC requirements. The automation of WB can be improved by combining traditional WB and flow system. As shown in Figure 2-23 (b), to improve the electrophoresis, PVDF membrane is attached to a translation stage [124]. Microchannels with 15μm depth and 50μm width are fabricated on a glass chip by wet etching. The chip is vertical to the translation stage and the outlet of microchannel contacts the PVDF membrane. The voltages of 3.9kV and 4.6kV are applied to sample reservoir (S) and buffer reservoir (BR) respectively. In the meantime, the translation stage moves with a speed of 4mm/min. The proteins are separated and deposited on the PVDF membrane. Then, primary bio-receptors and labelled secondary bio-receptors are immobilized to implement visualization. These processes are assisted by a syringe pump system to carry out the incubation while the reagent flows (Figure 2-23(c)) [22]. It reduces the incubation time from hours to around 20 minutes. The time required by separation and blotting transfer is reduced to around 8 minutes. The microfluidic WB completes an analysis within one hour. However, the whole set up is complex. High voltage of over 1kV is required for the set up [22], [124].

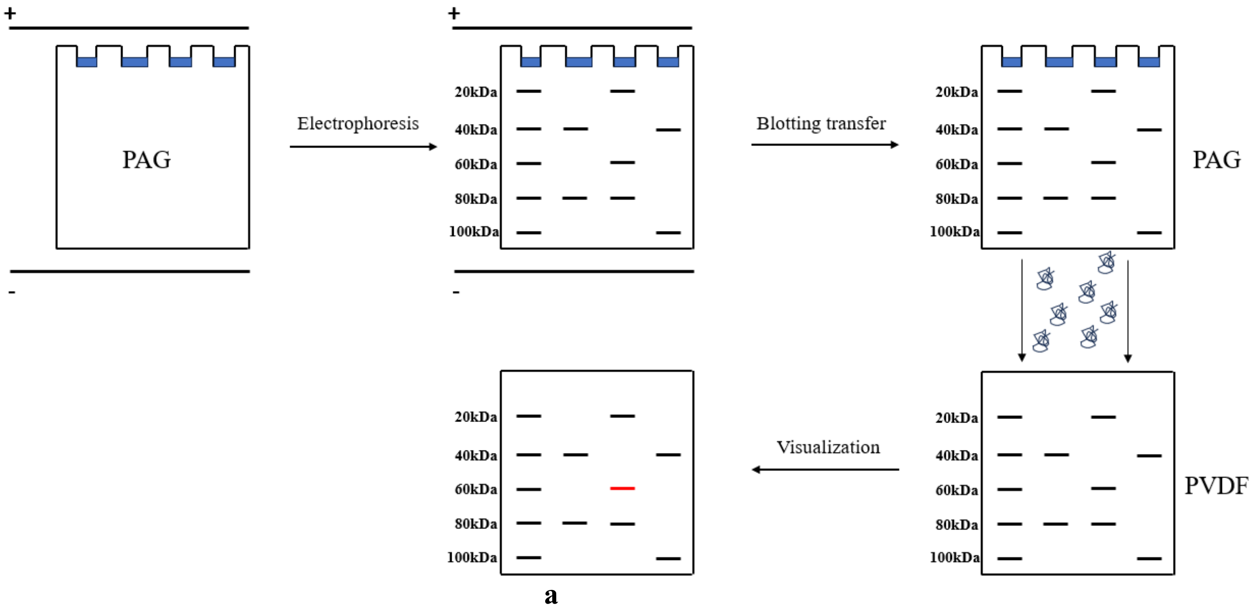

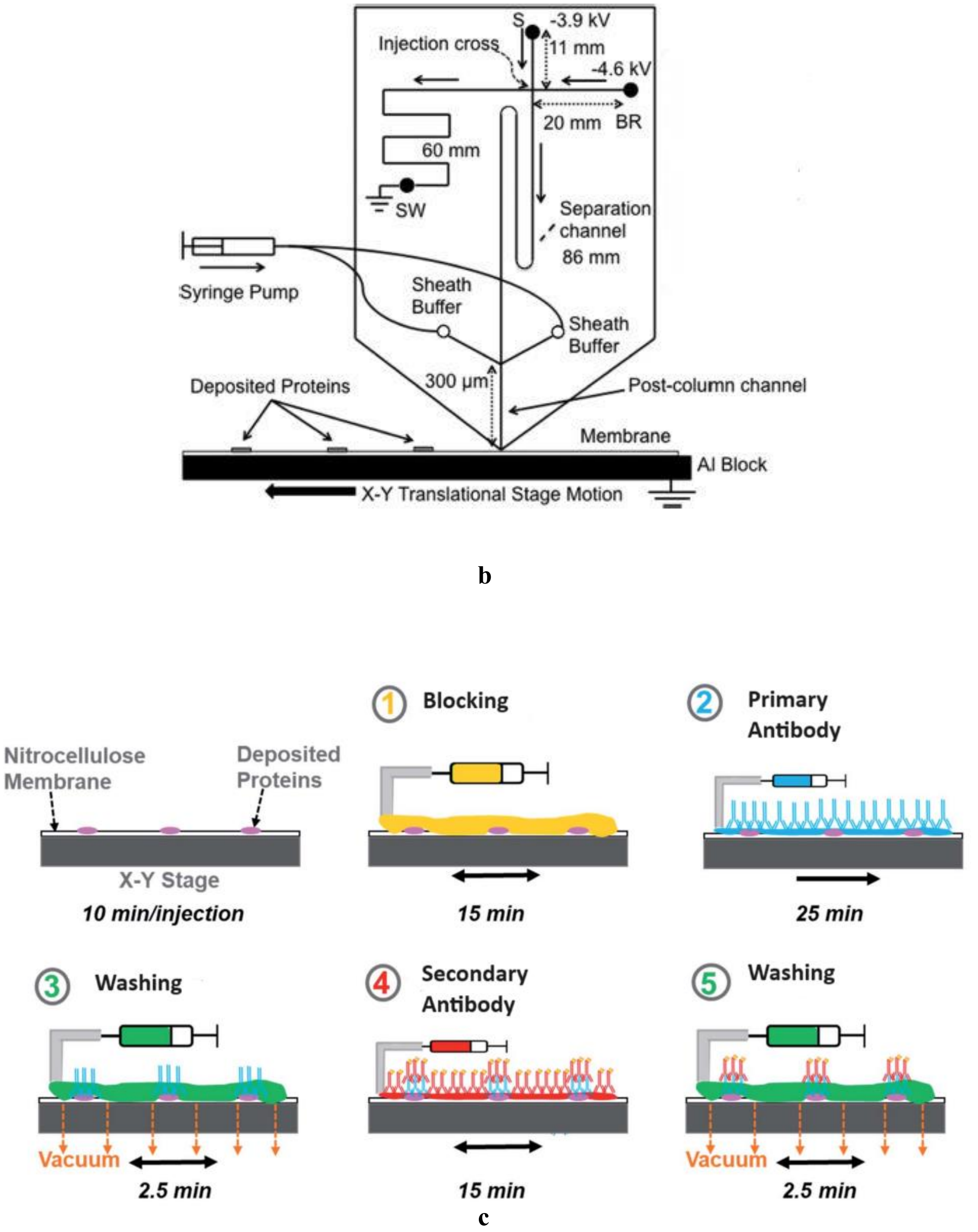

Figure 2- 23. The Western blotting technique. (a) Illustration of the principle of western blotting; (b) The electrophoresis assisted with a microfluidic chip and a translation stage sourced from [124]; (c) The visualization of analyte assisted with a syringe pump system sourced from [22].

2.3.3 Lateral Flow Assay

Lateral flow assay (LFA) is widely used in non-laboratory environments for a PoC tests [16], [125]. The LFA is based on a prefabricated polymetric strip with bioreceptors immobilized on it. As illustrated in Figure 2-24, the sample will move along the strip due to capillary effect. Analyte binds to the gold nanoparticles (AuNPs)-linked bio-receptors and gets immobilized in the test line [125]. Free AuNP-linked bio-receptors will keep moving to the control line and get immobilized [125]. AuNPs have red colour, which results in a colorimetric readout. The test line turns red if the sample contains target analyte and the control line turns red reflecting that the LFA works normally. An LFA can typically give a result within 15 to 30 minutes, and it is easy for people to follow the user manual [17], [128]. It's therefore suitable for PoC applications. Research has been carried out to improve the quantitative LFA. After the lateral flow, the test line changes colour. It is hard to tell the extent of colour change visually, which is related to the concentration of analyte. Therefore, optical detectors such as colorimeters are used to investigate it [26][127]. The test line could be extended to test channel, in which the bioreceptors are immobilized along a capillary channel. During lateral flow, the analyte and AuNPs-linked bio-receptors flow through the whole channel and are immobilized. The length of the colour-changed section of the channel is related to the concentration of analyte [128].

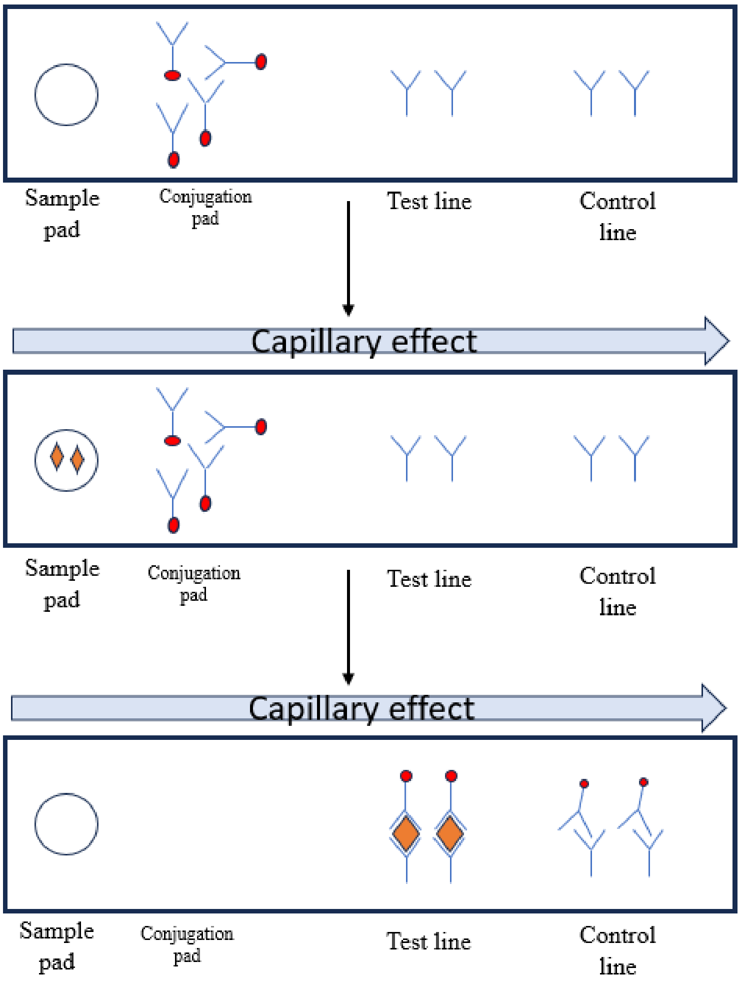

Figure 2- 24. Lateral flow assay

2.3.4 Plasmonic Technologies

Surface Plasmon Resonance (SPR) and Localised Surface Plasmon Resonance (LSPR) are plasmonic phenomena based on which biosensing is implemented. Surface Plasmon Resonance (SPR) is the phenomenon that light striking a metal film excites the oscillation of electrons' density. A Kretschmann configuration is widely exploited to implement SPR. As shown in Figure 2-25, the incident light first passes a glass prism and total internal reflection occurs due to the higher RI of the glass prism than the external medium. When the incident light illuminates the metal film with a certain angle, the conditions of SPR are met and the incident light is coupled into a Surface Plasmon (SP) [15]. The incident angle to excite a SP is related to the RI of the glass prism, the properties of the metal film, and the RI of the external medium [129]. A precise alignment of optical detectors and other devices is needed [23]. To implement biosensing with SPR, bio-receptors are immobilized on the external surface of a gold film. As the incident light strikes the gold film, light with suitable incident angle is coupled into a SP while other light is reflected towards a photodetector. The reflected light with the SP-excitation angle has much lower intensity than the light with other reflection angles [130]. As the target analytes bind to the bio-receptors on the surface of gold film, the SP-excitation angle will change [130]. SPR-based biosensor can implement real-time monitoring of association and dissociation processes [129], [130] and provides quantitative results. Current commercial SPR system are usually bulky and not suitable for PoC use as they integrate complex flow system, multiple channels, and automatic sampling systems to improve the automation and throughput [23]. A phenomenon similar to SPR is called localised surface plasmon resonance (LSPR), which is the collective oscillation of electrons in the array of metal nanoparticles (Figure 2-25(b)) [131]. LSPR can be excited by illuminating the sample. Light with certain wavelength is absorbed and LSPR is excited in the nanoparticles. The metal nanoparticles are functionalized with bio-receptors. When the target analytes bind to the bio-receptors, the reflectivity changes. A device consisting of optical system and flow system is made to improve the automation of LSPR-based assay [132]. It implements PoC test of procalcitonin. Plasmonic technologies are transferable. They can be implemented based on optical fibre [24].

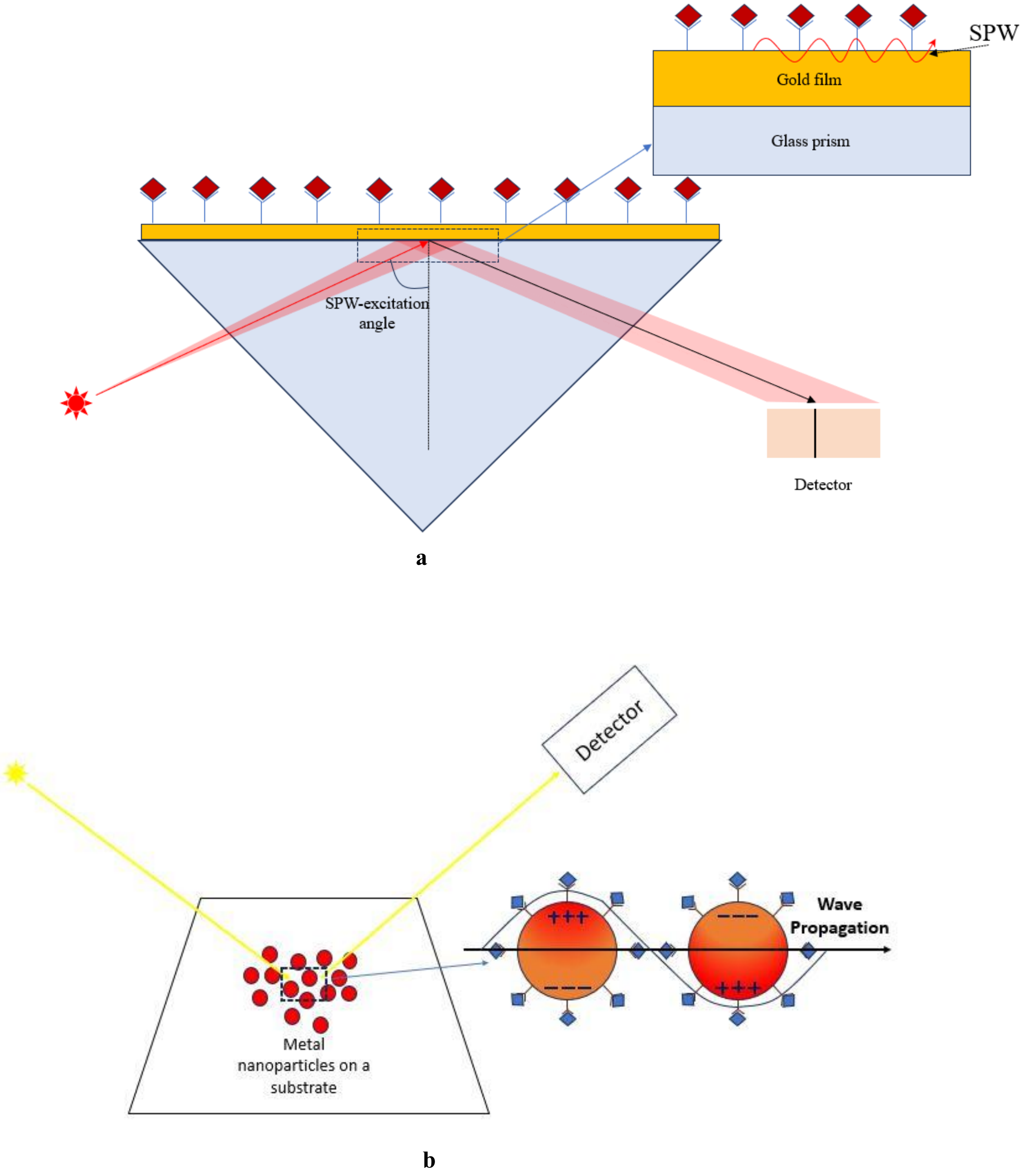

Figure 2- 25. Plasmonic platforms. (a) The Kretschmann configuration to implement SPR biosensing; (b) The biosensing based on LSPR.

2.3.5 Electrochemical Biosensors

The electrochemical biosensors are promising technologies to develop wearable and PoC devices [133]. As shown in Figure 2-26, an electrochemical sensor consists of two electrodes [134], [135]: the reference electrode provides a reference voltage for the system to work in a suitable regime; Bio-receptors are immobilized on the testing electrode. Biomolecules usually contain electrostatic charge. When target analytes bind to the bio-receptors, the electrical potential changes on the testing electrode. The analysing circuit is used to detecting the changes. It can be based on field effect transistor and electrochemical impedance spectroscopy [136], [137].

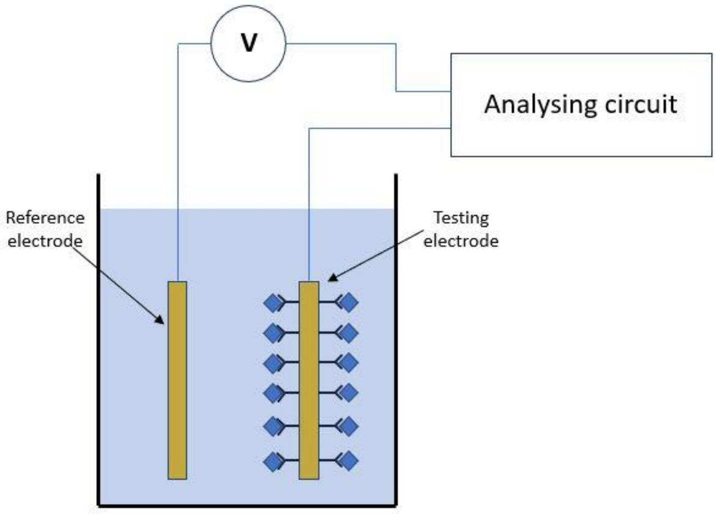

Figure 2- 26. An electrochemical biosensor

2.3.6 Quartz Crystal Microbalance

Quartz Crystal Microbalance (QCM) works based on piezoelectric effect [138], [139]. Bio-receptors are immobilized on a quartz chip. When electrical field is applied, mechanical stress is induced inside the quartz (Figure (2-27)) [138]. Released stress then induces electrical field. Therefore, oscillation is formed. Target analytes bind to the bio-receptors. The frequency is dependent on the mass of substance accumulated on the surface. QCM-based sensors have miniaturized sizes. However, they suffer from electromagnetic interference. Experiment is carried out in an electromagnetic shielding environment [35].

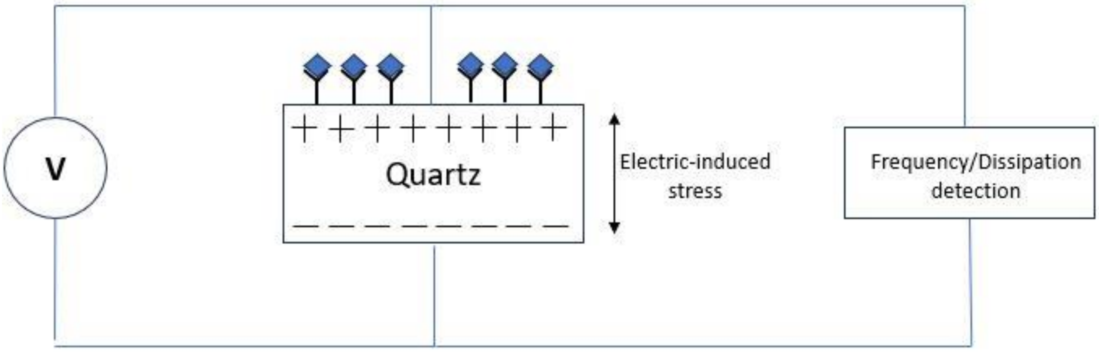

Figure 2- 27. A biosensor based on quartz crystal microbalance

2.3.7 Planer Optical Waveguides

As shown in Figure 2-8, the planner waveguides are fabricated based on a chip-like substrate. It implements certain manipulations on light by arranging optical path, which has a higher refractive index than surrounding medium. A Mach-Zehnder interferometer (MZI) has two optical paths in parallel (Figure 2-28(a)) [32]. When light enters an MZI, it splits into two paths. The two parts travel in parallel and interfere with each other at the output port. Interference pattern is formed in the output port as light experiences different phase shift when travelling through two different paths. A biosensor can be fabricated based on an MZI by functionalizing one path with bio-receptors [140]. When analytes bind to the bio-receptors, the RI on the surface increases. It can change the effective refractive index of light propagation modes and eventually causes change in interference pattern. A microring resonator has a circular waveguide between two straight waveguides (Figure 2-28(b)) [33]. When light enters the input port, it first travels though the straight waveguide and is coupled into the circular waveguide when the evanescent wave enters it. The light in the circular waveguide interferes with the input light after it travels one round. Interference pattern is formed at the output port. A biosensor can be made if bio-receptors is immobilized on the circular waveguide. The RI on the surface increases when analytes bind to the bio-receptors. It changes the phase shift when light travels through the circular waveguide and therefore changes the interference pattern. Planer optical waveguides need to be fabricated by photolithography or electron lithography, while optical fibres are more commercially available.

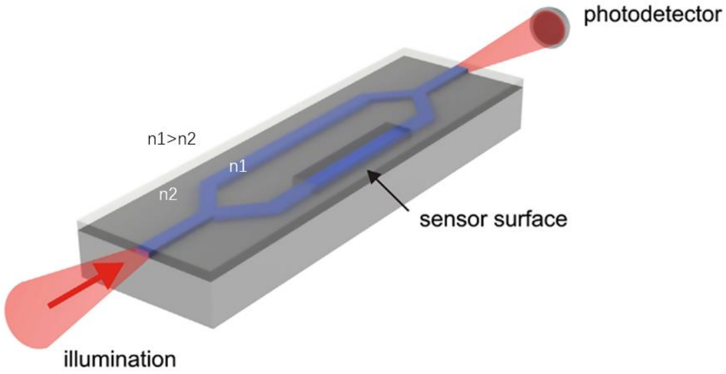

a

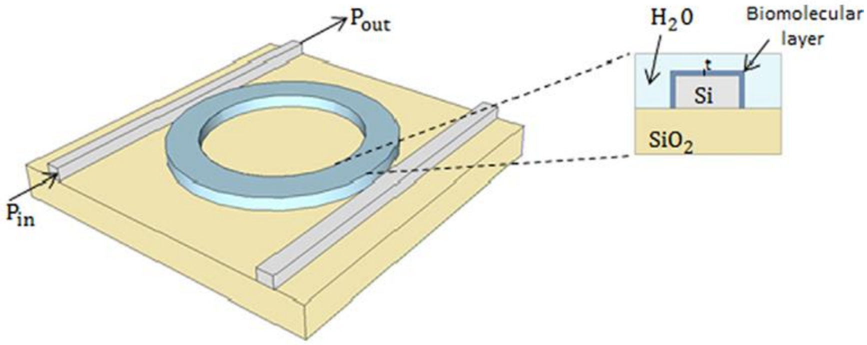

b

Figure 2- 28. Planer optical waveguides. (a) A Mach-Zehnder interferometer sourced from [32]; (b) A microring resonator sourced from [33].

2.3.8 Optical Fibre Biosensors

The development of optical fibre biosensors makes extensive use of the optical-fibre-sensor prototypes introduced in Section 2.2.3. The applications of these biosensors range from medicine/healthcare to food/agriculture. The most adopted technique to fabricate optical fibre biosensors is functionalizing different configurations with bio-receptors as per the requirements of different applications.

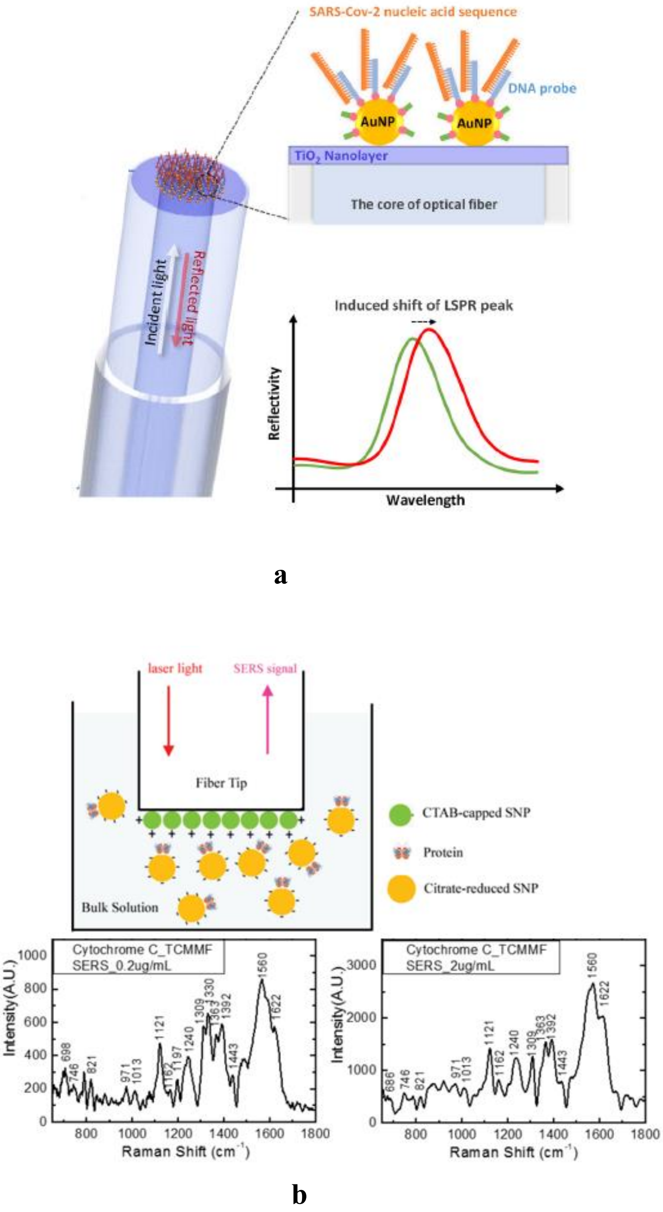

a

b

Figure 2- 29. Biosensors based on the tip of optical fibres. (a) The biosensor based on the LSPR excited on the tip of fibre sourced from [141]; (b) The surface-enhanced-Raman-scattering biosensor with SNPs immobilized on the tip sourced from [142].

A plasmonic biosensor based on the tip of an optical fibre is fabricated by immobilizing AuNPs (Figure 2-29(a)). The incident light excites Localised Surface Plasmon Resonance (LSPR) in the AuNPs array, which induces a reflectivity peak in the reflection spectrum [141], [143]-[145]. The wavelength and intensity of the reflectivity peak is dependent on the RI of the external medium [141], [143]-[145]. Bio-receptors are linked to AuNPs and the RI near the tip increases as target analytes are bound to the bio-receptors. Either the change of wavelength or intensity of reflectivity peak is monitored [141]. Various biomarkers have been analysed based on this structure such as Goat anti-human IgG (GaHIgG), SARS-Cov-2 mimetic DNA sequence, and various biochemicals [141], [143]-[145]. The LSPR technique is also driven forward by the development of new materials [146]. Surface-enhanced Raman scattering (SERS) can be implemented on the tip of optical fibre by depositing suitable metal nanoparticles such as gold nanoparticles (AuNPs) and silver nanoparticles (SNP) (Figure 2-29(b)). Incident laser light transmits through an optical fibre and illuminates the SNPs on the tip [142], [147], [148]. Light of a longer wavelength is generated due to Raman scattering. The scattered light transmits to the Raman detection system through the optical fibre. Two different strategies to detect analytes with SERS are found [142], [149], [150]: i) positively charged SNPs are deposited on the tip of fibre, the analyte is mixed with negatively charged SNPs, the negatively charged SNPs get bound to the tip of the fibre by electrostatic interactions, and the SERS signal changes; ii) bio-receptors are immobilized on the tip, analyte is linked to SNP, the analyte then gets bound to the bio-receptor, and the SERS signal changes. The first strategy doesn't make the sensor specific to the target analyte while the second does, as bio-receptors are applied in the second strategy [142], [149]. Both require a pre-process of the analyte to make it bound to SNPs. Besides, SERS should be excited by laser illumination [142], [147].

Biosensors based on the tip of an optical fibre have very small size and can be easily made into to a probe. However, the SERS sensor is not suitable for PoC use as they require a pre-mixture of sample and SNPs (SERS sensor). The plasmonic sensor suits the PoC requirement, however, the LSPR peak broadens asymmetrically during measurement which increases the complexity of signal processing [38].

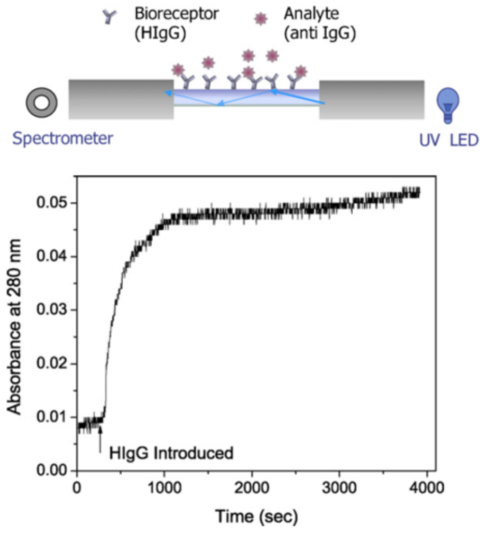

a

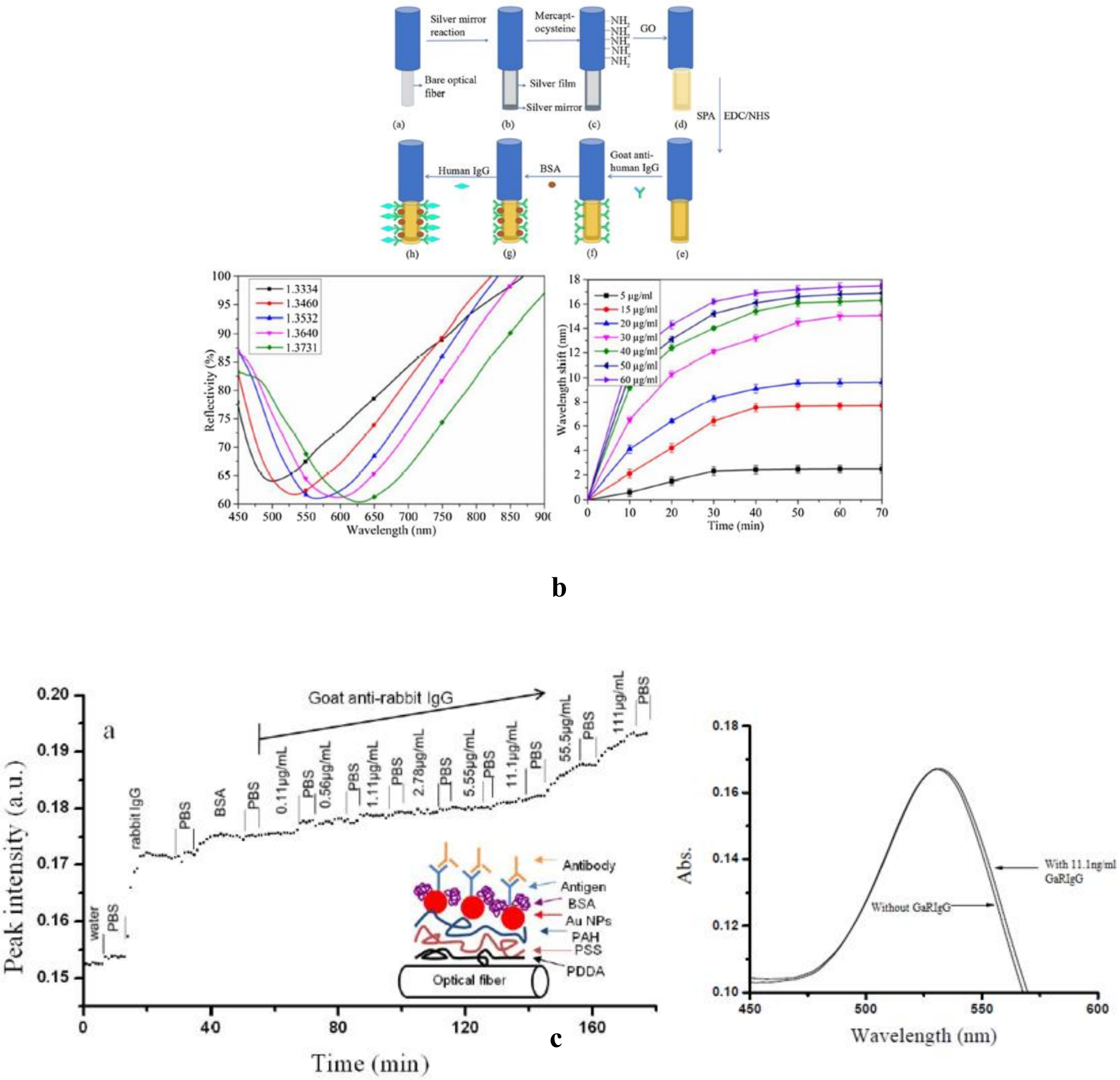

Figure 2- 30. Biosensors based on the cladding-removed optical fibre. (a) The biosensor based on the analyte's absorbance to detect GaHIgG sourced from [29]; (b) The biosensor based on the SPR excited on cladding-removed fibre to detect HIgG sourced from [31]; (c) The biosensor based on the LSPR excited on cladding-removed fibre to detect GaRIgG sourced from [151].

The transmitted light can interact with the surrounding medium using a cladding-removed region of an optical fibre. As shown in Figure 2-30, to design biosensors, the cladding-removed region is usually functionalized with bio-receptors. Biosensors can be designed based on the light absorbance of analytes. For example, the light absorbance at a wavelength of 280nm is measured to analyse the concentration of GaHIgG (Figure 2-30(a)) [29]. The sensor is fabricated by immobilizing human IgG (HIgG) on the surface of a cladding-removed region using Glutaraldehyde cross-linker. As GaHIgG gets bound to the HIgG, the absorbance at 280nm increases.

An SPR signal can be obtained based on a cladding-removed fibre (Figure 2-30(b)) [31], [152]. As discussed in Section 2.3.4, the SPR signal is sensitive to the change of external RI. SPR on the cladding-removed region results in attenuation bands in the transmission spectrum. An HIgG sensor is developed based on a cladding-removed fibre utilising the SPR phenomenon (Figure 2-30(b)) [31]. The cladding is removed at one end of optical fibre, and a silver mirror is coated on the tip. A layer of silver (Ag)/Graphene oxide (GO) film is coated on the surface of cladding-removed region. Light transmits to the cladding-removed region and is reflected. An SPR signal is excited in the Ag/GO film. GaHIgG is used as bio-receptor and immobilized on Ag/GO film with EDC/NHS cross-linker. An attenuation band appears in the reflection spectrum. As HIgG gets bound to the GaHIgG, the RI on the surface increases, which causes a red shift of the attenuation band. The SPR-based biosensor can also be built in transmission mode. Cladding is removed in the middle-section of an optical fibre, and gold film is coated [152]. A C-reactive protein (CRP) sensor is developed by immobilizing mouse anti-CRP antibody on the gold film with EDC/NHS cross-linker. Red shift of the attenuation band in the transmission spectrum is observed when CRP concentration increases. Similarly, LSPR signal is achieved by depositing AuNPs or gold nanorods (AuNRs) on the cladding-removed region [151], [153], [154]. The light within a specific wavelength window is absorbed due to LSPR [151]. A sensor to measure Goat anti-rabbit IgG (GaRIgG) is designed. Poly(diallyldimethylammonium chloride, PDDA)/poly(3,4-ethylenedioxythiophene) polystyrene sulfonate (PSS)/PAH/AuNPs is immobilized on the cladding-removed region by electrostatic interactions. Rabbit IgG is immobilized on the surface of AuNPs with EDC/NHS cross-linker. The absorbance increases as GaRIgG concentration increases (Figure 2-30(c)) [151]. A sensor to measure Goat anti-human IgG (GaHIgG) is designed [154]. The cladding-removed region of an optical fibre is treated with (3-Aminopropyl)triethoxysilane (APTES) to generate amine groups. AuNRs are absorbed to the amine groups. Human IgG is then immobilized on the surface of AuNRs with EDC/NHS cross-linker. The absorbance peak of LSPR shifts to longer wavelengths as GaHIgG concentration increases [154].

The cladding-removed optical fibre is a platform to implement the interaction between transmitting light and analyte. The design of biosensors can be based on the direct interaction such as the absorbance of analyte, or the indirect interaction such as exciting an SPR or LSPR on the coating.

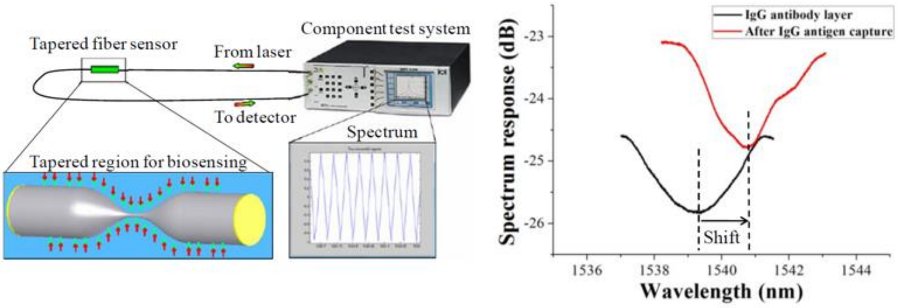

a

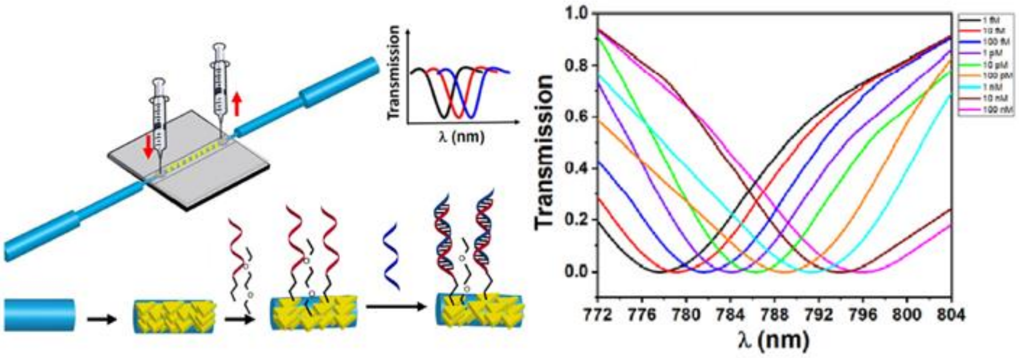

b

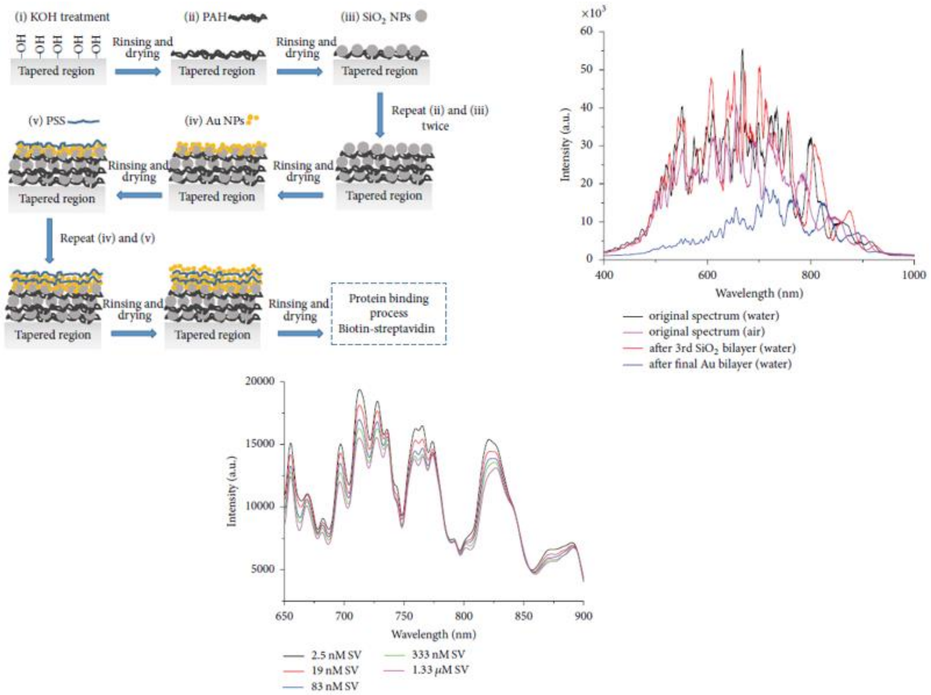

c

Figure 2- 31. Biosensors based on tapered optical fibre. (a)The biosensor based on the wavelength shift of interference pattern to detect antigen sourced from [155]; (b)The biosensor based on the LSPR to detect microRNA sourced from [[156]; (c)The biosensor based on the light loss to detect SV sourced from [157].

As discussed in Section 2.2.3, a tapered optical fibre facilitates the interaction between transmitting light and external medium similar to cladding-removed fibres. It also induces interference between different transmission modes. Both the transmitted intensity and the wavelength changes of the interference pattern can be analysed when designing a biosensor. A sensor to detect IgG-related antigen binding is developed by functionalizing the tapered region (Figure 2-31(a)) [155]. HIgG is immobilized on the tapered region using Glutaraldehyde cross-linker. The RI on the surface of the tapered region increases as IgG-related antigens bind which results in a wavelength shift of the interference pattern.

LSPR can be excited based on a tapered optical fibre. AuNPs are deposited on the tapered region, and LSPR is induced by an evanescent wave (Figure 2-31(b)). Three different AuNPs are used to design a biosensor to detect microRNA: gold nanosphere, gold nanorod, and gold nanoprism [156]. The AuNPs are then decorated by ssDNA using EDC/NHS cross-linker. The LSPR signal shifts to a longer wavelength as the analyte's concentration increases. LSPR signal is used in a different way to measure the concentration of alpha-fetoprotein (AFP) [158]. The anti-AFP antibodies are immobilized on the tapered region and AFPs bind to the antibodies. AuNPs decorated by a different type of anti-AFP antibodies bind to a different site on the APF molecule and the LSPR signal is observed near 520nm. The absorbance increases with AFP concentration as more AuNPs bind.

A sensor to detect streptavidin (SV) is designed by creating a silica-core gold-shell matrix on a tapered optical fibre (Figure 2-31(c)) [157]. PAH and silica nanoparticles (SiNPs) are deposited on the tapered region using layer-by-layer (LbL) method. The 250nm diameter SiNPs are then wrapped by 5nm AuNPs. The LSPR signal isn't observed in the transmission spectrum although AuNPs are deposited but the intensity of transmitted light decreases when SV concentration increases. Like the tapered fibre modified with silica-core gold-shell matrix, a tapered fibre with Au film sputtered on the tapered region is designed as an SV sensor. The transmission intensity between 500nm and 650nm decreases with an increasing SV concentration. The light attenuation is also observed with the biosensor to detect anti-Dengue IgG. Dengue's antigen is deposited on the tapered region using Glutaraldehyde cross-linker. Light absorbance between 304nm and 316nm increases with anti-Dengue IgG concentration [159].

Tapered optical fibres can implement the interaction between transmitting light and external medium and induce interference between core mode and cladding modes simultaneously. When developing biosensors based on a tapered optical fibre, the tapered region is functionalized with bio-receptors. Three investigation methods are used by different research groups: i) the wavelength shift of interference pattern caused by the RI change when analyte binds; ii) the change of LSPR signal caused by the RI change; iii) the change of transmitted intensity due to the light loss over the tapered region.

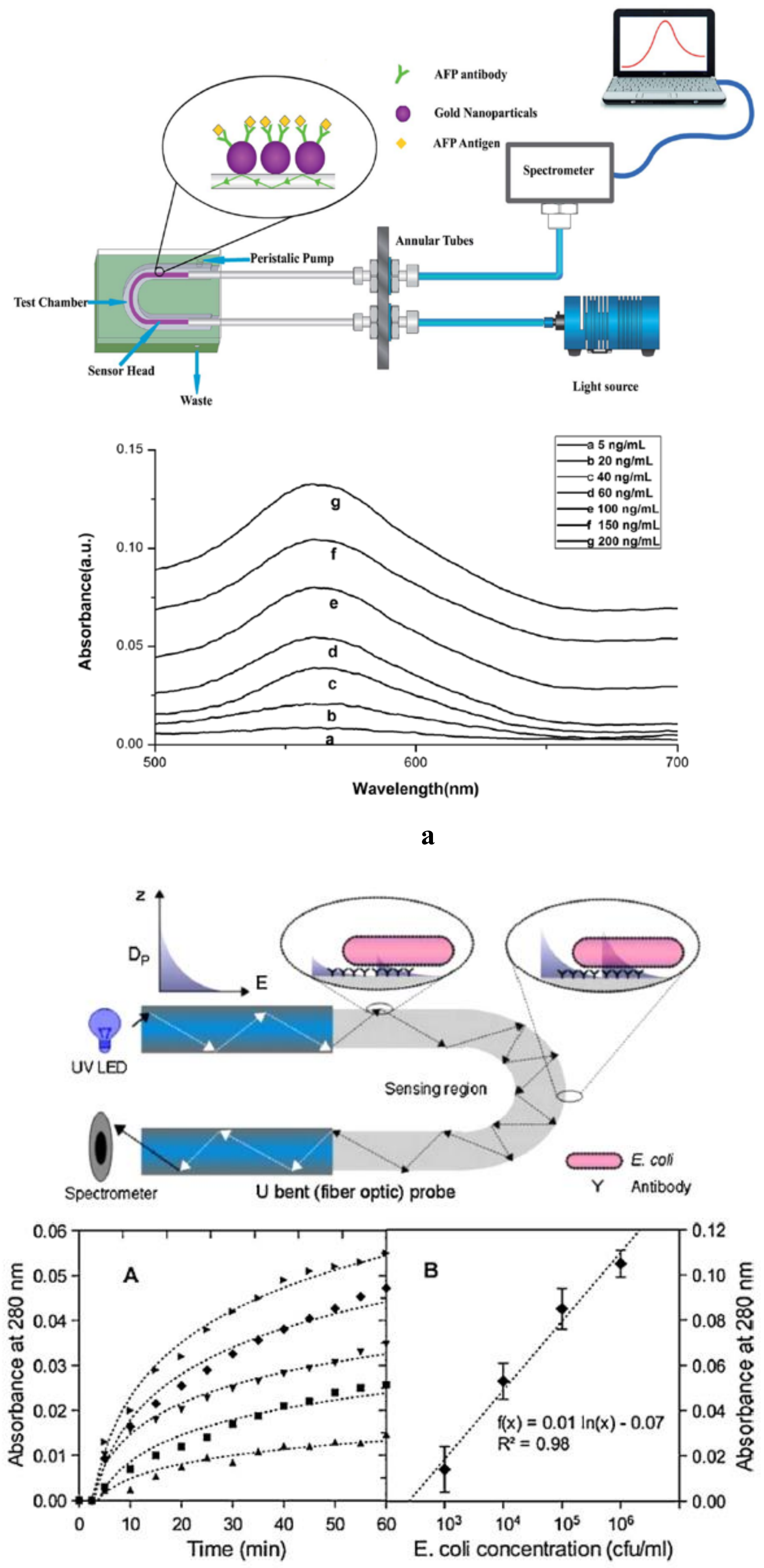

a

b

Figure 2- 32. The optical fibre biosensors based on a U-shape fibre. (a) The biosensor based on LSPR to detect AFP sourced from [160]; (b) The biosensor based on analyte's absorbance to detect E. coli bacteria sourced from [161].

Light can interact with the external medium when transmitting through the U-shape region. AuNPs are deposited on the surface of U-shape region, and LSPR is excited when light propagates (Figure 2-32(a)) [160]. The LSPR signal appears at a wavelength of around 560nm. AFP antibodies are immobilized on the AuNPs using EDC/NHS cross-linker. The light increases as AFPs bind and the absorbance around 560nm corresponds to AFP concentrations. This method is also applied to the development of biosensors to detect GaHIgG and rabbit anti-human IgG (RaHIgG) [162], [163]. The immobilization of AuNPs is done after the adsorption of analyte when designing an HIgG sensor [164]. The GaHIgGs are coated on the U-shape region using Glutaraldehyde cross-linker, then HIgGs bind to it. AuNPs decorated by a different type of GaHIgG bind to a different site on HIgGs. The light absorbance increases with the concentration of HIgG.

An SPR signal is obtained by sputtering a gold film on the U-shape region. A sensor to detect E.coli bacteria is designed by immobilizing E.coli antibodies on the gold film using EDC/NHS cross-linker. The SPR signal is enhanced when E.coli bacteria's concentration increases [165].

Apart from exciting LSPR or SPR signal, biosensor based on U-shape fibre can be developed by exploiting analytes' light absorbance [164]. E.coli bacteria have light absorbance around 280nm. E.coli antibodies are immobilized on U-shape region with Glutaraldehyde cross-linker (Figure 2-32(b)) [164]. Light absorbance at 280nm increases with E.coli concentration.

Two methods are found to be used for the development of biosensors based on U-shape fibre: i) coating the U-shape region with AuNPs or Au film to obtain LSPR or SPR signal; ii) the analyte immobilized on the U-shape region absorbs the light directly. The change of light absorbance is investigated for both cases.

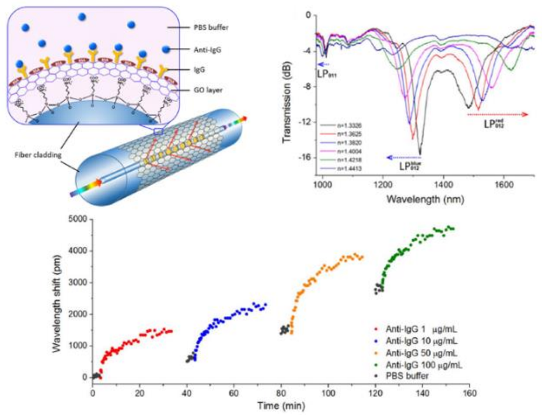

a

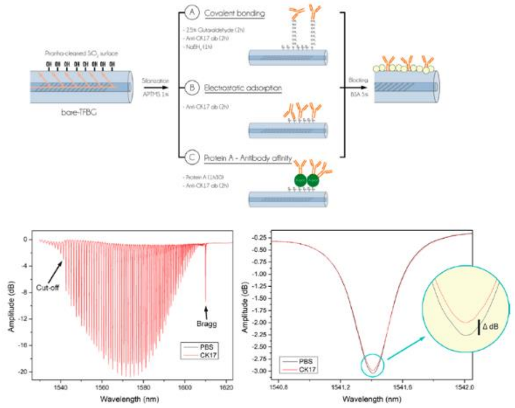

b

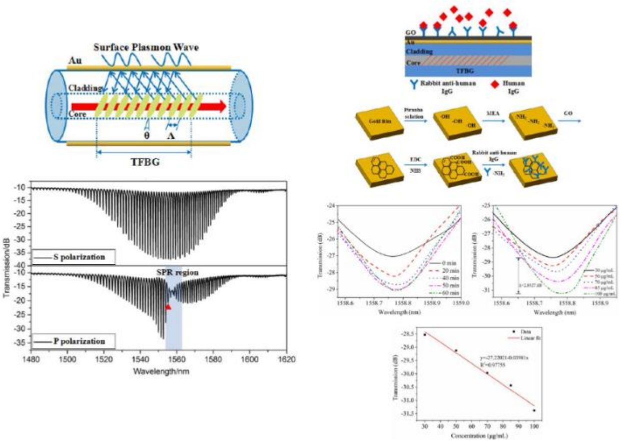

c

Figure 2- 33. Optical biosensors based on optical fibre gratings. (a) An optical fibre GaHIgG sensor based on LPG sourced from [37]; (b) An optical fibre Cytokeratin sensor based on TFBG sourced from [166]; (c) An optical fibre HIgG sensor based on the SPR excited on TFBG sourced from [167].

Various biosensors are developed based on long period gratings (LPG) and tilted fibre Bragg gratings (TFBG) [168], [169]. The transmission spectra of LPGs and TFBGs are sensitive to external RI. The design of biosensors relies on detecting the change of external RI with analyte concentration. A sensor to detect GaHIgG is developed on an LPG (Figure 2-33(a)) [37]. A layer of graphene oxide (GO) is coated on the LPG which is rich in carboxyl group (-COOH) and assists in functionalization. HIgGs are coated on the LPG using EDC/NHS cross-linker. The dual attenuation bands in the transmission spectrum separate further when GaHIgGs bind. Different methods are applied to functionalizing LPGs. A Human IgM (HIgM) sensor is developed by depositing PAH/SiNPs dual layers on an LPG [30]. The PAH and SiNPs are deposited using the layer-by-layer (LbL) method, and they are bound to each other by electrostatic forces. Then, the 100nm SiNPs are wrapped by 5nm AuNPs. Goat anti-human IgMs (GaHIgM) are immobilized on the AuNPs using EDC/NHS cross-linker. The separation between dual attenuation bands increases with IgM concentration. An E.coli bacteria sensor is developed based on an LPG by immobilizing E.coli antibodies using Glutaraldehyde cross-linker [170]. The wavelength shift of the attenuation band increases with E.coli concentration.

LPGs are sensitive to external RI. When designing biosensors based on them, bioreceptors are immobilized and wavelength shifts of attenuation bands are investigated. Three different methods to immobilize bio-receptors are found: i) a layer of GO is deposited on the grating region to provide carboxyl groups, and bio-receptors are immobilized using EDC/NHS cross-linker; ii) PAH/SiNPs dual layers are deposited using the layer-by-layer method, SiNPs are wrapped by AuNPs, and bio-receptors are linked to AuNPs using EDC/NHS cross-linker; iii) bio-receptors are immobilized on the grating region directly using Glutaraldehyde cross-linker.

Biosensors based on TFBGs can be fabricated by the direct immobilization of bio-receptors on the grating surface (Figure 2-33(b)). A Cytokeratin (CK) sensor is fabricated [166]. The bio-receptors anti-CK17 are immobilized by three different methods: i) covalent binding, anti-CK17s are immobilized using Glutaraldehyde cross-linker; ii) electrostatic adsorption, the positively charged amine group in anti-CK17 get bound to the negatively charged hydroxyl group (-OH) on grating surface; iii) antibody affinity, Protein A is coated on the grating region by physical adsorption, and Fc of anti-

CK17 is bound to Protein A. The amplitudes of attenuation bands decrease with an increasing CK concentration.

Many TFBG-based biosensors rely on SPR signals [167], [171], [172]. A gold film is sputtered on the grating region (Figure 2-33(c)) [167]. SPR signal is excited and investigated. For example, an HIgG sensor is developed. A layer of GO is deposited on the old film, which provides plenty of carboxyl groups on the surface for the following up functionalization. GaHIgGs are coated using EDC/NHS cross-linker. The transmission of the SPR region decreases when HIgG's concentration increases. Besides GO, 11-MUA is a widely used chemical to provide carboxyl groups for the following up EDC/NHS cross-linking [167]. The sulfhydryl group can easily bind to gold. The wavelength shift of the SPR signal is investigated in the design of biosensors. For example, a NT-proBNP (N-terminal B-type natriuretic peptide) sensor is designed [173]. The SPR signal shifts to a longer wavelength when the concentration of NT-proBNP increases.

TFBG-based biosensors are developed through two approaches: i) bio-receptors are immobilized directly on the grating region, the attenuation bands of the TFBG respond to the change of external RI when analyte's concentration change; ii) a layer of gold film is sputtered on the grating region, SPR signal is excited and changes with analyte's concentration. Both the intensity and wavelength can be investigated in these two designing methods.

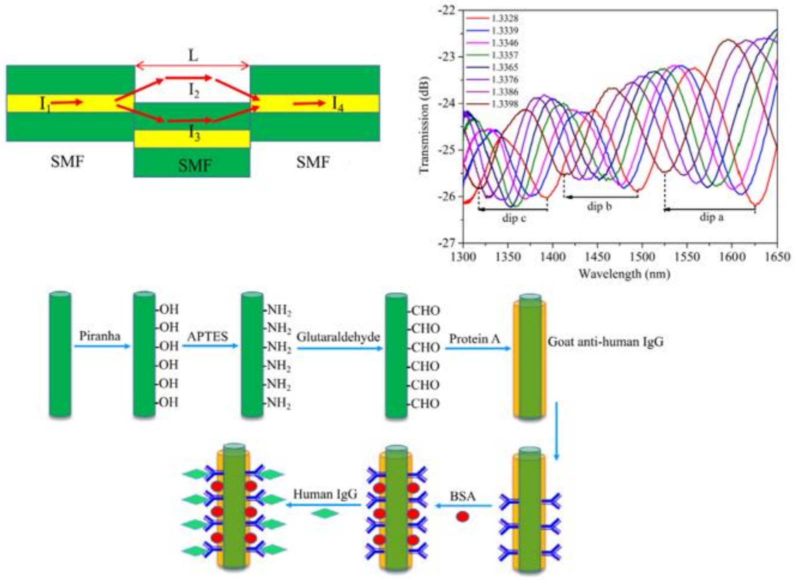

Figure 2- 34. An interferometric HIgG sensor based on core-offset fibre sourced from [39].

A Mach-Zehnder interferometer is fabricated by offsetting the core of a single-mode fibre (Figure 2-34). The core-mode light is coupled into multiple modes at the first core-offset interface. The transmission modes interfere with each other at the second core-offset interface and results in an interference pattern in the transmission spectrum [39]. The interference pattern shifts to a shorter wavelength when external RI increases [39]. When designing an HIgG sensor, protein A is first immobilized on the surface of fibre using Glutaraldehyde cross-linker, then GaHIgG binds to the protein A. A blue shift of the interference pattern is observed when HIgG concentration increases.

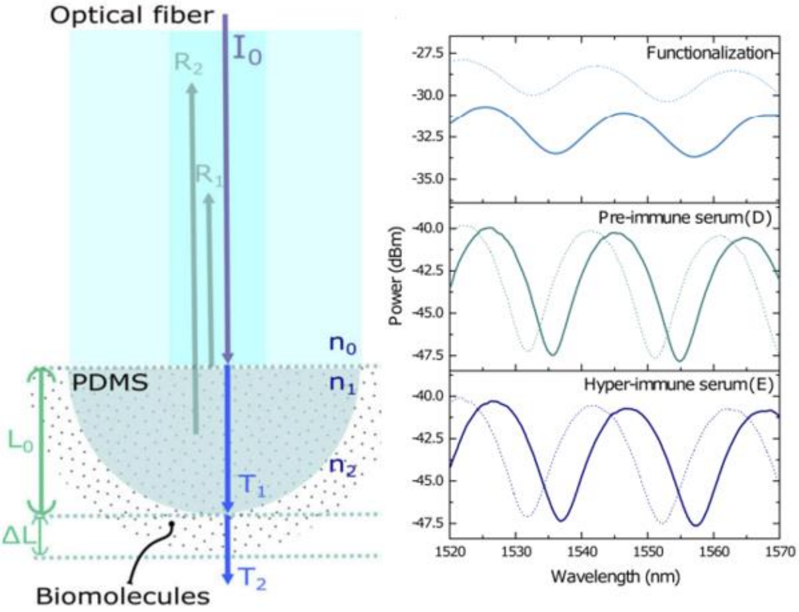

Figure 2- 35. Biosensor based on an FFPI to detect rabbit anti-lipid antibody sourced from [40].

A biosensor to detect rabbit anti-lipid antibody is shown in Figure 2-35. A Polydimethylsiloxane (PDMS) endcap is deposited on the end of a single mode fibre by dip-coating [40]. The PDMS works as an FP cavity [40]. Interference pattern is formed in the reflected spectrum. The lipid antigens (bio-receptor) are physically adsorbed to the surface of PDMS endcap [40]. When the target analytes bind to the bio-receptors, the thickness of the biomolecules' layer increases. It works as an extension of the FP cavity [40], which results in the interference pattern's shift to a longer wavelength.

Besides the biosensors based on the OFS prototypes, many novel structures are exploited such as S-tapered fibre [174], D-shape fibre [175], and photonic crystal [176]. They are either able to compensate for cross-interference from temperature or valuable explorations to new structures. Optical fibre sensors can be used along with microfluidic chips, which are substrates contains network of microchannels to implement more efficient manipulations on liquid-phase samples [177]. The sizes of the microchannels are around 100μm [177]. Miniaturized optical fibres can be inserted or embedded in the microchannels. Most commercial optical fibres have sizes over 100μm. Therefore, they need to be further miniaturized to fit microfluidic chips such as etching them with hydrofluoric acid [178]. Microfluidic chips have many applications in biomedicine such as deliver drugs and mimicking the function of organs [179]. Optical fibre sensor is a promising technology to monitoring analytes in microfluidic chips.

2.4 Discussion on Optical-Fibre Antibody Sensors

The main information of some optical-fibre antibody sensors is listed in Table 8-1. It includes sensors' platforms, analytes, the sensing mechanism, cross-linkers, measured signal, Limit of Detection (LoD), and Full Width Half Maximum (FWHM). Depending on the sensing mechanism, wavelength or intensity is observed during measurement. Wavelength is the more reliable signal to be investigated as it is immune to the cross-interference introduced by fluctuations of light source and detector. Sensors relying on analytes' absorbance and chemiluminescence show intensity-related signal change (intensity, absorbance, and transmission) during measurement such as GaHIgG sensor based on cladding removed fibre and HIgM sensor based on tip of a fibre [29], [180]. Besides, some plasmonic sensors also show intensity-related signal change [151], [162]-[164]. Sensors showing wavelength shifts have dips or peaks in the measured spectra, which are tracked during measurement. The FWHM measures the width of a dip or peak, which affects the Detection Accuracy (DA) on wavelength [181]. The relationship between DA and FWHM is described by Equation (2-26). The method to calculate FWHM is explained in Appendix A

$$DA \propto \frac{1}{FWHM} \tag{2-26}$$

Plasmonic sensors can be fabricated based on different OFS configurations [24]. Light excites SPR or LSPR in gold films or AuNPs when propagating through sensing areas. The plasmonic bands shift when analytes' concentration changes. The FWHMs of most plasmonic bands exceed 50nm [182]-[192], which is wider than other sensors' sensitive bands. Therefore, the DA is lower. FFPI-based sensors have interference patterns in their spectra. They are suitable to be made as a probe as the sensing area is based on the FP cavity on the tip of an optical fibre. The peaks and dips in the interference pattern have FWHM of about 23nm [40]. Therefore, there is a higher DA on them than on plasmonic bands. An FP cavity is fabricated by depositing a PDMS film on the tip with dip-coating method. The sensing principle of an FFPI-based antibody sensor is not fully investigated. The hypothesis is it responds to the change of thickness of outer layer as biomolecules are accumulated [40]. An FMI-based sensor also has interference pattern over the whole output spectrum. The FWHM is between 30nm and 50nm [39], [193], [194]. Therefore, the DA on them is higher than the DA on plasmonic bands but lower than the DA on an FFMI's interference pattern. An FMZI can be fabricated by splicing a distinctive section between two identical optical fibres. The quality of FMZI's interference pattern is dependent on the coupling and interference between different modes, which varies with external medium and the deviations of optical-fibre parameters during manufacturing. Therefore, more research activities need to be given to fabricating FMZI reliably. A helical intermediate period grating is a newly emerged platform based on which antibody sensor is developed [195]. After reviewing literatures, the only antibody sensor based on a helical intermediate period grating is an HIgG sensor developed in 2022. The grating has a grating period of 17.5μm. The helical intermediate period grating is fabricated by heating the optical fibre with hydrogen-oxygen flame. The fibre is placed on a moving bench and twisted by a highly precise rotator during heating. Therefore, a periodic mechanical perturbation is formed in the optical fibre. The grating length is controlled by the moving bench. Grating period is controlled together by rotating speed and moving speed. The attenuation bands in transmission spectrum have FWHM of around 11.7nm. A good DA can be achieved. It has the narrowest DA among all the sensors listed in Table 8-1. The grating period is controlled by heating-twisting method. It can be influenced by many factors such as the deviations of the mechanical properties of optical fibres and the fluctuations of the hydrogen-oxygen flame. Therefore, the reliability of this method needs to be investigated more. An LPG can be fabricated in hydrogen-loaded single-mode fibre or Germanium-Boron co-doped photosensitive single-mode fibre [30]. The attenuation bands in LPGs' transmission spectrum have FWHM narrower than 40nm. The DA on them is lower than on helical intermediate period grating's bands, comparable to FMZI's and FFPI's interference patterns, and higher than on plasmonic bands. LPG is fabricated with laser. The grating period can be controlled by amplitude masks.

Although manufacturing deviations on the optical fibre introduces variations to the performance of LPGs, amending the grating period can compensate for these [45], [46]. An LPG with acceptable performance can be achieved. A GaHIgG sensor is made based on an LPG. A LoD of 7ng/ml is achieved. It is the lowest LoD among all the GaHIgG sensors. It shows that LPG is a promising platform to fabricate highly sensitive antibody sensors. Other platforms such as S-shaped fibre and S-tapered fibre are not widely used. The reliability of the platform needs to be investigated more.

Overall, the advantages that an LPG possesses are:

1. The wavelengths of attenuation bands in the transmission spectrum are investigated during measurement such that the signal is not affected by the fluctuations of light source and detector.
2. The attenuation bands of an LPG have narrow FWHMs. A high DA can be achieved.
3. There are well-established methods to fabricate LPGs [30], [46]. The performance of an LPG can be optimized by amending its grating period. Since the grating period can be controlled easily and precisely, it compensates for the effects caused by the manufacturing tolerance of optical fibres.
4. A low LoD can be easily achieved with an LPG-based sensor.

Platform	**Analyte**	**Sensing mechanism**	**Cross-linker**	**Measured Signal**	**Limit of Detection (LoD)**	**FWHM**	**Reference**
Cladding -removed fibre	GaHIgG	Analyte's absorbance	Glutaraldehyde	Absorbance	0.1µg/ml	NA	[29]
	HIgG	SPR	EDC/NHS	Wavelength	0.04µg/ml	>250nm	[31]
	GaRIgG	LSPR	EDC/NHS	Intensity	Experimentally detect 0.56µg/ml	NA	[151]
	Human infliximab	SPR	EDC/NHS	Wavelength	23.5ng/ml	67nm	[182]
	HIgG	SPR	EDC/NHS	Wavelength	0.9µg/ml	100nm	[183]
	HIgG	LSPR	EDC/NHS	Wavelength	0.12µg/ml	140nm	[184]
	HIgG	LSPR	EDC/NHS	Wavelength	0.12µg/ml	138nm	[185]
	GaHIgG	LSPR	EDC/NHS	wavelength	256ng/ml	156nm	[186]
	GaRIgG	SPR	Dopamine	Wavelength	0.054µg/ml	86nm	[187]
	Human IgA (HigA)	SPR	EDC/NHS	Wavelength	1.1µg/ml	50nm	[188]

U-shape optical fibre	GaHIgG	LSPR	Glutaraldehyde	Absorbance	128ng/ml	NA	[162]
	RaHIgG & GaHIgG	LSPR	EDC/NHS	Absorbance	Not stated	NA	[163]
	HIgG	LSPR	Glutaraldehyde	Absorbance	1.05ng/ml	NA	[164]
	HIgG	SPR	Physical adsorption	Wavelength	19.7ng/ml	81nm	[189]
LPG	GaHIgG	Response to change of external RI	EDC/NHS	Wavelength	7ng/ml	37.5nm	[37]
	Human IgM (HIgM)	Response to change of external RI	EDC/NHS	Wavelength	Experimentally detect 15.6µg/ml HIgM	27nm	[30]
	Goat anti-Mouse IgG (GaMIgG)	Response to change of external RI	EDC/NHS	Wavelength	50ng/ml	17.9nm	[196]
FMZI	HIgG	Response to change of external RI	Glutaraldehyde	Wavelength	47ng/ml	50nm	[39]
	RaGIgG	Response to change of external RI	Physical adsorption	Wavelength	Experimentally detect 41.8µg/ml	50nm	[193]
	RaGIgG	Response to change of external RI	EDC/NHS	Wavelength	0.2µg/ml	33nm	[194]
	HIgG	SPR	Physical adsorption	Wavelength	1.75µg/ml	56nm	[190]
D-shape optical fibre	GaHIgG	LSPR	Glutaraldehyde	Absorbance	Experimentally detect 0.6µg/ml	NA	[175]
	HIgG	SPR	Physical adsorption	Wavelength	0.2µg/ml	60nm	[197]
	GaMIgG	Lossy Mode Resonance (LMR)	EDC/NHS	Wavelength	0.15pg/ml	116nm	[198]
FFPI	Rabbit anti-lipid antibody	Response to change of external RI	Physical adsorption	Wavelength	Not stated	23nm	[40]
Helix intermediate-period grating	HIgG	Response to change of external RI	Glutaraldehyde	Wavelength	4.7µg/ml	11.7nm	[195]
Photonic crystal	HIgG	SPR	EDC/NHS	Wavelength	0.01µg/ml	86nm	[191]

optical fibre	Goat anti-bovine IgG	SPR	Protein G adsorption	Wavelength	Experimentally detect 1μg/ml	79nm	[192]
	HIgG	Analyte's absorbance	Bio-receptors are not used	Absorbance	56μg/ml	NA	[176]
S-tapered optical fibre	HIgG	Response to change of external RI	Dopamine	Wavelength	0.028μg/ml	83nm	[174]
S-shape optical fibre	GaHIgG	Response to change of external RI	Glutaraldehyde	Absorbance	272ng/ml	NA	[199]
Tapered optical fibre	HIgG	Analyte's absorbance	Glutaraldehyde	Absorbance	Experimentally detect 100pg/ml	NA	[159]
Tip of optical fibre	HIgM	Chemiluminescence	6-maleimidohexanoic acid *n*-hydroxysuccinimide ester (EMCS)	Intensity	Not stated	NA	[180]
	HIgG	Analyte's absorbance	Biotin/NHS	Intensity	1μg/ml	NA	[200]
TFBG	HIgG	SPR	EDC/NHS	Transmission	0.5μg/ml	NA	[167]

Table 2- 1. The properties of optical-fibre antibody sensors.

2.5 Summary

Biomolecules like IgG, IgM, IgA, κ chain, and λ chain play important roles in human health. Diseases can cause abnormal changes in the sera concentrations of these biomolecules. Therefore, a fast and accurate determination of the concentrations of these biomolecules assists the diagnosis of diseases. Conventional measurement methods include Enzyme-Linked Immunosorbent Assay (ELISA), Western Blotting (WB), Lateral Flow Assay (LFA), and Surface Plasmon Resonance (SPR). These methods are either time & labour-consuming, unable to give real-time and quantitative results, or based on bulky equipment.

An optical fibre is a light waveguide constituting of core and cladding with distinct RIs. Light propagating in an optical fibre is confined in the core. A long period grating (LPG) is fabricated by periodically modulating the RI of the fibre core. Optical fibre sensors have the advantages such as light weight, small size, and immunity to electromagnetic interference. They have been widely used in structural monitoring, biomedical sensing, and Point-of-Care (PoC) instruments. Widely used optical fibre configurations include reflection-mode fibre with functional tip, cladding-removed fibre, U-shape fibre, tapered fibre, fibre Bragg grating (FBG), tilted fibre Bragg grating (TFBG), long period grating (LPG), in-fibre Fabry-Perot interferometer (FFPI), and in-fibre Mach-Zehnder interferometer (FMZI). Depending on if the optical fibre only transmits light during the sensing process or also participates in the modulation of light, an optical fibre sensor can be classified into extrinsic optical fibre sensor or intrinsic optical fibre sensor. FBG is mostly used for the measurement of physical parameters such as temperature, strain, pressure, curvature, heart and respiration rates. The other configurations have been used for biomolecular sensors. Sensors are fabricated by functionalizing the optical fibre with bio-receptors. The most widely used methods to immobilize bio-receptors are using cross-linkers such as EDC/NHS and Glutaraldehyde. Other methods also include direct physical adsorption, protein G adsorption, and using cross-linkers such as Dopamine, biotin/NHS, and EMCS. As an analyte's concentration increases, more of them bind to bio-receptors which causes the change of external RI and light absorbance. Sensors' spectra can change with external RI or light absorbance depending on configurations' characteristics. Moreover, many sensors are fabricated with the assistance of specific materials such as gold nanofilm, gold nanoparticles (AuNPs), indium tin oxide (ITO), and tin dioxide (SnO_2). The participation of these materials results in the excitations of different optical signals such as surface plasmon resonance (SPR), localized surface plasmon resonance (LSPR), and lossy mode resonance (LMR). Analytes bind to bio-receptors can induce changes of these signals as well, and they can be observed from the optical spectra of sensors. Commonly used spectral analysis methods include measuring the light intensities of specific wavelength ranges and tracking the wavelengths of specific optical intensity peaks or dips.

An LPG typically have a grating period of 50-500μm. Light is coupled from core mode into cladding modes when propagating through the grating area. It forms attenuation bands in the transmission spectrum that shift in wavelength when external RI changes. LPG-based biomolecular sensors rely on this characteristic. Comparing with sensors based on intensity change during measurement, LPG-based sensors are not affected by the fluctuations of the light source and detector. Also, an LPG's attenuation bands are more robust than bands induced by SPR or LSPR. They are narrower such that the minimum of a dip can be located easier. The FWHM of an SPR or LSPR's band is generally twice wider than an LPG's band. The fabrication process of an LPG is reliable.

Although the unpredictable manufacturing deviations on the optical fibre have effects on the working conditions of LPGs, it can be optimized by amending the grating period.

Having fast, accurate, miniaturized, flexible and easy-to-use devices to detect antibodies is important for improving medicine and healthcare industry. Owing to their unique geometry shapes, optical fibre sensors are miniaturized and flexible platforms to design antibody sensors for different scenarios. Among different optical fibre sensor configurations, LPGs is a more promising platform as they have high sensitivity to external RI and their wavelength-related signals are not affected by the fluctuation of light intensity. Various biomolecular sensors have been developed based on LPGs. However, due to the diversity of biomolecules, each sensor can detect only one analyte. Developing and testing new sensors for different analytes are always needed. LPG-based sensors suffer from the cross-sensitivity related to the change of ambient environment such as temperature and bulk RI of solution. The RI of real samples such as serum can vary a lot from patient to patient. After reviewing the literature, the information about the RI of human serum isn't found. However, the RI of albino rat serum changes with age. The RI of new-born rats' serum is about 1.34136, but it increases to around 1.35175 as the age reaches 597 days [201]. Therefore, methods to compensate for the cross-interference need to be investigated. Real samples such as human serum have complex compositions. Selectivity tests against other compositions need to be done on sensors to validate their specificity to target analytes. The gaps between current research status and needs related to LPG-based biomolecular sensors are listed below. The contributions of this work to filling in these gaps are included as well.

1. Although various biomolecular sensors have been developed, only a few of them are for human antibodies, which plays an important role in disease diagnosis. After reviewing literatures, it is found that a human IgM sensor has been developed based on LPG. Human IgG sensors are developed based on other configurations. Only one optical-fibre human IgA sensor is developed, and it's based on cladding-removed fibre. As discussed in Section 2.4, an LPG is expected to be more reliable than other configurations. In this work, sensors for IgA, IgG, and IgM are developed based on LPGs.
2. After literature review, sensors detecting antibodies by binding to their light chain haven't been designed. These sensors can assist in the measurement of

monoclonal protein (M protein), which plays an important role in the diagnosis and monitoring of myeloma-related diseases. Current detection of M protein mainly relies on electrophoresis, which can be complex and time consuming. Fast and miniaturized sensors to detect M protein are needed. Sensors to detect IgG-type M proteins are developed based on an LPG in this work.

3. Ideally, the developed sensor should have high selectivity to the target analyte, which means the sensor responds to target analyte much greater than to interfering substance. However, very few sensors' selectivity is investigated. In this work, selectivity tests are conducted on all the developed sensors.
4. LPG-based sensors suffer from the cross-sensitivity to temperature and bulk RI, which need to be compensated to achieve a more reliable detection. In this work, an IgM sensor with compensation for fluctuations of bulk RI and temperature is developed.

Chapter 3. Sensor Fabrication Methodology

In this work, the fabrication of sensors includes two parts: i) fabricating LPGs in photosensitive optical fibre; ii) the surface functionalization of LPGs. The LPGs are usually fabricated with two methods – the point-by-point method and fabrication with an amplitude mask [202], [203]. As shown in Figure 3-1(a), in the point-by-point method, the laser passes a narrow slit (width = half of a grating period) and illuminates a point on the photosensitive fibre. After a certain duration, the fibre is moved, and another point is exposed to the laser. In the second method, an amplitude mask is fabricated by making an array of slits, each the width of half a grating period on a thin laser-blocking sheet. As shown in Figure 3-1(b), when fabricating LPGs, the amplitude mask is placed between laser and photosensitive fibre. The laser light can pass the slits and illuminates several points on the fibre. The optical fibre and amplitude mask move together until a certain grating length is achieved.

In previous research, these two methods are compared [202]. LPGs with a grating period of 475μm are fabricated in PS1250/1500 photosensitive fibre (Fibrecore, UK) using a 264nm wavelength laser. The results show that these two methods achieve similar manufacturing quality in terms of the shapes of attenuation bands. However, point-by-point method is a lot more time-consuming. For a 3cm LPG, it takes only 10 minutes to fabricate with amplitude mask, while it takes 50 minutes to fabricate by point-by-point method [202].

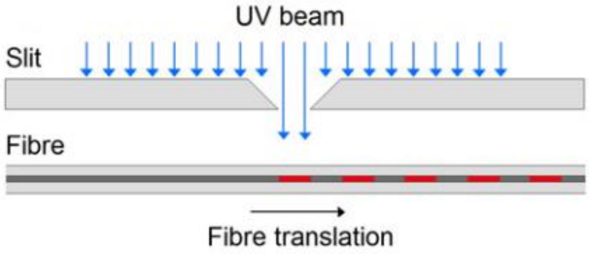

a

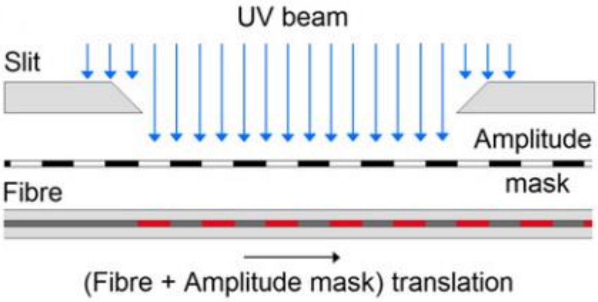

b

Figure 3- 1. The two laser-based methods to fabricate LPGs sourced from [202]. (a) The point-by-point method sourced from; (b) Fabrication with an amplitude mask.

The purpose of surface functionalization is to immobilize bio-receptors on the surface of LPGs. Many bio-receptors belong to the family of proteins, which are rich in amine groups (-NH_2) such that they can react with cross-linkers such as Glutaraldehyde or 11-MUA/EDC/NHS as shown in Figure 3-2.

In Section 3.1, the fabrication of LPGs with amplitude masks is explained, including the optical system and spectral change during fabrication. In Section 3.2, the surface functionalization processes are explained, including the surface functionalization with Glutaraldehyde cross-linker, the synthesis of AuNPs, and the surface functionalization with EDC/NHS cross-linker through the Layer-by-Layer (LBL) method.

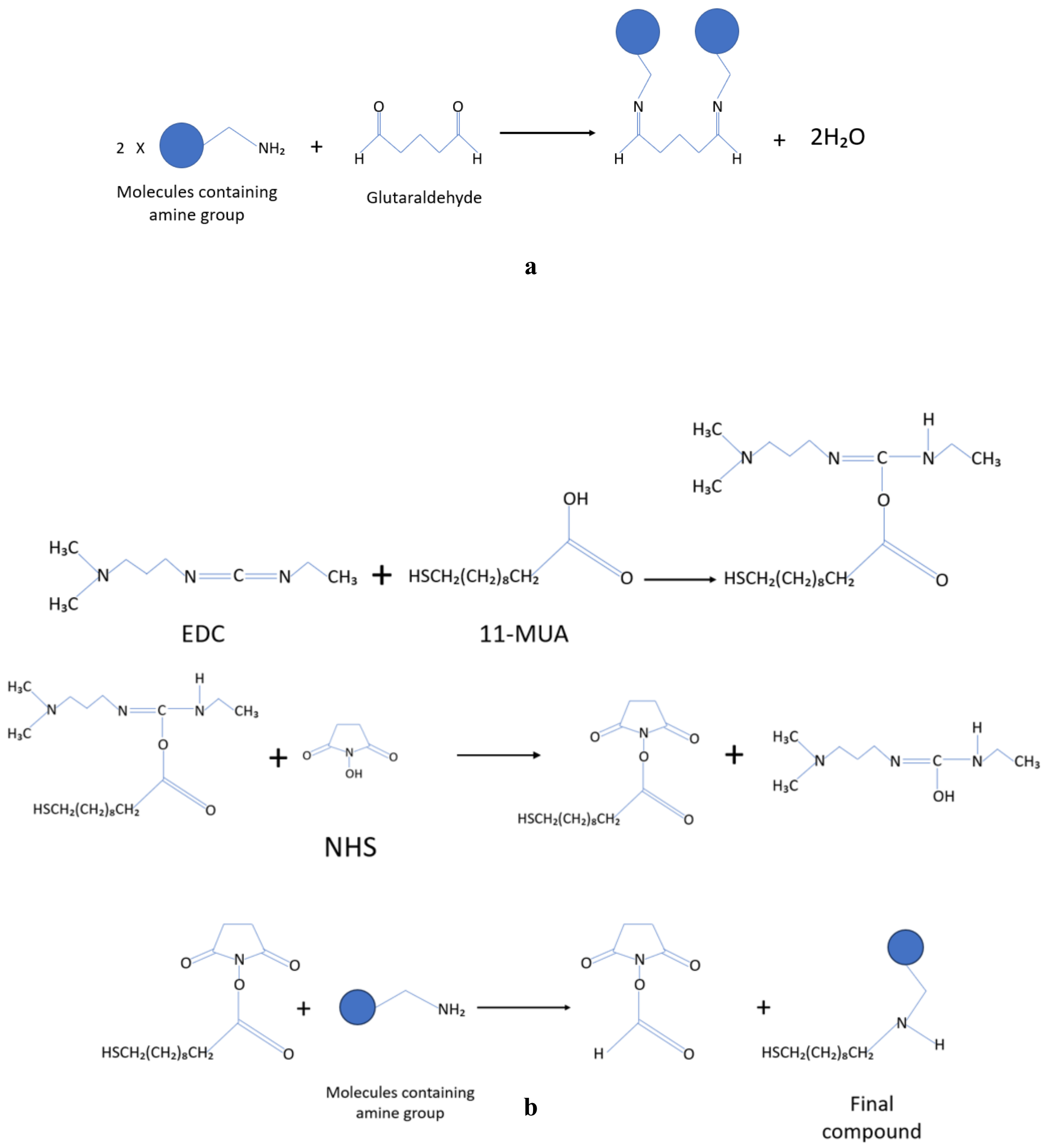

Figure 3- 2. Cross-linkers. (a) The reaction happens to Glutaraldehyde during cross-linking; (b) The reactions happen to 11-MUA, EDC, and NHS during cross-linking.

3.1 LPG Fabrication using Amplitude Masks

The LPGs used in this project are fabricated in PS750 photosensitive fibre (Fibrecore, UK) using a 266nm wavelength Nd:YAG laser (Q-smart 450 by Quantel). The diameter of the laser beam is approximately 6.5mm (measured at $1/e^2$ of peak intensity) and after passing through a focusing lens (4.5cm(L)×3cm(W), focal length=10cm) and is focused to a line on the photosensitive fibre (Figure 3-3 (a)). Situated between the fibre and the focusing lens is a steel amplitude mask (Suzhou Sunshine Laser Technology, China) which creates a structured light pattern (bright and dark fringes) on the surface of the photosensitive fibre (Figure 3-3(b)). The fibre core exposed to the laser illumination is modulated to a higher RI. The fibre and amplitude mask move together on a translation stage until the expected length of LPG is reached. The size of the amplitude mask is 9cm×1.5cm with slits region of 7cm×0.3cm (Figure 3-4(a)). There are multiple slits in the slit's region that have 50% duty cycle with a slit size varying with period. For example, the slit size of an amplitude mask with 100μm grating period is 50μm (Figure 3-4(b)). Figure 3-4 (a & b) are taken by the author and shared with Mr Mark East from the Centre of Additive Manufacturing, University of Nottingham by email for the discussion about the manufacturing of amplitude masks. Figure 3-4(b) is taken with OLYMPUS CX41 microscope.

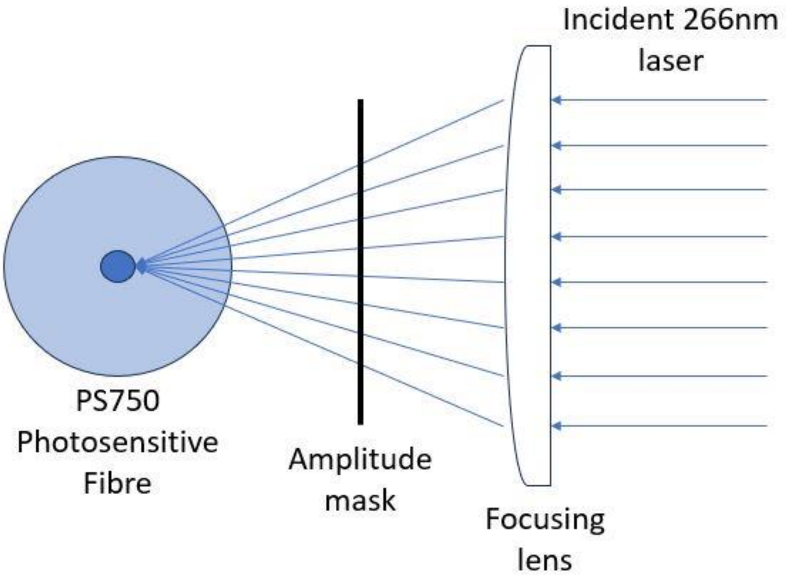

a

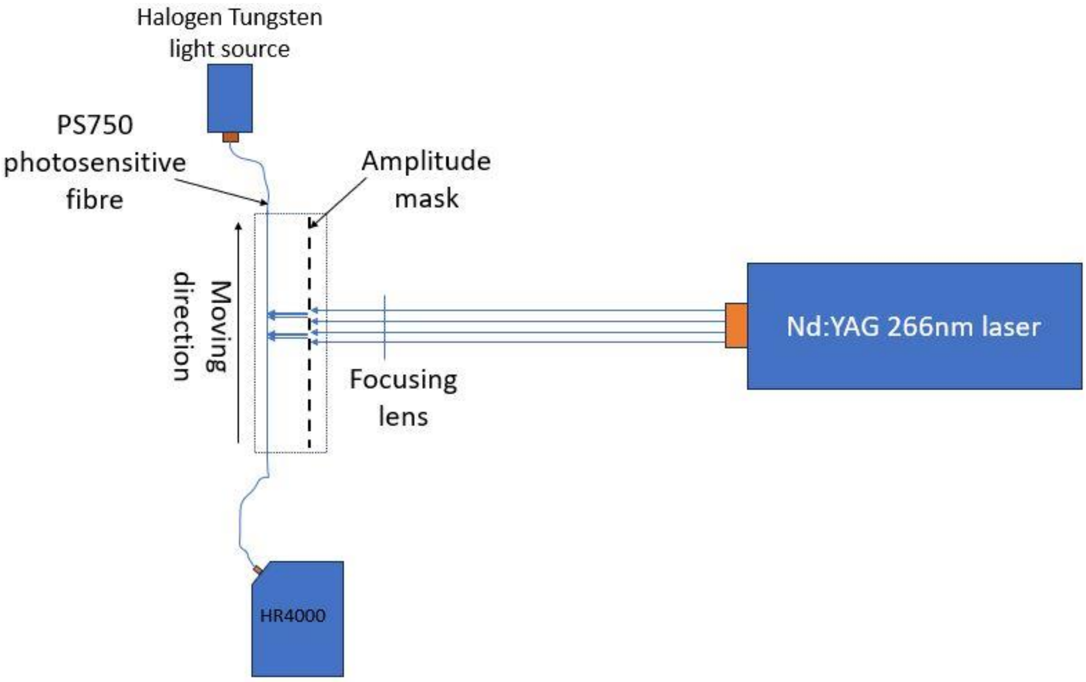

b

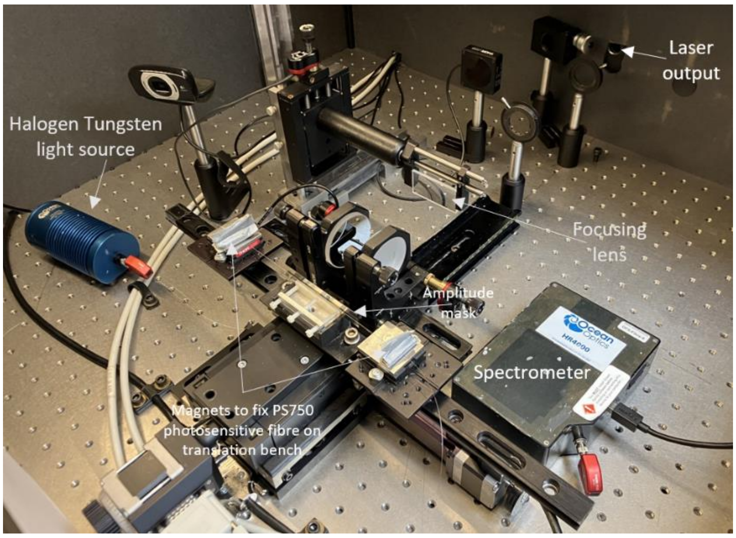

c

Figure 3- 3. The LPG fabrication set-up with amplitude mask. (a) side-view schematic; (b) Top view schematic; (c) The whole set-up.

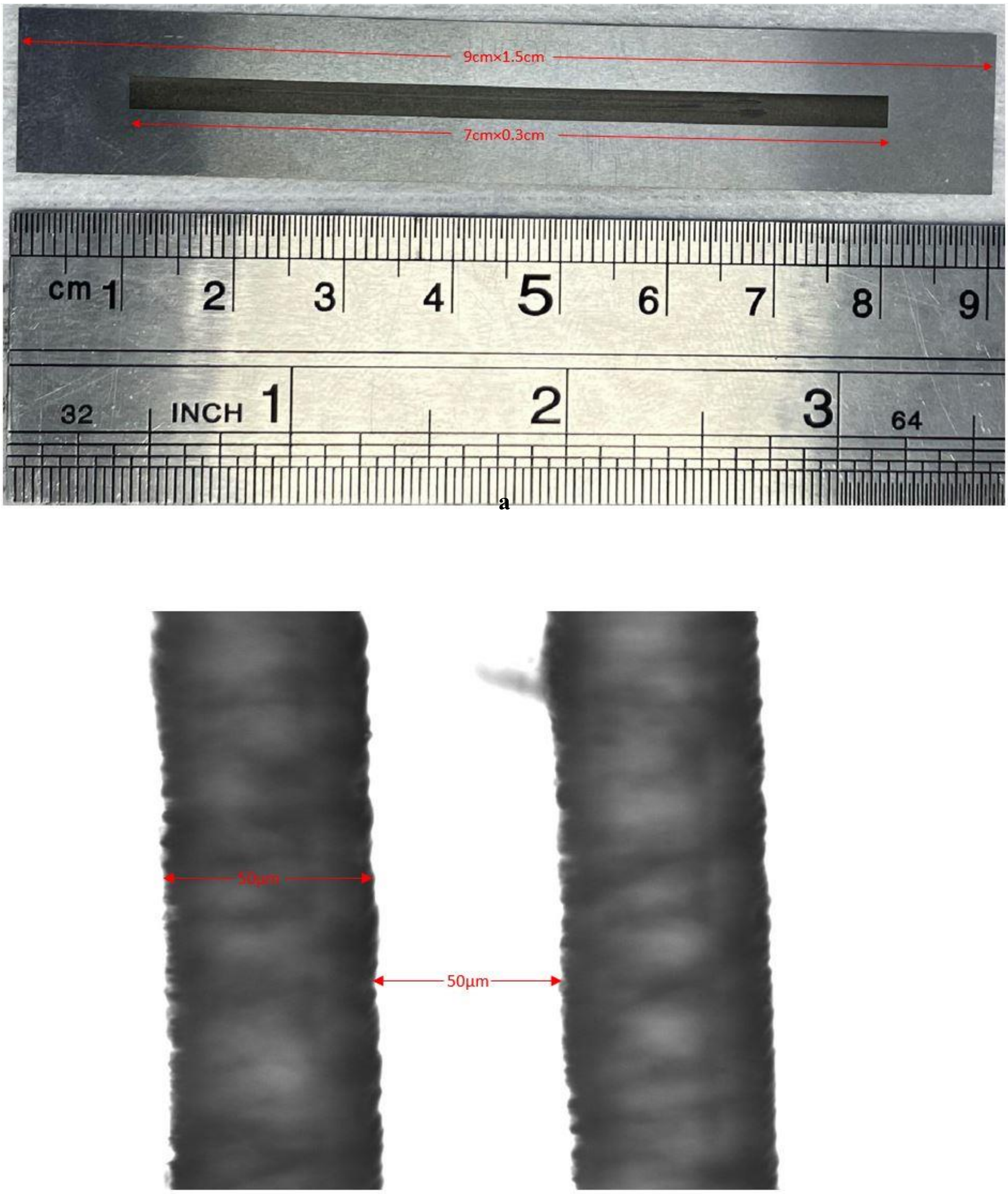

a

b

Figure 3- 4. An amplitude mask. (a) The size of an amplitude mask. (b) The amplitude mask under optical microscope.

PS750 photosensitive optical fibre is a Boron-Germanium (B, Ge) co-doped silica single mode fibre. The physical mechanism behind photosensitivity is still under debate [204]. However, it is a consensus that structural defects exist in Ge-doped silica fibre [205], [206]. The Ge or Si atom should connect to four oxygens to form stable structures $x\mathrm{GeO_2}\cdot y\mathrm{SiO_2}$ as shown in Figure 3-5(a) [205]. However, by manipulating the environment during manufacturing, structural defects are formed. There are several common recognized types of structural defects [205]: i) GeE' centre – a Ge atom is connected to three oxygens and has one unpaired electron (Figure 3-5(b)); ii) Two-fold coordinated Ge – a Ge atom has two unpaired electrons; iii) Neutral oxygen vacancy – a Ge atom is connected to another Ge atom (Figure 3-5(c)) or Si atom (Figure 3-5(d)). Photochemical reactions happen to these structural defects when they are exposed to UV light to change the RI of the fibre permanently. B-Ge co-doped optical fibre has much higher photosensitivity than Ge-doped fibre [207]. As B co-doping doesn't affect the Ge-related absorption to UV light, it is likely the higher photosensitivity is caused by photo-induced stress relaxation [207]. B doping increases the stress and UV light breaks the B-related bonds in optical fibre which releases the stress [207]. The relaxation of stress increases the RI due to the photo-elastic effect [207].

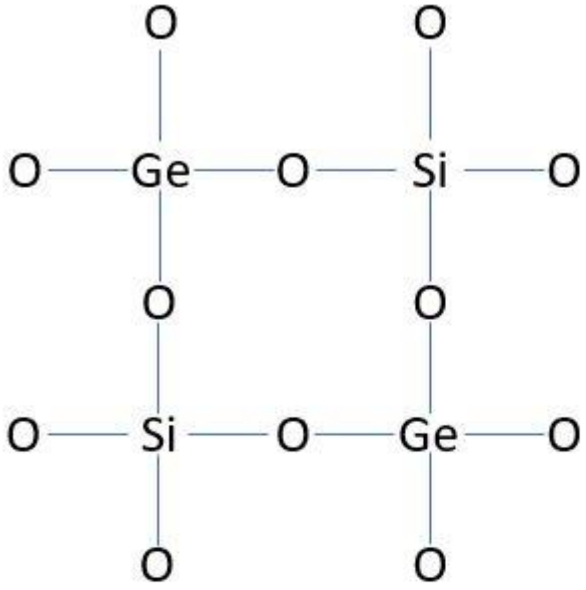

a

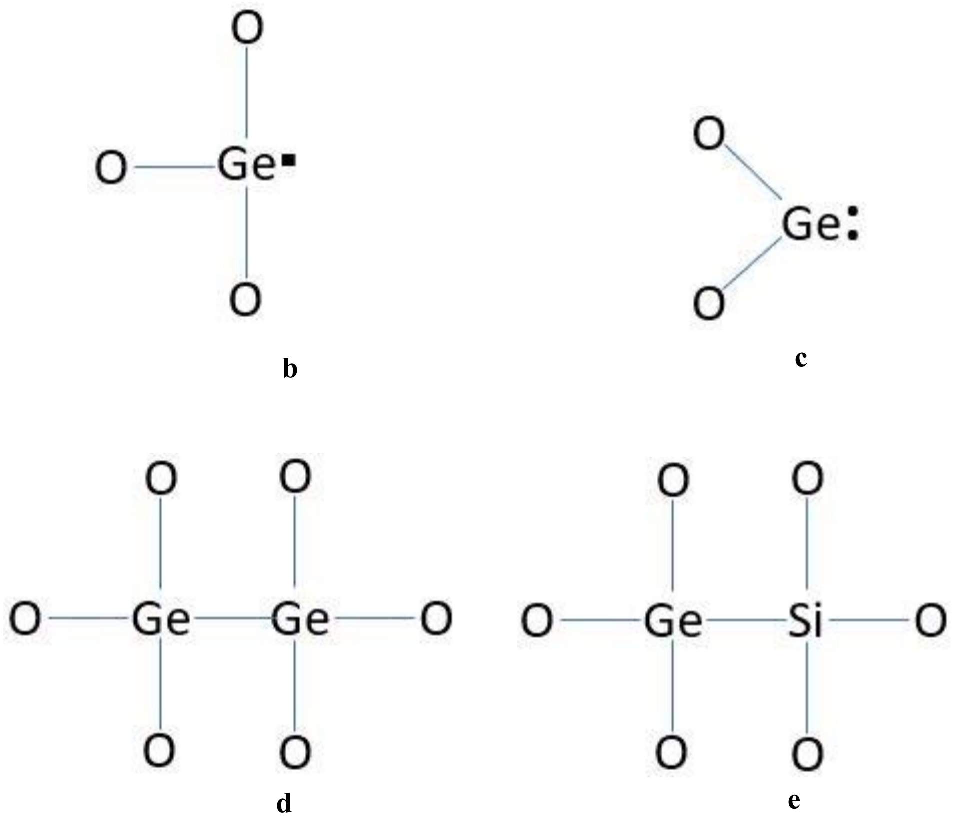

Figure 3- 5. The Molecular structures in Ge-doped silica optical fibre. (a) The normal xGeO2·ySiO2; (b) GeE' centre; (c) Two-fold coordinated Ge; (d) Ge-Ge neutral oxygen vacancy; (e) Ge-Si neutral oxygen vacancy.

Figure 3-6 (a) shows the change of transmission spectrum during an LPG fabrication. The translation stage keeps moving with a speed of 0.02mm/s during the fabrication. The length of the LPG increases gradually from 0 to the expected length (typically 3cm). The attenuation bands get deeper and narrower with an increasing LPG's length. The final transmission spectra vary due to the deviation of the manufacturing of the photosensitive fibre (Figure 3-5 (b)).

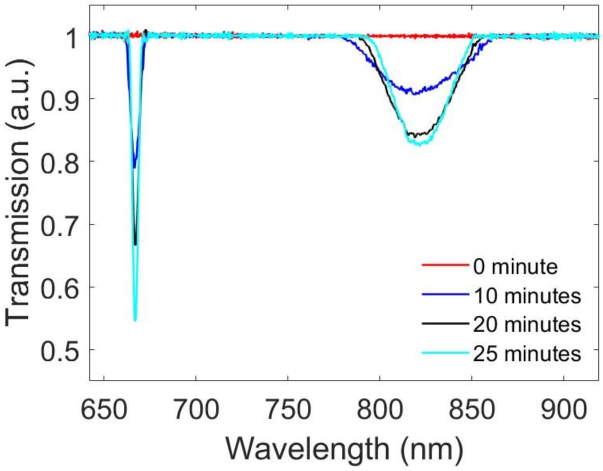

a

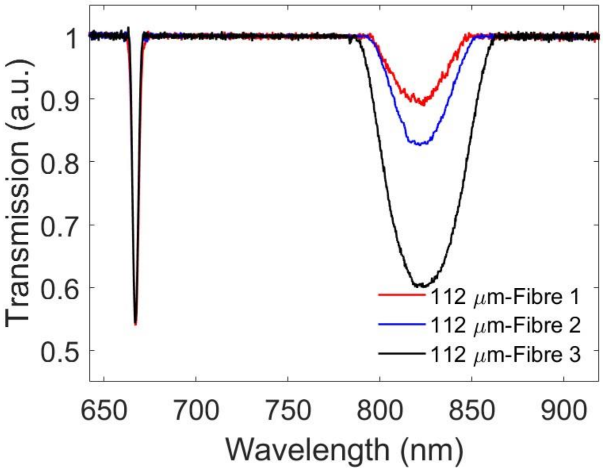

b

Figure 3- 6. LPG fabrication. (a) The change of spectrum during fabrication; (b) The difference among three independent fabrications with the same parameters.

3.2 Surface Functionalization

Two functionalization methods are adopted in this research: i) Layer-by-Layer-aided (LbL-aided) crosslinking with 11-MUA/EDC/NHS; ii) Direct cross-linking with Glutaraldehyde. They are both used to immobilize different bio-receptors on the surface of LPGs according to different applications.

3.2.1 Experimental set-ups

The two ends of the LPG are connected to a Halogen light source (Ocean Optics, USA) and a spectrometer (HR4000, Ocean Optics, USA) respectively. The LPG is placed in a homemade Teflon fibre bath (49mm(L)×3mm(W)×2mm(D)) (Figure 3-7(a)). Different solutions can be pipetted into the fibre bath such that the LPG is immersed. After the immersion, the solution can be removed with a suction pump (Flaem, Italy). A water heating bath (Grant Instrument, UK) is used for the temperature characterisation of LPGs (Figure 3-7(b)). The LPG is fixed on a metal holder with waterproof tape and placed in the water bath.

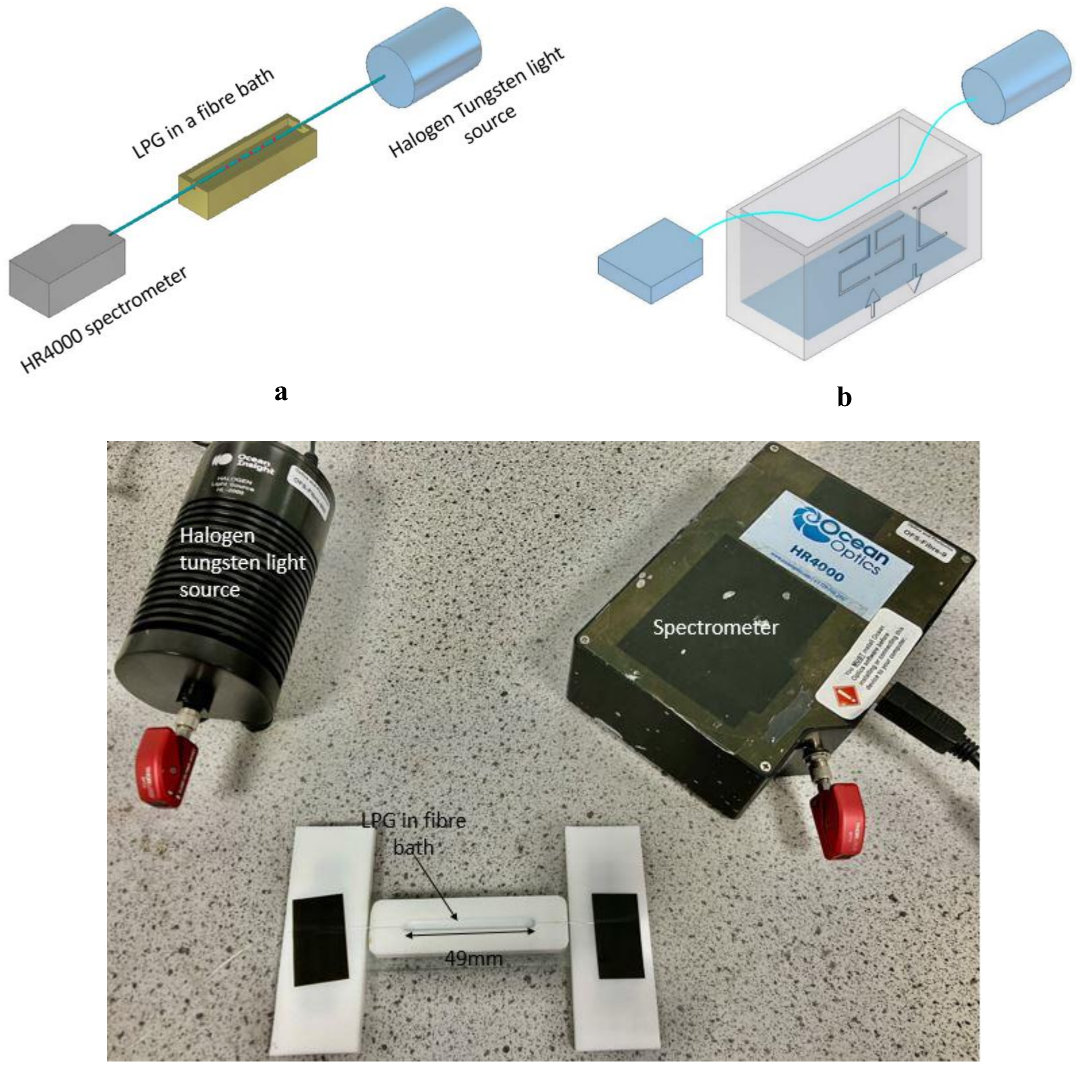

a **b**

c

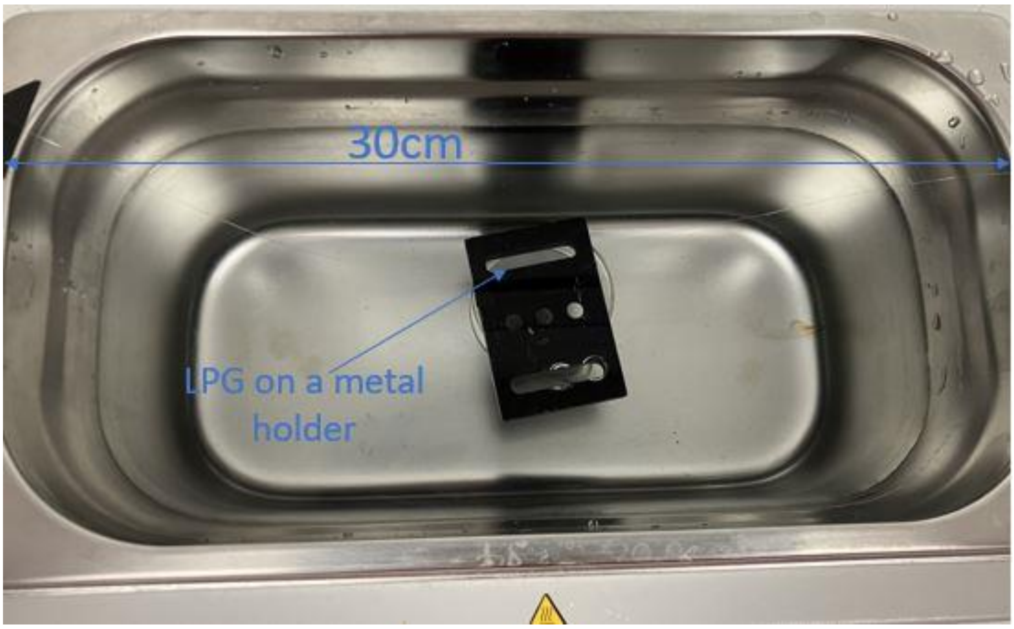

d

Figure 3- 7. The experimental set-ups. (a) An LPG placed in a fibre bath (49mm(L)×3mm(W)×2mm(D)) for surface functionalization and sample measurements; (b) An LPG placed in a water heating bath for temperature measurements; (c) Photo of the whole set-up with an LPG placed in the fibre bath; (d) Photo of an LPG placed in the water heating bath.

3.2.2 LbL-aided Crosslinking with 11-MUA/EDC/NHS

Layer-by-Layer assembly is a widely used method to build nanofilms on substrates. The protocol needs at least two different nanofilms. They should be oppositely charged such that dual layers are built up on the substrate by electrostatic forces [208].

3.2.2.1 Materials

Poly(allylamine hydrochloride, PAH), sodium borohydride ($NaBH_4$), gold (III) chloride trihydrate ($HAuCl_4·3H_2O$), (3-Aminopropyl)triethoxysilane (APTES), sulfuric acid (H_2SO_4, 95%~98%), hydrogen peroxide solution (H_2O_2, 35%), 3-Dimethylaminopropyl-N' -ethylcarbodiimide hydrochloride(EDC), N-hydroxysuccinimide (NHS), and 11-Mercaptoundecanoic acid (11- MUA) are purchased from Merck, UK. The silica nanoparticle (SiNPs, Snowtex-ZL, 20wt%, 70~100nm) is purchased from Nissan chemical, Japan.

3.2.2.2 Synthesis and Characterisation of Sub-5nm Gold Nanoparticles

The synthesis of sub-5nm gold nanoparticles (AuNPs) is achieved by reducing Au^{3+} ions to Au^0 atom. $NaBH_4$ is used as reducing agent.

$$9NaBH_4+2HAuCl_4 \longrightarrow 2Au^0+3NaB_3H_8+6NaCl+6H_2+2HCl$$

A protocol from [209] is followed. Stock solution 1 (St-S1) is 50mM $HAuCl_4{\cdot}3H_2O$ and 50mM HCl dissolved in Deionized (DI) water (Figure 3-8(a)). Stock solution 2 (St-S2) is 50mM $NaBH_4$ and 50mM NaOH dissolved in DI water (Figure 3-8(b)). 400µL St-S1 is added to 40mL DI water under room temperature with magnetic stirring (Figure 3-8(c)). After the colour becomes homogeneously yellow, add 1.2mL St-S2 to the solution. The solution turns red immediately (Figure 3-8(d)). Then, keep magnetically stirring the solution for one minute.

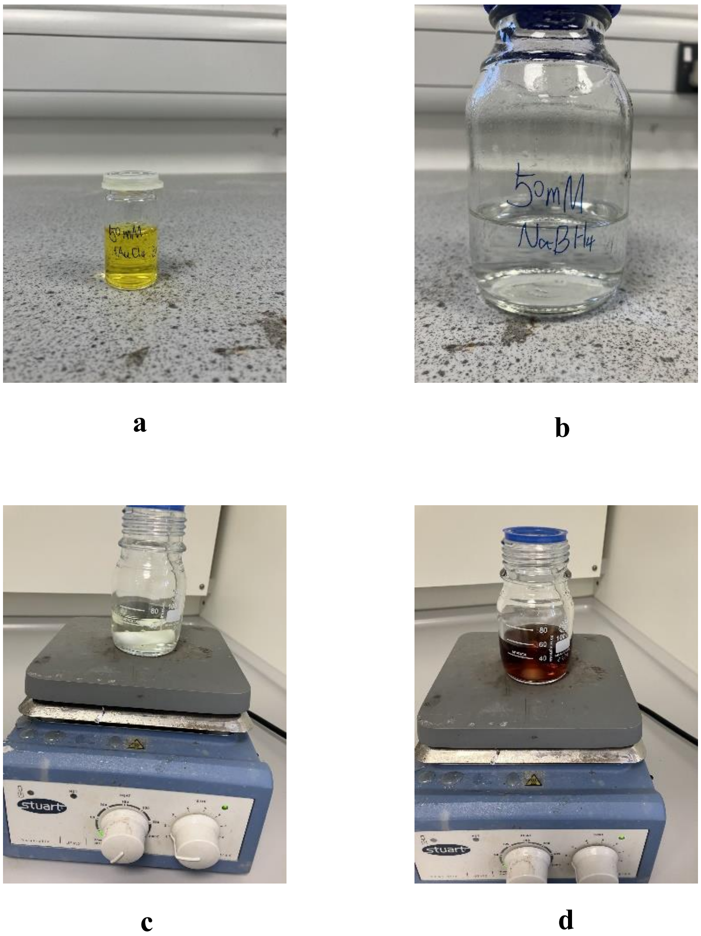

a

b

c

d

Figure 3- 8. The synthesis of sub-5nm AuNPs. (a) Stock solution 1 (St-S1) 50mM HAuCl4·3H2O and HCl dissolved in DI water; (b) Stock solution 2 (St-S2) 50mM NaBH4 and NaOH dissolved in DI water; (c) Add 400µL St-S1 to 40mL DI water and stir it magnetically; (d) Add 1.2mL St-S2 to the solution prepared in previous step under magnetically stirring.

The set-up to characterize the synthesized sub-5nm AuNPs is shown in Figure 3-9. A Halogen Tungsten light source with cuvette holder (ecoVIS, Ocean Optics) is used for the characterization. A 4.5mL quartz cuvette filled with AuNPs solution is placed in the cuvette. The incident light goes through the solution and is directed to a spectrometer (Flame, Ocean Optics) by an optical fibre.

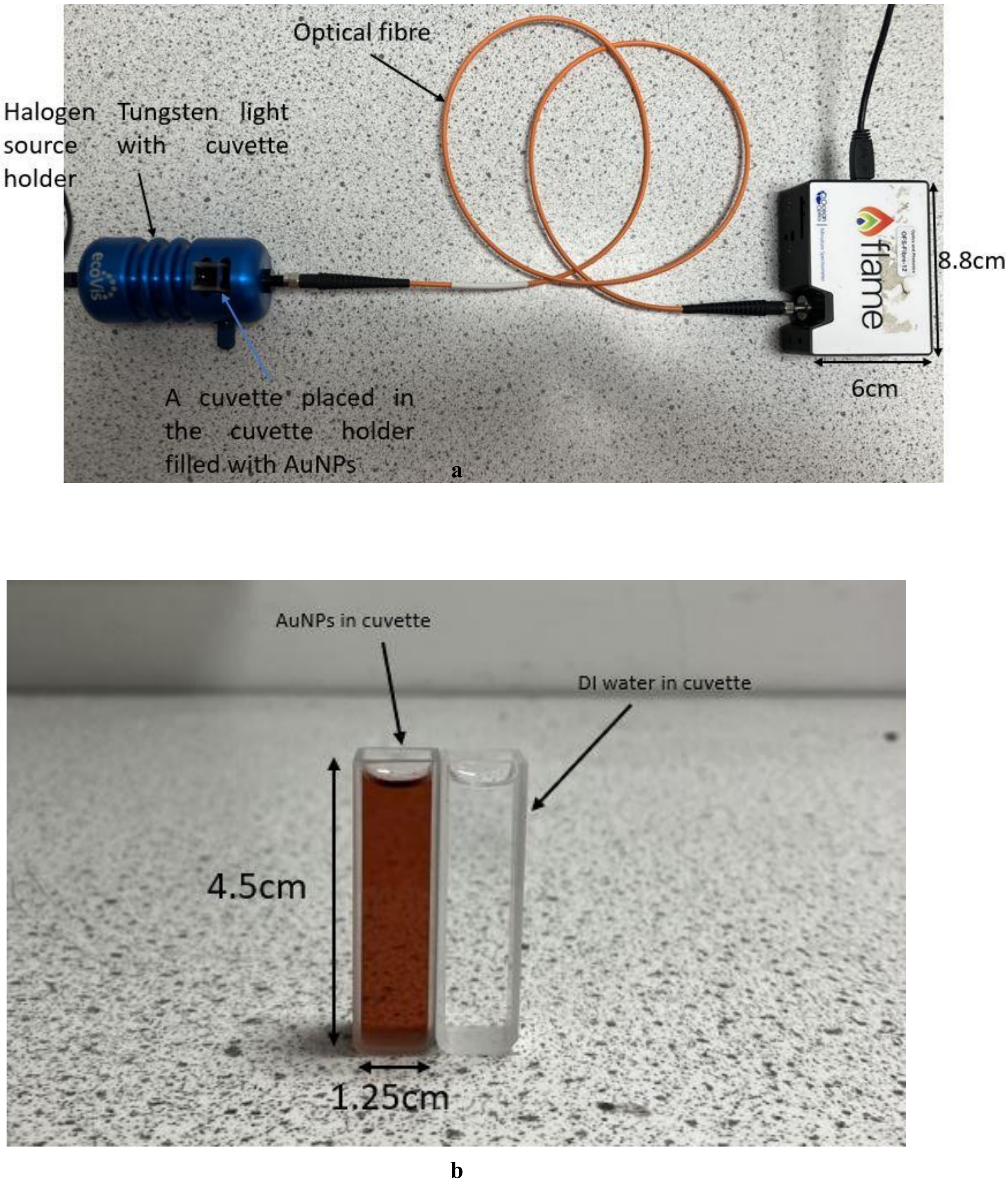

Figure 3- 9. The characterization of synthesized sub-5nm AuNPs. (a) The experimental set-up; (b) A comparison view of AuNPs and DI water.

The absorbance spectrum of the synthesized sub-5nm AuNPs solution is shown in Figure 3-10. An absorbance peak near 509.2nm is observed, which matches the absorbance character of sub-5nm AuNPs [209]. An image of the sub-5nm AuNPs taken with field-emission scanning electron microscopy is available in Appendix B, which is sourced from [209].

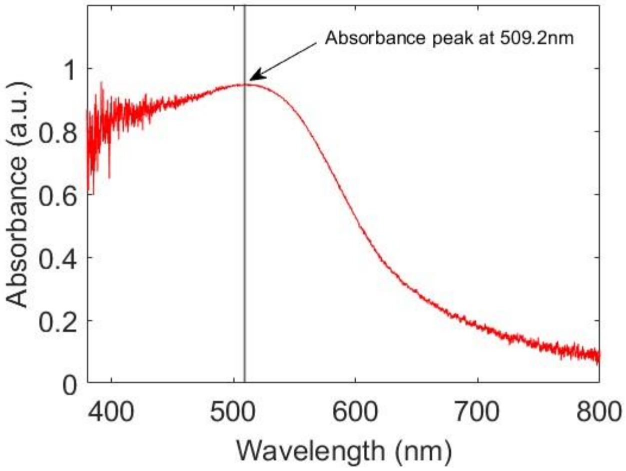

Figure 3- 10. The absorbance spectrum of sub-5nm AuNPs.

3.2.2.3 Immobilization of Bio-receptors

The whole process of the immobilization of bio-receptors is illustrated in Figure 3-11:

1. The LPG is immersed in Piranha solution (H_2SO_4:H_2O_2=3:1) for 20 minutes to remove organic contaminate and generate hydroxyl groups (-OH) on the surface.
2. The LPG is immersed in PAH solution (0.17wt% in DI water) for 15 minutes, followed by washing with DI water and drying with nitrogen. The positively charged PAH is adsorbed to the negatively charged hydroxyl groups on the LPG's surface.
3. The LPG is immersed in SiNPs solution (2wt% in DI water) for 15 minutes, followed by washing with DI water and drying with nitrogen. The negatively charged SiNPs are adsorbed to the positively charged PAH layer. Step 2 and Step 3 are repeated until the expected number of layers is reached.
4. The LPG is immersed into APTES solution (2 v/v% in Ethanol) for 20 minutes, followed by washing with DI water and ethanol alternately and drying in air over night (~17 hours). Amine groups ($-NH_2$) are formed in the PAH/SiNPs matrix.

5. The LPG is immersed in sub-5nm AuNPs solution, followed by washing with water and drying with nitrogen. The AuNPs are adsorbed to the amine groups.
6. The LPG is immersed in 11-MUA solution (4.4mg/ml in ethanol) for 30 minutes, followed by washing with ethanol and rinsing in DI water and drying with nitrogen. The sulfhydryl group (-SH) of 11-MUA can form covalent bonds with AuNPs.
7. The LPG is immersed in 4mg/ml EDC solution (in MES buffer, 19.5mg/ml with 0.5 wt% NaCl) for 20 minutes, followed by washing with PBS buffer and immediately immersing it in NHS solution (6.9mg/ml in PBS buffer). The LPG is ready for immobilizing bio-receptors on its surface (Figure 3-2 (b)).
8. The LPG is immersed in solution containing bio-receptor (e.g. 1mg/ml in PBS buffer) for 2 hours.

The size of AuNPs is less than 5% of the size of SiNPs. It is expected that two layers of PAH/SiNPs can form a porous matrix on the surface of LPG and AuNPs can diffuse into the matrix, which creates a film with good affinity to 11-MUA and subsequently more bio-receptors can be immobilized on the surface [30].

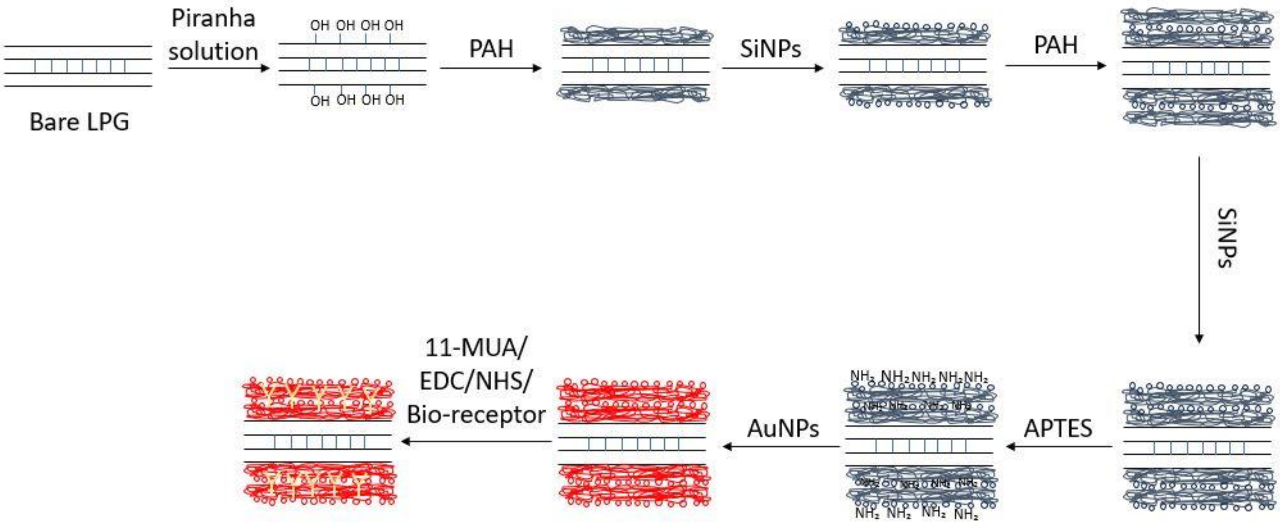

Figure 3- 11. The Layer-by-Layer assembly of nanofilms on the surface of an LPG

Scanning electron microscope (SEM) images of optical fibres are shown in Figure 3-12. They are taken with JEOL-7000F FEG-SEM (Oxford Instruments, UK) at Nano & Micro Scale Research Centre, University of Nottingham, UK. The fibre samples are either fixed on a glass slide for imaging the surface, or on a vertical holder for imaging cross-section (Appendix C). 10nm-thick iridium films are coated on the samples. An image of the surface of an LPG is shown in Figure 3-12(a & b). It is completely covered after the deposition of two layers of PAH/SiNPs (Figure 3-12(c & d)). The cross-section of a bare LPG is shown in Figure 3-12(e). The two layers of PAH/SiNPs has thickness of approximately 1μm (Figure 3-12(f)). Although there are some aggregates of SiNPs (Figure 3-12(d)). After checking the whole optical fibre with SEM, it can be confirmed that whole surface of an optical fibre is covered by SiNPs with good uniformity.

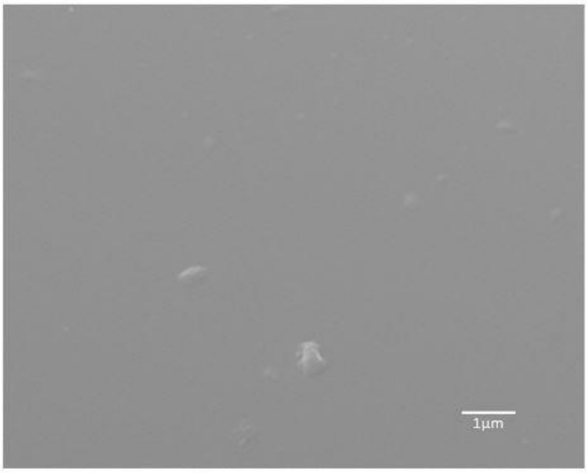

a

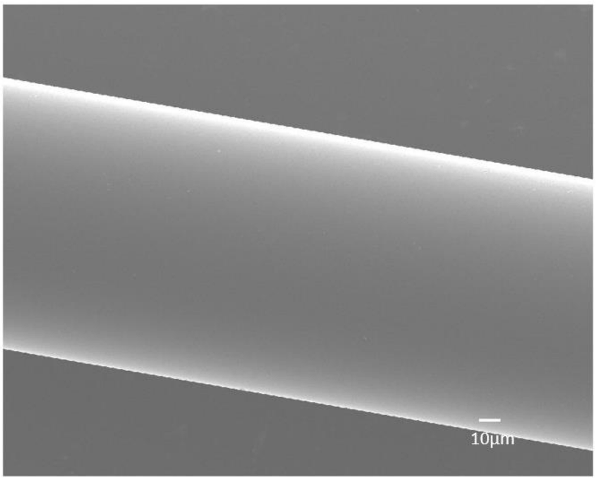

b

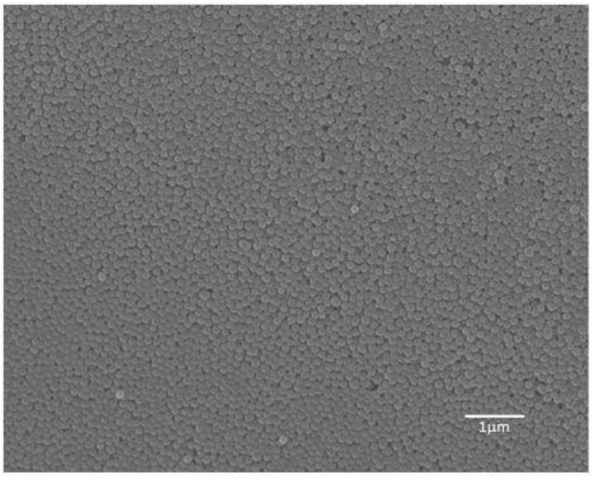

c

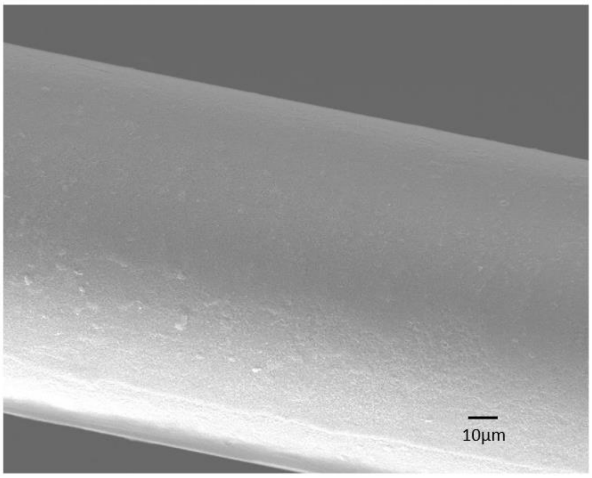

d

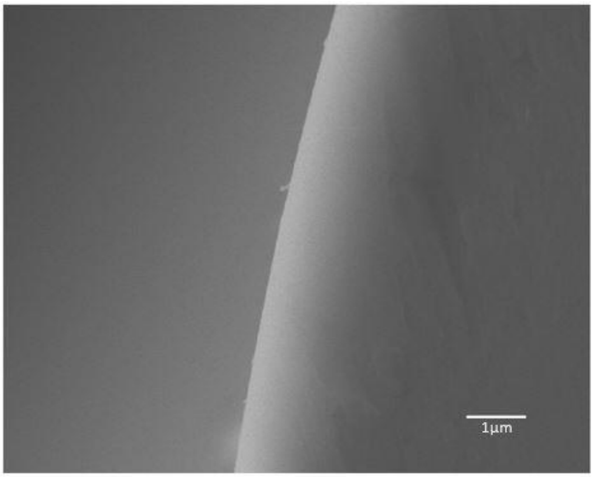

e

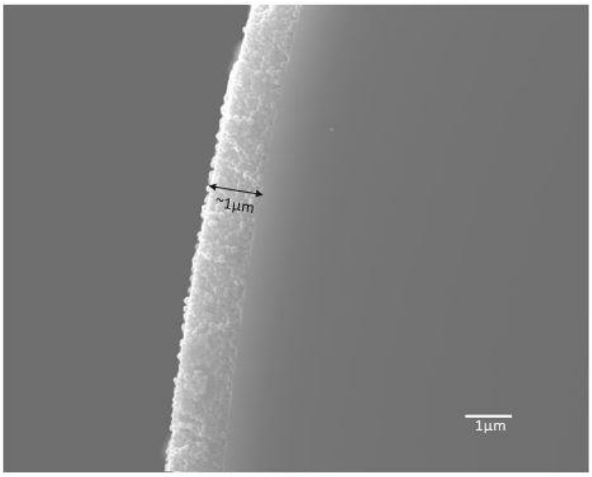

f

Figure 3- 12. The SEM images of the surface and cross-section of LPGs. (a) The surface of a bare LPG (~100μm^2 imaging area); (b) The surface of a bare LPG (~0.12mm^2 imaging area); (c) The surface of an LPG with 2 layers of PAH/SiNPs deposited (~100μm^2 imaging area); (d) The surface of an LPG with 2 layers of PAH/SiNPs deposited (~0.055mm^2 imaging area) (e) The cross-section of a bare LPG; (f) The cross-section of an LPG with 2 layers of PAH/SiNPs deposited.

3.2.3 Cross-linking with Glutaraldehyde

Glutaraldehyde is another widely used cross-linker besides 11-MUA/EDC/NHS. It has two aldehyde groups (-CHO) which can react with -NH_2. Before immobilizing bio-receptors on the surface of an LPG, many -NH_2 sites need to be generated.

3.2.3.1 Materials

(3-Aminopropyl)triethoxysilane (APTES), sulfuric acid (H_2SO_4, 95%~98%), hydrogen peroxide solution (H_2O_2, 35%), Glutaraldehyde solution (50wt% in H_2O) are purchased from Merck, UK.

3.2.3.2 Immobilization of Bio-receptors

The whole process of the immobilization of bio-receptors are illustrated in Figure 3-13:

1. The bare LPG is immersed in Piranha solution (H_2SO_4:H_2O_2=3:1) for 20 minutes. Organic contaminants are removed, and hydroxyl groups are generated on the surface.
2. The LPG is immersed in APTES solution (2 v/v% in Ethanol) for 20 minutes followed by washing with DI water and Ethanol alternately. Amine groups are generated on the surface of the LPG.

3. The LPG is immersed in Glutaraldehyde solution (50 wt% in H_2O) for 2 hours followed by washing with DI water. One aldehyde group of Glutaraldehyde reacts with the amine group on the LPG's surface to immobilize it.
4. The LPG is immersed in the relevant bio-receptor's solution (e.g. 1mg/ml in PBS buffer) for 2 hours. The amine groups of bio-receptors react with the free aldehyde groups of Glutaraldehyde. The bio-receptors are then immobilized on the surface of the LPG.

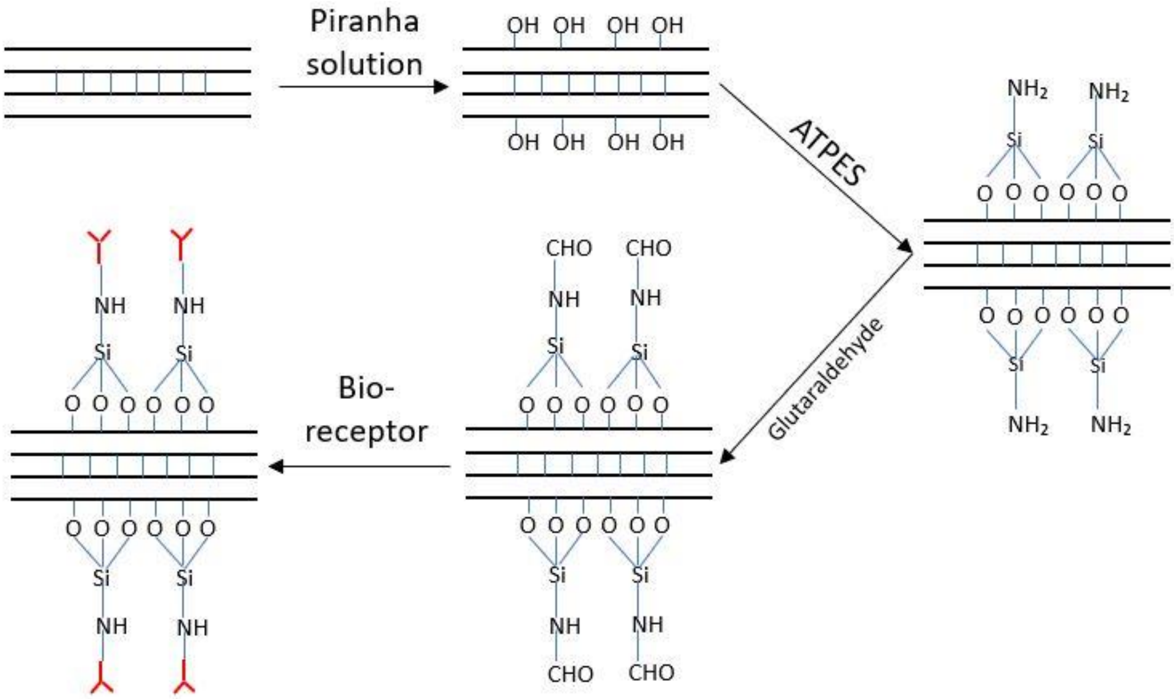

Figure 3- 13. Immobilization of bio-receptors on an LPG's surface with Glutaraldehyde cross-linker.

3.3 Summary

The methodologies to fabricate LPGs and functionalize the surface are described in this chapter. The LPGs are fabricated in PS750 photosensitive fibre using a 266nm Nd:Yrd laser and amplitude mask. This is more timesaving than the point-by-point method. Sub-5nm AuNPs are made from $HAuCl_4$ and $NaBH_4$. The solution of sub-5nm AuNPs has light absorbance peak at 509.2nm. An image of the AuNPs taken with field-emission scanning electron microscope is shown in Appendix, which is sourced from [209]. It is cheaper to synthesize AuNPs than using commercially available AuNPs, which costs 128 pounds for 25mL (Merck, UK). When functionalizing the surface with LbL-aided crosslinking with 11-MUA/EDC/NHS, the LPG is immersed into corresponding solutions sequentially. A matrix of PAH/SiNPs/AuNPs is deposited on the surface of an LPG. 11-MUA/EDC/NHS is linked to the AuNPs. The bio-receptors are immobilized on the surface through the reaction between -NH_2 of bio-receptors and 11-MUA/EDC/NHS. When functionalizing the surface with Glutaraldehyde, an LPG is immersed into ATPES and Glutaraldehyde sequentially to generate -CHO on the surface; bio-receptors are immobilized on the surface through the reaction between -NH_2 of bio-receptors and -CHO.

Chapter 4. LPG Simulations and Characterisations

The working principles of an LPG have been explained in Section 2.2.2. The development of biosensors based on an LPG exploits its response to external RI. An LPG's response to external RI is dependent on its working conditions, which is determined by grating period and optical fibre's properties. In this chapter, an LPG's working conditions and responses to external RI are explored. In Section 4.1, the working conditions of LPGs with different parameters are explained and compared, and the transmission spectra are simulated. In Section 4.2, different LPGs' responses to external RI are simulated and compared. In Section 4.3, an LPG is tested with different external RIs under four different scenarios: i) a bare LPG; ii) an LPG with PAH/SiNPs deposited on the surface; iii) an LPG with PAH/SiNPs/AuNPs; iv) Glutaraldehyde and BSA deposited on the surface. Finally, an LPG's response to temperature is investigated to understand a potential source of cross-sensitivity.

4.1 LPGs' Working Conditions and Transmission Spectra

When fabricating an LPG-based sensor, it should be fabricated with suitable working range and high sensitivity to external RI. By choosing a suitable grating period, an LPG can work near the Phase-Matching Conditions (PMC), under which the two attenuation bands from one resonance mode are very close to each other [210]. They are more sensitive to external RI than attenuation bands that work far away from the PMC [210]. The length of an LPG mainly affects the depth and width of attenuation bands. Recalling Equation (2-18), the wavelength of an attenuation band is dependent on the effective RI of the core mode n_{eff}^{co}, the effective RI of the corresponding cladding mode $n_{eff}^{cl,x}$, and the grating period Λ. n_{eff}^{co} and $n_{eff}^{cl,x}$ are related to the properties of the optical fibre (RIs and diameters of core and cladding) and light's wavelength. They are calculated from Equation (2-9). The parameters used for the simulation are listed in Table 4-1. They are the typical parameters of a photosensitive fibre (PS750, Fibercore), although there might be errors during manufacturing and these parameters might be slightly different.

PS750 Photosensitive Fibre	
Core Diameter (a_1)	5.2μm
Cladding Diameter (a_2)	125μm
Core RI (n_1)	1.4574
Cladding RI (n_2)	1.45227
Modulation depth (Δn_1)	0.9×10^{-4}
External RI (n_3)	1
Length of grating area	3cm

Table 4- 1. The typical parameters of PS750 photosensitive fibre used for simulations.

The effective RIs of core and cladding modes are shown in Figure 4-1(a & b) which decrease with wavelength. The resonance curves of grating period versus optical wavelength are shown in Figure 4-1(c) which indicate when attenuation bands occur. The grating period first increases with wavelength, and then decreases when it reaches a maximum. For example, for the 18th mode, the grating period reaches the maximum 105μm when the wavelength is approximately 850nm which defines the PMC. The transmission spectrum is shown in Figure 4-1(d) (blue curve). The 18th resonance mode (850nm) has a much wider attenuation band than the 17th (650nm). The transmission spectrum changes with grating period. The cross-section of the grating period line and the 17th resonance curve moves to a longer wavelength as the grating period increases. This effect is observed as a shift in the 17th-mode attenuation band from 644nm to 647nm to 650nm respectively when the grating period increases from 104.8μm to 105μm to 105.2μm (red→blue→black in Figure 4-1(d)). If the grating period is shorter than 105μm, the grating period line has two cross-sections with the 18th resonance curve and two attenuation bands exist for this mode. The wide attenuation band splits into two when the grating period decreases from 105μm to 104.8μm, while it gets shallower if the grating period increases to 105.2μm. The length of an LPG mainly affects the depth and width of attenuation bands but doesn't change the positions (Figure 4-1(e)). For an LPG with 105μm grating period, when the grating length increases from 1cm to 2cm to 3cm, the transmission of the 17th-mode attenuation band at 647nm decreases from 0.95 to 0.82 to 0.6 respectively, and the transmission of the 18th-mode 'U' shape band at 850nm decreases from 0.94 to 0.79 to 0.6 respectively. These trends are consistent with the spectra captured during the LPG fabrication process (Figure 3-6(a)).

The attenuation bands also get deeper with an increasing grating RI modulation depth (Figure 4-1(f)). In practice, the modulation depth can't be measured accurately, but it can be increased by increasing laser power and exposure time.

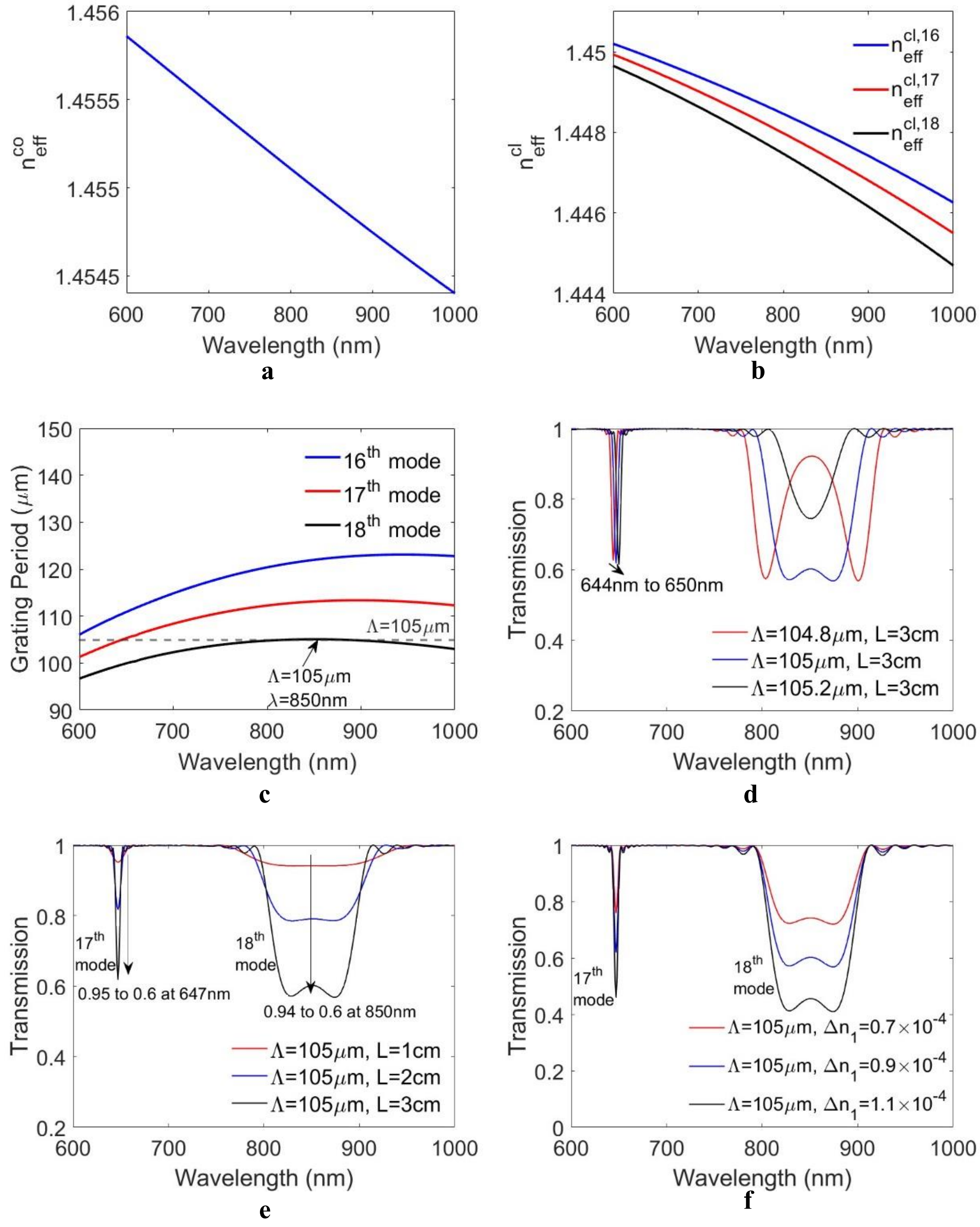

Figure 4- 1. The working parameters of an LPG in air (n3=1). (a) The effective RI of core mode n_{eff}^{co}; (b) The effective RI of the 16th to 18th cladding modes $n_{eff}^{cl,16}$, $n_{eff}^{cl,17}$, and $n_{eff}^{cl,18}$; (c) The resonance curves of the 16th to 18th mode; (d) Comparison of the transmission spectra of LPGs with 3cm grating length and 104.8µm, 105µm, or 105.2µm grating period; (e) Comparison of the transmission spectra of LPGs with 105µm grating period and 1cm, 2cm, or 3cm grating length; (f) Comparison of the transmission spectra of LPGs with 105µm grating period and 0.7×10-4, 0.9×10-4, or 1.1×10-4 modulation depth.

Deviations in the fabrication of photosensitive fibre can cause changes in an LPG's transmission spectrum and it can be compensated by amending the grating period. The original parameters are listed in Table 4-1. To investigate the effect of these parameters on an LPG's transmission spectrum, one of the original parameters is modified at a time and the transmission spectrum is plotted. After this, the grating period is amended to achieve a similar spectrum under modified different parameter. As shown in Figure 4-2(a), all three resonance curves move upwards to longer grating periods if the core diameter (a_1) decreases from 5.2μm to 5.1μm, and the Λ=105μm line intersects twice with the 18th mode resonance curve. The 'U' shape attenuation band in the transmission spectrum splits into two narrower bands. The 17th-mode attenuation band shifts from 647μm to 638μm, and the transmission decreases from 0.61 to 0.58 (Figure 4-2(b), Red→Blue). By increasing the grating period, the separation between two intersections of grating period line and the 18th-mode resonance curve gets closer. The LPG with 5.1μm core diameter and 105.8μm grating period has an 'U' shape band in its transmission spectrum (Figure 4-2(b), Blue→Black). Both the 17th-mode and 18th-mode bands locate at almost the same wavelengths comparing to the LPG with original parameters. Similarly, the resonance curves move to longer grating periods if the cladding diameter (a_2) increases from 125μm to 126μm (Figure 4-2(c)). The 18th-mode 'U' shape attenuation band splits into two narrower bands (Figure 4-2(d), Red→Blue). The 17th-mode band shifts from 647nm to 637nm, and the transmission increases from 0.61 to 0.62. After increasing the grating period from 105μm to 106.1μm, the two bands corresponding to the 18th resonance mode merge into a 'U' shape band and the 17th-mode band shift to a longer wavelength (Figure 4-2(d), Blue→Black). Comparing to the LPG with original parameters, both attenuation bands locate at longer wavelengths. The fluctuations in the RI of cladding or core can also cause changes in the transmission spectrum. The resonance curves move to longer wavelengths with a decreasing core RI or increasing cladding RI. As core RI decreases from 1.4574 to 1.4573, the 'U' shape band splits into two, the 17th-mode band shifts from 647nm to 627nm, and its transmission increases from 0.61 to 0.64 (Figure 4-2(f), Red→Blue). The two narrow bands merge into a 'U' shape band when grating period increases from 105μm to 106μm (Figure 4-2(f), Blue→Black) and the 17th-mode band shift to a longer wavelength. Compared with the LPG with original parameters, both attenuation bands locate at shorter wavelengths. An increasing cladding RI from 1.45227 to 1.4523 also cause the splitting of the 'U' shape band and the blue shift of the 17th-mode band from 647nm to

641nm, and its transmission increases from 0.61 to 0.63. After increasing the grating period to 105.3μm, the two narrow bands merge into a ‘U’ shape band and the 17th-mode band shifts to a longer wavelength. However, both attenuation bands locate at shorter wavelengths compared with the LPG with original parameters.

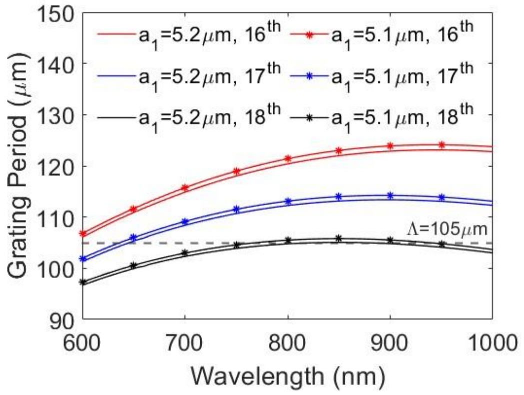

a

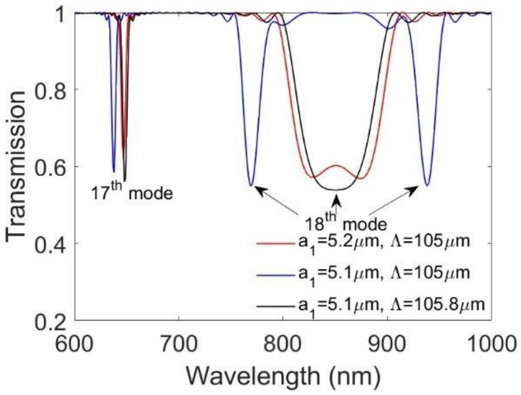

b

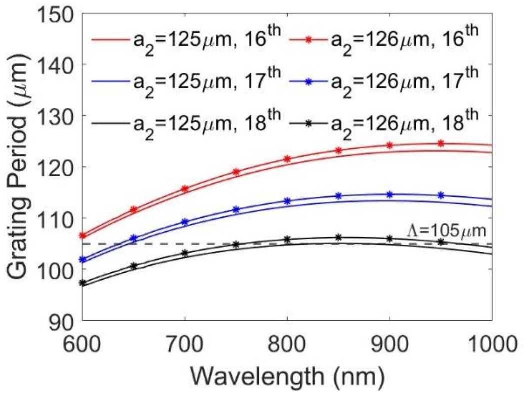

c

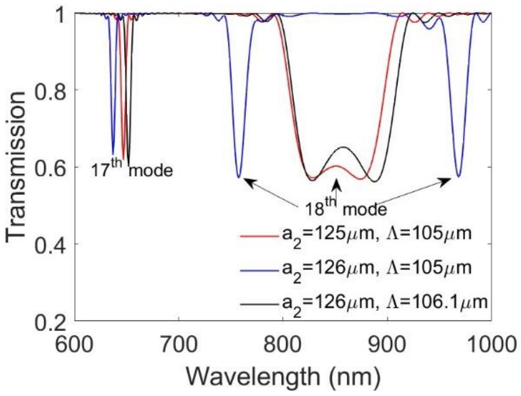

d

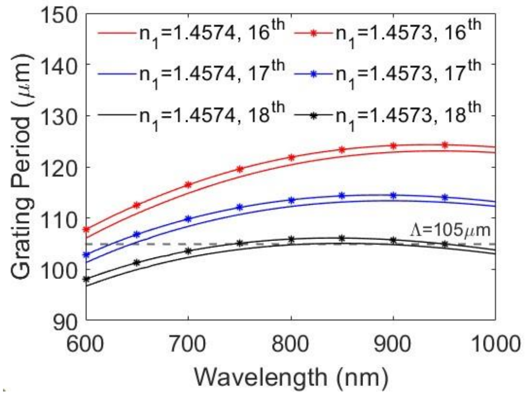

e

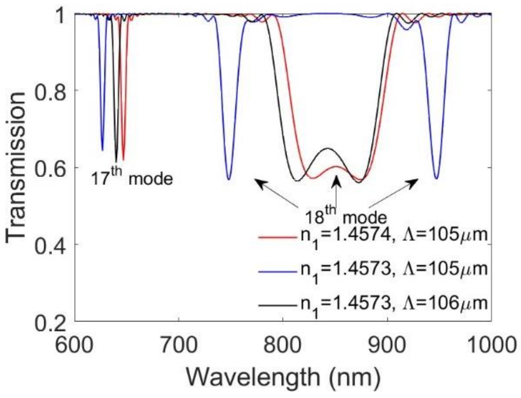

f

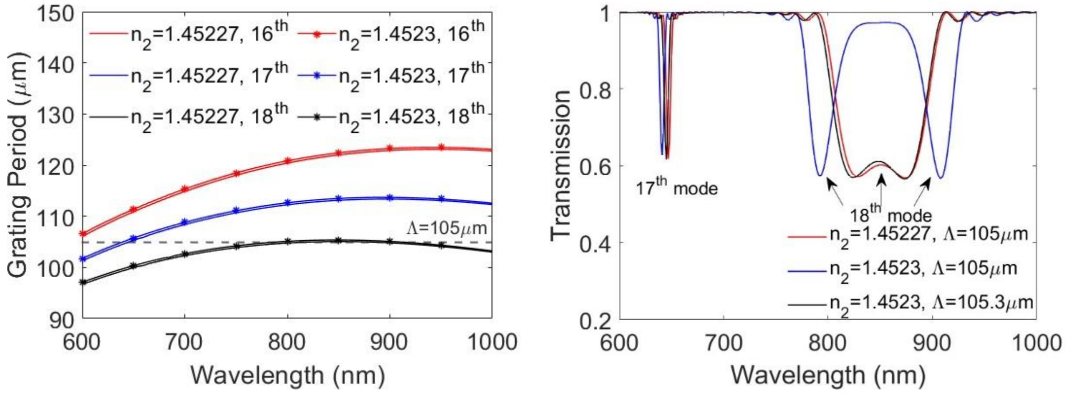

g h

Figure 4- 2. Comparison of LPGs when the PS750 photosensitive fibre's parameters fluctuate. (a) resonance curves when the core diameter decreases from 5.2µm to 5.1µm; (b) transmission spectra when the core diameter decreases from 5.2µm to 5.1µm; (c) resonance curves when the cladding diameter increases from 125µm to126µm; (d) transmission spectra when the cladding diameter increases from 125µm to 126µm; (e) resonance curves when the core RI decreases from 1.4574 to 1.4573; (f) transmission spectra when the core RI decreases from 1.4574 to 1.4573; (g) resonance curves when the cladding RI increases from 1.45227 to 1.4523; (h) transmission spectra when the cladding RI increases from 1.45227 to 1.4523.

The working conditions and transmission spectra of LPGs with different parameters are simulated in this section. Grating length, grating period, and modulation depth are the LPGs' parameters that can be manipulated during fabrication. To make an LPG operate at the PMC, the grating period line should cross the resonance curve at its local maxima. A wide 'U' shape attenuation band can be observed in the transmission spectrum. As the grating period deviates from the optimal value, the grating period line can have zero or two intersections with the resonance curve, the 'U' shape band will become shallower or splits into two bands respectively. The attenuation band corresponding to a lower resonance mode than the 'U' shape band locates at a shorter wavelength and shifts to a longer wavelength with an increasing grating period. The length of an LPG affects the depth and width of the attenuation bands. With an increasing length, the wave coupling is enhanced at the resonance wavelength described by Equation (2-18) as the phase is exactly matched, and more light is coupled into cladding mode; The interference between cladding mode and core mode light happens after propagating a long distance due to the phase mismatching. The coupling strength between core mode and cladding modes is enhanced with an increasing modulation depth. Therefore, the attenuation bands get deeper. The photosensitive fibre parameters might fluctuate during manufacturing. Qualitatively, the decrease of core diameter or increase of cladding diameter makes the resonance curves move to a longer wavelength, and the ‘U’ shape band splits into two, and the band corresponding to the lower resonance mode shifts to a shorter wavelength. The decrease of core RI or increase of cladding RI makes the resonance curves move to longer wavelengths as well. The grating period line has two intersections with the 18th-mode resonance curve which results in the ‘U’ shape band splitting into two. The intersection of grating period line and 17th-mode resonance curve moves to a shorter wavelength. Therefore, the band of the 17th mode shifts to a shorter wavelength. There are two types of deviations of optical fibre’s parameters: i) the inter-batch deviation, which is the deviation between two different batches of optical fibre; ii) intra-batch deviation, which is deviation within the same batch of optical fibre and expected to be smaller than inter-batch deviation. By amending the grating period, it is possible to compensate for inter-batch deviations to make LPGs work around PMC as a few testing LPGs can be fabricated to find the most suitable period. However, intra-batch deviation is harder to be compensated as the working conditions are unknown until LPGs are fabricated.

4.2 Simulation of LPGs in Different External Refractive Indices

An LPG’s response to external RI is mainly caused by the changes of cladding modes which can cause shifts of the resonance curves and induce wavelength shifts of attenuation bands. Since different grating period lines have different cross-sections with resonance curves, the grating period can affect attenuation bands’ wavelength shifts with external RI. Using the parameters shown in Table 4-1, simulations in Section 4.2.1 illustrate how LPGs respond to external RI. The LPGs’ lengths are 3cm, and modulation depths are 0.9×10^{-4}. Three different grating periods are investigated, 104.8μm, 105μm, and 105.2μm. As explained in Section 4.1, the inter-batch parameters’ deviation can be compensated by amending the grating period, but the intra-batch parameters’ deviations are much harder to be compensated as the working condition of an LPG is unknown until it is fabricated. Simulations in Section 4.2.2 can explain how the small deviations of optical fibre’s parameters affect LPG’s response to external RI. Grating length and modulation depth are 3cm and 0.9×10^{-4} respectively. Grating period is fixed at 105.2μm. A deviation is introduced to the parameters shown in Table 4-1 every time.

4.2.1 LPGs’ responses to external refractive indices with different grating periods

As most biomolecules are dissolved in water-based solvents, they have RIs of about 1.3326, like water. The external RI (n_3) used for simulation starts from 1.3326 and gradually increases to 1.3734. As shown in Figure 4-3(a), the resonance curves shift to longer wavelengths as n_3 increases. The separation increases between the two intersections of the grating period lines and the 18th resonance curve. The two attenuation bands corresponding to the 18th cladding mode move further from each other (Figure 4-3(a, c, e)) and the 17th-mode bands move to shorter wavelengths (Figure 4-3(b, d, f)). This corresponds to the blue shift of the intersection of the grating period line and the 17th-mode resonance curve. The wavelengths of the 3 LPGs' attenuation bands are listed in Table 4-2 and the separation of the two bands of the 18th resonance mode is also calculated. The wavelength shifts are the wavelength differences between each attenuation band and the attenuation band in the case of 1.3326 external RI.

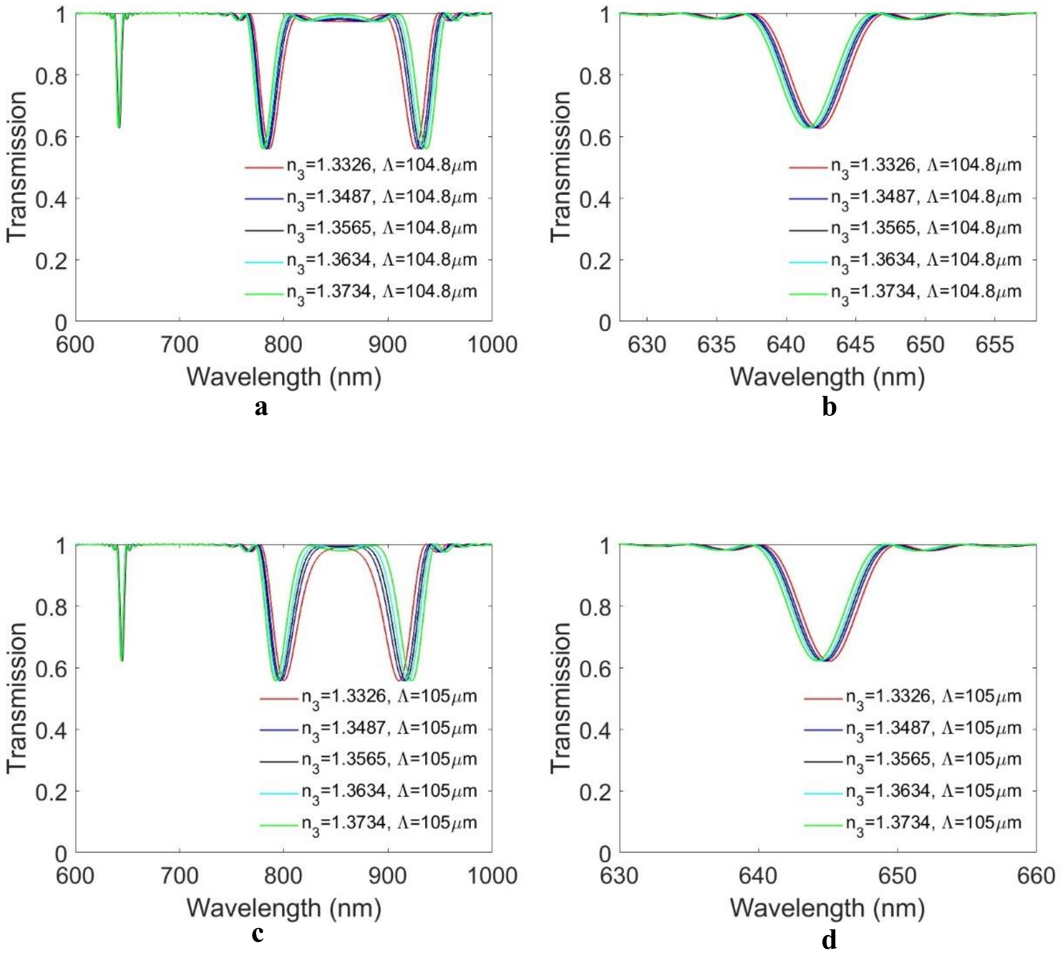

a **b**

c **d**

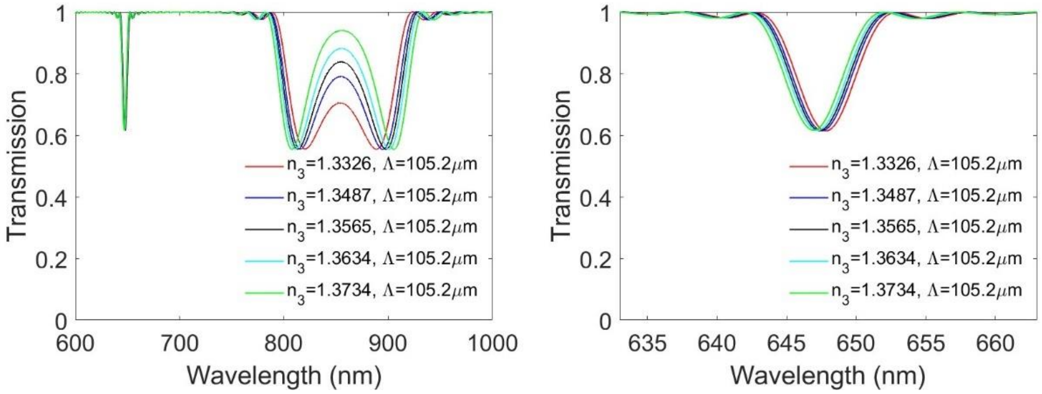

e

f

Figure 4- 3. The transmission spectra of LPGs under different external RI. (a) The transmission spectra of the LPG with 104.8µm grating period under external RIs ranging from 1.3326 to 1.3734; (b) The 17th-mode band of the LPG with 104.8µm grating period under external RIs ranging from 1.3326 to 1.3734; (c) The transmission spectra of the LPG with 105µm grating period under external RIs ranging from 1.3326 to 1.3734; (d) The 17th-mode band of the LPG with 105µm grating period under external RIs ranging from 1.3326 to 1.3734; (e) The transmission spectra of the LPG with 105.2µm grating period under external RIs ranging from 1.3326 to 1.3734; (f) The 17th-mode band of the LPG with 105.2µm grating period under external RIs ranging from 1.3326 to 1.3734.

104.8μm						
	17th-mode band		18th-mode first band	18th-mode second band	Separation between two 18th-mode bands	
	Wavelength	Wavelength Shift (absolute value)			Value	Wavelength Shift
1.3326	642.3nm	0	786.3nm	926.5nm	140.2nm	0
1.3487	642.1nm	0.2nm	784.2nm	930nm	145.8nm	5.6nm
1.3565	641.9nm	0.4nm	783nm	931.9nm	148.9nm	8.7nm
1.3634	641.8nm	0.5nm	781.9nm	933.8nm	151.9nm	11.7nm
1.3734	641.5nm	0.8nm	780nm	937nm	157nm	16.8nm
105μm						
	17th-mode band		18th-mode first band	18th-mode second band	Separation between two 18th-mode bands	
	Wavelength	Wavelength Shift (absolute value)			Value	Wavelength Shift

1.3326	645.1nm	0	800.4nm	910.6nm	110.2nm	0
1.3487	644.8nm	0.3nm	797.6nm	914.7nm	117.1nm	6.9nm
1.3565	644.6nm	0.5nm	796nm	917.1nm	121.1nm	10.9nm
1.3634	644.5nm	0.6nm	794.5nm	919.3nm	124.8nm	14.6nm
1.3734	644.2nm	0.9nm	792.2nm	923nm	130.8nm	20.6nm
105.2μm						
	17th-mode band		18th-mode first band	18th-mode second band	Separation between two 18th-mode band	
	Wavelength	Wavelength Shift (absolute value)			Value	Wavelength Shift
1.3326	647.8nm	0	820.3nm	888.8nm	68.5nm	0
1.3487	647.5nm	0.3nm	815.7nm	894.8nm	79.1nm	10.6nm
1.3565	647.4nm	0.4nm	813.4nm	897.9nm	84.5nm	16nm
1.3634	647.2nm	0.6nm	811.1nm	900.9nm	89.8nm	21.3nm
1.3734	646.9nm	0.9nm	807.7nm	905.6nm	97.9nm	29.4nm

Table 4- 2. The wavelengths of LPGs' three attenuation bands under external RIs ranging from 1.3326 to 1.3734.

The wavelengths of the attenuation bands of the three LPGs under different external RIs are shown in Table 4-2. It can be observed that the sensitivity to external RI is higher when using wavelength shifts of two 18th-mode bands than that of an individual band i.e. the wavelength shifts of the separation between two 18th-mode bands are over twenty times greater than the wavelength shifts of the individual 17th-mode bands when the grating period is 104.8μm. The wavelength shifts of the 17th-mode bands and the separations between the two 18th-mode bands are calibrated linearly with external RI. The 17th-mode bands of the LPGs with 104.8μm, 105μm, and 105.2μm grating period have sensitivity to external RI of 19.3nm/RIU, 21.7nm/RIU, and 21.5nm/RIU respectively (Figure 4-4(a)), with the coefficients of determination (R^2) equalling 96.7%, 99%, and 97.5% respectively. The 18th-mode bands of the LPGs with 104.8μm, 105μm, and 105.2μm grating period have the sensitivity to external RI of 407.86nm/RIU, 502.53/RIU, and 717.14nm/RIU respectively (Figure 4-4(b)), with R^2 equalling 99.17%, 99.37%, and 99.73% respectively. As shown in Figure 4-4(c), the

18th-mode curve has maxima at around 850nm. The grating period increases with wavelength between 600nm and 850nm with a decreasing slope, and it decreases with wavelength between 850nm and 1000nm with an increasing slope. The grating period line has one intersection with the 17th-mode curve. The slope of the 17th-mode curve at the intersection is greater than the slope of the 18th-mode curve at its two intersections with grating period line. Therefore, when external RI increases, the wavelength shifting rate of the intersection of 17th-mode curve and grating period line is lower than the wavelength shifting rates of the intersections of 18th-mode curve and grating period line. The 17th-mode band has lower sensitivity to the change of external RI than the 18th-mode bands. When the grating period increases, the grating period line approaches the maxima of the resonance curve. The slopes of the resonance curve at its intersections with grating period line decreases. Therefore, the 18th-mode bands have higher sensitivity to external RI change in terms of wavelength shift when the grating period increases.

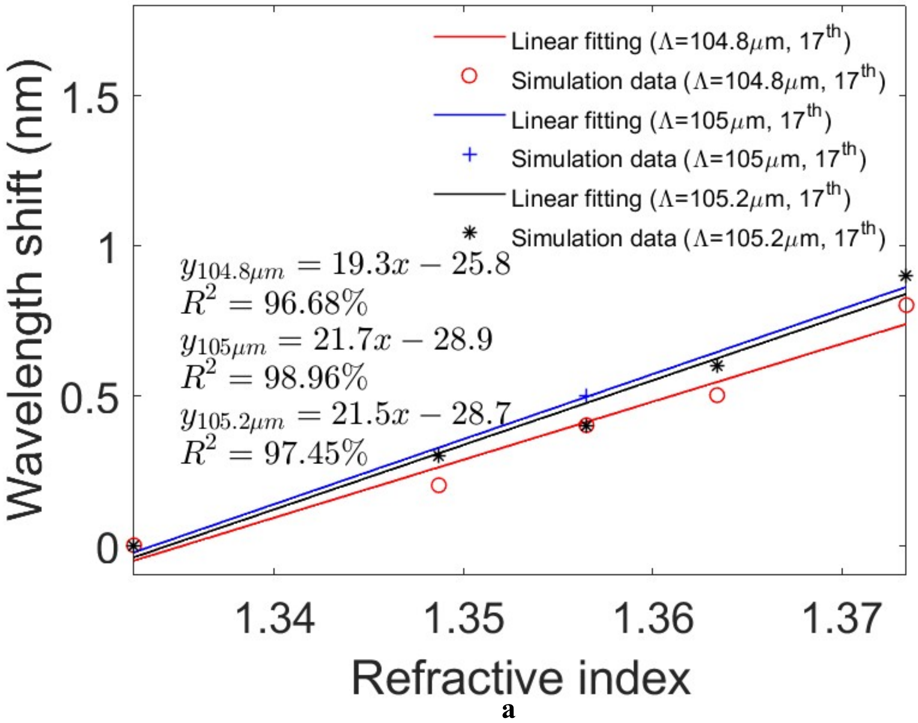

a

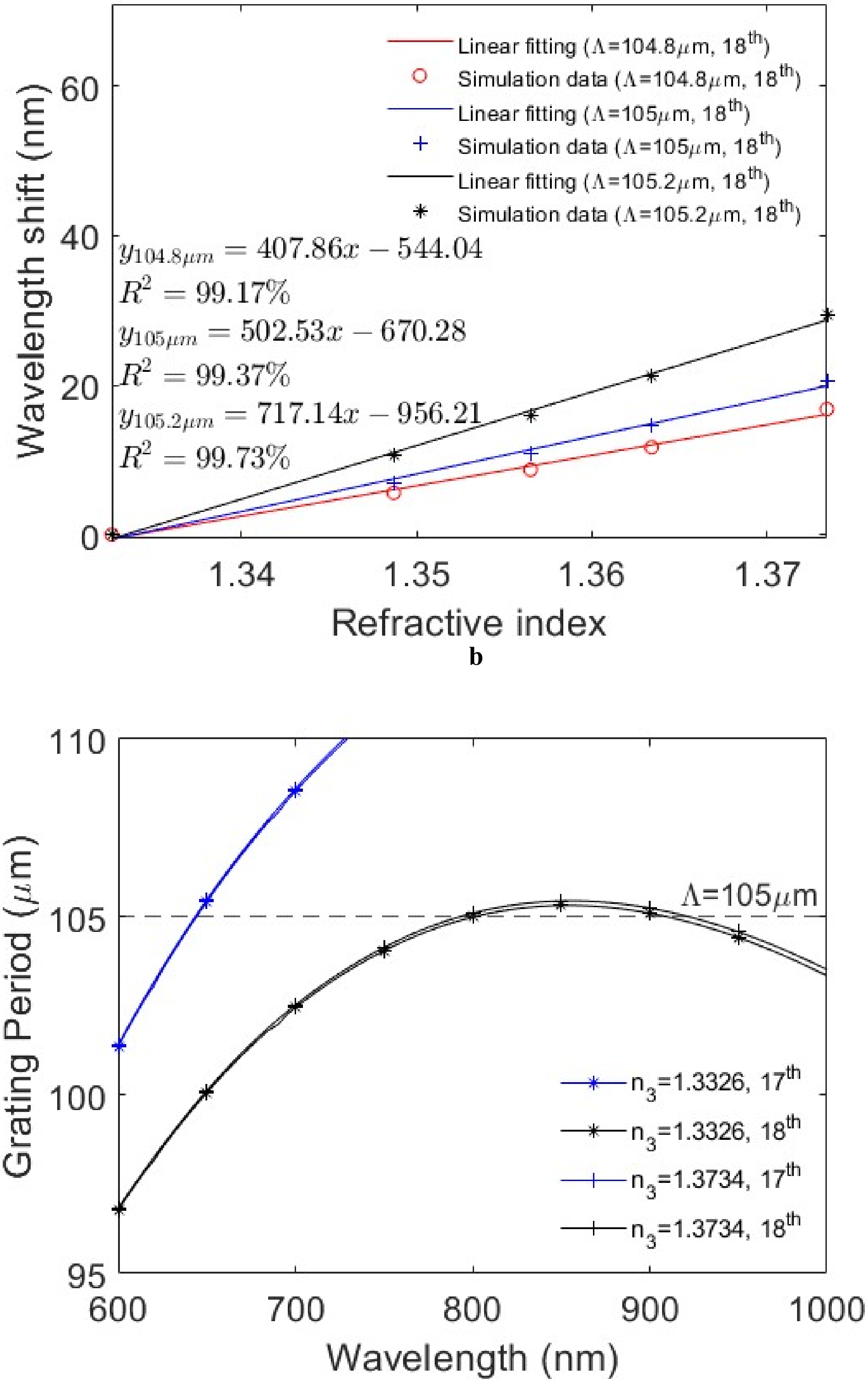

b

c

Figure 4- 4. Calibration curves of attenuation bands' wavelength shifts versus external RI. (a) The calibration curves of the 17th-mode bands' wavelength shifts versus RI; (b) The calibration curves of the increments of the separation between the two 18th-mode bands versus external RI; (c) The resonance curves under different external RI (n3).

4.2.2 LPGs' responses to external refractive indices with deviated optical fibre's parameters

The effects of parameters' deviations on an LPG's response to external RI is investigated. The introduced parameters' deviations are: i) a decreasing core RI (Figure 4-5 (a, b)); ii) an increasing cladding RI (Figure 4-5 (c, d)); iii) a decreasing core diameter (Figure 4-5 (e, f)); iv) an increasing cladding diameter. Recalling the results of Section 4.1. With these four deviations, the LPG shifts away from PMC. The responses are qualitatively the same as the responses shown in Figure 4-3. With the external RI increasing, the two 18th-mode attenuation bands move oppositely and the separation between them increases (Figure 4-5(a, c, e, g)). It corresponds to the 18th-mode resonance curve moving to longer wavelengths and the two intersections between it and the grating period line moving away from each other. The 17th-mode attenuation band moves to shorter wavelengths as external RI increases (Figure 4-5(b, d, f, h)). It corresponds to the 17th-mode resonance curve moves to loner wavelengths and the intersection between it and grating period line moves to shorter wavelengths. The calibration curves between the 17th-mode wavelength shifts and external RI are shown in Figure 4-5 (i). The calibration curves between the 18th-mode wavelength shifts and external RI are shown in Figure 4-5 (j). The LPG with original parameters has the highest sensitivity to the change of external RI in terms of attenuation bands' wavelength shift. It is because the deviations of optical parameters make LPG's working condition moving away from PMC. With the core RI increases from 1.45227 to 1.4523, the sensitivity to external RI decreases from 717.14nm/RIU to 440.75nm/RIU.

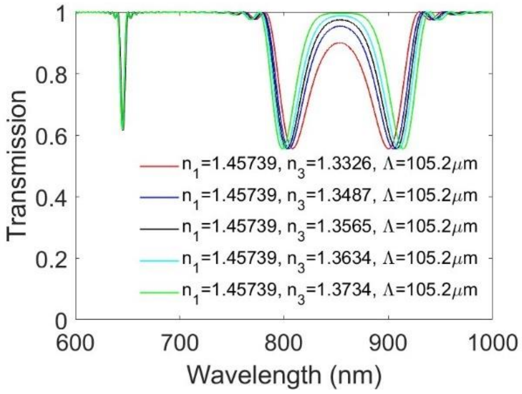

a

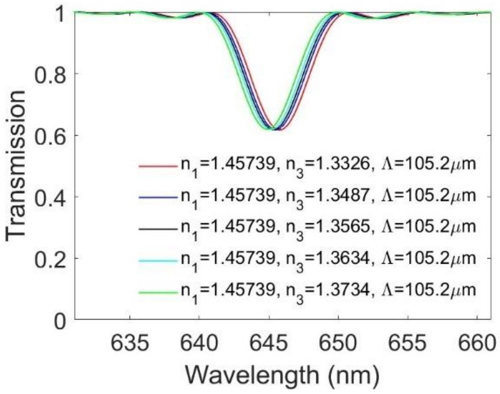

b

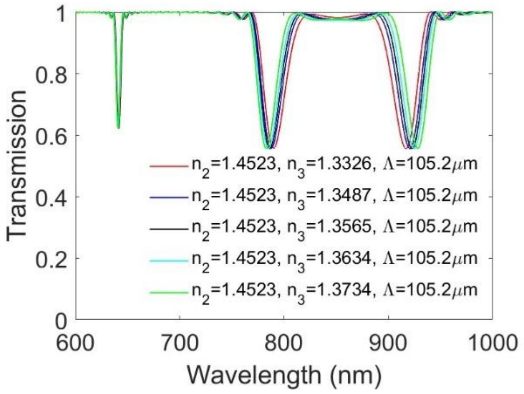
Transmission
Wavelength (nm)
n_2=1.4523, n_3=1.3326, Λ=105.2μm
n_2=1.4523, n_3=1.3487, Λ=105.2μm
n_2=1.4523, n_3=1.3565, Λ=105.2μm
n_2=1.4523, n_3=1.3634, Λ=105.2μm
n_2=1.4523, n_3=1.3734, Λ=105.2μm
0
0.2
0.4
0.6
0.8
1
600
700
800
900
1000

c

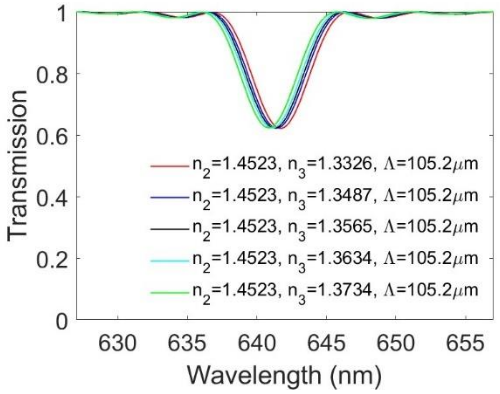
Transmission
Wavelength (nm)
n_2=1.4523, n_3=1.3326, Λ=105.2μm
n_2=1.4523, n_3=1.3487, Λ=105.2μm
n_2=1.4523, n_3=1.3565, Λ=105.2μm
n_2=1.4523, n_3=1.3634, Λ=105.2μm
n_2=1.4523, n_3=1.3734, Λ=105.2μm
0
0.2
0.4
0.6
0.8
1
630
635
640
645
650
655

d

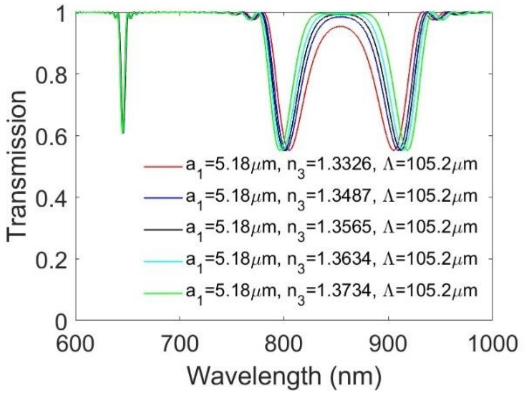
Transmission
Wavelength (nm)
a_1=5.18μm, n_3=1.3326, Λ=105.2μm
a_1=5.18μm, n_3=1.3487, Λ=105.2μm
a_1=5.18μm, n_3=1.3565, Λ=105.2μm
a_1=5.18μm, n_3=1.3634, Λ=105.2μm
a_1=5.18μm, n_3=1.3734, Λ=105.2μm
0
0.2
0.4
0.6
0.8
1
600
700
800
900
1000

e

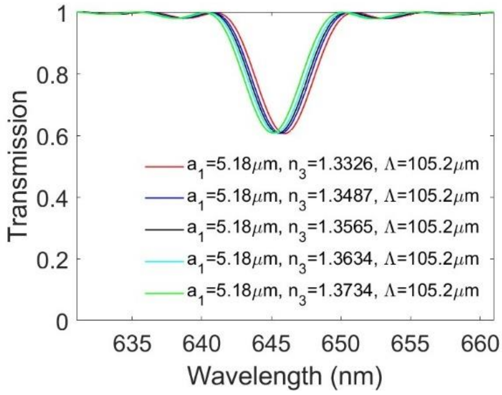
Transmission
Wavelength (nm)
a_1=5.18μm, n_3=1.3326, Λ=105.2μm
a_1=5.18μm, n_3=1.3487, Λ=105.2μm
a_1=5.18μm, n_3=1.3565, Λ=105.2μm
a_1=5.18μm, n_3=1.3634, Λ=105.2μm
a_1=5.18μm, n_3=1.3734, Λ=105.2μm
0
0.2
0.4
0.6
0.8
1
635
640
645
650
655
660

f

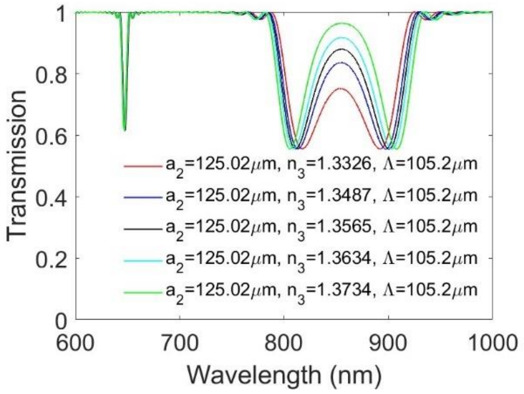
Transmission
Wavelength (nm)
a_2=125.02μm, n_3=1.3326, Λ=105.2μm
a_2=125.02μm, n_3=1.3487, Λ=105.2μm
a_2=125.02μm, n_3=1.3565, Λ=105.2μm
a_2=125.02μm, n_3=1.3634, Λ=105.2μm
a_2=125.02μm, n_3=1.3734, Λ=105.2μm
0
0.2
0.4
0.6
0.8
1
600
700
800
900
1000

g

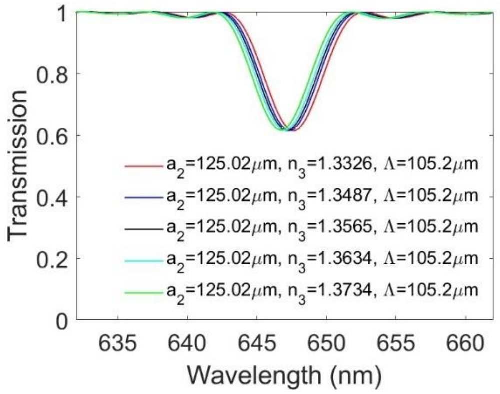
Transmission
Wavelength (nm)
a_2=125.02μm, n_3=1.3326, Λ=105.2μm
a_2=125.02μm, n_3=1.3487, Λ=105.2μm
a_2=125.02μm, n_3=1.3565, Λ=105.2μm
a_2=125.02μm, n_3=1.3634, Λ=105.2μm
a_2=125.02μm, n_3=1.3734, Λ=105.2μm
0
0.2
0.4
0.6
0.8
1
635
640
645
650
655
660

h

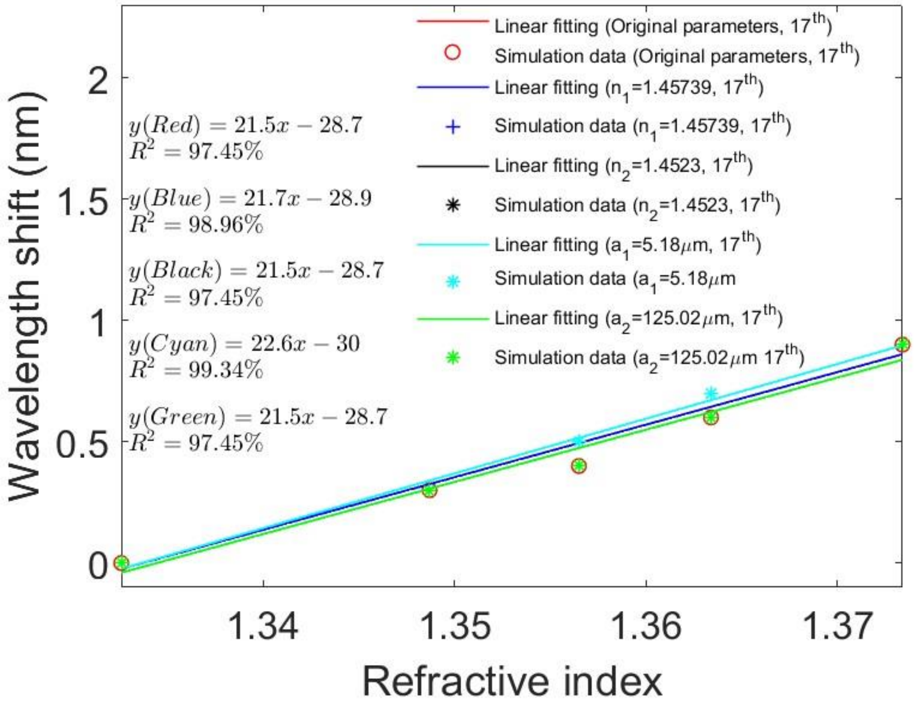
Wavelength shift (nm)
Refractive index
0
0.5
1
1.5
2
1.34
1.35
1.36
1.37
$y(Red) = 21.5x - 28.7$
$R^2 = 97.45\%$
$y(Blue) = 21.7x - 28.9$
$R^2 = 98.96\%$
$y(Black) = 21.5x - 28.7$
$R^2 = 97.45\%$
$y(Cyan) = 22.6x - 30$
$R^2 = 99.34\%$
$y(Green) = 21.5x - 28.7$
$R^2 = 97.45\%$
Linear fitting (Original parameters, 17^{th})
Simulation data (Original parameters, 17^{th})
Linear fitting (n_1=1.45739, 17^{th})
Simulation data (n_1=1.45739, 17^{th})
Linear fitting (n_2=1.4523, 17^{th})
Simulation data (n_2=1.4523, 17^{th})
Linear fitting (a_1=5.18μm, 17^{th})
Simulation data (a_1=5.18μm
Linear fitting (a_2=125.02μm, 17^{th})
Simulation data (a_2=125.02μm 17^{th})

i

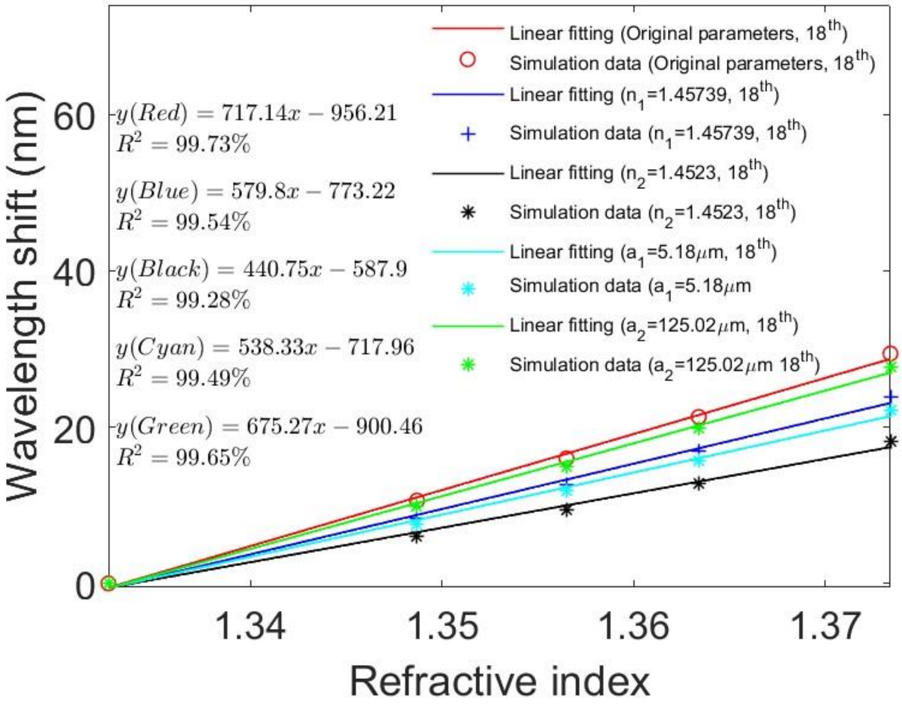

j

Figure 4- 5. The transmission spectra of LPGs with deviated parameters under different external RI. (a) The transmission spectra of the LPG with 105.2µm grating period and 1.45739 core RI under external RIs ranging from 1.3326 to 1.3734; (b) The 17th-mode band of the LPG with 105.2µm grating period and 1.45739 core RI under external RIs ranging from 1.3326 to 1.3734; (c) The transmission spectra of the LPG with 105.2µm grating period and 1.4523 cladding RI under external RIs ranging from 1.3326 to 1.3734; (d) The 17th-mode band of the LPG with 105.2µm grating period and 1.4523 cladding RI under external RIs ranging from 1.3326 to 1.3734; (e) The transmission spectra of the LPG with 105.2µm grating period and 5.18µm core diameter under external RIs ranging from 1.3326 to 1.3734; (f) The 17th-mode band of the LPG with 105.2µm grating period and 5.18µm core diameter under external RIs ranging from 1.3326 to 1.3734; (g) The transmission spectra of the LPG with 105.2µm grating period and 125.02µm cladding diameter under external RIs ranging from 1.3326 to 1.3734; (h) The 17th-mode band of the LPG with 105.2µm grating period and 105.2µm core diameter under external RIs ranging from 1.3326 to 1.3734; (i) The calibration curve of the 17th-mode bands' wavelength shift and external RI; (j) The calibration curve of the 18th-mode bands' wavelength shift and external RI

4.3 Characterizations of LPG

An LPG's property that the wavelength of attenuation band changes with external RI makes it feasible to develop LPG-based biomolecular sensors. The analysis of an LPG's response to external RI can be conducted by simulation (Section 4.2), but laboratory environments are more complicated. For example, LPGs suffer from cross-sensitivity to temperature fluctuations. Furthermore, as functional films are deposited on the surface of LPGs, they might affect the responses to external RI by affecting the effective

RI of the cladding. Therefore, an LPG's responses to external RIs and temperatures in laboratory environments are investigated experimentally in this section.

4.3.1 LPG Coatings

The methodologies to functionalize an LPG have been introduced in Section 3.2. An LPG with 105μm grating period and 3cm length is used. The transmission spectra are the ratio between measured spectra and estimated emission spectra. A detailed explanation on the data processing is available in Appendix D. The transmission spectra of the LPG during the coating of PAH/SiNPs and AuNPs are shown in Figure 4-6(a). Two layers of PAH/SiNPs are deposited on the LPG which increases the RI on the surface of the LPG. The separation between the two attenuation bands increases by 3nm and 2.9nm when the first layer and second layer of PAH/SiNPs are deposited respectively. Then, the separation increases by 2.8nm when LPG is coated with APTES. Finally, AuNPs with sub-5nm size are deposited and the separation increases by 5.5nm. The coatings can be removed by rinsing the LPG in Piranha solution for 24 hours. The same LPG is then coated with Bovine Serum Protein (BSA, Merck UK) using Glutaraldehyde cross-linker (Figure 4-6(b)). The separation between the two bands increases by 1.2nm when APTES is deposited. Then, Glutaraldehyde is deposited, and the separation increases by 1nm. Finally, BSA is deposited, and separation increases by 2nm. Depositing a film on the surface of LPG changes its structure. When measuring external RI, a bare LPG has a 3-layer structure: core-cladding-medium, while a coated LPG has a 4-layer structure: core-cladding-film-medium. It has some similarity to increasing the thickness of cladding. However, it's not the same since film and cladding have different RI. It's hard to analyse the 4-layer structure numerically since the model is too complex. Therefore, their responses to the change of external RI are investigated experimentally.

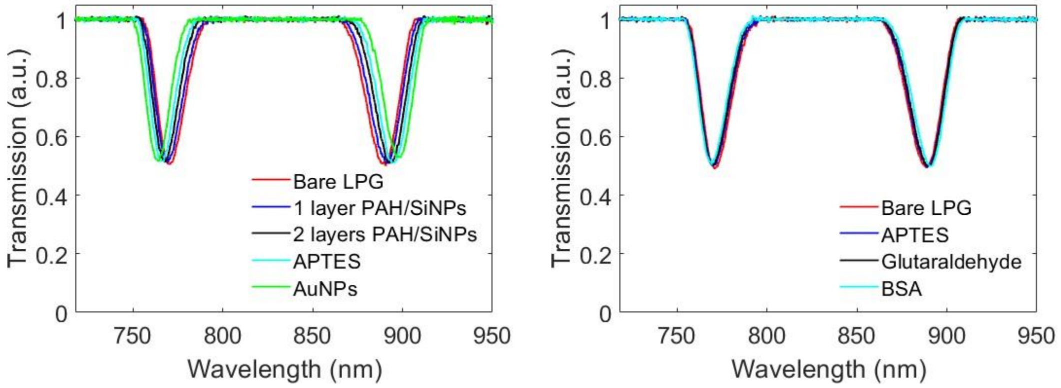

a b

Figure 4- 6. The transmission spectra of an LPG with different surface coatings. (a) Coating of AuNPs with LbL assembly; (b) Coating of Glutaraldehyde.

4.3.2 Measurement of External Refractive Indices with LPG

The responses to external RIs of an LPG with different coatings (bare, 2 layers of PAH/SiNPs (PAH/SiNPs)$_2$, (PAH/SiNPs)$_2$/AuNPs, Glutaraldehyde/BSA) are investigated. The experimental set-up is explained in Section 3.2.1 (Figure 3-1(a)). The LPG is placed in the bath holder and five solutions with different RIs ranging from 1.3326 to 1.3734 are pipetted into the bath holder. The LPG is immersed in each solution for at least 5 minutes and the old solution is then suctioned off (Flaem suction pump). The same measurements are conducted for two rounds. In each round, the external RI increases from 1.3326 to 1.3734, and then decreases from 1.3734 to 1.3326. The solutions with different RIs are prepared by dissolving different amount of Sodium Chloride (NaCl) into DI water. The relationship between RI and the concentration of NaCl are listed in Table 4-3. The RIs are determined with a commercial refractometer (Reichert 13940000, Depew, NY, USA).

	Volume of Water	Mass of NaCl	Concentration
1.3326	20mL	0	0
1.3487	20mL	1929mg	8.8 wt%
1.3565	20mL	3033mg	13.7 wt%
1.3634	20mL	4057mg	16.9wt%
1.3734	20mL	5781mg	22.4wt%

Table 4- 3. The relationship between the concentration of NaCl and solution's RI.

Figure 4-7(a) shows the transmission spectra of bare LPG in different external RIs. Figure 4-7 (c, e, & g) shows the transmission spectra of the LPG with (PAH/SiNPs)$_2$, (PAH/SiNPs)$_2$/AuNPs, and Glutaraldehyde/BSA on the surface. No matter what surface coating is applied, the change of the transmission spectrum has the same trend as the bare LPG. Two attenuation bands move oppositely and the separation between them increases which matches the trends of the simulation results in Section 4.2. The real-time changes of the separations of bare LPG, LPG with (PAH/SiNPs)$_2$, LPG with (PAH/SiNPs)$_2$/AuNPs, and Glutaraldehyde/BSA are shown in Figure 4-7 (b, d, f, & h) respectively. Before pipetting the solution with a new RI into the fibre bath, old solution needs to be pumped out. There is a short period (~30s) that the LPG is exposed to air, therefore, the spikes appear in the signal. All the signals are stable within 5 minutes after a new solution is added. The calibrations of the LPG's responses versus the external RI are shown in Figure 4-7(i). The bare LPG has response to external RI with sensitivity of approximately 332.8nm/RIU. (PAH/SiNPs)$_2$/AuNPs coating improves the sensitivity to approximately 464.9nm/RIU (~40% higher than the bare LPG). The deposition of AuNPs to improve the sensitivity of an LPG's response to external RI has been reported before [211], [212]. The deposition of AuNPs on the surface can affect the cladding modes' profile such that their effective RIs have higher changing rates with external RI . The Glutaraldehyde/BSA coating has little effect on the sensitivity. The (PAH/SiNPs)$_2$ coating improves the sensitivity to approximately 370.7nm/RIU (~11% higher than the bare LPG). The deposition of PAH/SiNPs to improve the sensitivity of an LPG's response to external RI has been reported before [213]. It is because the nanofilms on the surface can change an LPG's cladding modes.

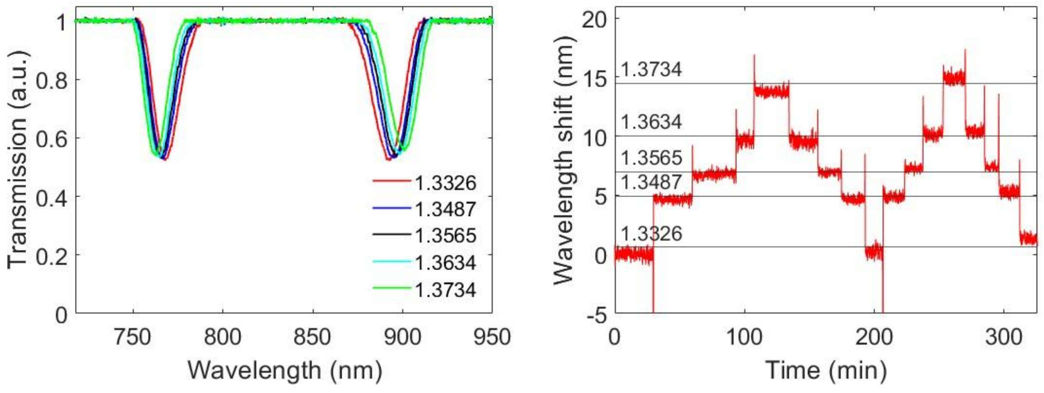

a

b

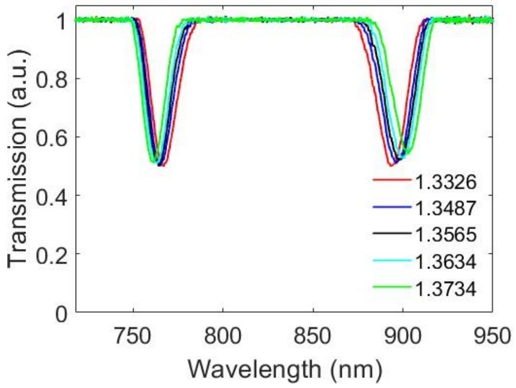
Transmission (a.u.)
0
0.2
0.4
0.6
0.8
1
750
800
850
900
950
Wavelength (nm)
1.3326
1.3487
1.3565
1.3634
1.3734

c

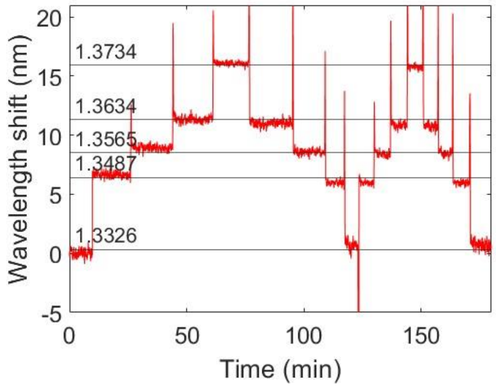
Wavelength shift (nm)
-5
0
5
10
15
20
0
50
100
150
Time (min)
1.3734
1.3634
1.3565
1.3487
1.3326

d

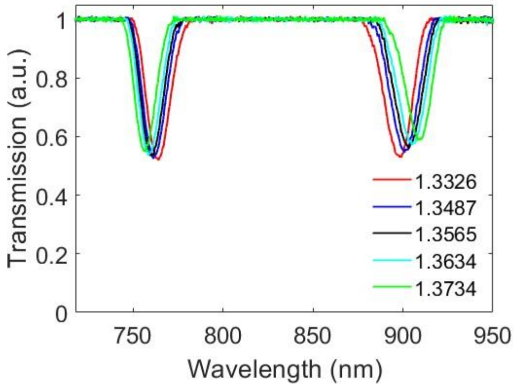
Transmission (a.u.)
0
0.2
0.4
0.6
0.8
1
750
800
850
900
950
Wavelength (nm)
1.3326
1.3487
1.3565
1.3634
1.3734

d

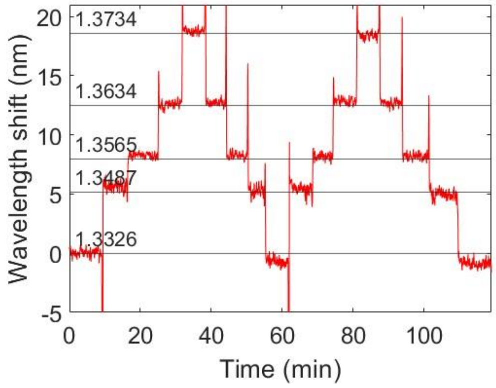
Wavelength shift (nm)
-5
0
5
10
15
20
0
20
40
60
80
100
Time (min)
1.3734
1.3634
1.3565
1.3487
1.3326

e

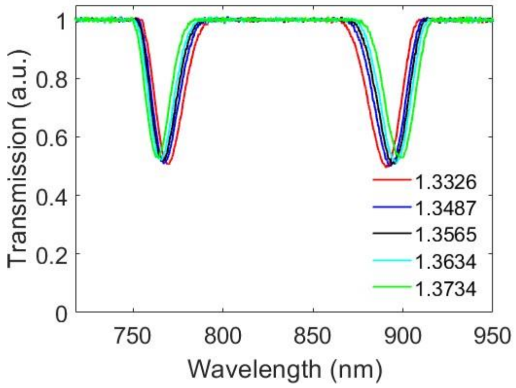
Transmission (a.u.)
0
0.2
0.4
0.6
0.8
1
750
800
850
900
950
Wavelength (nm)
1.3326
1.3487
1.3565
1.3634
1.3734

f

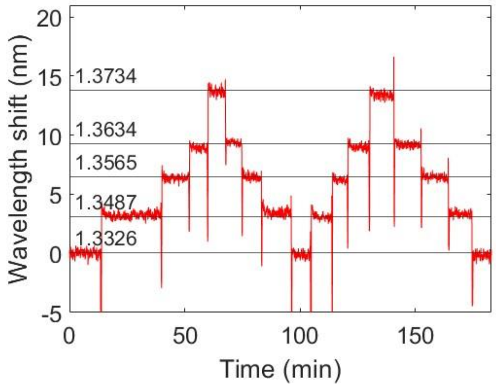
Wavelength shift (nm)
-5
0
5
10
15
20
0
50
100
150
Time (min)
1.3734
1.3634
1.3565
1.3487
1.3326

g

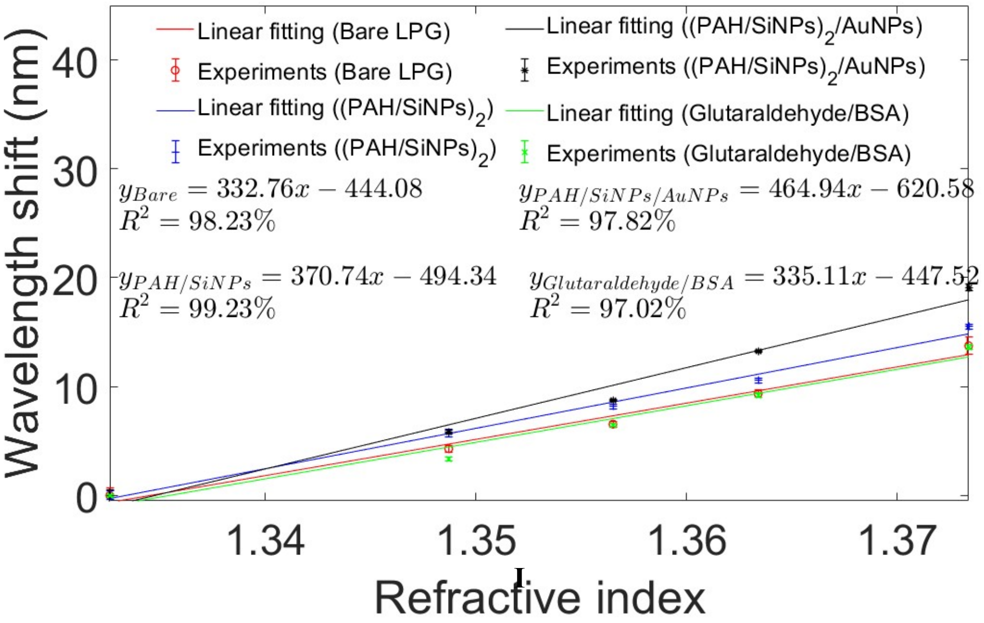

Figure 4- 7. The measurements of external RIs with an LPG with different surface coating. (a) Transmission spectra of a bare LPG in different external RIs; (b) Real-time changes of the separation between two attenuation bands of a bare LPG; (c) Transmission spectra of an LPG with (PAH/SiNPs)2/AuNPs coating in different external RIs; (f) Real-time changes of the separation between two attenuation bands of the LPG with (PAH/SiNPs)2/AuNPs coating; (g) Transmission spectra of an LPG with Glutaraldehyde/BSA coating in different external RIs; (h) Real-time changes of the separation between two attenuation bands of the LPG with (PAH/SiNPs)2/AuNPs coating; (I) Calibration of the four measurements of external RIs

4.3.3 Measurement of Temperature with an LPG

The measurement of temperature with an LPG is conducted with the set-up shown in Figure (3-7(b)). The temperature increases from 25°C to 30°C with 1°C increments. The transmission spectra at different temperatures demonstrate that the separation between the two bands increases with temperature (Figure 4-8(a)). The band located between 750nm and 790nm shift to shorter wavelengths (Figure 4-8(b)). The band located between 870nm and 910nm shift to longer wavelengths (Figure 4-8(c)). The real-time increments of the separation between the two bands are shown in Figure 4-8(d) with the band separation following temperature changes. The calibration of the wavelength shift and temperature is shown in Figure 4-8(d). From 25°C to 30°C, the separation between two bands increases linearly (R^2=98.32%) with a sensitivity of approximately 1.1nm/°C. The laboratory temperature is maintained around 22°C. The signal shift caused by laboratory temperature fluctuation is smaller than 0.03nm (Appendix E).

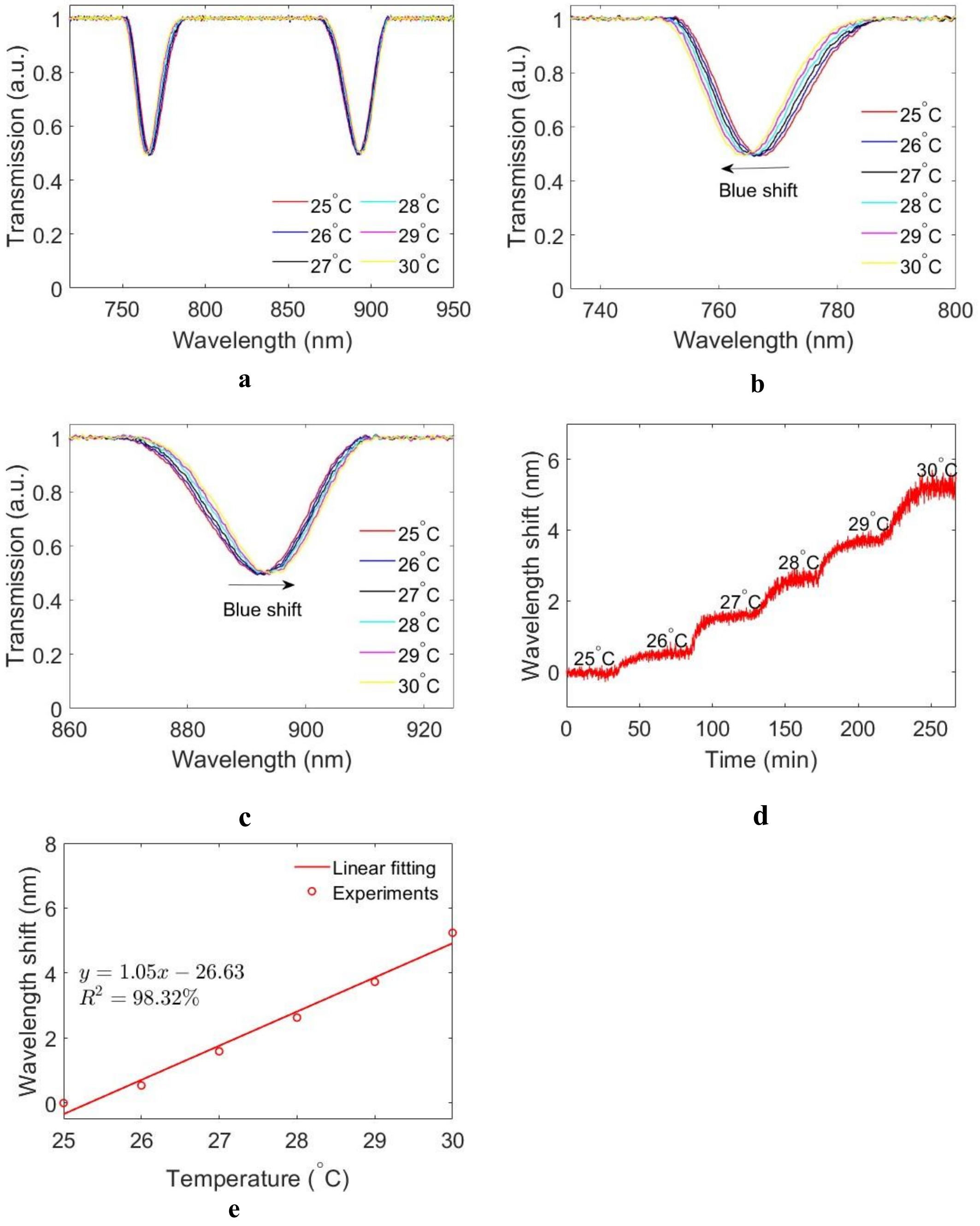

a b c d e

Figure 4- 8. The measurement of temperature with an LPG. (a) Transmission spectra of the LPG in different temperatures; (b) Blue shift of the band between 750nm and 790nm; (c) Red shift of the band between 870nm and 910nm; (d) Real-time change of the separation between two bands; (e) Calibration of the change of the separation versus temperature.

4.4 Summary

The working condition of an LPG is dependent on the grating period and the parameters of the optical fibre such as the diameter and RIs of core and cladding. The length and modulation depth of the grating affects the depth of the attenuation bands. An LPG can work at the PMC by manipulating the grating period, in which case the two attenuation bands of the same resonance mode merges into each other such that there is a big ‘U’ shape band in the transmission spectrum. As the external RI increases, the big ‘U’ shape band gradually splits into two narrower bands and the separation between them increases. LPGs’ bands operating at or near the PMC have higher sensitivity (>20 times) to external RI in terms of the wavelength shifts than bands operating away from the PMC. The surface coatings on an LPG can change the sensitivity of attenuation bands to the change of external RI. For an LPG with 105µm grating period and 3cm length, it has sensitivity to external RI of approximately 332.8nm/RI. The deposition of two layers of PAH/SiNPs increases it by about 10%, and the deposition of $(PAH/SiNPs)_2$/AuNPs increases it by about 40%. This is because the surface coatings can change the cladding modes’ profiles thus the effective RIs changes quicker with external RI. The deposition of Glutaraldehyde/BSA on the LPG hardly changes the sensitivity to external RI. The LPG also responds to the change of temperature. The dual bands shift with the temperature with the rate of approximately 1.1nm/°C in the range between 25°C and 30°C.

Chapter 5. Immunoglobulin A, G, and M Sensors

5.1 Introduction

Results presented in this chapter were published by the author in [214]. Immunoglobulin (Ig) A, G, and M play important roles in the diagnosis and monitoring of diseases such as the infection of Hepatitis E virus and COVID-19 [215], [216], [217]. IgA, IgG, and IgM sensors are developed based on Long Period Gratings (LPG). Three LPGs with 105μm period are fabricated in PS750 photosensitive fibre. They are functionalized with LbL-aided crosslinking with 11-MUA/EDC/NHS. Poly (allylamine hydrochloride, PAH), silica nanoparticles (SiNPs), and gold nanoparticles (AuNPs) are deposited on the surface of the LPGs. The bio-receptors anti-IgA, anti-IgG, and anti-IgM are immobilized on the LPGs to fabricate IgA sensor, IgG sensor, and IgM sensor respectively. They are tested with 10μg/ml-200μg/ml IgA, 1μg/ml-90μg/ml IgG, and 10μg/ml-320μg/ml IgM. The Limit of Detections (LoD) are 8.59μg/ml, 7.38μg/ml, and 7.02μg/ml respectively. The linear ranges of them are 0-30μg/ml, 0-90μg/ml, and 0-80μg/ml respectively. Relative Standard Deviation (RSD) is a key parameter to evaluate the reproducibility of a sensor [218]. The RSDs of IgA sensor, IgG sensor, and IgM sensor are 17.9%, 30.3%, and 62.4% respectively. The selectivity of IgA sensor, IgG sensor, and IgM sensor are evaluated by the ratio of response to target analyte to the response to interfering analyte. They are 30.67, 18.45, and 15.25 respectively.

5.2 Materials and Methodology

IgA, IgG, and IgM sensors are designed separately based on three LPGs. The LPGs are fabricated in PS750 photosensitive fibre (Fibrecore, UK) with 105μm amplitude mask. They are functionalized using the LbL method as described in Section 3.2.2. Briefly, two PAH/SiNPs dual layers and AuNPs are deposited on the surface of the LPGs. 11-MUA/EDC/NHS cross-linkers are then generated on the LPGs as they are ready for the immobilization of bio-receptors. Anti-human IgA antibody produced in goat (α-chain specific, anti-IgA), Anti-human IgG antibody produced in goat (Fc specific, anti-IgG), Anti-human IgM antibody (μ-chain specific, anti-IgM), IgA from human serum, IgG from human serum, and IgM from human serum are purchased from Merck, UK. After building PAH/SiNPs/AuNPs layers on the surface, the LPGs are then immersed on 1mg/ml anti-IgA, anti-IgG, and anti-IgM solutions (in PBS buffer) for one hour to fabricate IgA sensor, IgG sensor, and IgM sensor respectively.

The sensors are place in a homemade Teflon fibre bath (49mm(L)×3mm(W)×2mm(D), Figure 3-7(a)) when characterizing. The sensors are immersed in the solutions containing corresponding antibodies. After a period of approximately 20 minutes, old solution is pumped out using a suction pump (Flaem, Italy) and new solution with a higher antibody concentration is added to the Teflon fibre bath. IgA and IgG are dissolved in PBS buffer. IgA concentration ranges from 10μg/ml to 200μg/ml. IgG concentration ranges from 1μg/ml to 90μg/ml. IgM is dissolved in Tris buffer. The concentration ranges from 10μg/ml to 320μg/ml. The selectivity tests of the three sensors are conducted with the other two antibodies. First, the sensors are immersed in solution containing 80μg/ml interfering antibody 1 for approximately 20 minutes. Then, the old solution is pumped out. Secondly, solutions containing 80μg/ml interfering antibody 2 are added. The sensors are immersed for approximately 20 minutes and old solution are pumped out. Finally, sensors are immersed in solutions containing 80μg/ml target antibodies for approximately 20 minutes. The three sensors are tested separately with this protocol.

5.3 IgA Sensor

The transmission spectra during the functionalization process are shown in Figure 5-1(a). The two attenuation bands move oppositely and the separation between them increases as the RI on the surface increases when the materials are immobilized. The separation between the two attenuation bands keeps increasing with IgA concentration (Figure 5-1(b)). The real-time changing of the separation is shown in Figure 5-1(c). The signal gets stabilized within 20 minutes after the solution is pipetted in. The calibration curve is shown in Figure 5-1(d). The coefficient of determination (R^2) of 99.84% is achieved with an exponential fitting. The error bar is the standard deviation of the data acquired by multiple independent measurements. The linear range of the sensor's response is between 0 and 30μg/ml with an R^2 of 96.72% (Figure 5-1(g)) The Limit of Detection (LoD) is 8.59μg/ml calculated with Equation 5-1.

$$LoD = \frac{3.3S_y}{S} \quad 5\text{-}1$$

Where S_y is the standard deviation of the signal in buffer solution (baseline); S is the slope of linear fitting curve.

The selectivity is calculated with Equation 5-2.

$$Selectivity = \frac{R_t}{R_I} \quad 5\text{-}2$$

Where R_t is the response to target analyte; R_I is the highest response to interfering substance. As shown in Figure 5-1(f), the selectivity of an IgA sensor is tested against IgM and IgG. The sensor's response to IgM is 0.06nm, which is higher than the response to IgG. Its response to IgA is 1.84nm. The selectivity of the IgA sensor is 30.67. The Relative Standard Deviation (RSD) of a sensor's response is calculated with Equation 5-3 [218]:

$$RSD = \max\left(\frac{S}{W}\right) \quad 5\text{-}3$$

Where W is the non-zero signal during measurement; S is the standard deviation corresponding to each W (Figure 5-1(f)). The RSD of a sensor's response is the maximum standard deviation to signal ratio during measurement. For example, when IgA concentration is 30μg/ml, S is 0.3nm and W is 1.66nm. $\frac{S}{W}$ reaches maximum. The RSD of IgA sensor's response is 17.9%.

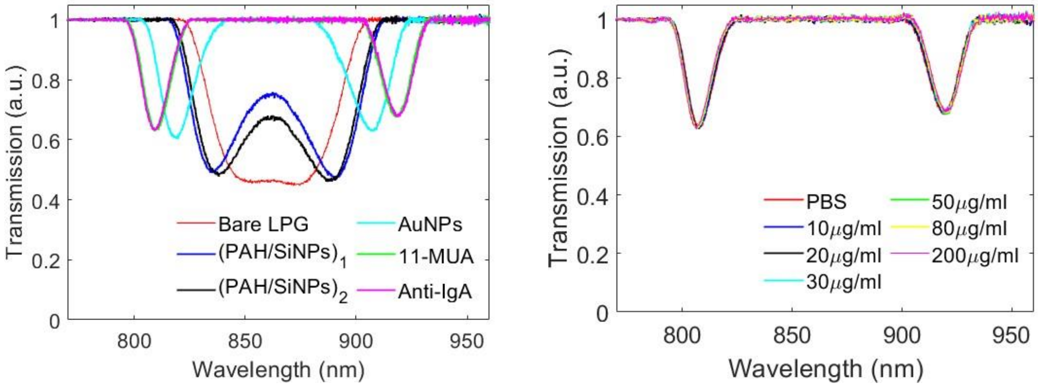

a b

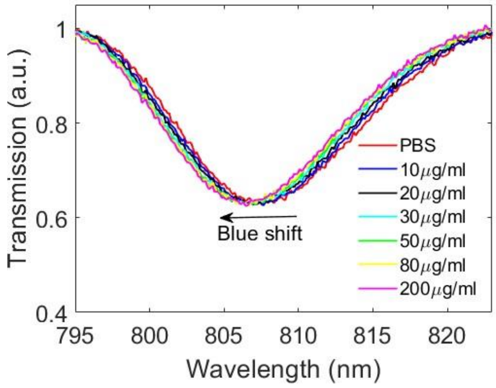
Transmission (a.u.)
Wavelength (nm)
Blue shift
PBS
10μg/ml
20μg/ml
30μg/ml
50μg/ml
80μg/ml
200μg/ml
1
0.8
0.6
0.4
795
800
805
810
815
820

c

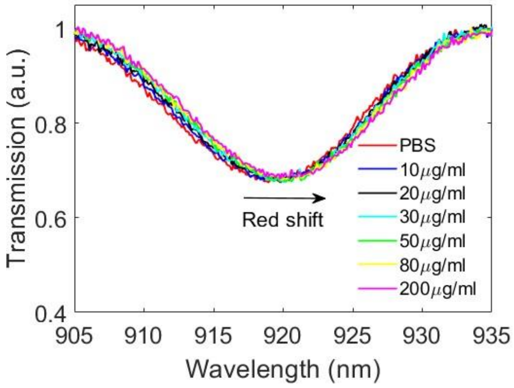
Transmission (a.u.)
Wavelength (nm)
Red shift
PBS
10μg/ml
20μg/ml
30μg/ml
50μg/ml
80μg/ml
200μg/ml
1
0.8
0.6
0.4
905
910
915
920
925
930
935

d

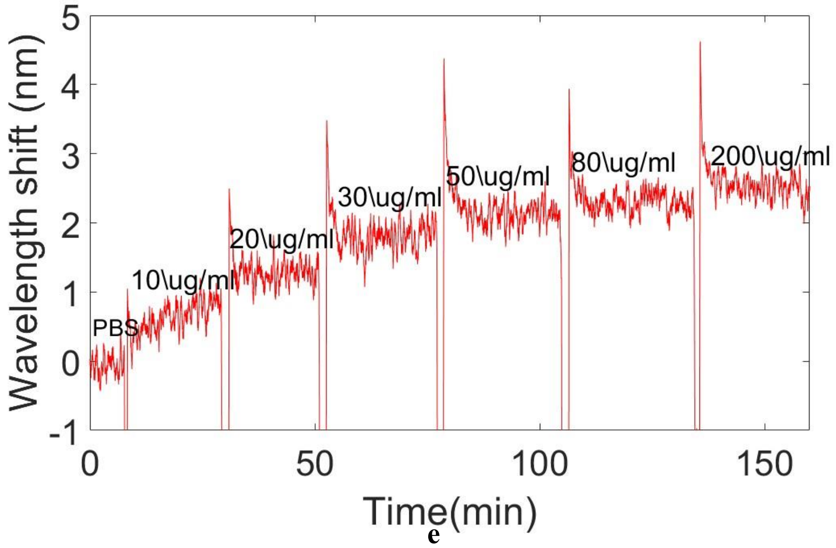
Wavelength shift (nm)
Time(min)
PBS
10\ug/ml
20\ug/ml
30\ug/ml
50\ug/ml
80\ug/ml
200\ug/ml
5
4
3
2
1
0
-1
0
50
100
150

e

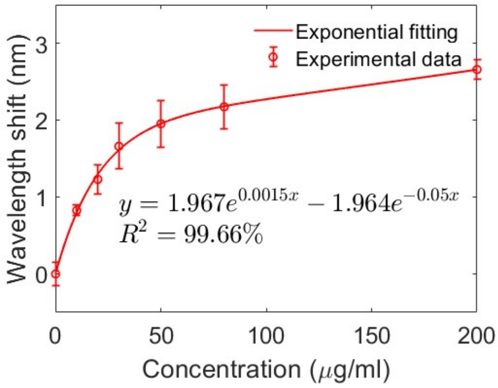
Exponential fitting
Experimental data
$y = 1.967e^{0.0015x} - 1.964e^{-0.05x}$
$R^2 = 99.66\%$
Wavelength shift (nm)
Concentration (μg/ml)
3
2
1
0
0
50
100
150
200

f

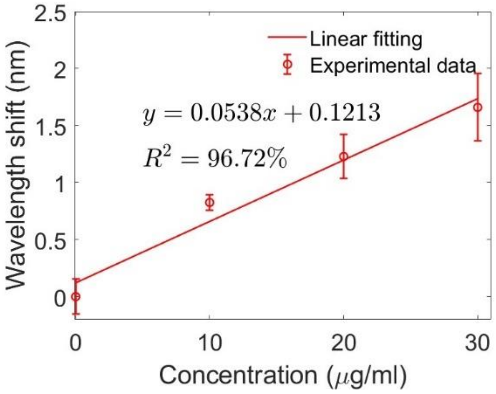
Linear fitting
Experimental data
$y = 0.0538x + 0.1213$
$R^2 = 96.72\%$
Wavelength shift (nm)
Concentration (μg/ml)
2.5
2
1.5
1
0.5
0
0
10
20
30

g

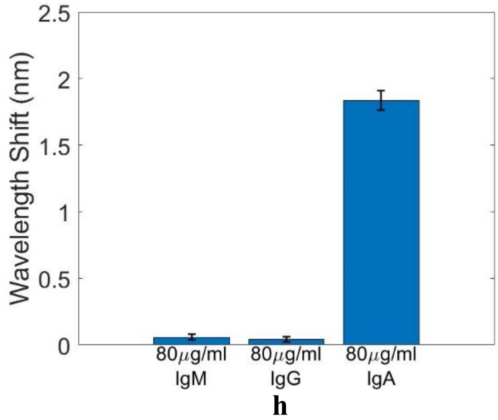

Figure 5- 1. The fabrication and characterization of an IgA sensor. (a) The transmission spectra during the fabrication of the IgA sensor; (b) The transmission spectra during the measurement of IgA; (c) The blue shift of the attenuation band near 805nm during the measurement of IgA; (d) The red shift of the attenuation band near 920nm during the measurement of IgA; (e) The real-time wavelength shift of the attenuation band during the measurement of IgA; (f) The calibration curve of the IgA sensor's response from 0 to 200µg/ml; (g) The linear fitting curve of the IgA sensor's response from 0 to 30µg/ml; (h) The attenuation bands' wavelength shift during the selectivity test on the IgA sensor.

5.4 IgG Sensor

The U-shape band splits into two narrower bands after the deposition of one layer of PAH/SiNPs, and they keep moving oppositely during the surface functionalization (Figure 5-2(a)). The transmission spectra of the sensor in the solution with different IgG concentrations are shown in Figure (5-2(b). The band near 780nm shifts to shorter wavelengths when IgG concentration increases (Figure (5-2(c)), and the band near 875nm shifts to longer wavelengths (Figure (5-2(d)). The real-time wavelength shift is shown in Figure (5-2(e)). The signal changes linearly with IgG concentration (R^2=97.19%) (Figure 5-3(f)). The error bar is the standard deviation of the data acquired from two independent measurements. The LoD of the IgG sensor is 7.38µg/ml, calculated with Equation (5-1). The selectivity is 18.45, calculated with Equation (5-2). The RSD is 30.31%, calculated with Equation (5-3).

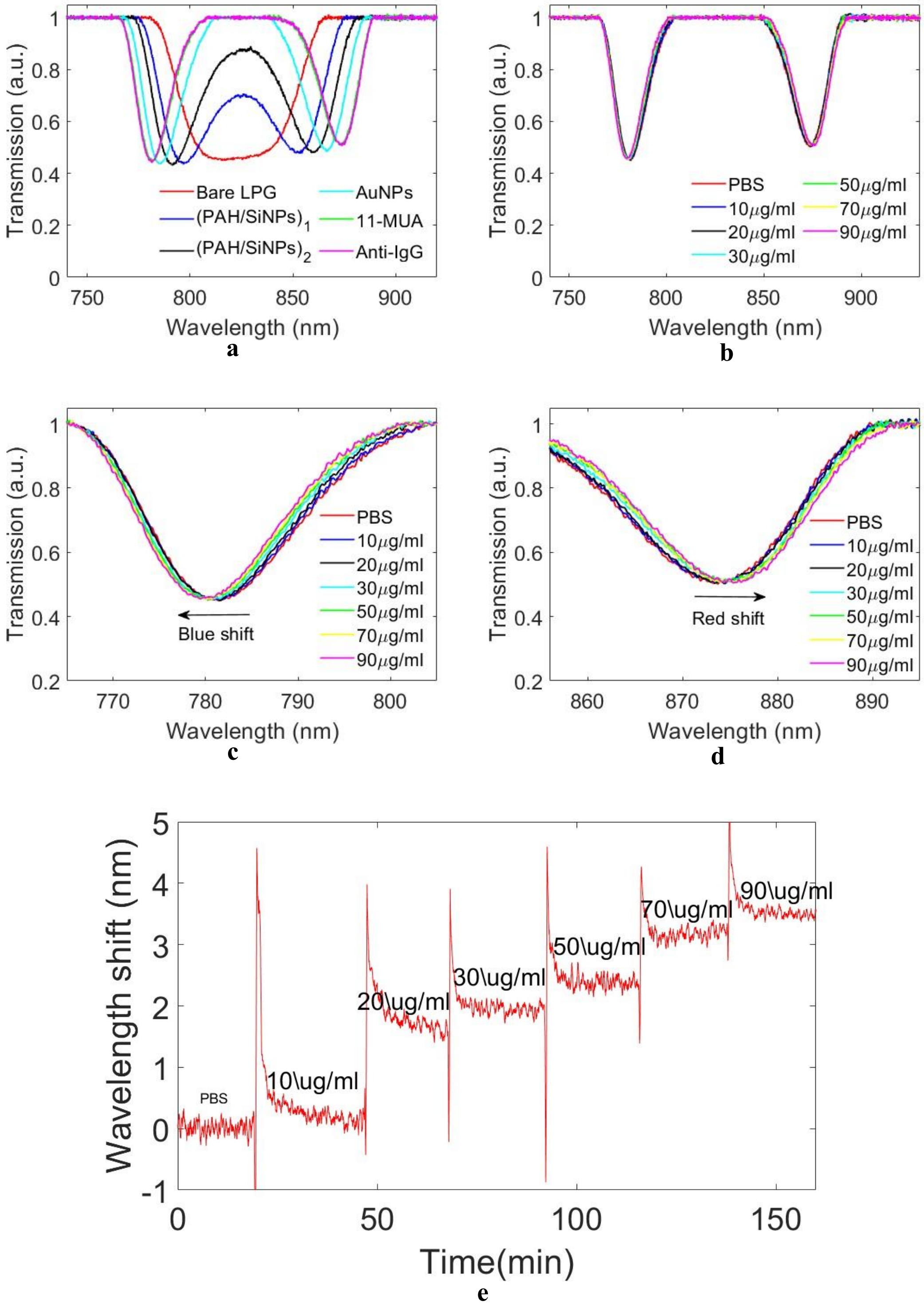
Transmission (a.u.)
Wavelength (nm)
Bare LPG
(PAH/SiNPs)$_1$
(PAH/SiNPs)$_2$
AuNPs
11-MUA
Anti-IgG
PBS
10μg/ml
20μg/ml
30μg/ml
50μg/ml
70μg/ml
90μg/ml
Blue shift
Red shift
Wavelength shift (nm)
Time(min)
PBS
10\ug/ml
20\ug/ml
30\ug/ml
50\ug/ml
70\ug/ml
90\ug/ml

a

b

c

d

e

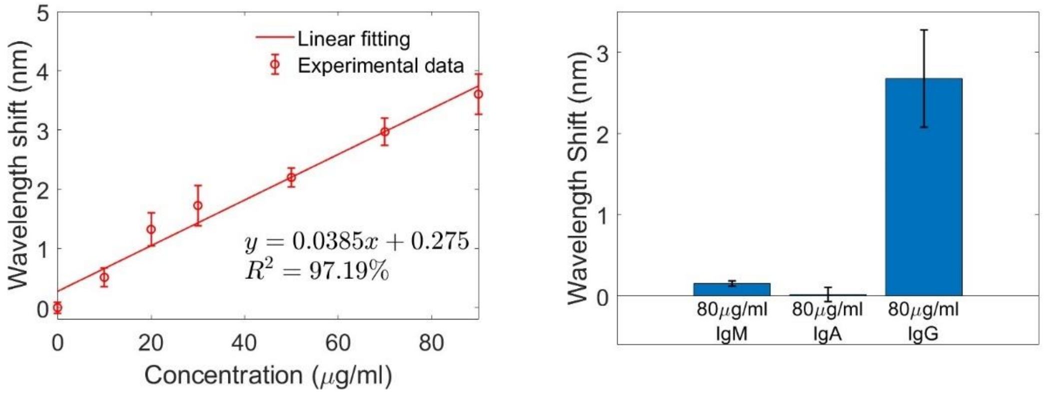

f g

Figure 5- 2. The fabrication and characterization of an IgG sensor. (a) The transmission spectra during the fabrication of the IgG sensor; (b) The transmission spectra during the measurement of IgG; (c) The blue shift of the attenuation band near 820nm during the measurement of IgG; (d) The red shift of the attenuation band near 910nm during the measurement of IgA; (e) The real-time wavelength shift of the attenuation band during the measurement of IgG; (f) The calibration curve of the IgG sensor; (g) The attenuation bands' wavelength shift during the selectivity test on the IgG sensor.

5.5 IgM Sensor

The U-shape band near 820nm splits into two narrower bands after the deposition of one layer of PAH/SiNPs. The separation between them keeps increasing during the surface functionalization. The transmission spectra of the sensor in the solution with different IgM concentrations are shown in Figure (5-3(b)). The attenuation band near 780nm keeps moving to shorter wavelengths (Figure 5-3(c)) and the band near 875nm keeps moving to longer wavelengths (Figure 5-3(d)). The real-time wavelength shift is shown in Figure 5-2(e). The exponential fitting curve of sensor's response between 0 and 320µg/ml is shown in Figure 5-3(d). (R^2=99.66%). The error bar is the standard deviation of the data acquired from multiple independent measurements. The linear range of the sensor is between 0 and 80µg/ml (R^2=95.58) (Figure 5-3(g)). The LoD is 7.02µg/ml, which is calculated with Equation 5-1. The selectivity is 15.25, which is tested against IgA and IgM and calculated with Equation 5-2. The RSD is 62.4%, calculated with Equation (5-3).

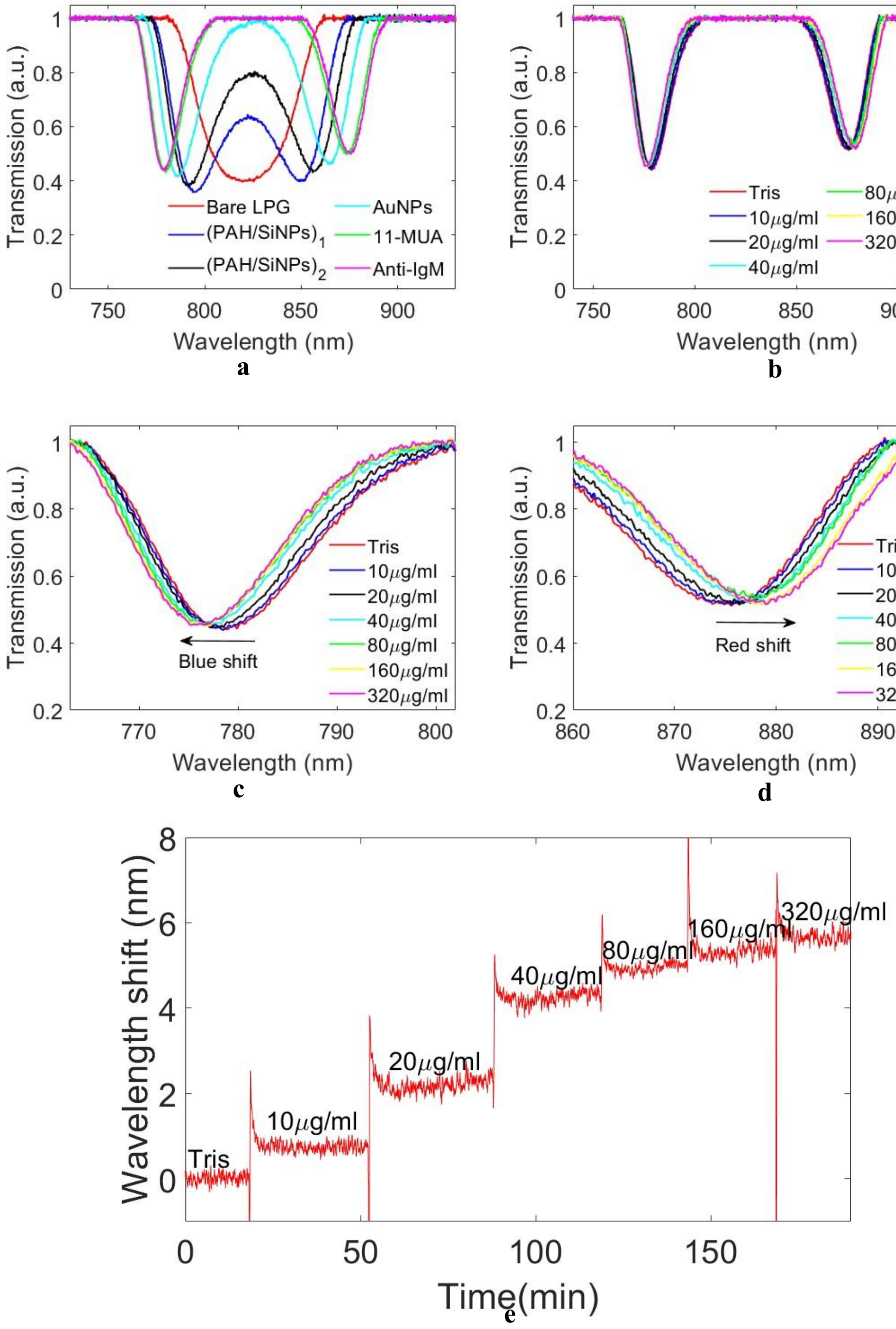
Transmission (a.u.)
Wavelength (nm)
Bare LPG
(PAH/SiNPs)$_1$
(PAH/SiNPs)$_2$
AuNPs
11-MUA
Anti-IgM
Tris
10μg/ml
20μg/ml
40μg/ml
80μg/ml
160μg/ml
320μg/ml
Blue shift
Red shift
Wavelength shift (nm)
Time(min)
0
50
100
150
750
800
850
900
770
780
790
800
860
870
880
890
0
0.2
0.4
0.6
0.8
1
2
4
6
8

a b

c d

e

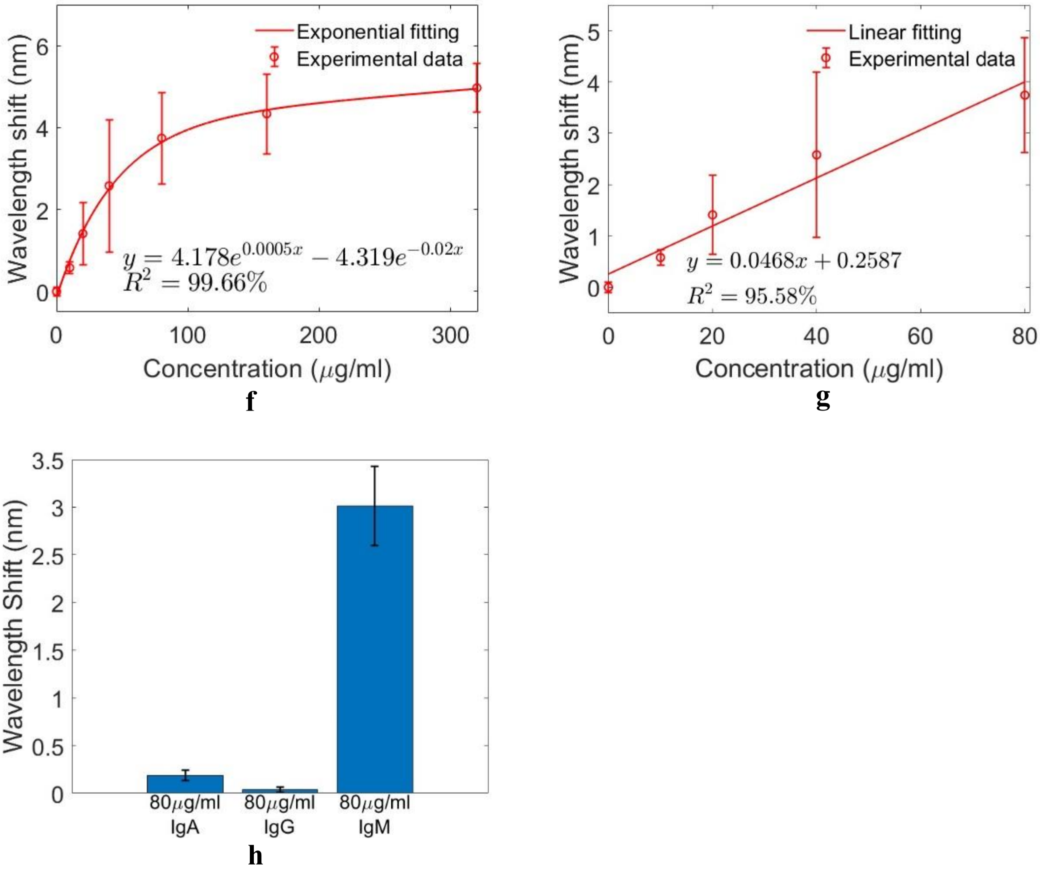

f **g**

h

Figure 5- 3. The fabrication and characterization of an IgM sensor. (a) The transmission spectra during the fabrication of the IgM sensor; (b) The transmission spectra during the measurement of IgM; (c) The blue shift of the attenuation band near 830nm during the measurement of IgM; (d) The red shift of the attenuation band near 890nm during the measurement of IgM; (e) The real-time wavelength shift of the attenuation band during the measurement of IgM; (f) The calibration curve of the IgM sensor; (g) The linear fitting curve of IgM sensor's response between 0 and 80µg/ml; (h) The attenuation bands' wavelength shift during the selectivity test on the IgM sensor.

5.6 Discussion

The IgA, IgG, and IgM sensors are fabricated based on three LPGs. They have 105µm grating period and 3cm grating length. However, the transmission spectra are different from each other. When the bare LPGs are immersed in DI water, the IgG sensor has a U-shape band near 850nm (red curve in Figure 5-1(a)), but IgG sensor and IgM sensors have U-shape band near 830nm (red curves in Figure 5-2(a) and Figure 5-3(a) respectively). It is most likely because of the deviation of the parameters of the optical fibre. Recalling the results of Section 4.1, these deviations affect the working conditions of LPGs. The sensitivity of an LPG's response to external RI gets lower as its working condition shifts away from PMC. Therefore, the reproducibility of the sensors is affected if measures are not taken to compensate for the deviations. By amending the grating period, an LPG can be fabricated to work around PMC. However, there's always deviations in optical-fibre parameters, which are inevitable and unpredictable. Improving optical fibre manufacturing technique is an approach to optimize LPG-based sensors. All the three sensors are fabricated with the LbL assembly method. In the last step during the fabrication, anti-IgA, anti-IgG, and anti-IgM are immobilized on the LPG to fabricate IgA sensor, IgG sensor, and IgM sensor respectively. The concentration of the bio-receptors used for the fabrication is 1mg/ml. A good selectivity can be achieved with this concentration. IgG sensors made with 100µg/ml and 500µg/ml anti-IgG have poor selectivity (Appendix F). All the three sensors successfully measure the target analytes. It shows the feasibility and transferability of the sensor platform and fabrication method. The main characteristics of the sensors developed in this work and other similar sensors are listed in Table 5-1. The LoD of the IgA sensor developed in this work is 8.59µg/ml. The selectivity is 30.67. The linear range is 0 to 30µg/ml. The RSD is 17.9%. The IgA concentration in human serum ranges from 0.8mg/ml to 3mg/ml. It needs to be diluted by 100 folds with PBS buffer to fit the linear range. The LoD the IgA sensor based on cladding-removed fibre is 1.1µg/ml. Light intensity is measured, which can be affected by the fluctuations of light source and detector. The LoD of the IgG sensor developed in this work is 7.38µg/ml, which is much higher than the LoDs of IgG sensors based on other platforms. These IgG sensors measure light intensity, which suffers from fluctuations of light source and detector. The linear range of the IgG sensor is 0 to 90µg/ml. It is sufficient for detecting the IgG in human serum, which ranges from 6mg/ml to 16mg/ml. Human serum needs to be diluted by 200 times with PBS buffer to fit IgG sensor's linear range. The selectivity of the IgG sensor is 18.45. The anti-IgG used to fabricate IgG sensor has some cross-sensitivity to IgM (Appendix C). The selectivity of the cladding-removed IgG sensor is >50, which was tested against rabbit IgG. The RSD of the developed IgG sensor is 30.3%. The IgM sensor developed in this work has an LoD of 7.02µg/ml and selectivity of 15.53. The anti-IgM used to fabricate IgM sensor has cross-sensitivity to human IgA (Appendix G). The linear range is 0 to 80µg/ml. IgM concentration in human serum is from 0.4mg/ml to 2.5mg/ml. It needs to be diluted by 30 folds with Tris buffer to fit IgM sensor's linear range. The RSD of IgM sensor is 62.4%, which is twice of IgG sensor's RSD and three times of IgA sensor's RSD. The higher the RSD, the lower the reproducibility of the sensor is. An RSD of 10% have been considered acceptable for PoC devices [218]. The sensors developed in this work doesn't meet the requirement. The bio-/chemical processes are complex. The quality of chemicals and bio-receptors can vary. Manual operations might not be precise enough. Small variations are introduced to every fabrication step. To investigate and improve the reproducibility of a sensor, more surface chemical analysis techniques is needed such as Raman spectroscopy and X-ray photoelectron spectroscopy [37], [219]. Every step of the surface functionalization can be analysed and optimized to achieve a higher consistency. The sensor's selectivity is highly dependent on the bio-receptors. An approach to improve a sensor's selectivity is to use bio-receptors with high specificity to the target analyte. Collaborations with biologists are needed to choose suitable bio-receptors. After reviewing literatures, a reference value of an acceptable selectivity is not found. A sensor should be evaluated in real clinical trials to see if its performance satisfies requirements.

Analyte	**Platform**	**LoD**	**Selectivity**	**Experimentally measured range**	**Linear range**	**RSD**	**Reference**
IgA	Cladding-removed fibre	1.1µg/ml	Not stated	1.95µg/ml to 500µg/ml	0-50µg/ml	32.4%	[188]
IgA	LPG	8.59µg/ml	30.67	10µg/ml to 200µg/ml	0-30µg/ml	17.9%	This work
IgG	Cladding-removed fibre	0.04µg/ml	>50	6µg/ml to 60µg/ml	0-30µg/ml	33.3%	[22]
IgG	Tapered optical fibre	0.1µg/ml	Not stated	0.1µg/ml to 1µg/ml	0-1µg/ml	Not Stated	[159]
IgG	U-shape fibre	1.05fg/ml	Not stated	1fg/ml to 100µg/ml	0-1pg/ml	11.5%	[164]
IgG	LPG	7.38µg/ml	18.45	10µg/ml to 90µg/ml	0-90µg/ml	30.3%	This work
IgM	LPG	Able to detect 15.6µg/ml IgM	Not Stated	15.6µg/ml to 1mg/ml	Not stated	Not stated	[21]
IgM	LPG	7.02µg/ml	15.25	10µg/ml to 320µg/ml	0-80µg/ml	62.4%	This work

Table 5- 1. The characteristics of antibody sensors.

5.7 Conclusion

IgA, IgG, and IgM sensors are developed based on three LPGs with the LbL assembly method. Although the three LPGs are all fabricated in PS750 photosensitive fibre with 105µm amplitude mask, the transmission spectra are different from each other due to the deviation of optical fibre's properties. The IgA sensor measures 10µg/ml to 200µg/ml IgA experimentally. Its LoD is 8.59µg/ml, and selectivity is 30.67. The linear range is 0 to 30µg/ml. Human serum needs to be diluted by 100 folds to make IgA concentration fit the linear range. The RSD is 17.9%. The IgG sensor measures 10µg/ml to 90µg/ml IgG experimentally. Its LoD is 7.38µg/ml, and selectivity is 18.45. The linear range is 0 to 90µg/ml. Human serum needs to be diluted by 200 folds to make IgG concentration fits the linear range. The RSD is 30.31%. The IgM sensor measures 10µg/ml to 320µg/ml IgM experimentally. Its LoD is 3.79µg/ml, and selectivity is 15.25. The linear range is 0 to 80µg/ml. Human serum needs to be diluted by 30 folds to make IgM concentration fit the linear range. The RSD is 62.4%. All the sensors have sufficient capability to detect the target analyte from human serum although their LoDs are higher than other similar sensors. The reproducibility of sensors can be investigated and improved with the assistance of surface chemical analysis techniques such as Raman spectroscopy and X-ray photoelectron spectroscopy. The overall performance of the sensors should be evaluated in real clinical trials.

Chapter 6. Measurements of IgG-Type Monoclonal Proteins

Measuring Monoclonal Proteins (M-protein) plays an important role in the diagnosis and monitoring of plasma cell dyscrasias. Nowadays, the measurements of M-proteins are mostly conducted with electrophoresis, which requires complex sample processing and take several hours to get a result. IgG Kappa M-protein (IgG_κ) and IgG Lambda M-protein (IgG_λ) sensors are developed based on LPG in this work. The IgG_κ sensor has a limit of detection (LoD) of 3.8µg/ml, a linear range from 0 to 20µg/ml, and RSD of 46.1%, and a selectivity of 9.73. The IgG_λ sensor has an LoD of 3.77µg/ml, a linear range from 0 to 20µg/ml, an RSD of 40.3%, and a selectivity of 29.7. The sensors have sufficient sensitivity to detect the target M proteins in clinic.

6.1 Introduction

Plasma cell dyscrasias can cause the malignant proliferation of B cells [220]. B cells produce the components that constitutes Immunoglobulin (Ig) [41]. Ig is constituted of heavy chain and light chain [41]. There are five types of heavy chains (α, γ, ε, δ, and µ chains) and two types of light chains (κ and λ chains) [41]. A heavy chain can bind to only one type of light chain to form a whole Ig. For example, a γ chain can only bind to λ chains to form IgG (IgG_λ); another γ chain can only bind to κ chain to form IgG (IgG_κ). For healthy people, the 7 types of chains (5 heavy chains and two light chains) are balanced. However, for people with plasma cell dyscrasias, one type of chain exceeds the normal range, while other types of chain maintain a normal level or decrease [221]. For example, for IgG_κ myeloma patients, excessive γ chains are produced and the γ chains only bind to κ chain. As a result, IgG_κ exceeds the normal level. The proteins produced by the malignant B cells are also called Monoclonal Proteins (M protein). In clinic, the level of M proteins is used as the diagnostic criterion of monoclonal gammopathy of undermined significance (MGUS), smoldering multiple myeloma (SMM) [1], [11]. MGUS and SMM are considered as early stages of MM. Measuring M protein's concentration in patient's serum are used as gold standard of monitoring disease progression [12].

The detection of M proteins is conducted with protein electrophoresis and immunofixation [222], [223]. They require complex sample processing and bulky equipment and take several hours to get a result. M proteins sensors have never been designed based on optical fibre sensors before. M proteins have the same molecular structures as normal antibodies. Bio-receptors for heavy chains are used to design sensors for normal antibodies, while designing sensors for M proteins needs bio-receptors for light chains.

Sensors to detect IgG$_{\kappa}$ and IgG$_{\lambda}$ are designed based on an LPG in this work. From the review of literature, these are the first IgG$_{\kappa}$ and IgG$_{\lambda}$ sensors designed based on an optical fibre. The IgG$_{\kappa}$ sensor has a Limit of Detection (LoD) of 2.78μg/ml and IgG$_{\lambda}$ sensor has an LoD of 2.75μg/ml. The selectivity of the IgG$_{\kappa}$ sensor and IgG$_{\lambda}$ sensor is 9.73 and 29.7 respectively. Furthermore, a sensor of whole IgG is tested with IgG$_{\kappa}$ and IgG$_{\lambda}$. The LoD for IgG$_{\kappa}$ is 2.77μg/ml and 2.85μg/ml respectively. In healthy adults' serum, the concentration of IgG$_{\lambda}$ ranges from 1.97mg/ml to 5.71mg/ml and the concentration of IgG$_{\kappa}$ ranges from 4.03mg/ml to 9.78mg/ml. The sensors designed in this work have the capability to detect them.

6.2 Materials and Methodology

The LPG is fabricated in PS750 photosensitive fibre with 105μm amplitude mask. The sensors are fabricated with Glutaraldehyde cross-linker as explained in Section 3.2.3. Anti-human λ chain antibody (bound and free) produced in goat (anti-λ), anti-human κ chain antibody (bound and free) produced in goat (anti-κ), anti-human IgG antibody (Fc specific) produced in goat (anti-IgG), borate buffer saline, and albumin from human serum (HSA) are purchased from Merck, UK. The anti-λ and anti-κ are bioreceptors for IgG$_{\lambda}$ and IgG$_{\kappa}$ chain respectively. Human IgG Kappa (IgG$_{\kappa}$) and human IgG Lambda (IgG$_{\lambda}$) are purchased from Cambridge Bioscience, UK. After the functionalization with Glutaraldehyde, the LPG is immersed in anti-κ, anti-λ, and anti-IgG to fabricate sensors for IgG$_{\kappa}$, IgG$_{\lambda}$, and whole IgG respectively. After an immersion period of 2 hours in the solution of bio-receptor, the immobilization of bio-receptors on the LPG is almost saturated (Appendix H) The functional coatings can be removed by immersing the LPG in Piranha solution overnight (~17 hours). The cleaned LPG can be used again to make another sensor.

The IgG$_{\kappa}$ sensor and IgG$_{\lambda}$ sensors are tested in the solutions of target analyte with the concentration ranging from 5μg/ml to 40μg/ml. The whole IgG sensor is tested in both IgG$_{\kappa}$ solution and IgG$_{\lambda}$ solution. The concentration of the analyte ranges from 5μg/ml to 40μg/ml. The sensor is placed in a home-made Teflon fibre bath and immersed in solution with analyte. After waiting for an immersion period of approximately 25 minutes, the old solution is pumped out with a suction pump and new solution is pipetted into the fibre bath. The selectivity of the IgG$_{\kappa}$ sensor and IgG$_{\lambda}$ sensor is conducted by comparing the sensors' responses to target analytes and sensors' responses to HSA and the other M protein. First, the sensors are immersed in 80μg/ml HSA solution. After waiting for a period of 25 minutes, the HSA solution is suctioned out. Secondly, the sensor is immersed in 80μg/ml interfering M protein (IgG$_\kappa$ interferes IgG$_\lambda$ sensor, IgG$_\lambda$ interferes IgG$_\kappa$ sensor). After waiting for a period of 25 minutes, the old solution is suctioned out. Thirdly, the sensor is immersed in solution with 80μg/ml target analyte. The immersion period is 25 minutes.

6.3 IgG$_\kappa$ Sensor

The transmission spectra of bare LPG and LPG after surface functionalization are shown in Figure 6-1(a). There are two attenuation bands in the transmission spectrum. As APTES, Glutaraldehyde, and anti-κ are deposited on the surface, the attenuation bands move oppositely and the separation between them increases. The sensor's transmission spectrum changes with the concentration of IgG$_\kappa$ (Figure 6-1(b)). As the concentration increases from 0 to 40μg/ml, the attenuation bands near 780nm moves to shorter wavelengths (Figure 6-1(c)) and the attenuation band near 860nm moves to longer wavelengths (Figure 6-1(d)). The calibration curve is achieved with 2nd-order polynomial fitting (Figure 6-1(e)). R^2 is 99.62%. The linear range of the sensor is 0 to 20μg/ml (R^2=96.7%) (Figure 6-1(g)). A comparison of the sensor's responses to HSA, IgG$_\lambda$, and IgG$_\kappa$ is shown in Figure 6-1(f). The selectivity is 9.73, which is calculated with Equation (5-2). The LoD is 3.8μg/ml, calculated with Equation (5-1). The RSD of the sensor is 46.1%, calculated with Equation (5-3).

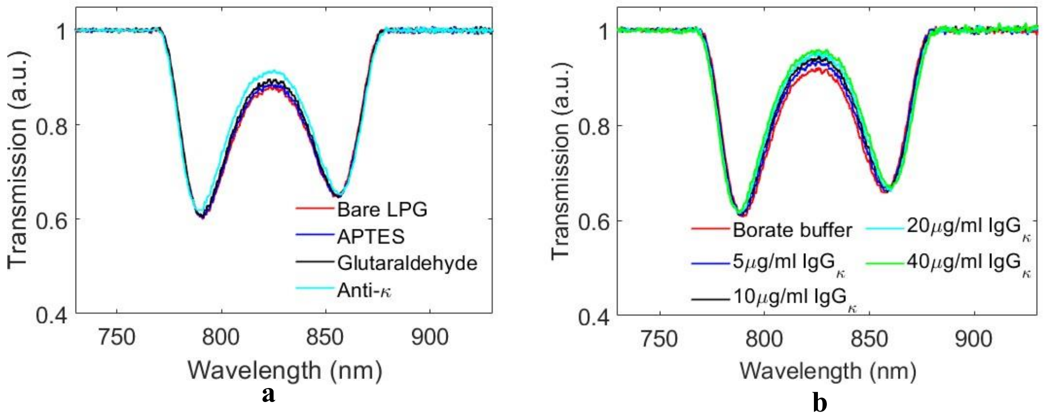

a

b

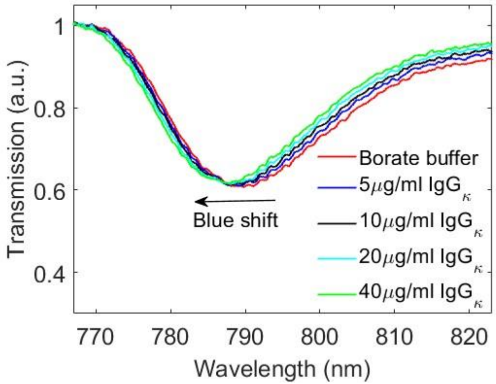
Transmission (a.u.)
1
0.8
0.6
0.4
770
780
790
800
810
820
Wavelength (nm)
Blue shift
Borate buffer
5μg/ml IgGκ
10μg/ml IgGκ
20μg/ml IgGκ
40μg/ml IgGκ

c

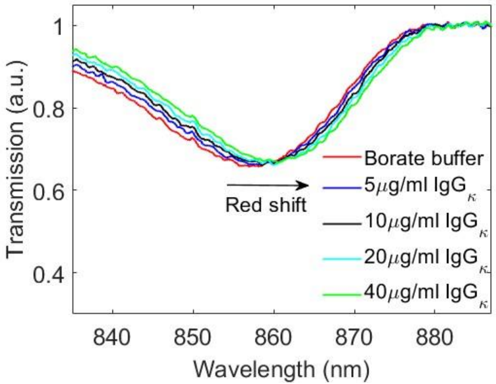
Transmission (a.u.)
1
0.8
0.6
0.4
840
850
860
870
880
Wavelength (nm)
Red shift
Borate buffer
5μg/ml IgGκ
10μg/ml IgGκ
20μg/ml IgGκ
40μg/ml IgGκ

d

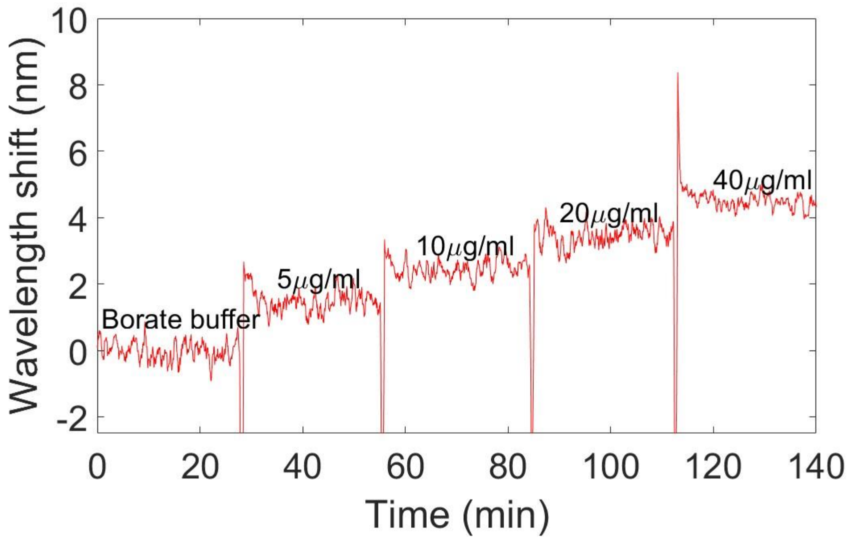
Wavelength shift (nm)
10
8
6
4
2
0
-2
0
20
40
60
80
100
120
140
Time (min)
Borate buffer
5μg/ml
10μg/ml
20μg/ml
40μg/ml

e

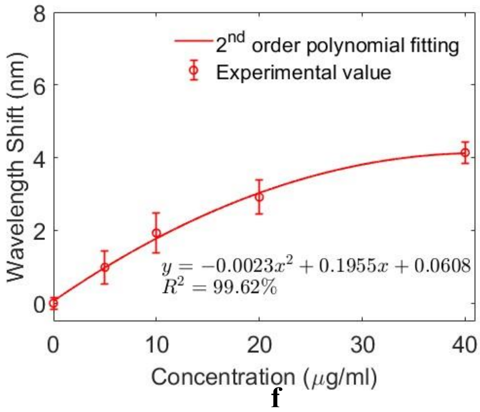
Wavelength Shift (nm)
8
6
4
2
0
0
10
20
30
40
Concentration (μg/ml)
2nd order polynomial fitting
Experimental value
y = −0.0023x² + 0.1955x + 0.0608
R² = 99.62%

f

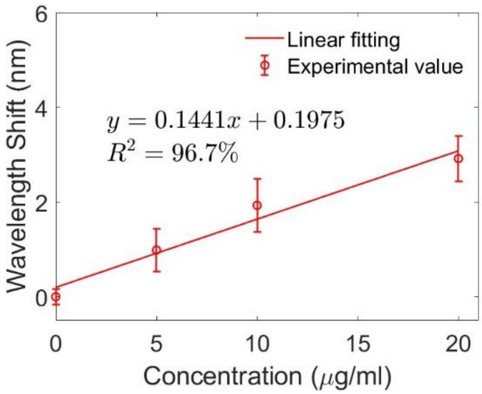
Wavelength Shift (nm)
6
4
2
0
0
5
10
15
20
Concentration (μg/ml)
Linear fitting
Experimental value
y = 0.1441x + 0.1975
R² = 96.7%

g

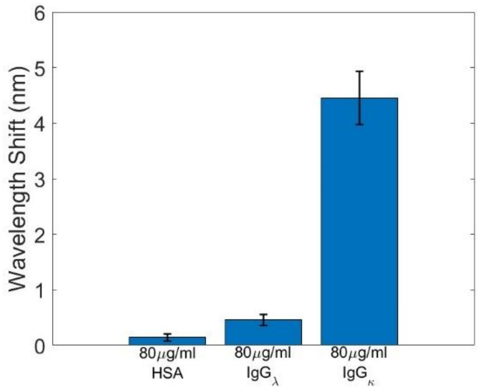

h

Figure 6- 1. The IgGκ sensor. (a) The transmission spectra during the surface functionalization of the LPG; (b) The transmission spectra during the measurement of IgGκ; (c) The blue shift of the attenuation band near 790nm; (d) The red shift of the attenuation band near 860nm; (e) The real-time wavelength shift during the measurement; (f) The calibration curve of the IgGκ sensor; (g) The linear fitting curve of the $IgG_κ$ sensor's response between 0 and 20μg/ml; (h) The selectivity test on the IgGκ sensor.

6.4 $IgG_λ$ Sensor

There are two attenuation bands in the transmission spectrum. They move oppositely and the separation between them increases after surface functionalization (Figure 6-2(a)). The transmission spectrum changes with $IgG_λ$ concentration (Figure 6-2(b)). The attenuation band near 790nm shifts to shorter wavelengths (Figure 6-2(c)) when $IgG_λ$ concentration increases and the attenuation band near 860nm moves to longer wavelengths (Figure 6-2(d)). The wavelength shift changes from 0 to nearly 5nm as $IgG_λ$ concentration changes from 0 to 40μg/ml (Figure 6-2(e)). The calibration is done with 2nd-order polynomial fitting (Figure 6-2(f)) with R^2 equal to 99.23%. The linear range of the sensor is 0 to 20μg/ml (R^2=95.63%) (Figure 6-2(g)). A comparison of the sensor's response to $IgG_λ$ and responses to HSA and $IgG_κ$ is shown in Figure 6-2(g). The selectivity of the sensor is 29.7, which is calculated with Equation (5-2). The LoD of the sensor is 3.77μg/ml, which is calculated from Equation (5-1). The RSD is 40.3%, which is calculated with Equation (5-3).

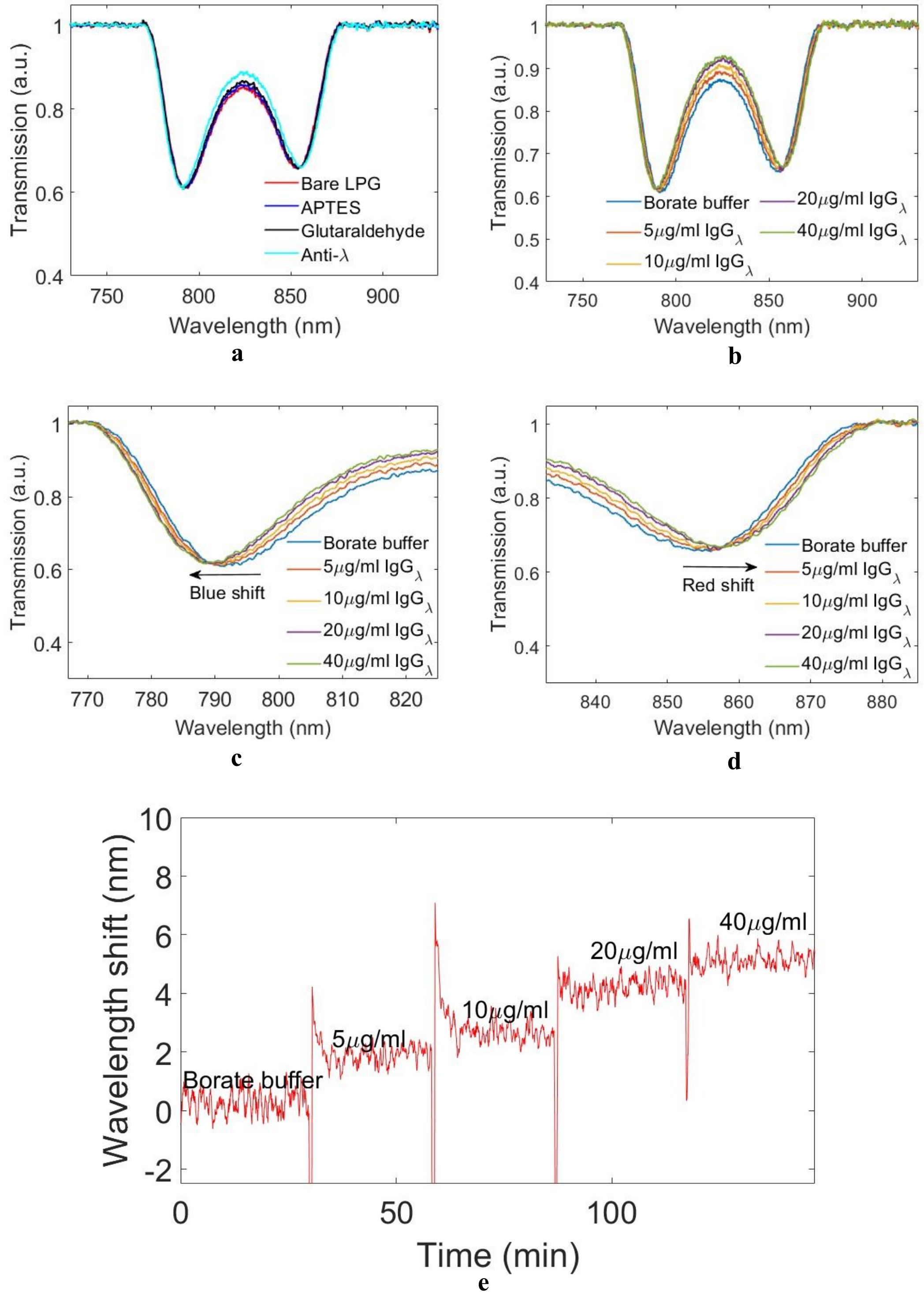
Transmission (a.u.)
Wavelength (nm)
Bare LPG
APTES
Glutaraldehyde
Anti-λ
Borate buffer
5μg/ml IgG$_\lambda$
10μg/ml IgG$_\lambda$
20μg/ml IgG$_\lambda$
40μg/ml IgG$_\lambda$
Blue shift
Red shift
Wavelength shift (nm)
Time (min)
Borate buffer
5μg/ml
10μg/ml
20μg/ml
40μg/ml

a **b** **c** **d** **e**

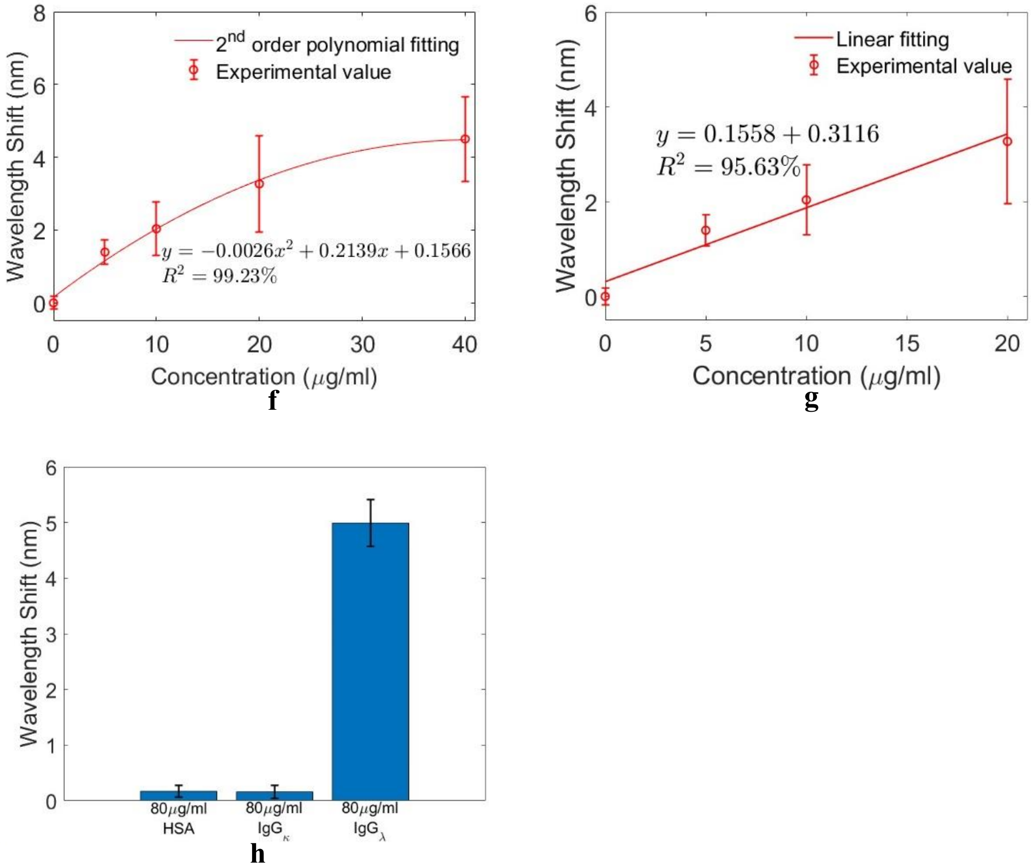

Figure 6- 2. The IgG$_\lambda$ sensor. (a) The transmission spectra during the surface functionalization of the LPG; (b) The transmission spectra during the measurement of IgG$_\lambda$; (c) The blue shift of the attenuation band near 790nm; (d) The red shift of the attenuation band near 860nm; (e) The real-time wavelength shift during the measurement; (f) The calibration curve of the IgGλ sensor; (g) The linear fitting curve of the IgG$_\lambda$ sensor's response between 0 and 20μg/ml; (h) The selectivity test on the IgGλ sensor.

6.5 Measuring IgG$_\kappa$ and IgG$_\lambda$ with Whole IgG Sensor

Anti-κ and anti-λ bio-receptors used in section 6.2 and 6.3 bind to light chains of antibodies. However, light chains exist in all types of antibodies. The IgG$_\kappa$ and IgG$_\lambda$ sensors fabricated with anti-κ and anti-λ can be affected by other types of M proteins in human serum. For example, IgM$_\lambda$ and IgM$_\kappa$ can affect the measurement of IgG$_\lambda$ and IgG$_\kappa$ respectively. Therefore, additional measurements are required to determine the type of M protein. Anti-IgG (F$_c$ specific) is used to fabricate IgG sensors. The sensor responds to IgG$_\kappa$ and IgG$_\lambda$ with similar sensitivity.

There are two attenuation bands in the transmission spectrum. As shown in Figure 6-3(a), during the surface functionalization, the two attenuation bands move oppositely and the separation between them increases after each layer of coating (APTES, Glutaraldehyde, and anti-IgG). The two attenuation bands keep moving further from each other as the IgG$_\kappa$ (Figure 6-2(b)) or IgG$_\lambda$ (Figure 6-2(e)) concentration increases. The band near 780nm moves to shorter wavelengths (Figure 6-3(c & f) and the band near 880nm (Figure 6-3(d & g)) moves to longer wavelengths. The real-time wavelength shifts during the measurements of IgG$_\kappa$ and IgG$_\lambda$ are shown in Figure 6-3(h) and Figure 6-3(i) respectively. The calibration curves are achieved with 2nd-order polynomial fitting. The R^2 of IgG$_\kappa$ and IgG$_\lambda$ measurements are 99.94% and 99.93% respectively. The error bars are calculated from the standard deviation of three independent measurements. The linear ranges of IgG$_\kappa$ and IgG$_\lambda$ measurements are 0 to 20μg/ml with R^2 equalling 99.03% and 99.68% respectively. The LoDs when measuring IgG$_\kappa$ and IgG$_\lambda$ are 3.63μg/ml and 3.73μg/ml respectively, which are calculated from Equation (5-1). The RSDs of the sensor when measuring IgG$_\kappa$ and IgG$_\lambda$ are 35.4% and 42% respectively.

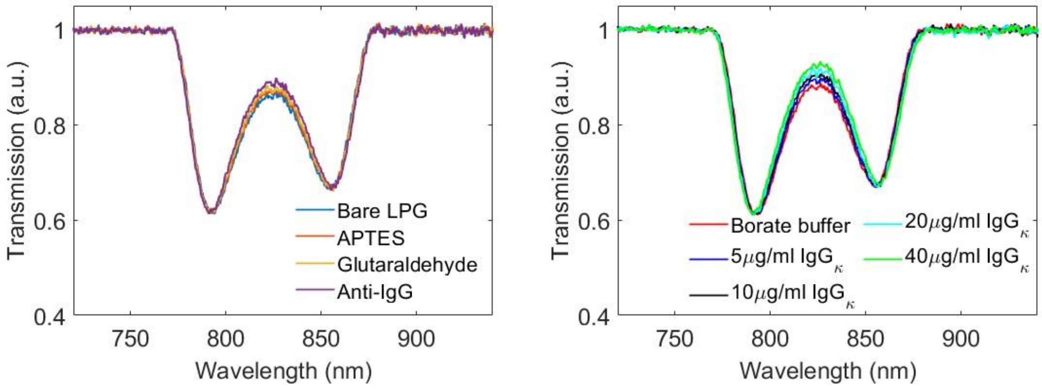

a **b**

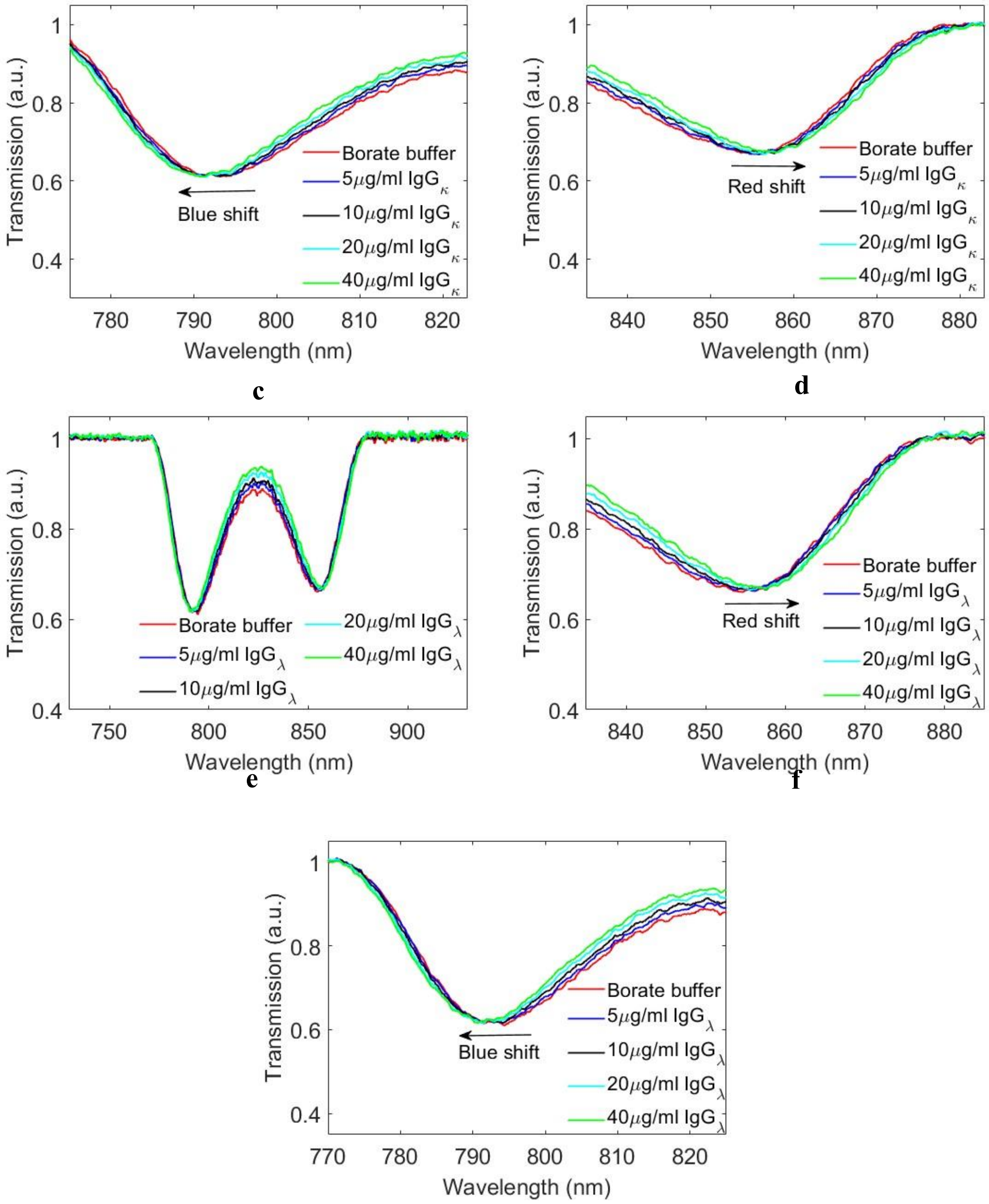
Transmission (a.u.)
Wavelength (nm)
Borate buffer
5μg/ml IgG$_\kappa$
10μg/ml IgG$_\kappa$
20μg/ml IgG$_\kappa$
40μg/ml IgG$_\kappa$
Blue shift
Red shift
5μg/ml IgG$_\lambda$
10μg/ml IgG$_\lambda$
20μg/ml IgG$_\lambda$
40μg/ml IgG$_\lambda$
0.4
0.6
0.8
1
780
790
800
810
820
840
850
860
870
880
750
900
770

c

d

e

f

g

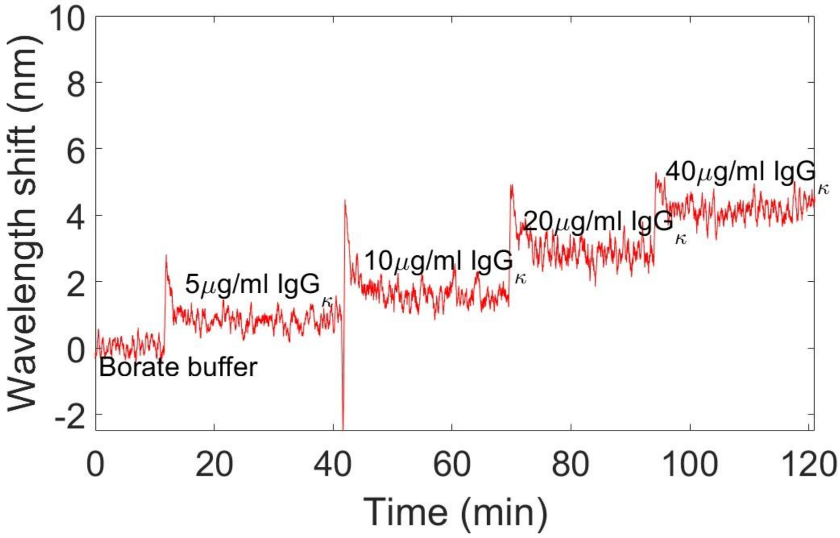
Wavelength shift (nm)
10
8
6
4
2
0
-2
0
20
40
60
80
100
120
Time (min)
Borate buffer
5μg/ml IgG$_\kappa$
10μg/ml IgG$_\kappa$
20μg/ml IgG$_\kappa$
40μg/ml IgG$_\kappa$

h

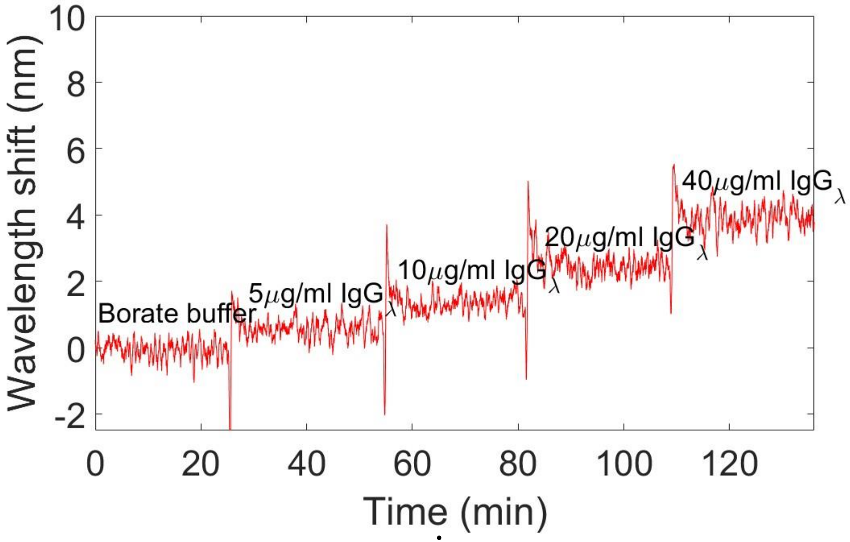
Wavelength shift (nm)
10
8
6
4
2
0
-2
0
20
40
60
80
100
120
Time (min)
Borate buffer
5μg/ml IgG$_\lambda$
10μg/ml IgG$_\lambda$
20μg/ml IgG$_\lambda$
40μg/ml IgG$_\lambda$

i

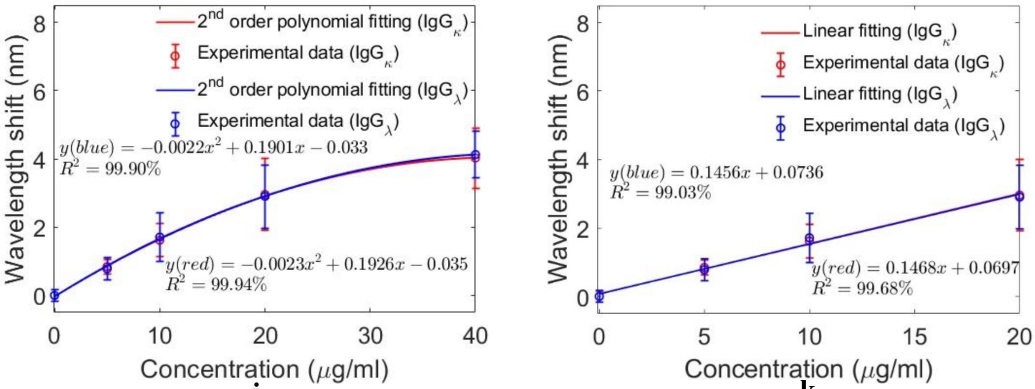

j k

Figure 6- 3. The measurement of IgGκ and IgGλ with a whole IgG sensor. (a) The transmission spectra during the surface functionalization of LPG; (b) The transmission spectra during the measurement of IgGκ; (c) The blue shift of the attenuation band near 790nm during IgGκ measurement; (d) The red shift of the attenuation band near 860nm during IgGκ measurement; (e) The transmission spectra during the measurement of IgGλ; (f) The blue shift of the attenuation band near 790nm during IgGλ measurement; (g) The red shift of the attenuation band near 860nm during IgGλ measurement; (h) The real-time wavelength shift during IgGκ measurement; (i) The real-time wavelength shift during IgGλ measurement; (j) The calibration curves of the measurements of IgGκ (red) and IgGλ (blue); (k) The linear fitting curve of IgGκ (red) and IgGλ (blue)'s responses between 0 and 20µg/ml.

6.6 Discussion

Due to the structural similarity between different types of M proteins, the determinations of IgG$_\kappa$ and IgG$_\lambda$ need both sensors, sensor with anti-κ/λ and sensor with anti-IgG. The sensor fabricated with anti-κ can detect IgG$_\kappa$ with an LoD of 3.8µg/ml. The selectivity of the sensor is 9.73. It has response to IgG$_\lambda$ as the anti-κ can bind to λ chain and the binding strength is approximately 10% of the binding strength to κ chain (product specification). The linear range of IgG$_\kappa$ sensor is 0 to 20µg/ml. The RSD is 46.1%. The sensor fabricated with anti-λ can detect IgG$_\lambda$ with an LoD of 3.77µg/ml. The selectivity of the sensor is 29.7, which is much higher than the selectivity of IgG$_\kappa$ sensor. It is most likely because the anti-λ has higher specificity than anti-κ. The linear range of IgG$_\lambda$ sensor is 0 to 20µg/ml. The RSD is 40.3%. The sensor fabricated with anti-IgG can detect the F$_c$ of IgG, therefore, it responds both IgG$_\kappa$ and IgG$_\lambda$ with similar LoDs (IgG$_\kappa$: 3.63µg/ml, IgG$_\lambda$: 3.73µg/ml). The linear ranges of whole IgG sensor are 0 to 20µg/ml when measuring both IgG$_\kappa$ and IgG$_\lambda$. The RSDs are 35.4% and 42% when measuring IgG$_\kappa$ and IgG$_\lambda$ respectively. The route to detect IgG-type M proteins consists of two steps: i) sensor with anti-IgG can determine if IgG-type proteins exceeds normal range or not; ii) sensor with anti-κ/λ can determine if the type of M protein is IgG$_\kappa$ or IgG$_\lambda$. It is quite similar to the two steps of immunofixation [224]. The concentration of

M protein in plasma cell dyscrasias patients' serum can reach 30mg/ml. It needs to be diluted by 1500 folds to fit sensors' linear ranges. The RSDs of the sensors developed in this work doesn't meet the requirements for PoC devices, which is 10%. As discussed in Section 5.6, more surface chemical analysis techniques need to be used to investigate and improve the surface functionalization, which is hoped to improve the reproducibility of the sensor.

6.7 Conclusion

Sensors to detect IgG-type M proteins are developed based on LPG in this work. The IgG$_{\kappa}$ sensor is developed by immobilizing anti-κ on LPG. Anti-κ binds to κ chain in IgG$_{\kappa}$. The LoD of the sensor is 3.8μg/ml, and the selectivity is 9.73. The IgG$_{\lambda}$ sensor is developed with anti-λ, which binds to λ chain of IgG$_{\lambda}$. The LoD of the IgG$_{\lambda}$ sensor is 2.75μg/ml, and selectivity is 27.9. A whole IgG sensor is fabricated by immobilizing anti-IgG, which binds to the F$_{c}$ of IgG. The sensor can detect IgG$_{\kappa}$ and IgG$_{\lambda}$ with LoDs of 2.77μg/ml and 2.85μg/ml respectively. Since κ chain and λ chain exist in all types of antibodies, other antibodies such as IgM$_{\kappa}$ and IgM$_{\lambda}$ are interfering substance to the sensors developed with anti-κ/λ. The determinations of IgG-type M proteins consist of two steps: i) test the sample with whole IgG sensor to see if it exceeds the normal range; ii) if IgG exceeds the normal range, test the sample with IgG$_{\kappa}$ or IgG$_{\lambda}$ sensor to determine the type of M protein. Serum of patients with plasma cell dyscrasias needs to be diluted by 1500 folds with borate buffer to fit sensors' linear ranges. The reproducibility of the sensors doesn't satisfy the requirements for PoC devices.

Chapter 7. Immunoglobulin M Sensor Based on Long Period Grating Mach-Zehnder Interferometer with Compensation for the Fluctuations of Temperature and Bulk Refractive Index

This chapter is modified from the author's previous publication [225]. A long period grating Mach-Zehnder interferometer (LPGMZI) that consists of two identical long period gratings (LPG) in a single fibre is developed to measure Immunoglobulin M (IgM). The measured spectrum has fringes due to the interference between core mode and cladding mode. This sensor exhibits the advantages of an LPG. By analysing the fringes and envelope, the sensor has the potential to compensate for the unwanted signal changes due to bulk refractive index (RI) and temperature fluctuations. The external RI was measured from 1.3326 to 1.3734 in two different scenarios: i) only the connecting section between the two LPGs is immersed or ii) the whole LPGMZI is immersed. The fringes shift with the external RI in both scenarios, whereas the envelope stays still in case i) or shifts at the same rate as fringes in case ii). The LPGMZI's response to temperature between 25°C and 30°C is also investigated. An IgM sensor is developed by functionalizing the connecting section of the LPGMZI. The functionalized connecting section is immersed in IgM solution with concentration ranging from 20μg/ml to 320μg/ml. The Limit of Detection (LoD) is 15μg/ml, the linear range is from 0 to 80μg/ml, the RSD is 27.33%, and the selectivity is 18.48.

7.1 Introduction

A long period grating (LPG) is currently a widely used platform for developing chemical sensors and biosensors [168], [226]. An LPG's advantages such as light weight, small size, and immunity to electromagnetic interference make it an ideal platform for designing Point-of-Care (PoC) portable biosensors [28]. These sensors provide a more labour-saving and faster sensing than ELISA as they do not require a labelling step [30]. LPG-based biosensors detect the change of refractive index (RI) on the surface upon molecular binding. The main sources of cross-sensitivities of LPG-based biosensors include temperature fluctuations and changes of external medium's RI (bulk RI) [227]. Many efforts have been made to overcome these problems. For example, a plasmonic sensor with gold nanofilm deposited on the surface of a tilted fibre Bragg grating (FBG) can discriminate surface RI and bulk RI [228]. The same function can be implemented using an LPG with a micro-cavity in the middle [229]. A core-offset Mach-Zehnder interferometer fabricated in series with an FBG can implement simultaneous measurement of temperature and RI [230], as does an LPG fabricated in series with an FBG [231].

The long period grating Zach-Zehnder interferometer (LPGMZI) described in this work consists of two identical LPGs in a single fibre. As shown in Figure 7-1, two identical LPGs are fabricated in series and light propagates through the fibre from left to right. LPG1 couples light from core mode into cladding mode; the cladding-mode light propagates along the connecting section and is coupled into the core by LPG2, where it interferes with the light has remained within the core. The interference pattern is analysed on a spectrometer.

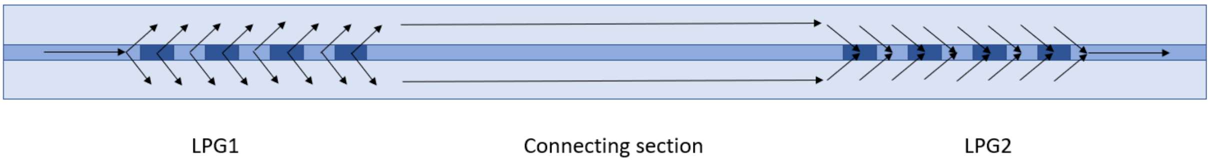

Figure 7- 1. Structure of an LPGMZI.

The transmission spectrum has fringes due to the interference between the core mode and cladding modes, which has potential to compensate for unwanted signal change caused by bulk RI changes and temperature fluctuations.

The interference pattern in an LPGMZI's transmission spectrum changes with temperature, and a uniform temperature change over the whole LPGMZI results in the fringes and envelope shifting at the same rate [232]. The interference pattern is also sensitive to external RIs. The fringes and envelope shift when the whole LPGMZI is immersed in solutions with different RIs [223]. In comparison to other methods [227], the LPGMZI is a more elegant structure to compensate for both bulk RI and temperature changes with a single calibration step, a simpler set-up, and a simpler fabrication method.

Chemical and biosensors are developed by depositing functional films on an LPGMZI. An ammonia (NH_3) sensor has previously been designed by depositing a graphene film on the connecting section of an LPGMZI, which absorbs NH_3 to change RI on the surface [234]. Similarly, a zeolitic imidazole framework (ZIF-8) film is deposited on an LPGMZI to detect volatile organic compounds (VOCs) such as methanol and toluene [235]. A Mach-Zehnder interferometer can also be fabricated by cascading two identical chirped LPGs [236]. A biosensor to detect Escherichia coli (E.coli) has been developed by depositing bio-receptors on the connecting section [236]. In all the literatures about LPGMZI, the fringes are analysed, but the fringes' envelope is not investigated quantitatively.

In this work, an LPGMZI is fabricated and characterized. The fringes and envelope are measured and analysed to provide a more thorough investigation of an LPGMZI and more robust sensing. In the temperature measurement, the temperature over the whole LPGMZI changes uniformly. The envelope and fringes shift with temperature at the same rate of approximately 0.4nm/°C. The external RI measurements are carried out in two scenarios: i) the whole LPGMZI or ii) only the connecting section is immersed in solutions with different RI. In scenario i), the fringes and envelope shift with external RI at the same rate of approximately 94.6nm/RI. In scenario ii), the fringes shift with external RI at a rate of approximately 75.4nm/RI, while the envelope doesn't have wavelength shift. An IgM sensor is developed based on LPGMZI. It is demonstrated that the sensor has a Limit of Detection (LoD) of 15µg/ml, a linear range from 0 to 80µg/ml, an RSD of 27.33%, and a selectivity of 18.48.

7.2 Methodology

7.2.1 Experimental Set-ups and Signal Processing

LPGs are fabricated in photosensitive fibre (PS750, Fibercore, UK) using a 266nm wavelength laser and amplitude mask with 113.5µm grating period. The two LPGs are 2cm in length and the separation between them is 6cm. The number of fringes increases with the separation [237]. A 6cm separation is chosen to ensure the envelope and high-frequency components are distinguishable in the frequency domain.

The experimental set-up used for different refractive index measurements is shown in Figure 7-2. The LPGMZI is placed in a home-made, 3-section Polylactic Acid (PLA) fibre bath (middle section 4.5cm(L)×0.5cm(W)×0.3cm(D), LPG sections 2.75cm(L)×0.5cm(W)×0.3cm(D)). The connecting section is placed in the middle section. The two LPGs are located either side and are connected through small crevices (0.3mm), which ensures that the solution does not leak between sections due to the hydrophobicity of fibre bath's material. The experimental set-up used for temperature measurements is shown in Figure 3-7(b).

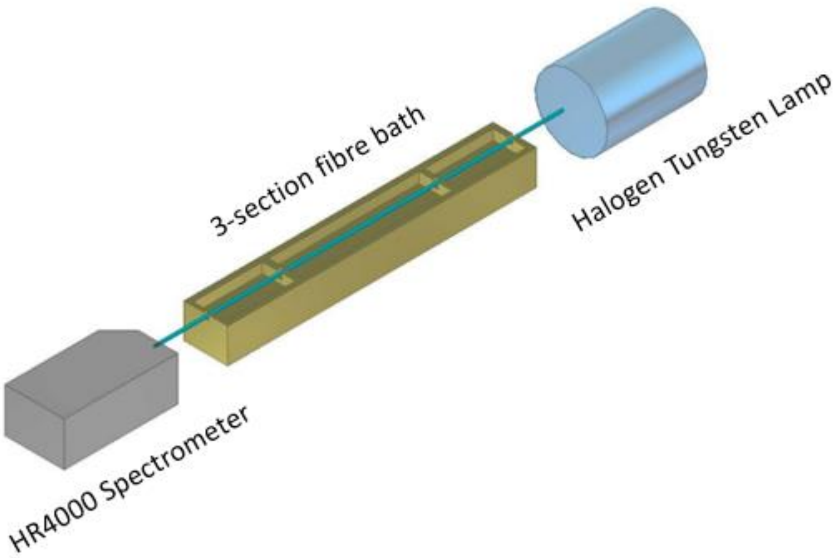

Figure 7- 2. Experimental set-up. An LPGMZI is placed in a home-made 3-section fibre bath holder with two LPGs in the sections on either side (2.75cm(L)×0.5cm(W)×0.3cm(D)) and a connecting section in the middle (4.5cm(L)×0.5cm(W)×0.3cm(D)).

External RI Measurement

In the external RI measurements, the responses of fringes and envelope are investigated in two scenarios: i) only connecting section is immersed in RI solutions or ii) the whole LPGMZI is immersed in RI solutions. The purpose of these experiments is to demonstrate the different responses of fringes and envelope in the two scenarios. In both scenarios, the immersion region is first immersed in solution with a RI of 1.3326. Then, the old solution is pumped out using a suction pump and new solution with a higher RI is pipetted into the fibre bath. The immersion period of each solution is approximately 20 minutes. In temperature measurements, the temperature changes uniformly over the whole LPGMZI from 25°C to 30°C with an increment of 1°C.

IgM measurement

In IgM measurements, the surface-functionalized connecting section is immersed in IgM+Tris buffer solutions with the concentration varying from 0 to 320μg/ml. The two LPGs are left in air. For each solution, the immersion period is approximately 20 minutes. Then, old solution is pumped out using suction pump and new solution with a higher IgM concentration is pipetted in. The cross-sensitivity test is conducted with IgA and IgG. The surface functionalized connecting section is immersed in 80μg/ml IgG, IgA, and IgM sequentially. In all the measurements, the wavelengths of fringes and envelope are investigated.

Theory

The fringes in the spectrum are caused by the interference between cladding and core modes. The phase of the fringes relative to their envelope is determined by the difference between optical path lengths between core mode and cladding modes as described by Equation 7-1 [238]:

$$\Phi = \frac{2\pi}{\lambda}\left({n_{eff}}^{co} - {n_{eff}}^{cl}\right)L \tag{7-1}$$

Where Φ is the phase of fringes; λ is the wavelength of light; ${n_{eff}}^{co}$ and ${n_{eff}}^{cl}$ are the effective RI of core mode and cladding mode respectively; L is the length of connecting section.

Signal Processing

In this work, the wavelengths of fringes and envelope are measured and analysed. A discrete Fourier transform (DFT) is applied to extract the envelope from the transmission spectrum:

$$X[k] = \sum_{n=1}^{N-1} x[n]e^{-j\frac{2\pi nk}{N}} \tag{7-2(a)}$$

$$x[n] = \sum_{k=1}^{N-1} X[k]e^{j\frac{2\pi nk}{N}} \tag{7-2(b)}$$

Where $x[n]$ is the original signal, which is the transmission spectrum in this work; *N* is the number of samples in the signal; $X[k]$ is the frequency-domain representation of $x[n]$, where *k* is the wavenumber.

An example of the signal processing is shown in Figure 7-3. First, the DFT (equation 7-2(a)) is applied to the transmission spectrum (Figure 7-3(a)) to obtain a frequency-domain representation (Figure 7-3(b)). The envelope and high-frequency components are distinguishable by visual inspection of the frequency-domain representation. There is a local minimum at the wavenumber of 45.45nm^{-1}. These frequency components can be separated from each other by applying low- and high-pass filters with square cut-offs at 45.45nm^{-1} to obtain its envelope (Figure 7-3(c)) and high-frequency components (Figure 7-3(d)), respectively. The envelope is represented as a wide dip (~30nm). The high-frequency components are represented as narrow fringes. A dip-finding method is used to track the wavelengths of envelope and fringes during the measurements.

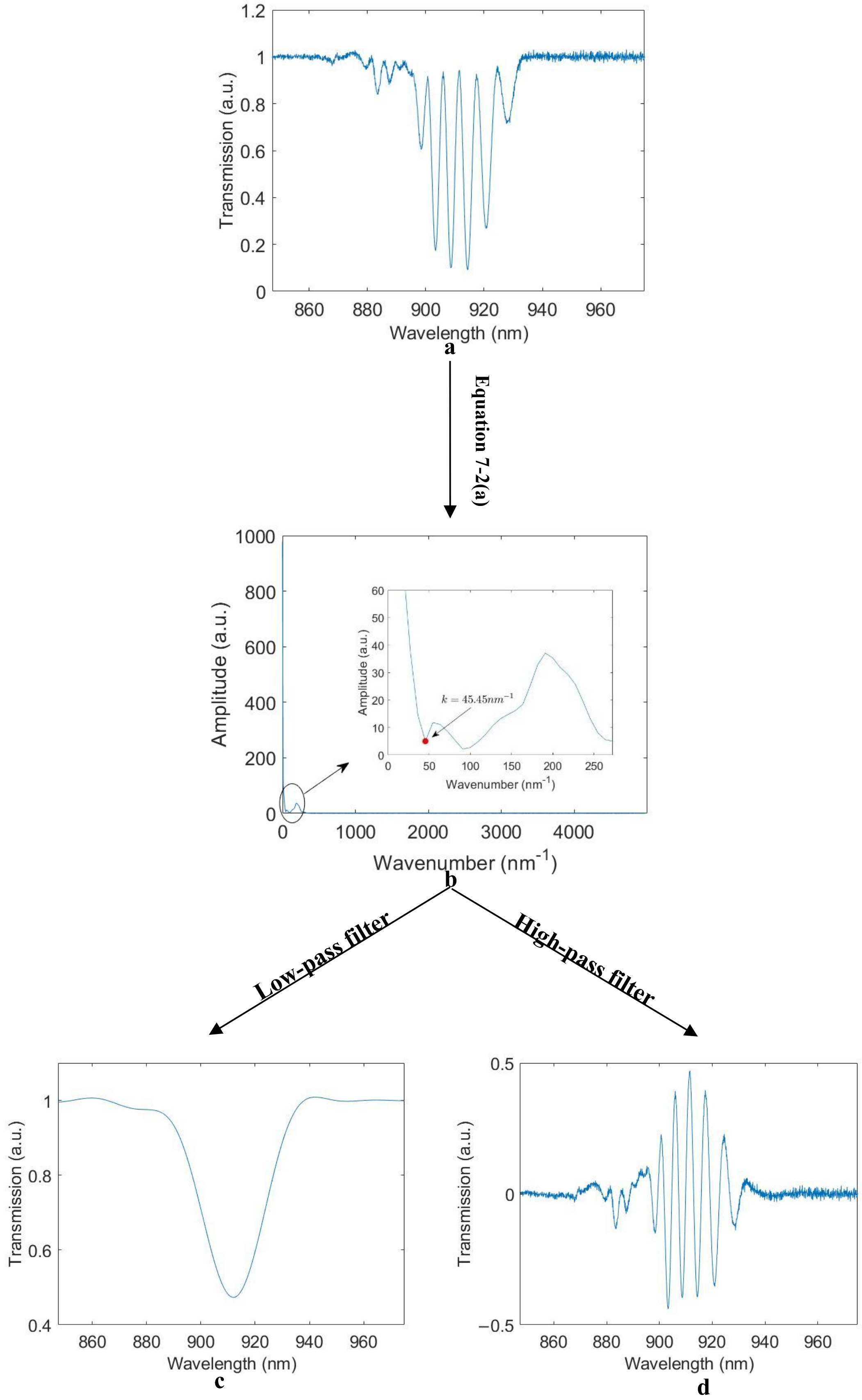

Figure 7- 3. The signal processing. (a) The transmission spectrum; (b) The frequency-domain representation of the transmission spectrum; (c) The envelope of the

transmission spectrum; (d) The high-frequency component of the transmission spectrum.

7.2.2 Materials and Functionalization of LPGMZI

3-Aminopropyltriethoxysline (APTES), Tris buffer, sodium chloride, sulfuric acid, peroxide solution (H_2O_2), ethanol, glutaric dialdehyde solution (Glutaraldehyde, 50% in H_2O), IgM from human serum, IgG from human serum, IgG from human serum, and anti-human IgM antibody produced in goat (anti-IgM) are purchased from Merck, UK.

The connecting section is immersed in Piranha solution for 20 minutes to remove contamination and generate hydroxyl groups on the surface. Then, it is washed with DI water and dried with nitrogen (N_2). Secondly, the connecting section is immersed in APTES solution (2 v/v% in ethanol) for 20 minutes, followed by washing with DI water and ethanol alternately and drying in air overnight (~16 hours). Thirdly, the connecting section is immersed in Glutaraldehyde (50% in H_2O) for 2 hours followed by washing with DI water. Fourthly, the connecting section is immersed in 1mg/ml anti-IgM solution (dissolved in PBS buffer) followed by washing with PBS buffer. The process is illustrated in Figure 7-4.

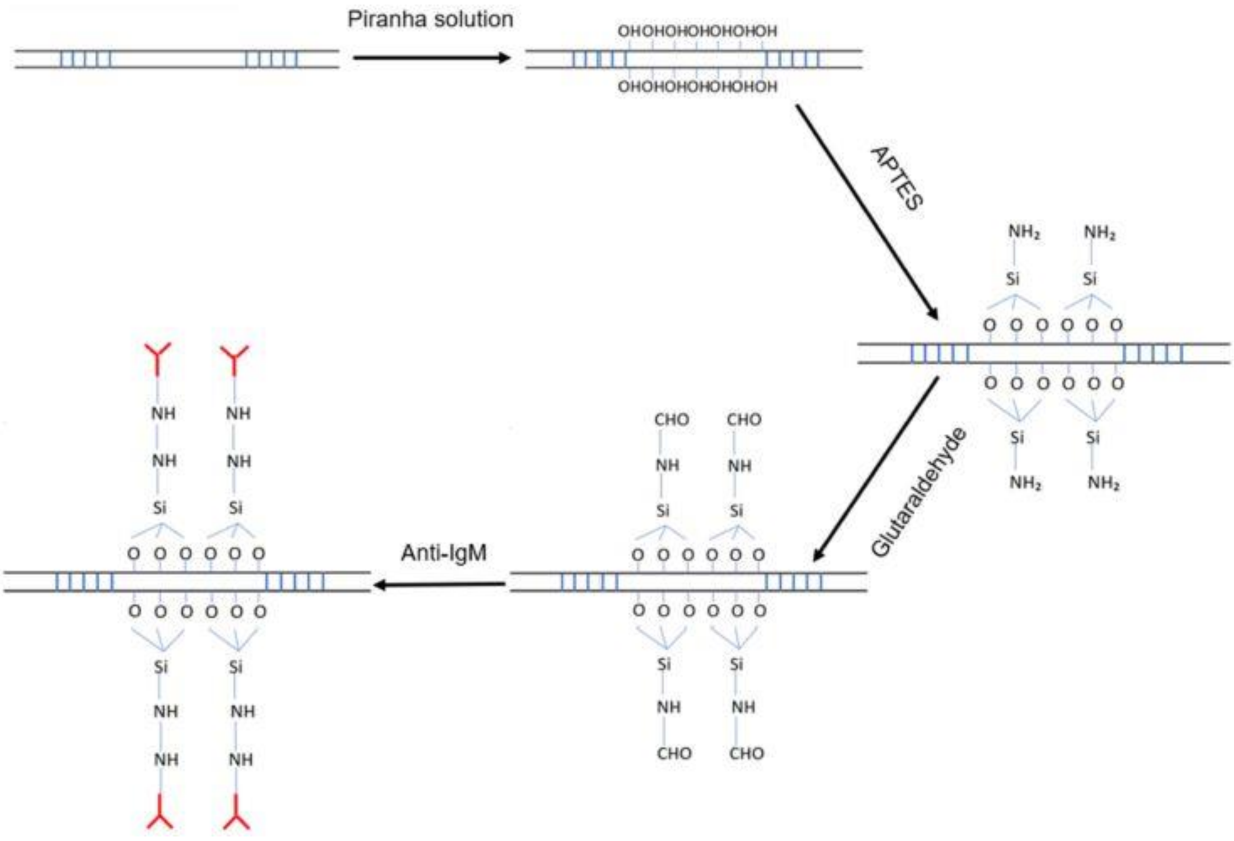

Figure 7- 4. The surface functionalization of an LPGMZI.

7.3 Results

Three measurements with LPGMZI are conducted. For RI measurement, if only the connecting section is immersed, the wavelength shift of fringes increases with external RI while the wavelength of envelope stays static; if the whole LPGMZI is immersed, the wavelength shifts of envelope and fringes increase with external RI at the same rate. For temperature measurement, the wavelength shifts of envelope and fringes increase at the same rate when temperature increases homogeneously over the whole LPGMZI. For IgM measurement, the wavelength shift of fringes increases with IgM concentration, while the wavelength of the envelope remains static. The response to IgM decreases with temperature.

7.3.1 External RI Measurement with LPGMZI

As shown in Figure 7-5(a & c), there are 6 dips in the transmission spectrum (fringes). There are 4 dips that have normalised transmission lower than 0.4. The dip with the second shortest wavelength is tracked and compared for all the measurements in this chapter as its shifting rate with external RI in closest to the shifting rate of the envelope (Appendix E). When the whole LPGMZI is immersed in solution, all the dips in the fringes move together to shorter wavelengths, so the envelope also moves (Figure 7-5(a)). The real-time wavelength shifts of envelope and fringes are shown in Figure 7-5(b) - they are almost coincidental. When only the connecting section is immersed in solution, the dips in the transmission spectrum move to shorter wavelengths and the relative depths of them change (Figure 7-5(c)). Although the depth of the envelope decreases when the external RI increases, it can be observed from Figure 7-5(d) that the wavelength shift of the envelope (~0.01nm) is tiny in comparison to the wavelength of fringes (~3.12nm). The wavelength shifts of the fringes in these two scenarios are calibrated with linear fitting (Figure 7-5(e)). It has a lower sensitivity when only the connecting section is immersed, which is 79% of the sensitivity when the whole LPGMZI is immersed.

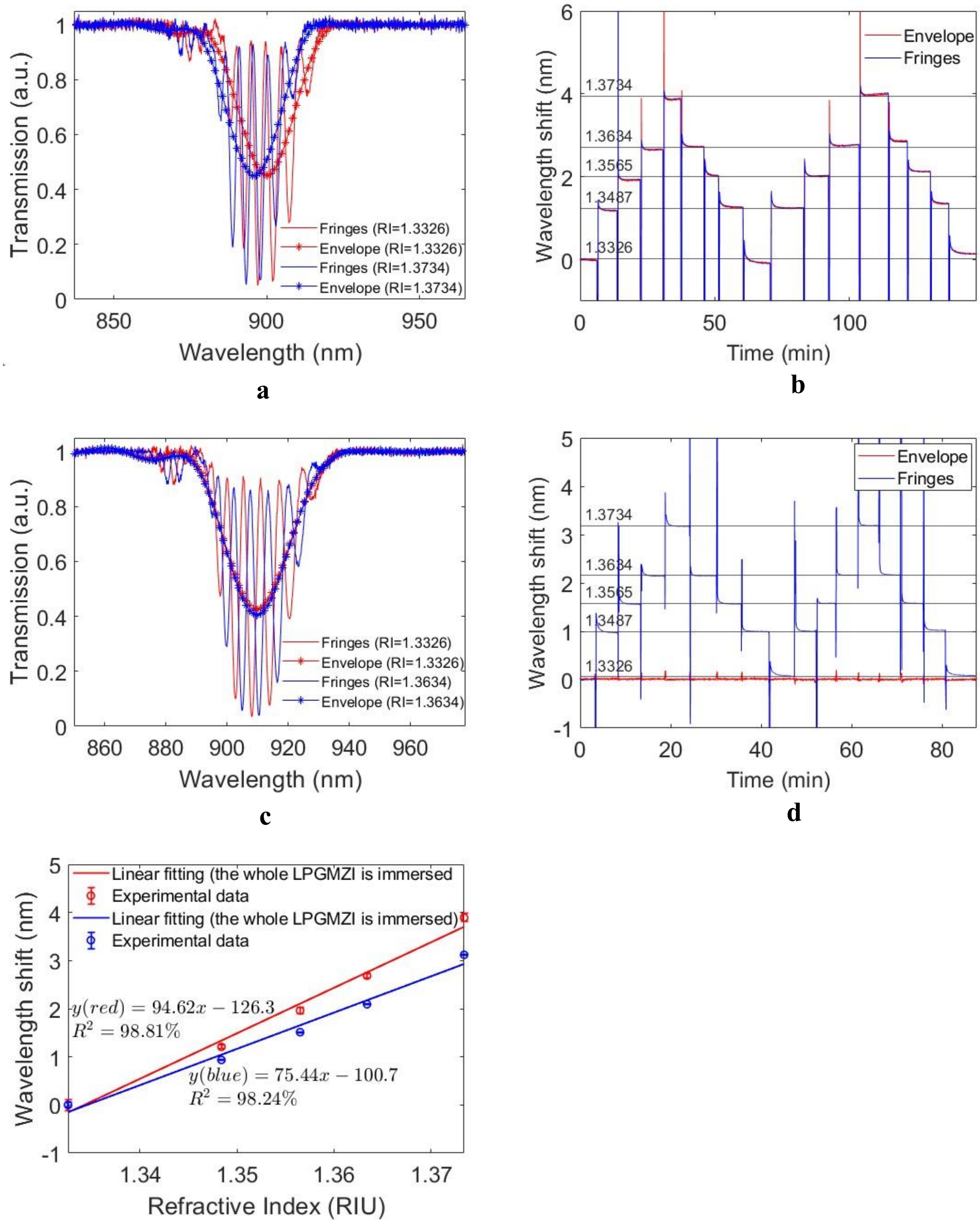

a **b**

c **d**

e

Figure 7- 5. The external RI measurements with an LPGMZI. (a) The transmission spectra and envelopes when the whole LPGMZI is immersed in the solution; (b) The wavelength shifts of envelope and fringes when the whole LPGMZI is immersed in solution; (c) The transmission spectra and envelopes when the whole LPGMZI is immersed in the solution; (d) The wavelength shifts of the envelope and fringes when only the connecting section is immersed in solution; (e) The calibration curves of the fringes' response to external RI in two different scenarios.

7.3.2 Temperature Measurement with LPGMZI

As the temperature increases from 25℃ to 30℃, the fringes and envelope shift to shorter wavelengths (Figure 7-6(a)). The real-time wavelength shifts of envelope and fringes are shown in Figure 7-6(b). Similar to Section 7.3.1, there are four dips whose transmission is lower than 0.4. Only the dip with the second shortest wavelength is tracked as its changing rate with temperature is the most comparable with the changing rate of the envelope among all the four dips. The real-time wavelength shift of the other three dips is available in Appendix E. The difference between the fringes' wavelength shift and envelope's wavelength shift is shown in Figure 7-6(c) - it almost remains zero. The calibration curve between wavelength shift and temperature is shown in Figure 7-6(d). A Coefficient of Determination (R^2) of 99.98% is achieved with a linear fitting. The sensitivity of the wavelength shift to temperature change is approximately 0.4nm/°C.

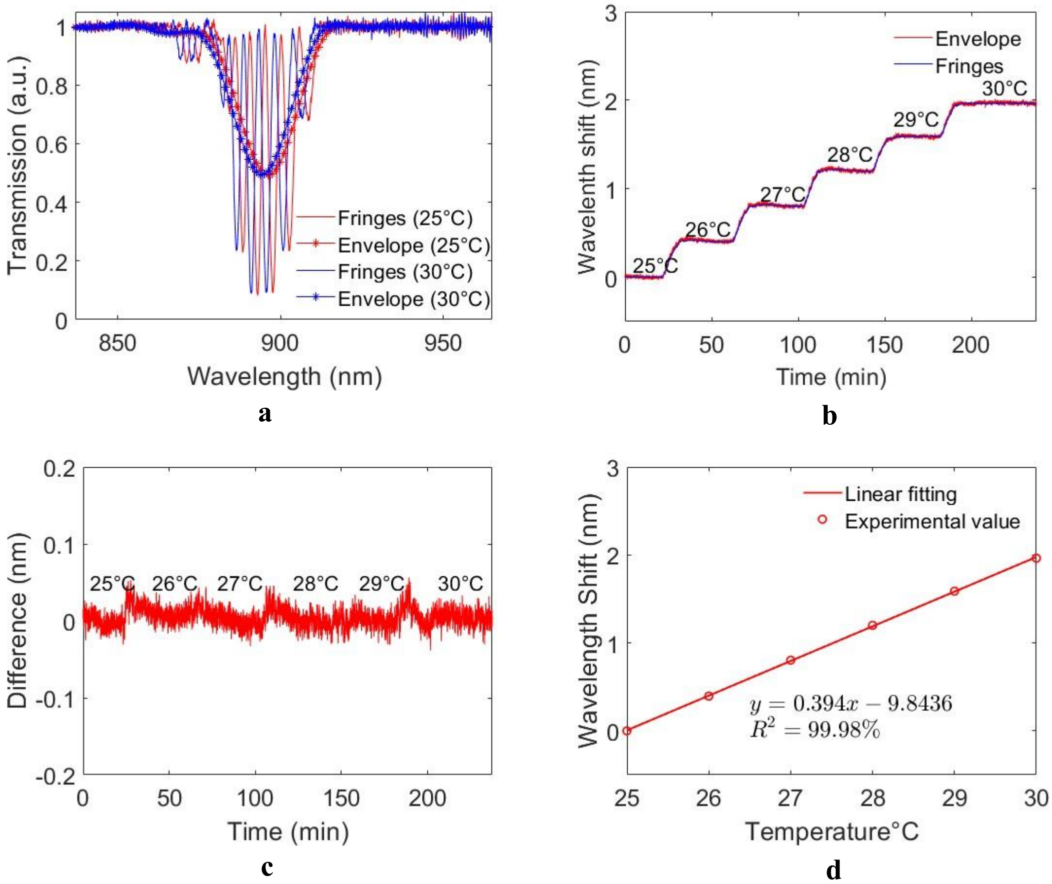

Figure 7- 6. The temperature measurement with LPGMZI. (a) The transmission spectra and envelopes at different temperatures. (b) The real-time wavelength shifts of fringes and envelope when the temperature increases from 25°C to 30°C. (c) The difference between the wavelength shift of fringes and the wavelength shift of the envelope. (d) The calibration curve of wavelength shift to temperature.

7.3.2 IgM Sensor

From the results of Section 7.3.1 and Section 7.3.2, the dip with the third shortest wavelength has the most comparable wavelength changing rate with envelope. Therefore, this dip is tracked during the fabrication and test of the IgM sensor. The transmission spectra (fringes & envelope) during the surface functionalization are shown in Figure 7-7(a). The fringes shift to shorter wavelengths (Figure 7-7(b)). The envelope almost doesn't shift in wavelength, but its amplitude fluctuates (Figure 7-7(c)). The transmission spectra of the IgM sensor in Tris buffer and solution with IgM concentration of 320µg/ml are shown in Figure 7-7(d). Similar to the changes during the surface functionalization process, the fringes shift to shorter wavelengths (Figure 7-7(e)). The envelope doesn't shift in wavelength, but its amplitude changes (Figure 7-7(f)). The real-time wavelength shifts of fringes and envelope are shown in Figure 7-7(g). The wavelength shift of fringes increases with IgM concentration, while the wavelength shift of the envelope almost doesn't change. The difference between them is calculated (Figure 7-7(h)). The calibration between the difference and IgM concentration between 0 and 320µg/ml is performed by exponential fitting (Figure 7-7(i)). A Coefficient of Determination of 99.84% is achieved. The linear range is 0 to 80µg/ml (R^2=96.97%) (Figure 7-7(j)). The LoD of the sensor is 15µg/ml, which is calculated with Equation (5-1). The error bar is the standard deviation of data acquired from multiple independent measurements. The RSD of the sensor is 27.33%, which is calculated with Equation (5-3). Measurements of 80µg/ml IgM is performed under three different temperatures (Figure 7-7(j)). The response of the sensor decreases with temperature. The selectivity of the sensor is 18.48 (Figure 7-7(k)), which is calculated from Equation (5-2).

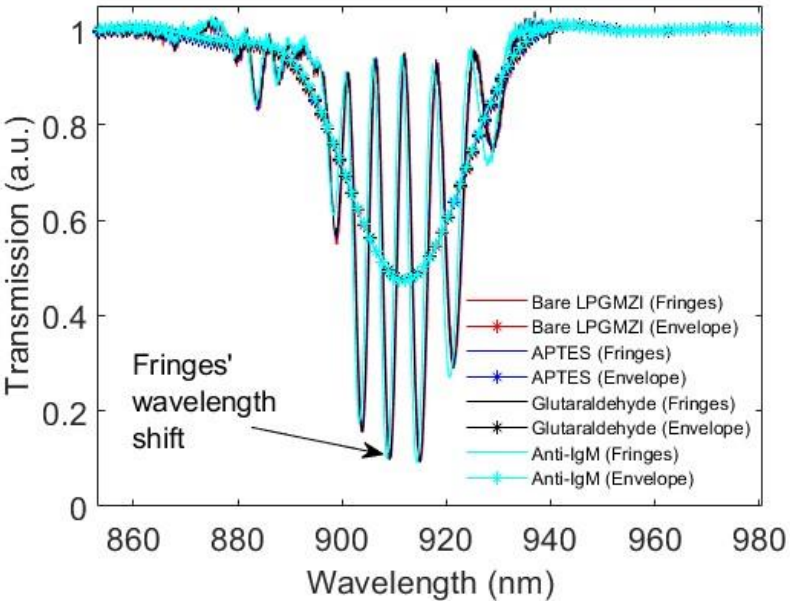

a

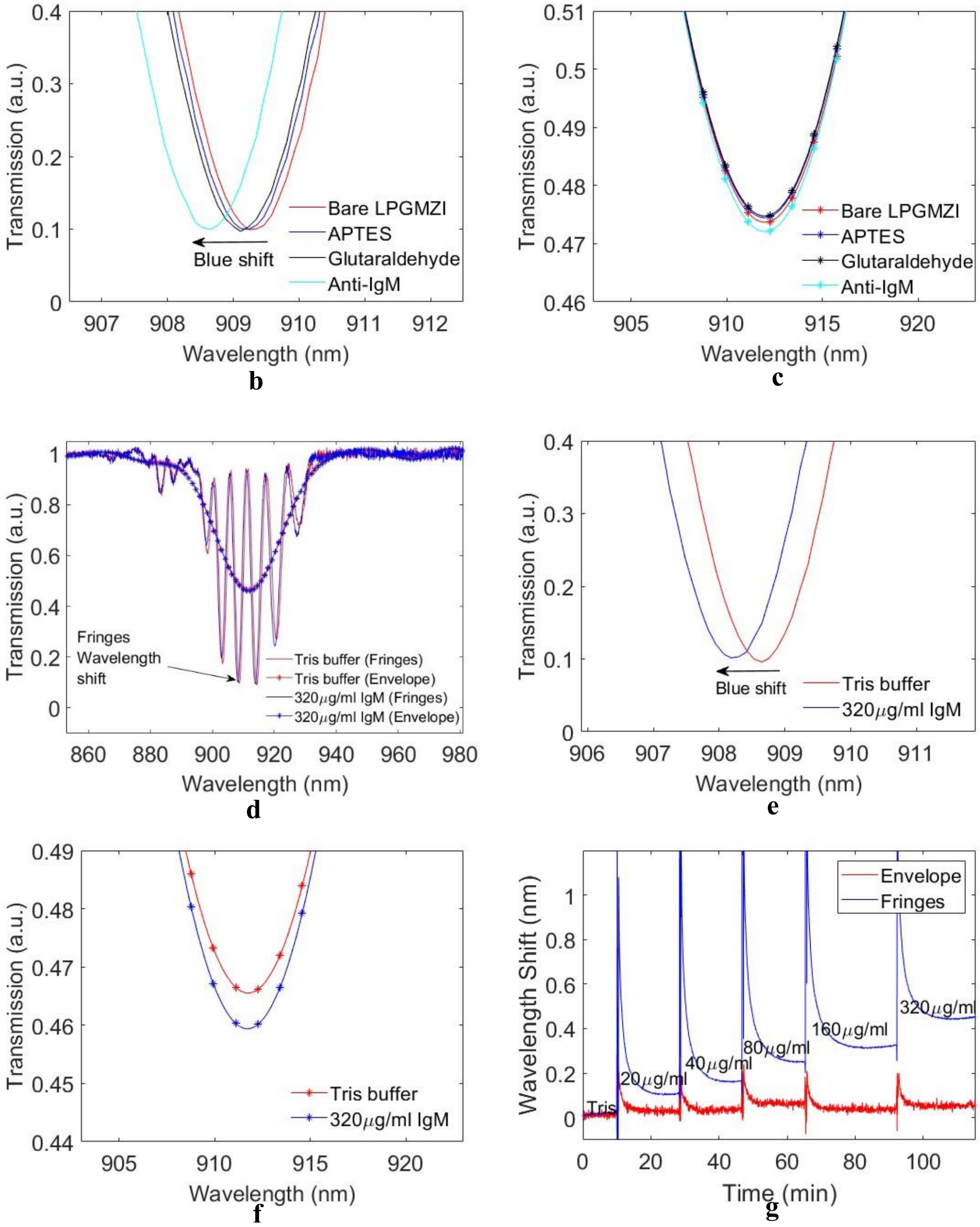
Transmission (a.u.)
Wavelength (nm)
Bare LPGMZI
APTES
Glutaraldehyde
Anti-IgM
Blue shift
Fringes Wavelength shift
Tris buffer (Fringes)
Tris buffer (Envelope)
320μg/ml IgM (Fringes)
320μg/ml IgM (Envelope)
Tris buffer
320μg/ml IgM
Wavelength Shift (nm)
Time (min)
Envelope
Fringes
Tris
20μg/ml
40μg/ml
80μg/ml
160μg/ml
320μg/ml

b

c

d

e

f

g

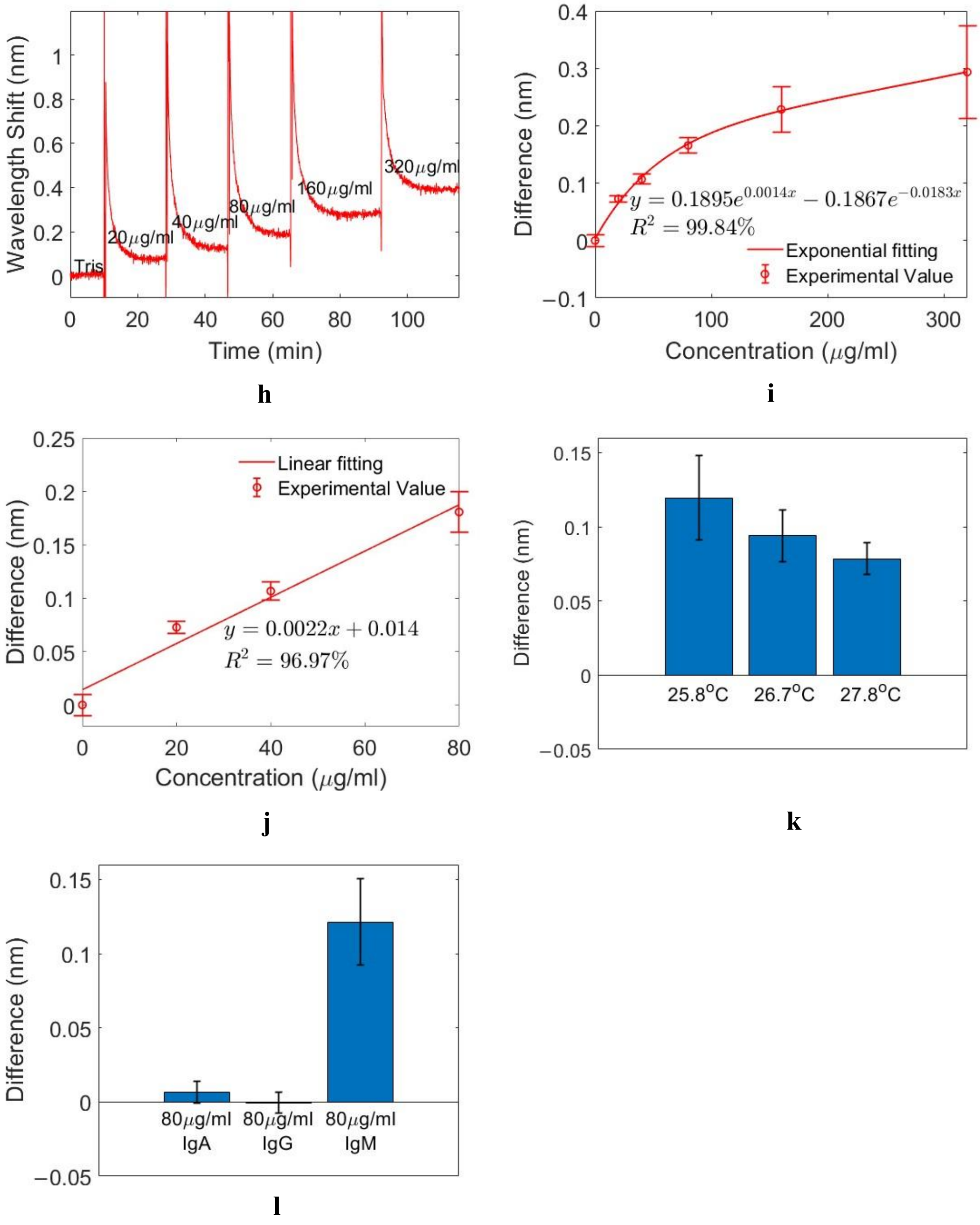

h

i

j

k

l

Figure 7- 7. The IgM sensor. (a) The transmission spectra and envelopes during the surface functionalization; (b) The blue shift of fringes during functionalization; (c) The envelopes during functionalization; (d) The transmission spectra and envelopes under zero and 320µg/ml IgM; (e) The blue shift of the fringes with increasing IgM concentration; (f) The envelopes under different IgM concentrations; (g) The real-time wavelength shifts of fringes and envelope during IgM measurement; (h) The difference between the wavelength shifts of fringes and envelope; (i) The calibration curve between the difference and IgM concentration; (j) The linear fitting curve of IgM sensor's response between 0 and 80µg/ml; (k) The responses of the IgM sensor to 80µg/ml IgM under three different temperatures; (l) The IgM sensor's responses to 80µg/ml IgA, IgG, and IgM

7.4 Discussion

Depending on the scenarios, the LPGMZI responds to external RI in different ways. If only the connecting section is immersed in solution, the wavelength shift of fringes increases with external RI and the envelope's wavelength doesn't change. The position of the envelope is dependent on the working conditions of two LPGs. The two identical LPGs are exposed to air and external RIs of them are one. Recalling Equation (2-18), the attenuation band of either LPG doesn't change during measurement. The interference between light only happens within the attenuation band. Therefore, the envelope remains static, and fringes shift relative to the envelope. If the whole LPGMZI is immersed in solution, the working conditions of the two LPGs change with external RI during the measurement. The wavelength shifts of envelope and fringes increase with external RI at the same rate. Recalling Equation (7-1), substituting the λ with Equation (2-18), Equation (7-3) is obtained:

$$\Phi = \frac{2\pi L}{\Lambda} \qquad 7\text{-}3$$

Where Φ is the phase of fringes; Λ is grating period; L is the length of the connecting section. The phase of the fringes is only dependent on the grating period and the length of the connecting section. The change of external RI only affects the effective RI of the cladding mode, and therefore doesn't affect the phase. The fringes and envelope shift with external RI at the same rate. When the temperature over the whole LPGMZI changes homogeneously, the fringes and envelope shift with temperature at the same rate, which matches the previous results [232]. When the temperature changes, the working conditions of the two LPGs change. The effective RIs of both cladding mode and core mode change with temperature, but they don't affect the phase of fringes. The length of the connecting section (L) and the grating period (Λ) increase with temperature due to thermal expansion, but the phase doesn't change. A detailed derivation is available in Appendix J. Therefore, fringes and envelope shift with temperature at the same rate. The external RI on the surface of the functionalized connecting section increases when more IgM is bound, and the two LPGs are placed in air. In this case, the envelope doesn't shift but the fringes shift with IgM concentration. The response to IgM decreases when temperature increases. It is most likely because the binding strength between IgM and its bio-receptor gets weaker with an increasing temperature [239]. The linear range of the sensor is 0 to 80μg/ml. IgM concentration ranges from 2.5mg/ml to 4 mg/ml in human serum, it needs to be diluted by 30 folds with Tris buffer to fit the linear range. The selectivity of the sensor is 18.48. It has a small response to IgA (~0.007nm) as the anti-IgM can bind to IgA (Material data sheet). The LoD of the sensor is 15µg/ml and RSD is 27.33%. As the envelope of an LPGMZI changes with external RI and temperature at the same rate as the fringes, it can be used as a reference to compensate for the unexpected fluctuations of the interfering source by simply subtracting envelope's wavelength shift from fringes' wavelength shift. However, there is nonspecific binding between IgM and the LPG [240], which affects the envelope as well if the whole LPGMZI is immersed in the IgM sample (Appendix K). The main characteristics of a few previously developed IgM sensors are listed in Table 7-1 for comparison. The selectivity of the IgM sensor developed in this chapter has comparable selectivity to the IgM sensor based on a single LPG developed in Chapter 5. The two sensors are fabricated with the same bio-receptor, which has cross-sensitivity to human IgA (Appendix G). The strength is around 5% of the reaction to human IgM. The selectivity of the sensor is approximately 15.5% higher than localized surface plasmon resonance (LSPR) based sensor [241], and 30% higher than a whispering-gallery-mode (WGM) microsphere based sensor [242]. The high selectivity is most likely due to the contributions of surface functionalization protocol. The anti-IgM is immobilized on the surface of connecting section with Glutaraldehyde. The connecting section is immersed in anti-IgM solution for 2 hours to immobilize it. All the binding sites on the surface of LPGMZI are occupied by the anti-IgM. The LSPR-based sensor is also made using Glutaraldehyde, but it was based on a gold film, which might degrade the quality of surface functionalization. The WGM-microsphere-based sensor is fabricated by physically absorbing the bio-receptor, which might lead to a lower surface coverage of bio-receptor. The reproducibility of the sensor doesn't satisfy the requirements for PoC devices, which need the RSD to be less than 10%. A detailed investigation on the surface functionalization can help improve the reproducibility as explained in Section 5.6. The requirements on selectivity are not found from literature. The sensor can be tested in clinical trials to evaluate its overall performance. The IgM sensors generally have too high RSD to satisfy the requirements of PoC devices [218], it might be a result of the complexity of bio-/chemical processes.

Platform	**LoD**	**Selectivity**	**Experimentally Measured Range**	**Linear Range**	**RSD**	**Reference**
LPG	7.02µg/ml	15.25	10µg/ml-320µg/ml	0-80µg/ml	62.4%	This work Chapter V
LSPR on substrate	1µg/ml	~16	1µg/ml-100µg/ml	1µg/ml-100µg/ml	18.9%	[241]
WGM microsphere	2µg/ml	~14.2	1µg/ml-100µg/ml	1µg/ml-10µg/ml	75%	[242]
LPG	15pg/mm^2	Not Stated	15.6µg/ml-1mg/ml	Not Stated	Not Stated	[30]
LPGMZI	15µg/ml	18.48	20µg/ml-320µg/ml	0-80µg/ml	27.33%	This work

Table 7- 1. The characteristics of IgM sensors.

7.5 Conclusion

An LPGMZI is investigated in this chapter. It is made by fabricating two identical LPGs in series. An LPMZI can respond to external RI in two different ways: i) if the external RI changes over the whole LPGMZI, the fringes and its envelope shift with external RI at same rate of 94.62nm/RIU; ii) if the external RI only changes over the connecting section, the fringes shift with sensitivity of 75.44nm/RIU, and the envelope doesn't have wavelength shift. When the temperature over the whole LPGMZI changes homogeneously, the fringes and envelope shift with temperature at the same rate of 0.394nm/°C. The IgM sensor based on LPGMZI has an LoD of 15µg/ml, a linear range from 0 to 80µg/ml, an RSD of 27.33%, and a selectivity of 18.48. The selectivity of the sensor is comparable with the IgM based on a single LPG developed in Chapter 5 and is 15.5% and 30% higher than LSPR-based sensor and WGM-microsphere-based sensor. The response to IgM decreases when the temperature increases. The envelope of an LPGMZI can be used as reference to monitor fluctuations of external RI and temperature. The unexpected fluctuations of these two interfering sources can be compensated by subtracting the envelope's wavelength shift from the fringes' wavelength shift. However, in practice, the nonspecific binding between biomolecules and bare LPG can affect the envelope as well if the whole LPGMZI is immersed in the sample. Therefore, more work needs to be done to prevent nonspecific binding between biomolecules and the bare LPG, such as depositing a film of poly (ethylene glycol, PEG) on the LPGs [243]

Chapter 8. Conclusion and Future Work

8.1 Conclusion

The relationships between the optical properties of LPGs and their transmission spectra are investigated, and human IgG, IgA, and IgM sensors are fabricated and characterized in this work.

An LPG works at PMC when the grating period line intersects the resonance curve at its maxima (Chapter 4). A U-shape attenuation band appears in the LPG's transmission spectrum. By increasing or decreasing the grating period, the grating period line has zero or two intersections with resonance curve. The U-shape attenuation band splits into two narrower bands or gets shallower. The resonance curves move to longer wavelengths in five scenarios: i) the cladding diameter increases; ii) the RI of cladding increases; iii) the core diameter decreases; iv) the RI of core decreases; v) the external RI increases. If the parameters change in opposite ways, the resonance curves move to shorter wavelengths. These parameters are possible to vary during the manufacturing of optical fibre, which affects the fabrication of LPGs. By amending the grating period, an LPG working around PMC can be fabricated in an optical fibre with deviated parameters although the positions of attenuation bands can shift from their original positions (LPG fabricated in optical fibre with original parameters). The inter-batch deviations of optical fibre's parameters can be compensated by this approach. The attenuation bands have higher sensitivity to the change of external RI in terms of their wavelength shifts when an LPG works closer to PMC. In this case the intersections of grating period and resonance curve moves with higher rates in wavelengths. The two attenuation bands move oppositely as external RI increases, with the separation between them getting larger. An LPG with different coatings is tested in different external RI ranging from 1.3326 to 1.3734. A bare LPG can detect the change of external RI with sensitivity of approximately 332.8nm/RIU. An LPG with two layers PAH/SiNPs coatings has sensitivity of approximately 370.8nm/RIU. LPG with $(PAH/SiNPs)_2/AuNPs$ coatings has sensitivity of approximately 464.9nm/RIU. LPG with BSA immobilized on the surface using Glutaraldehyde has sensitivity of approximately 335.1nm/RIU. The bare LPG can respond to temperature change with sensitivity of approximately 1.1nm/°C in the range of 25°C to 30°C.

Human IgA, IgG, and IgM sensors are developed based on single LPGs (Chapter 5). IgA, IgG, and IgM are measured in the range of 10μg/ml to 200μg/ml, 10μg/ml to

90μg/ml, and 10μg/ml to 320μg/ml respectively. They are fabricated with the method of LbL-aided crosslinking with 11-MUA/EDC/NHS. The IgA sensor has an LoD of 8.59μg/ml, a selectivity of 30.67, a linear range between 0 and 30μg/ml and an RSD of 17.9%. The IgG sensor has an LoD of 7.38μg/ml and a selectivity of 18.45, with some cross-sensitivity to human IgM. Its linear range is between 0 and 90μg/ml, and RSD is 30.3%. The IgM sensor has an LoD of 7.02μg/ml and selectivity of 15.25, with some cross-sensitivity to human IgG. The linear range is between 0 and 80μg/ml. The RSD is 62.4%. The work in Chapter 5 proves the feasibility of developing IgA, IgG, and IgM sensor based on LPGs by the method of LbL-aided crosslinking with 11-MUA/EDC/NHS. Real sample (human serum) needs to be diluted by 100 folds, 200 folds, and 30 folds to fit the linear ranges of IgA sensor, IgG sensor, and IgM sensor respectively.

A set of sensors to detect IgG-type related M proteins is developed based on single LPGs with Glutaraldehyde (Chapter 6). They are an IgG$_\kappa$ sensor, an IgG$_\lambda$ sensor, and a whole IgG sensor. IgG$_\kappa$ and IgG$_\lambda$ are measured in the range of 5μg/ml to 40μg/ml. The IgG$_\kappa$ sensor has an LoD of 3.8μg/ml, a selectivity of 9.73, and linear range between 0 and 20μg/ml, and an RSD of 46.1%. It has cross-sensitivity to IgG$_\lambda$. The IgG$_\lambda$ sensor has an LoD of 3.77μg/ml, a selectivity of 29.7, a linear range between 0 and 20μg/ml, and an RSD of 40.3%. The whole IgG sensor responds to both IgG$_\kappa$ and IgG$_\lambda$ with LoD of 3.63μg/ml and 3.73μg/ml respectively. Its linear range is between 0 and 20μg/ml. The RSDs for IgG$_\kappa$ measurement and IgG$_\lambda$ measurement are 35.4% and 42% respectively. The whole IgG sensor can be used to tell if IgG exceeds normal value. IgG$_\kappa$ and IgG$_\lambda$ sensor can be used to tell if it's IgG$_\kappa$ or IgG$_\lambda$ M protein. The concentration of M protein in plasma cell dyscrasias patients' serum reaches 30mg/ml. It needs to be diluted by 1500 folds to fit sensors' linear ranges.

An LPGMZI is made by fabricating two identical LPGs in series in a single optical fibre. The lengths of the two LPGs are 2cm. The separation between them is 6cm. The interference pattern is present in the transmission spectrum due to the interference between core mode and cladding mode. There is a local minimum at 45.45nm^{-1} in the frequency domain of the transmission spectrum. Low-pass filter with cut-off of 45.45nm^{-1} is applied to acquire envelope. The LPGMZI respond to the change of external RI in the range of 1.3326 to 1.3734 in two different ways: i) if the whole LPGMZI is immersed, the fringes and envelope shift with external RI at the same rate of 94.63nm/RIU; ii) if only the connecting section is immersed, the fringes shift with external RI at a rate of 75.44nm/RIU, while the envelope doesn't shift in wavelength. When the temperature changes homogeneously over the whole LPGMZI in the range of 25°C to 30°C, the envelope and fringes shift at the same rate of 0.394nm/°C. An IgM sensor is fabricated by immobilizing anti-IgM on the connecting section with Glutaraldehyde. It measures IgM in the range of 20μg/ml to 320μg/ml with an LoD of 15μg/ml, a selectivity of 18.48, a linear range between 0 and 80μg/ml, and an RSD of 27.33%. Human serum needs to be diluted by 30 folds to make IgM concentration fit the sensor's linear range. The sensitivity of the sensor decreases with increasing temperature.

The main characteristics of the sensors developed in this work are listed in Table 8-1. Human serum needs to be diluted to make the analytes' concentration fit the linear ranges of the sensors. After reviewing literatures, it can be concluded that optical-fibre antibody sensors' detection ranges are much lower than the analytes' concentration in human serum. Therefore, from a practical standpoint, there is no need to keep improving the sensitivity of the sensors. Instead, more work can be done to improve the reproducibility and reliability of sensors and save labour during sensor fabrication process. For example, an automatic LPG-immersion machine with environmental control can be designed for the surface functionalization which is hoped to reduce the error caused by manual operation; More technologies such as Raman spectroscopy and X-ray photoelectron spectroscopy can be introduced to investigate the surface functionalization process [37], [219]; The selectivity tests on the sensors show that sensors have higher response to their target analytes than to interfering substance, which is vital for giving reliable results. Considering concrete requirements on selectivity are not found and the complexity of the compositions in real samples, evaluating the sensors in real clinical environment with a large number of samples is a feasible approach to assess the sensors' reliability and validate them for clinical use.

Platform	**Chapter**	**Analyte**	**Experimentally Measured Range**	**LoD**	**RSD**	**Linear Range**	**Selectivity**
LPG	5	IgA	10μg/ml-200μg/ml	8.59μg/ml	17.9%	0-30μg/ml (R^2=96.72%)	30.67 (against IgG and IgM)
LPG	5	IgG	10μg/ml-90μg/ml	7.38μg/ml	30.3%	0-90μg/ml (R^2=97.19%)	18.45 (against IgM)

LPG	5	IgM	10µg/ml-320µg/ml	7.02µg/ml	62.4%	0-80µg/ml (R^2=95.58%)	15.25 (against IgA)
LPG	6	IgG_{κ}	5µg/ml-40µg/ml	3.8µg/ml	46.1%	0-20µg/ml (R^2=95.58%)	9.73(against IgG_{λ})
LPG	6	IgG_{λ}	5µg/ml-40µg/ml	3.77µg/ml	40.3%	0-20µg/ml (R^2=95.58%)	29.7(against IgG_{κ})
LPG	6	IgG_{κ}	5µg/ml-40µg/ml	3.63µg/ml	35.4%	0-20µg/ml (R^2=95.58%)	Can't distinguish IgG_{κ} and IgG_{λ}
	6	IgG_{λ}	5µg/ml-40µg/ml	3.73µg/ml	42%	0-20µg/ml (R^2=95.58%)	
LPGMZI	7	IgM	20µg/ml-320µg/ml	15µg/ml	27.33%	0-80µg/ml (R^2=96.97%)	18.48 (against IgA)

Table 8- 1. The characteristics of the sensors developed in this work.

8.2 Future work

The feasibility of designing human antibodies sensors based on LPGs has been proven in this work. All the sensors developed in this work has sufficient sensitivity to detect human antibodies from human serum. The sensors can be improved in three aspects: i) further investigating and improving the sensors' characteristics (reproducibility, selectivity, LoD, linear range, miniaturisation, reliability, and robustness); ii) developing more application scenarios of the sensors; iii) evaluating sensors. The relationships among the three modules are illustrated in Figure 8-1. Module i) and Module ii) facilitate each other. With improved sensors' characteristics, they can be applied to different areas. The sensors should be improved as per the requirements of applications. The designed sensor prototypes need to be evaluated (Module iii)) with a large number of samples in real application environment. If the sensors' performance doesn't satisfy the requirements, the characteristics of the sensors need to be improved with the information acquired in Module iii).

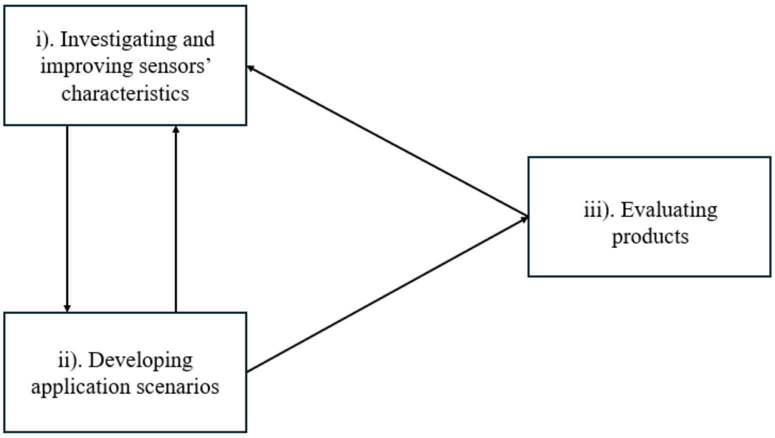

Figure 8-1 Relationship among three approaches to improve LPG-based antibody sensors

As stated in Section 8.1, the antibody sensors developed in this work are sensitive enough to measure target analytes from human serum. The reproducibility and selectivity of the sensors is influenced by the complexity of bio-/chemical process. It needs to be evaluated in real application environments to confirm if the reproducibility is sufficient or not. In general, to improve the whole reproducibility and reliability of antibody sensors, the quality of each single fabrication step needs to be controlled. Two objectives need to be achieved: i) Developing a methodology to analyse the functional groups on the surface of LPGs; ii) Designing an automatic LPG-immersion machine with environmental control to reduce the error cause by manual operation and environmental fluctuations during surface functionalization. Raman spectroscopy and X-ray photoelectron spectroscopy have been applied to investigate the surface composition of biosensors [31], [244]. Both methods can be used to acquire quantitative information which is related to the density of specific functional groups [245], [246], [247]. It is helpful to collaborate with chemists to apply these chemical analysis techniques to the investigation of surface functionalization of LPGs. The density and uniformity of target functional groups are the information of the highest interest. An automatic LPG-immersion system can be designed to inject and pump out solution to LPG fibre bath with a constant flow rate. The error caused by manual operation can be minimized by this approach. Temperature plays an important role in chemical process. Therefore, the automatic system should have a temperature control. Given that APTES is used to generate amine groups on the surface of an LPG, which is affected by humidity [248]. The automatic system is hoped to be able to maintain humidity. The selectivity of sensors is highly dependent on the quality of bio-receptors. It is helpful to collaborate with biologist and chemist to develop bio-receptors with high specificity to target analytes. Being miniaturized and robust is vital to its potential to be developed as PoC sensors. PoC sensors need to work in non-laboratory environments such as home and office. There might not be space for bulky equipment. Therefore, it would be good if sensors can be miniaturized. Being resistant to hazardous environments reduce the cost of packaging and transportation, which improve PoC sensors' accessibility to public. The sensors developed in this work use a halogen tungsten light source and spectrometer, which can be replaced by light emitting diode (LED) and photodiode [249]. A photodiode detects the change of light intensity. Therefore, the antibody sensors need to be calibrated to get the relationship between analytes' concentration and intensity change. An LPG is fragile as its diameter is only 125μm. Integrating LPG with microfluidic chip can make it more robust, which can protect it from being mechanically damaged. Microfluidic chips contain network of microchannels. LPG can be placed in a microchannel and solution to be analysed is added to the microchannel [250].

Applying LPG-based antibody sensors to different scenarios is dependent on the development of different industries such as medicine and healthcare. PoC diagnostic devices play an important role in public health [251]. They can help screen people with infectious diseases and suppress the transmission [251]. Recalling the COVID-19 pandemic during 2020 and 2022, screening virus carriers is an important part of public management. LFA is a widely used platform to develop PoC devices. Comparing to LFA, LPG-based sensors are more fragile and need a spectrometer as interrogation device. Biochips, which are also called 'Lab on chip'. They are used to investigate bio-/chemical processes [252]. Combining LPG-based sensors with biochips is a promising direction. For example, an immunological chip helps people understand the function of human immune system [253]. It needs a module on the chip for biomarker analysis. LPG-based sensors have small sizes, which makes them suitable to be integrated onto biochips. Some biochips use LFA to do biomarker analysis [252]. It might because LFA is more accessible than LPG-based sensors. To integrate LPG-based sensors onto biochips, engineers need to collaborate with biologists. Precision medicine can design personalized treatment for people to minimize the effects of individual variability [254]. Implantable bio-/chemical sensors facilitate precision medicine by implementing in-vivo measurement of biomarkers and providing more real-time information [255].

LPG-based sensors are small in dimension, and it has been proven that LPG-based sensors can work in reflection-mode by depositing a reflective film on the tip (Appendix). An IgG sensor based on reflection-mode LPG achieves a linear range of 0 to 80μg/ml, an LoD of 15.39, and an RSD of 32.7%. LPG-based sensors working in reflection mode is suitable to be implanted. Besides sensors' characteristics, many other factors need to be considered to develop and promote implantable biosensors such as ethics and social impacts.

Due to the complexity of bio-/chemical process, the products need to be evaluated in real application environments. As different application has different requirements, it's better to have different specialists to take part in the evaluation such as doctors, engineers, statisticians, biologists, and chemists. They can help design protocol, set criteria, analyse results, and provide advice for further improvement. When evaluating a diagnostic device, diagnostic sensitivity and specificity are two important characteristics [256]. They reflect a sensor's capability to give correct results. If the sensor's performance doesn't satisfy the requirements, it'll be helpful if the samples can be analysed my more sophisticated tools or equipment. For example, a detailed composition analysis on the samples can help figure out if the sensor has cross-sensitivity to any substances in the sample. The information can be used to improve the sensor.

References

[1]. S. V. Rajkumar and S. Kumar, "Multiple myeloma: diagnosis and treatment," in *Mayo Clinic Proceedings*, 2016, vol. 91, no. 1: Elsevier, pp. 101-119.

[2]. Y. F. Wang and M. Kobayashi, "Antibody detection: Principles and applications," *Advanced Techniques in Diagnostic Microbiology,* pp. 53-73, 2012.

[3]. K. Nothelfer, P. J. Sansonetti, and A. Phalipon, "Pathogen manipulation of B cells: the best defence is a good offence," *Nature Reviews Microbiology,* vol. 13, no. 3, pp. 173-184, 2015.

[4]. D. Hames and N. Hooper, *BIOS Instant Notes in Biochemistry*. Taylor & Francis, 2004.

[5]. R. W. Peeling *et al.*, "Evaluation of diagnostic tests: dengue," *Nature Reviews Microbiology,* vol. 8, no. Suppl 12, pp. S30-S37, 2010.

[6]. S. M. Wang and S. D. Sekaran, "Early diagnosis of Dengue infection using a commercial Dengue Duo rapid test kit for the detection of NS1, IGM, and IGG," *The American journal of tropical medicine and hygiene,* vol. 83, no. 3, p. 690, 2010.

[7]. S. A. Ejazi, S. Ghosh, and N. Ali, "Antibody detection assays for COVID-19 diagnosis: an early overview," *Immunology and cell biology,* vol. 99, no. 1, pp. 21-33, 2021.

[8]. J. Van Elslande *et al.*, "Diagnostic performance of seven rapid IgG/IgM antibody tests and the Euroimmun IgA/IgG ELISA in COVID-19 patients," *Clinical Microbiology and Infection,* vol. 26, no. 8, pp. 1082-1087, 2020.

[9]. H. Ma *et al.*, "Serum iga, igm, and igg responses in covid-19," *Cellular & molecular immunology,* vol. 17, no. 7, pp. 773-775, 2020.

[10]. https://www.southtees.nhs.uk/services/pathology/tests/immunoglobulins-igg-iga-igm/, accessed 27/Jan/2024.

[11]. T. Morrison, R. A. Booth, K. Hauff, P. Berardi, and A. Visram, "Laboratory assessment of multiple myeloma," *Advances in clinical chemistry,* vol. 89, pp. 1-58, 2019.

[12]. K. A. Udd, T. M. Spektor, and J. R. Berenson, "Monitoring multiple myeloma," *Clin Adv Hematol Oncol,* vol. 15, no. 12, pp. 951-961, 2017.

[13]. K. Shah and P. Maghsoudlou, "Enzyme-linked immunosorbent assay (ELISA): the basics," *British journal of hospital medicine,* vol. 77, no. 7, pp. C98-C101, 2016.

[14]. B. T. Kurien and R. H. Scofield, "Western blotting," *Methods,* vol. 38, no. 4, pp. 283-293, 2006.

[15]. J. Homola, S. S. Yee, and G. Gauglitz, "Surface plasmon resonance sensors," *Sensors and actuators B: Chemical,* vol. 54, no. 1-2, pp. 3-15, 1999.

[16]. R. Hnasko, *Elisa*. Springer, 2015.

[17]. N. Rafat, L. Brewer, N. Das, D. J. Trivedi, B. K. Kaszala, and A. Sarkar, "Inexpensive high-throughput multiplexed biomarker detection using enzymatic metallization with cellphone-based computer vision," *ACS sensors,* vol. 8, no. 2, pp. 534-542, 2023.

[18]. X. Hu, X. Gao, S. Chen, J. Guo, and Y. Zhang, "DropLab: an automated magnetic digital microfluidic platform for sample-to-answer point-of-care testing—development and application to quantitative immunodiagnostics," *Microsystems & Nanoengineering,* vol. 9, no. 1, p. 10, 2023.

[19]. B. T. Kurien and R. H. Scofield, "Western blotting: an introduction," *Western blotting: Methods and protocols,* pp. 17-30, 2015.

[20]. G. H. Meftahi, Z. Bahari, A. Zarei Mahmoudabadi, M. Iman, and Z. Jangravi, "Applications of western blot technique: From bench to bedside," *Biochemistry and Molecular Biology Education,* vol. 49, no. 4, pp. 509-517, 2021.

[21]. T. Mahmood and P.-C. Yang, "Western blot: technique, theory, and trouble shooting," *North American journal of medical sciences,* vol. 4, no. 9, p. 429, 2012.

[22]. N. E. Arvin, M. Dawod, D. T. Lamb, J. P. Anderson, M. D. Furtaw, and R. T. Kennedy, "Fast immunoassay for microfluidic western blotting by direct deposition of reagents onto capture membrane," *Analytical Methods,* vol. 12, no. 12, pp. 1606-1616, 2020

[23]. R. P. Kooyman *et al.*, *Handbook of surface plasmon resonance*. Royal Society of Chemistry, 2008.

[24]. T. Allsop and R. Neal, "A review: Evolution and diversity of optical fibre plasmonic sensors," *Sensors,* vol. 19, no. 22, p. 4874, 2019.

[25]. M. Sajid, A.-N. Kawde, and M. Daud, "Designs, formats and applications of lateral flow assay: A literature review," *Journal of Saudi Chemical Society,* vol. 19, no. 6, pp. 689-705, 2015.

[26]. P.-Y. Chen *et al.*, "The early detection of immunoglobulins via optical-based lateral flow immunoassay platform in COVID-19 pandemic," *PLoS One,* vol. 16, no. 7, p. e0254486, 2021.

[27]. G. Keiser, *Optical fiber communications*. McGraw-Hill New York, 2000.

[28]. R. Correia, S. James, S. Lee, S. Morgan, and S. Korposh, "Biomedical application of optical fibre sensors," *Journal of Optics,* vol. 20, no. 7, p. 073003, 2018.

[29]. V. Sai, T. Kundu, C. Deshmukh, S. Titus, P. Kumar, and S. Mukherji, "Label-free fiber optic biosensor based on evanescent wave absorbance at 280 nm," *Sensors and Actuators B: Chemical,* vol. 143, no. 2, pp. 724-730, 2010.

[30]. L. Liu *et al.*, "Highly sensitive label-free antibody detection using a long period fibre grating sensor," *Sensors and Actuators B: Chemical,* vol. 271, pp. 24-32, 2018.

[31]. Q. Wang and B.-T. Wang, "Surface plasmon resonance biosensor based on graphene oxide/silver coated polymer cladding silica fiber," *Sensors and Actuators B: Chemical,* vol. 275, pp. 332-338, 2018.

[32]. P. Kozma, F. Kehl, E. Ehrentreich-Förster, C. Stamm, and F. F. Bier, "Integrated planar optical waveguide interferometer biosensors: A comparative review," *Biosensors and Bioelectronics,* vol. 58, pp. 287-307, 2014.

[33]. C. Ciminelli, F. Dell'Olio, D. Conteduca, C. Campanella, and M. Armenise, "High performance SOI microring resonator for biochemical sensing," *Optics & laser technology,* vol. 59, pp. 60-67, 2014.

[34]. D. Grieshaber, R. MacKenzie, J. Vörös, and E. Reimhult, "Electrochemical biosensors-sensor principles and architectures," *Sensors,* vol. 8, no. 3, pp. 1400-1458, 2008.

[35]. Y. Yang, Y. Tu, X. Wang, J. Pan, and Y. Ding, "A label-free immunosensor for ultrasensitive detection of ketamine based on quartz crystal microbalance," *Sensors,* vol. 15, no. 4, pp. 8540-8549, 2015.

[36]. S. W. James and R. P. Tatam, "Optical fibre long-period grating sensors: characteristics and application," *Measurement science and technology,* vol. 14, no. 5, p. R49, 2003.

[37]. C. Liu *et al.*, "Graphene oxide functionalized long period grating for ultrasensitive label-free immunosensing," *Biosensors and Bioelectronics,* vol. 94, pp. 200-206, 2017.

[38]. P. Chen, N. T. Tran, X. Wen, Q. Xiong, and B. Liedberg, "Inflection point of the localized surface plasmon resonance peak: a general method to improve the sensitivity," *ACS sensors,* vol. 2, no. 2, pp. 235-242, 2017.

[39]. B.-T. Wang and Q. Wang, "An interferometric optical fiber biosensor with high sensitivity for IgG/anti-IgG immunosensing," *Optics Communications,* vol. 426, pp. 388-394, 2018.

[40]. M. S. Cano-Velázquez, L. M. López-Marín, and J. Hernández-Cordero, "Fiber optic interferometric immunosensor based on polydimethilsiloxane (PDMS) and bioactive lipids," *Biomedical Optics Express,* vol. 11, no. 3, pp. 1316-1326, 2020.

[41]. P. Lydyard, A. Whelan, and M. Fanger, *BIOS Instant notes in immunology*. Taylor & Francis, 2011.

[42]. L. W. Schindler, *Understanding the immune system* (no. 93). Diane Publishing, 1993.

[43]. J. H. Duarte, "Functional switching," *Nature immunology,* vol. 17, no. Suppl 1, pp. S12-S12, 2016.

[44]. W. B. Allan, *Fibre optics: theory and practice*. Springer Science & Business Media, 2012.

[45]. R. Y.-N. Wong, D. H. J. Juan, M. Ibsen, and P. P. Shum, "Optical fibre long-period grating sensors operating at and around the phase matching turning point," *Applications of Optical Fibers for Sensing,* vol. 1, 2019.

[46]. F. Esposito, "Chemical sensors based on long period fiber gratings: A review," *Results in Optics,* vol. 5, p. 100196, 2021.

[47]. T. Erdogan, "Cladding-mode resonances in short-and long-period fiber grating filters," *JOSA A,* vol. 14, no. 8, pp. 1760-1773, 1997.

[48]. T. Erdogan, "Fiber grating spectra," *Journal of lightwave technology,* vol. 15, no. 8, pp. 1277-1294, 1997.

[49]. D. Savastru, S. Miclos, M. Tautan, I. Lancranjan, N. Akbar, and B. OA, "Numerical simulation methods applied at fiber grating sensors design," in *Modeling and Simulation in Engineering Sciences*: IntechOpen, 2016.

[50]. M. P. Sehgal and M. H. Dua, "Designing of a Long Period Fiber Grating (LPFG) Using Optigrating Simulation Software," 2015.

[51]. B. H. Lee, Y. Liu, S. B. Lee, S. S. Choi, and J. N. Jang, "Displacements of the resonant peaks of a long-period fiber grating induced by a change of ambient refractive index," *Optics Letters,* vol. 22, no. 23, pp. 1769-1771, 1997.

[52]. L. Alwis, T. Sun, and K. Grattan, "Developments in optical fibre sensors for industrial applications," *Optics & Laser Technology,* vol. 78, pp. 62-66, 2016.

[53]. S. Tabassum and R. Kumar, "Advances in fiber-optic technology for point-of-care diagnosis and in vivo biosensing," *Advanced Materials Technologies,* vol. 5, no. 5, p. 1900792, 2020.

[54]. J. Fraden and J. King, *Handbook of modern sensors: physics, designs, and applications*. Springer, 2004.

[55]. L. Liu, F. Hao, S. P. Morgan, R. Correia, A. Norris, and S. Korposh, "A reflection-mode fibre-optic sensor for breath carbon dioxide measurement in healthcare," *Sensing and Bio-Sensing Research,* vol. 22, p. 100254, 2019.

[56]. C. He, L. Liu, S. Korposh, R. Correia, and S. P. Morgan, "Volatile organic compound vapour measurements using a localised surface plasmon resonance optical fibre sensor decorated with a metal-organic framework," *Sensors,* vol. 21, no. 4, p. 1420, 2021.

[57]. L. Liu, S. P. Morgan, R. Correia, S.-W. Lee, and S. Korposh, "Multi-parameter optical fiber sensing of gaseous ammonia and carbon dioxide," *Journal of Lightwave Technology,* vol. 38, no. 7, pp. 2037-2045, 2020.

[58]. L. Liu, S. Korposh, D. Gomez, R. Correia, B. R. Hayes-Gill, and S. P. Morgan, "Localised plasmonic hybridisation mode optical fibre sensing of relative humidity," *Sensors and Actuators B: Chemical,* vol. 353, p. 131157, 2022.

[59]. C. He, S. Korposh, R. Correia, L. Liu, B. R. Hayes-Gill, and S. P. Morgan, "Optical fibre sensor for simultaneous temperature and relative humidity measurement: Towards absolute humidity evaluation," *Sensors and Actuators B: Chemical,* vol. 344, p. 130154, 2021.

[60]. M. S. Soares *et al.*, "Immunosensing based on optical fiber technology: Recent advances," *Biosensors,* vol. 11, no. 9, p. 305, 2021.

[61]. A. J. Y. Tan, S. M. Ng, P. R. Stoddart, and H. S. Chua, "Theoretical model and design considerations of U-shaped fiber optic sensors: A review," *IEEE Sensors Journal,* vol. 20, no. 24, pp. 14578-14589, 2020.

[62]. A. J. Y. Tan, S. M. Ng, P. R. Stoddart, and H. S. Chua, "Trends and applications of U-shaped fiber optic sensors: a review," *IEEE Sensors Journal,* vol. 21, no. 1, pp. 120-131, 2020.

[63]. Z. Tang *et al.*, "A U-shape fibre-optic pH sensor based on hydrogen bonding of ethyl cellulose with a sol-gel matrix," *Journal of Lightwave Technology,* vol. 39, no. 5, pp. 1557-1564, 2021.

[64]. F. U. Hernandez *et al.*, "U-shape functionalized optical fibre sensors for measurement of anaesthetic propofol," *Sensors and Actuators B: Chemical,* vol. 372, p. 132653, 2022.

[65]. S. Ahmed, Y. Park, H. Okuda, S. Ono, S. Korposh, and S.-W. Lee, "Fabrication of humidity-resistant optical fiber sensor for ammonia sensing using diazo resin-photocrosslinked films with a porphyrin-polystyrene binary mixture," *Sensors,* vol. 21, no. 18, p. 6176, 2021.

[66]. M. Hernaez, A. G. Mayes, and S. Melendi-Espina, "Lossy mode resonance generation by graphene oxide coatings onto cladding-removed multimode optical fiber," *IEEE Sensors Journal,* vol. 19, no. 15, pp. 6187-6192, 2019.

[67]. I. Del Villar *et al.*, "Sensors Based on Thin-Film Coated Cladding Removed Multimode Optical Fiber and Single-Mode Multimode Single-Mode Fiber: A Comparative Study," *Journal of Sensors,* vol. 2015, no. 1, p. 763762, 2015.

[68]. J. M. Corres, I. D. Villar, F. J. Arregui, and I. R. Matias, "Analysis of lossy mode resonances on thin-film coated cladding removed plastic fiber," *Optics letters,* vol. 40, no. 21, pp. 4867-4870, 2015.

[69]. A. Abdelghani, J. Chovelon, N. Jaffrezic-Renault, C. Ronot-Trioli, C. Veillas, and H. Gagnaire, "Surface plasmon resonance fibre-optic sensor for gas detection," *Sensors and Actuators B: Chemical,* vol. 39, no. 1-3, pp. 407-410, 1997.

[70]. A. K. C. Theoderaj, D. J. Inbaraj, and C. Mangalaraj, "CdS coated clad-modified fiber optic sensor for detection of NO2 gas," *Materials Research Express,* vol. 6, no. 10, p. 1050c8, 2019.

[71]. S. Manivannan, A. Saranya, B. Renganathan, D. Sastikumar, G. Gobi, and K. C. Park, "Single-walled carbon nanotubes wrapped poly-methyl methacrylate fiber optic sensor for ammonia, ethanol and methanol vapors at room temperature," *Sensors and Actuators B: Chemical,* vol. 171, pp. 634-638, 2012.

[72]. B.-C. Deboux, E. Lewis, P. J. Scully, and R. Edwards, "A novel technique for optical fiber pH sensing based on methylene blue adsorption," *Journal of lightwave technology,* vol. 13, no. 7, pp. 1407-1414, 1995.

[73]. S. Korposh, S. W. James, S.-W. Lee, and R. P. Tatam, "Tapered optical fibre sensors: Current trends and future perspectives," *Sensors,* vol. 19, no. 10, p. 2294, 2019.

[74]. M. M. Alkhabet *et al.*, "Room temperature operated hydrogen sensor using palladium coated on tapered optical fiber," *Materials Science and Engineering: B,* vol. 287, p. 116092, 2023.

[75]. D. Tiwari, K. Mullaney, S. Korposh, S. W. James, S.-W. Lee, and R. P. Tatam, "An ammonia sensor based on Lossy Mode Resonances on a tapered optical fibre coated with porphyrin-incorporated titanium dioxide," *Sensors and Actuators B: Chemical,* vol. 242, pp. 645-652, 2017.

[76]. M. Majumder, T. K. Gangopadhyay, A. K. Chakraborty, K. Dasgupta, and D. K. Bhattacharya, "Fibre Bragg gratings in structural health monitoring—Present status and applications," *Sensors and Actuators A: Physical,* vol. 147, no. 1, pp. 150-164, 2008.

[77]. C. Shi, Z. Tang, H. Zhang, and Y. Liu, "Development of an FBG-based wearable sensor for simultaneous respiration and heartbeat measurement," *IEEE Transactions on Instrumentation and Measurement,* vol. 72, pp. 1-9, 2022.

[78]. L. Li *et al.*, "Embedded FBG-based sensor for joint movement monitoring," *IEEE Sensors Journal,* vol. 21, no. 23, pp. 26793-26798, 2021.

[79]. J. Janting, J. K. Pedersen, G. Woyessa, K. Nielsen, and O. Bang, "Small and robust all-polymer fiber Bragg grating based pH sensor," *Journal of Lightwave Technology,* vol. 37, no. 18, pp. 4480-4486, 2019.

[80]. J. Albert, L. Y. Shao, and C. Caucheteur, "Tilted fiber Bragg grating sensors," *Laser & Photonics Reviews,* vol. 7, no. 1, pp. 83-108, 2013.

[81]. X. Dong, H. Zhang, B. Liu, and Y. Miao, "Tilted fiber Bragg gratings: Principle and sensing applications," *Photonic Sensors,* vol. 1, pp. 6-30, 2011.

[82]. C. Zhang *et al.*, "Pd/Au nanofilms based tilted fiber Bragg grating hydrogen sensor," *Optics Communications,* vol. 502, p. 127424, 2022.

[83]. J. Yu, Z. Wu, X. Yang, X. Han, and M. Zhao, "Tilted fiber Bragg grating sensor using chemical plating of a palladium membrane for the detection of hydrogen leakage," *Sensors,* vol. 18, no. 12, p. 4478, 2018.

[84]. Y.-D. Chiu, C.-W. Wu, and C.-C. Chiang, "Tilted fiber Bragg grating sensor with graphene oxide coating for humidity sensing," *Sensors,* vol. 17, no. 9, p. 2129, 2017.

[85]. A. L. Aldaba, Á. González-Vila, M. Debliquy, M. Lopez-Amo, C. Caucheteur, and D. Lahem, "Polyaniline-coated tilted fiber Bragg gratings for pH sensing," *Sensors and Actuators B: Chemical,* vol. 254, pp. 1087-1093, 2018.

[86]. J. Hromadka, B. Tokay, R. Correia, S. P. Morgan, and S. Korposh, "Carbon dioxide measurements using long period grating optical fibre sensor coated with metal organic framework HKUST-1," *Sensors and Actuators B: Chemical,* vol. 255, pp. 2483-2494, 2018.

[87]. Y. Wang, Y. Liu, F. Zou, C. Jiang, C. Mou, and T. Wang, "Humidity sensor based on a long-period fiber grating coated with polymer composite film," *Sensors,* vol. 19, no. 10, p. 2263, 2019.

[88]. Y.-P. Wang and Y.-J. Rao, "A novel long period fiber grating sensor measuring curvature and determining bend-direction simultaneously," *IEEE Sensors Journal,* vol. 5, no. 5, pp. 839-843, 2005.

[89]. Q. Wang, C. Du, J. Zhang, R. Lv, and Y. Zhao, "Sensitivity-enhanced temperature sensor based on PDMS-coated long period fiber grating," *Optics Communications,* vol. 377, pp. 89-93, 2016.

[90]. C. Zhu *et al.*, "Advances in fiber-optic extrinsic Fabry–Perot interferometric physical and mechanical sensors: A review," *IEEE Sensors Journal,* vol. 23, no. 7, pp. 6406-6426, 2023.

[91]. C. S. Monteiro *et al.*, "Fiber Fabry-Perot interferometer for curvature sensing," *Photonic Sensors,* vol. 6, pp. 339-344, 2016.

[92]. G. K. Costa *et al.*, "In-fiber Fabry-Perot interferometer for strain and magnetic field sensing," *Optics express,* vol. 24, no. 13, pp. 14690-14696, 2016.

[93]. Y. Huang, T. Wei, Z. Zhou, Y. Zhang, G. Chen, and H. Xiao, "An extrinsic Fabry–Perot interferometer-based large strain sensor with high resolution," *Measurement science and technology,* vol. 21, no. 10, p. 105308, 2010.

[94]. X. Zhou and Q. Yu, "Wide-range displacement sensor based on fiber-optic Fabry–Perot interferometer for subnanometer measurement," *IEEE sensors journal,* vol. 11, no. 7, pp. 1602-1606, 2010.

[95]. J. Xu, G. Pickrell, X. Wang, W. Peng, K. Cooper, and A. Wang, "A novel temperature-insensitive optical fiber pressure sensor for harsh environments," *IEEE Photonics Technology Letters,* vol. 17, no. 4, pp. 870-872, 2005.

[96]. W. Ma *et al.*, "CO_2 Gas Sensing Using Optical Fiber Fabry–Perot Interferometer Based on Polyethyleneimine/Poly (Vinyl Alcohol) Coating," *IEEE Photonics Journal,* vol. 9, no. 3, pp. 1-8, 2017.

[97]. J. S. Santos, I. M. Raimundo Jr, C. M. Cordeiro, C. R. Biazoli, C. A. Gouveia, and P. A. Jorge, "Characterisation of a Nafion film by optical fibre Fabry–Perot

interferometry for humidity sensing," *Sensors and Actuators B: Chemical,* vol. 196, pp. 99-105, 2014.

[98]. H. Fu *et al.*, "High-sensitivity Mach–Zehnder interferometric curvature fiber sensor based on thin-core fiber," *IEEE Sensors Journal,* vol. 15, no. 1, pp. 520-525, 2014.

[99]. V. Bhardwaj, K. Kishor, and A. C. Sharma, "Tapered optical fiber geometries and sensing applications based on Mach-Zehnder Interferometer: A review," *Optical Fiber Technology,* vol. 58, p. 102302, 2020.

[100]. B. H. Lee *et al.*, "Interferometric fiber optic sensors," *sensors,* vol. 12, no. 3, pp. 2467-2486, 2012.

[101]. X. Li *et al.*, "A review of specialty fiber biosensors based on interferometer configuration," *Journal of Biophotonics,* vol. 14, no. 6, p. e202100068, 2021.

[102]. H. Sun, S. Yang, X. Zhang, L. Yuan, Z. Yang, and M. Hu, "Simultaneous measurement of temperature and strain or temperature and curvature based on an optical fiber Mach–Zehnder interferometer," *Optics Communications,* vol. 340, pp. 39-43, 2015.

[103]. S. Gao, C. Ji, Q. Ning, W. Chen, and J. Li, "High-sensitive Mach-Zehnder interferometric temperature fiber-optic sensor based on core-offset splicing technique," *Optical Fiber Technology,* vol. 56, p. 102202, 2020.

[104]. H. Fu *et al.*, "Implementation and characterization of liquid-level sensor based on a long-period fiber grating Mach–Zehnder interferometer," *IEEE sensors journal,* vol. 11, no. 11, pp. 2878-2882, 2011.

[105]. M. Sun, Y. Jin, and X. Dong, "All-fiber Mach–Zehnder interferometer for liquid level measurement," *IEEE Sensors Journal,* vol. 15, no. 7, pp. 3984-3988, 2015.

[106]. P. Mehrotra, "Biosensors and their applications–A review," *Journal of oral biology and craniofacial research,* vol. 6, no. 2, pp. 153-159, 2016.

[107]. A. Haleem, M. Javaid, R. P. Singh, R. Suman, and S. Rab, "Biosensors applications in medical field: A brief review," *Sensors International,* vol. 2, p. 100100, 2021.

[108]. Z. Li *et al.*, "Development and clinical application of a rapid IgM-IgG combined antibody test for SARS-CoV-2 infection diagnosis," *Journal of medical virology,* vol. 92, no. 9, pp. 1518-1524, 2020.

[109]. A. Petherick, "Developing antibody tests for SARS-CoV-2," *The Lancet,* vol. 395, no. 10230, pp. 1101-1102, 2020.

[110]. K. R. Steingart *et al.*, "A systematic review of commercial serological antibody detection tests for the diagnosis of extrapulmonary tuberculosis," *Postgraduate medical journal,* vol. 83, no. 985, pp. 705-712, 2007.

[111]. J. R. Crowther, *The ELISA guidebook*. Springer Science & Business Media, 2008.

[112]. R. B. Schasfoort, *Handbook of surface plasmon resonance*. Royal Society of Chemistry, 2017.

[113]. Y. Xiong, Y. Leng, X. Li, X. Huang, and Y. Xiong, "Emerging strategies to enhance the sensitivity of competitive ELISA for detection of chemical contaminants in food samples," *TrAC Trends in Analytical Chemistry,* vol. 126, p. 115861, 2020.

[114]. A. C. Murphy, M. E. Wechsler, and N. A. Peppas, "Recent advancements in biosensing approaches for screening and diagnostic applications," *Current Opinion in Biomedical Engineering,* vol. 19, p. 100318, 2021.

[115]. K. Iha *et al.*, "Ultrasensitive ELISA developed for diagnosis," *Diagnostics,* vol. 9, no. 3, pp. 78-86, 2019.

[116]. D. T. Mourya *et al.*, "Diagnosis of Kyasanur forest disease by nested RT-PCR, real-time RT-PCR and IgM capture ELISA," *Journal of virological methods,* vol. 186, no. 1-2, pp. 49-54, 2012.

[117]. S. Aydin, "A short history, principles, and types of ELISA, and our laboratory experience with peptide/protein analyses using ELISA," *Peptides,* vol. 72, pp. 4-15, 2015.

[118]. N. Kohmer, S. Westhaus, C. Rühl, S. Ciesek, and H. F. Rabenau, "Clinical performance of different SARS-CoV-2 IgG antibody tests," *Journal of Medical Virology,* vol. 92, no. 10, pp. 2243-2247, 2020.

[119]. D. Zhao, J. Li, C. Peng, S. Zhu, J. Sun, and X. Yang, "Fluorescence immunoassay based on the alkaline phosphatase triggered in situ fluorogenic reaction of o-phenylenediamine and ascorbic acid," *Analytical chemistry,* vol. 91, no. 4, pp. 2978-2984, 2019.

[120]. B. Dong *et al.*, "Fluorescence immunoassay based on the inner-filter effect of carbon dots for highly sensitive amantadine detection in foodstuffs," *Food chemistry,* vol. 294, pp. 347-354, 2019.

[121]. G. Mao *et al.*, "Ratiometric fluorescence immunoassay of SARS-CoV-2 nucleocapsid protein via Si-FITC nanoprobe-based inner filter effect," *Nano research,* vol. 16, no. 4, pp. 5383-5390, 2023.

[122]. P. J. Tighe, R. R. Ryder, I. Todd, and L. C. Fairclough, "ELISA in the multiplex era: potentials and pitfalls," *PROTEOMICS–Clinical Applications,* vol. 9, no. 3-4, pp. 406-422, 2015.

[123]. A. P. Demchenko, "Photobleaching of organic fluorophores: quantitative characterization, mechanisms, protection," *Methods and applications in fluorescence,* vol. 8, no. 2, p. 022001, 2020.

[124]. S. Jin *et al.*, "Multiplexed western blotting using microchip electrophoresis," *Analytical chemistry,* vol. 88, no. 13, pp. 6703-6710, 2016.

[125]. E. B. Bahadır and M. K. Sezgintürk, "Lateral flow assays: Principles, designs and labels," *TrAC Trends in Analytical Chemistry,* vol. 82, pp. 286-306, 2016.

[126]. M. Jauset-Rubio *et al.*, "Ultrasensitive, rapid and inexpensive detection of DNA using paper based lateral flow assay," *Scientific reports,* vol. 6, no. 1, p. 37732, 2016.

[127]. A. E. Urusov, A. V. Zherdev, and B. B. Dzantiev, "Towards lateral flow quantitative assays: detection approaches," *Biosensors,* vol. 9, no. 3, p. 89, 2019.

[128]. Z. Li, H. Chen, and P. Wang, "Lateral flow assay ruler for quantitative and rapid point-of-care testing," *Analyst,* vol. 144, no. 10, pp. 3314-3322, 2019.

[129]. J. Homola, "Surface plasmon resonance sensors for detection of chemical and biological species," *Chemical reviews,* vol. 108, no. 2, pp. 462-493, 2008.

[130]. J. Homola, "Present and future of surface plasmon resonance biosensors," *Analytical and bioanalytical chemistry,* vol. 377, pp. 528-539, 2003.

[131]. S. Unser, I. Bruzas, J. He, and L. Sagle, "Localized surface plasmon resonance biosensing: current challenges and approaches," *Sensors,* vol. 15, no. 7, pp. 15684-15716, 2015.

[132]. L. L. Sun, Y. S. Leo, X. Zhou, W. Ng, T. I. Wong, and J. Deng, "Localized surface plasmon resonance based point-of-care system for sepsis diagnosis," *Materials Science for Energy Technologies,* vol. 3, pp. 274-281, 2020.

[133]. J. R. Windmiller and J. Wang, "Wearable electrochemical sensors and biosensors: a review," *Electroanalysis,* vol. 25, no. 1, pp. 29-46, 2013.

[134]. S. Farid *et al.*, "Detection of Interferon gamma using graphene and aptamer based FET-like electrochemical biosensor," *Biosensors and Bioelectronics,* vol. 71, pp. 294-299, 2015.

[135]. N. J. Ronkainen, H. B. Halsall, and W. R. Heineman, "Electrochemical biosensors," *Chemical Society Reviews,* vol. 39, no. 5, pp. 1747-1763, 2010.

[136]. R. Ohno *et al.*, "Electrochemical impedance spectroscopy biosensor with interdigitated electrode for detection of human immunoglobulin A," *Biosensors and Bioelectronics,* vol. 40, no. 1, pp. 422-426, 2013.

[137]. T. Wadhera, D. Kakkar, G. Wadhwa, and B. Raj, "Recent advances and progress in development of the field effect transistor biosensor: A review," *Journal of Electronic Materials,* vol. 48, pp. 7635-7646, 2019.

[138]. M. Pohanka, "Quartz crystal microbalance (QCM) sensing materials in biosensors development," *International Journal of Electrochemical Science,* vol. 16, no. 12, p. 211220, 2021.

[139]. P. Hampitak *et al.*, "A point-of-care immunosensor based on a quartz crystal microbalance with graphene biointerface for antibody assay," *ACS sensors,* vol. 5, no. 11, pp. 3520-3532, 2020.

[140]. C. Dhote, A. Singh, and S. Kumar, "Silicon photonics sensors for biophotonic applications—a review," *IEEE Sensors Journal,* vol. 22, no. 19, pp. 18228-18239, 2022.

[141]. Y. Zhang *et al.*, "Ultraminiature optical fiber-tip directly-printed plasmonic biosensors for label-free biodetection," *Biosensors and Bioelectronics,* vol. 218, p. 114761, 2022.

[142]. X. Yang, C. Gu, F. Qian, Y. Li, and J. Z. Zhang, "Highly sensitive detection of proteins and bacteria in aqueous solution using surface-enhanced Raman scattering and optical fibers," *Analytical chemistry,* vol. 83, no. 15, pp. 5888-5894, 2011.

[143]. Y. Xu, M. Xiong, and H. Yan, "A portable optical fiber biosensor for the detection of zearalenone based on the localized surface plasmon resonance," *Sensors and Actuators B: Chemical,* vol. 336, p. 129752, 2021.

[144]. H.-M. Kim, M. Uh, D. H. Jeong, H.-Y. Lee, J.-H. Park, and S.-K. Lee, "Localized surface plasmon resonance biosensor using nanopatterned gold particles on the surface of an optical fiber," *Sensors and Actuators B: Chemical,* vol. 280, pp. 183-191, 2019.

[145]. Y. Lin, Y. Zou, and R. G. Lindquist, "A reflection-based localized surface plasmon resonance fiber-optic probe for biochemical sensing," *Biomedical optics express,* vol. 2, no. 3, pp. 478-484, 2011.

[146]. B. Doiron *et al.*, "Quantifying figures of merit for localized surface plasmon resonance applications: a materials survey," *Acs Photonics,* vol. 6, no. 2, pp. 240-259, 2019.

[147]. S. Managò *et al.*, "Tailoring lab-on-fiber SERS optrodes towards biological targets of different sizes," *Sensors and Actuators B: Chemical,* vol. 339, p. 129321, 2021.

[148]. K. Ehrlich *et al.*, "pH sensing through a single optical fibre using SERS and CMOS SPAD line arrays," *Optics Express,* vol. 25, no. 25, pp. 30976-30986, 2017.

[149]. U. Dinish, C. Y. Fu, K. S. Soh, B. Ramaswamy, A. Kumar, and M. Olivo, "Highly sensitive SERS detection of cancer proteins in low sample volume using hollow core photonic crystal fiber," *Biosensors and Bioelectronics,* vol. 33, no. 1, pp. 293-298, 2012.

[150]. X. Li *et al.*, "A SERS nano-tag-based fiber-optic strategy for in situ immunoassay in unprocessed whole blood," *Biosensors and Bioelectronics,* vol. 92, pp. 517-522, 2017.

[151]. Y. Shao, S. Xu, X. Zheng, Y. Wang, and W. Xu, "Optical fiber LSPR biosensor prepared by gold nanoparticle assembly on polyelectrolyte multilayer," *Sensors,* vol. 10, no. 4, pp. 3585-3596, 2010.

[152]. A. Aray *et al.*, "SPR-based plastic optical fibre biosensor for the detection of C-reactive protein in serum," *Journal of biophotonics,* vol. 9, no. 10, pp. 1077-1084, 2016.

[153]. A. Urrutia, J. Goicoechea, P. J. Rivero, A. Pildain, and F. J. Arregui, "Optical fiber sensors based on gold nanorods embedded in polymeric thin films," *Sensors and Actuators B: Chemical,* vol. 255, pp. 2105-2112, 2018.

[154]. J. Cao, M. H. Tu, T. Sun, and K. T. Grattan, "Wavelength-based localized surface plasmon resonance optical fiber biosensor," *Sensors and Actuators B: Chemical,* vol. 181, pp. 611-619, 2013.

[155]. Y. Tian, W. Wang, N. Wu, X. Zou, and X. Wang, "Tapered optical fiber sensor for label-free detection of biomolecules," *Sensors,* vol. 11, no. 4, pp. 3780-3790, 2011.

[156]. T. Liyanage, M. Lai, and G. Slaughter, "Label-free tapered optical fiber plasmonic biosensor," *Analytica Chimica Acta,* vol. 1169, p. 338629, 2021.

[157]. A. Urrutia *et al.*, "Novel highly sensitive protein sensors based on tapered optical fibres modified with Au-based nanocoatings," *Journal of Sensors,* vol. 2016, 2016.

[158]. K. Li, G. Liu, Y. Wu, P. Hao, W. Zhou, and Z. Zhang, "Gold nanoparticle amplified optical microfiber evanescent wave absorption biosensor for cancer biomarker detection in serum," *Talanta,* vol. 120, pp. 419-424, 2014.

[159]. M. A. Mustapa, M. H. A. Bakar, Y. M. Kamil, A. Syahir, and M. A. Mahdi, "Bio-functionalized tapered multimode fiber coated with dengue virus NS1 glycoprotein for label free detection of anti-Dengue virus NS1 IgG antibody," *IEEE Sensors Journal,* vol. 18, no. 10, pp. 4066-4072, 2018.

[160]. G. Liang, Z. Zhao, Y. Wei, K. Liu, W. Hou, and Y. Duan, "Plasma enhanced label-free immunoassay for alpha-fetoprotein based on a U-bend fiber-optic LSPR biosensor," *Rsc Advances,* vol. 5, no. 31, pp. 23990-23998, 2015.

[161]. R. Bharadwaj *et al.*, "Evanescent wave absorbance based fiber optic biosensor for label-free detection of E. coli at 280 nm wavelength," *Biosensors and Bioelectronics,* vol. 26, no. 7, pp. 3367-3370, 2011.

[162]. V. Sai, T. Kundu, and S. Mukherji, "Novel U-bent fiber optic probe for localized surface plasmon resonance based biosensor," *Biosensors and Bioelectronics,* vol. 24, no. 9, pp. 2804-2809, 2009.

[163]. R. Bharadwaj, S. Mukherji, and S. Mukherji, "Probing the localized surface plasmon field of a gold nanoparticle-based fibre optic biosensor," *Plasmonics,* vol. 11, pp. 753-761, 2016.

[164]. R. Bandaru *et al.*, "U-bent fiber optic plasmonic biosensor platform for ultrasensitive analyte detection," *Sensors and Actuators B: Chemical,* vol. 321, p. 128463, 2020.

[165]. A. d. S. Arcas, F. d. S. Dutra, R. C. Allil, and M. M. Werneck, "Surface plasmon resonance and bending loss-based U-shaped plastic optical fiber biosensors," *Sensors,* vol. 18, no. 2, p. 648, 2018.

[166]. M. Loyez, J. Albert, C. Caucheteur, and R. Wattiez, "Cytokeratins biosensing using tilted fiber gratings," *Biosensors,* vol. 8, no. 3, p. 74, 2018.

[167]. Q. Wang, J.-Y. Jing, and B.-T. Wang, "Highly sensitive SPR biosensor based on graphene oxide and staphylococcal protein a co-modified TFBG for human IgG

detection," *IEEE Transactions on Instrumentation and Measurement,* vol. 68, no. 9, pp. 3350-3357, 2018.

[168]. F. Chiavaioli, F. Baldini, S. Tombelli, C. Trono, and A. Giannetti, "Biosensing with optical fiber gratings," *Nanophotonics,* vol. 6, no. 4, pp. 663-679, 2017.

[169]. A. B. Socorro-Leránoz, D. Santano, I. Del Villar, and I. Matias, "Trends in the design of wavelength-based optical fibre biosensors (2008–2018)," *Biosensors and bioelectronics: X,* vol. 1, p. 100015, 2019.

[170]. S. M. Tripathi *et al.*, "Long period grating based biosensor for the detection of Escherichia coli bacteria," *Biosensors and Bioelectronics,* vol. 35, no. 1, pp. 308-312, 2012.

[171]. Á. González-Vila, D. Kinet, P. Mégret, and C. Caucheteur, "Narrowband interrogation of plasmonic optical fiber biosensors based on spectral combs," *Optics & Laser Technology,* vol. 96, pp. 141-146, 2017.

[172]. M. Lobry *et al.*, "Multimodal plasmonic optical fiber grating aptasensor," *Optics express,* vol. 28, no. 5, pp. 7539-7551, 2020.

[173]. M. Vidal *et al.*, "Relevance of the spectral analysis method of tilted fiber Bragg grating-based biosensors: a case-study for heart failure monitoring," *Sensors,* vol. 22, no. 6, p. 2141, 2022.

[174]. H. Liu *et al.*, "Temperature-insensitive label-free sensors for human IgG based on S-tapered optical fiber sensors," *IEEE Access,* vol. 9, pp. 116286-116293, 2021.

[175]. J. K. Virk, S. Das, R. Kaler, H. Singh, and T. Kundu, "D-shape optical fiber probe dimension optimization for LSPR based bio-sensor," *Optical Fiber Technology,* vol. 71, p. 102930, 2022.

[176]. J. Rabah, A. Mansaray, R. Wynne, and M. Duran, "Human Immunoglobulin Class G (I g G) Antibody Detection With Photonic Crystal Fiber," *Journal of Lightwave Technology,* vol. 34, no. 4, pp. 1398-1404, 2016.

[177]. Y. Zhao, X.-g. Hu, S. Hu, and Y. Peng, "Applications of fiber-optic biochemical sensor in microfluidic chips: A review," *Biosensors and Bioelectronics,* vol. 166, p. 112447, 2020.

[178]. B. Puygranier and P. Dawson, "Chemical etching of optical fibre tips—Experiment and model," *Ultramicroscopy,* vol. 85, no. 4, pp. 235-248, 2000.

[179]. N. Azizipour, R. Avazpour, D. H. Rosenzweig, M. Sawan, and A. Ajji, "Evolution of biochip technology: A review from lab-on-a-chip to organ-on-a-chip," *Micromachines,* vol. 11, no. 6, p. 599, 2020.

[180]. D. Atias *et al.*, "Chemiluminescent optical fiber immunosensor for the detection of IgM antibody to dengue virus in humans," *Sensors and Actuators B: Chemical,* vol. 140, no. 1, pp. 206-215, 2009.

[181]. J. Jing *et al.*, "Performance improvement approaches for optical fiber SPR sensors and their sensing applications," *Photonics Research,* vol. 10, no. 1, pp. 126-147, 2021.

[182]. L. Zeni *et al.*, "A portable optical-fibre-based surface plasmon resonance biosensor for the detection of therapeutic antibodies in human serum," *Scientific reports,* vol. 10, no. 1, p. 11154, 2020.

[183]. S. Shi *et al.*, "A polydopamine-modified optical fiber SPR biosensor using electroless-plated gold films for immunoassays," *Biosensors and Bioelectronics,* vol. 74, pp. 454-460, 2015.

[184]. M. Lu, H. Zhu, L. Hong, J. Zhao, J.-F. Masson, and W. Peng, "Wavelength-tunable optical fiber localized surface plasmon resonance biosensor via a diblock copolymer-templated nanorod monolayer," *ACS Applied Materials & Interfaces,* vol. 12, no. 45, pp. 50929-50940, 2020.

[185]. M. Lu *et al.*, "Comparative study of block copolymer-templated localized surface plasmon resonance optical fiber biosensors: CTAB or citrate-stabilized gold nanorods," *Sensors and Actuators B: Chemical,* vol. 329, p. 129094, 2021.

[186]. J. Cao, M. H. Tu, T. Sun, and K. T. Grattan, "Wavelength-based localized surface plasmon resonance optical fiber biosensor," *Sensors and Actuators B: Chemical,* vol. 181, pp. 611-619, 2013.

[187]. K. Liu *et al.*, "Multi-layer optical fiber surface plasmon resonance biosensor based on a sandwich structure of polydopamine-MoSe 2@ Au nanoparticles-polydopamine," *Biomedical Optics Express,* vol. 11, no. 12, pp. 6840-6851, 2020.

[188]. A. Shoji *et al.*, "Development of a surface plasmon resonance sensor using an optical fiber prepared by electroless displacement gold plating and its application to immunoassay," *Talanta,* vol. 240, p. 123162, 2022.

[189]. H. Song, Q. Wang, and W.-M. Zhao, "A novel SPR sensor sensitivity-enhancing method for immunoassay by inserting MoS2 nanosheets between metal film and fiber," *Optics and Lasers in Engineering,* vol. 132, p. 106135, 2020.

[190]. Y. Zheng, T. Lang, B. Cao, J. Jin, R. Dong, and H. Feng, "Fiber optic SPR sensor for human Immunoglobulin G measurement based on the MMF-NCF-MMF structure," *Optical Fiber Technology,* vol. 46, pp. 179-185, 2018.

[191]. Q. Wang and B. Wang, "Sensitivity enhanced SPR immunosensor based on graphene oxide and SPA co-modified photonic crystal fiber," *Optics & Laser Technology,* vol. 107, pp. 210-215, 2018.

[192]. W. C. Wong *et al.*, "Photonic crystal fiber surface plasmon resonance biosensor based on protein G immobilization," *IEEE Journal of Selected Topics in Quantum Electronics,* vol. 19, no. 3, pp. 4602107-4602107, 2013.

[193]. A. B. Socorro *et al.*, "Fiber-optic immunosensor based on an etched SMS structure," *IEEE Journal of Selected Topics in Quantum Electronics,* vol. 23, no. 2, pp. 314-321, 2016.

[194]. Y. Cardona-Maya, A. B. Socorro, I. Del Villar, J. L. Cruz, J. M. Corres, and J. F. Botero-Cadavid, "Label-free wavelength and phase detection based SMS fiber immunosensors optimized with cladding etching," *Sensors and Actuators B: Chemical,* vol. 265, pp. 10-19, 2018.

[195]. J. Zhong *et al.*, "All fiber-optic immunosensors based on elliptical core helical intermediate-period fiber grating with low-sensitivity to environmental disturbances," *Biosensors,* vol. 12, no. 2, p. 99, 2022.

[196]. F. Chiavaioli *et al.*, "Towards sensitive label-free immunosensing by means of turn-around point long period fiber gratings," *Biosensors and Bioelectronics,* vol. 60, pp. 305-310, 2014.

[197]. M. Chen, T. Lang, B. Cao, Y. Yu, and C. Shen, "D-type optical fiber immunoglobulin G sensor based on surface plasmon resonance," *Optics & Laser Technology,* vol. 131, p. 106445, 2020.

[198]. F. Chiavaioli *et al.*, "Femtomolar detection by nanocoated fiber label-free biosensors," *ACS sensors,* vol. 3, no. 5, pp. 936-943, 2018.

[199]. S. Chauhan, N. Punjabi, D. Sharma, and S. Mukherji, "Evanescent wave absorption based S-shaped fiber-optic biosensor for immunosensing applications," *Procedia Engineering,* vol. 168, pp. 117-120, 2016.

[200]. M. Szczerska, P. Wityk, and P. Listewnik, "The SARS-CoV-2 specific IgG antibodies biophotonic sensor," *Journal of Biophotonics,* vol. 16, no. 1, p. e202200172, 2023.

[201]. S. Hatai, "The refractive index of the blood serum of the albino rat at different ages," *Journal of Biological Chemistry,* vol. 35, no. 3, pp. 527-552, 1918.

[202]. B. J. O'Regan and D. N. Nikogosyan, "Femtosecond UV long-period fibre grating fabrication with amplitude mask technique," *Optics Communications,* vol. 284, no. 24, pp. 5650-5654, 2011.

[203]. R. Z. V. Costa, R. C. Kamikawachi, M. Muller, and J. L. Fabris, "Thermal characteristics of long-period gratings 266 nm UV-point-by-point induced," *Optics Communications,* vol. 282, no. 5, pp. 816-823, 2009.

[204]. C. Janer, A. Carballar, L. Navarro, J. Galo, and R. Rubio, "Photosensitivity color-center model for Ge-doped silica preforms," *IEEE Photonics Journal,* vol. 5, no. 4, pp. 6100511-6100511, 2013.

[205]. V. Grubsky, *Photosensitivity of germanium-doped silica glass and fibers*. University of Southern California, 1999.

[206]. E. Salik, *Photosensitivity of germanium-doped optical fibers and its enhancement by strain*. University of Southern California, 2001.

[207]. D. Williams, B. Ainslie, J. Armitage, R. Kashyap, and R. Campbell, "Enhanced UV photosensitivity in boron codoped germanosilicate fibres," *Electronics Letters,* vol. 29, no. 1, pp. 45-47, 1993.

[208]. M. M. De Villiers, D. P. Otto, S. J. Strydom, and Y. M. Lvov, "Introduction to nanocoatings produced by layer-by-layer (LbL) self-assembly," *Advanced drug delivery reviews,* vol. 63, no. 9, pp. 701-715, 2011.

[209]. M. N. Martin, J. I. Basham, P. Chando, and S.-K. Eah, "Charged gold nanoparticles in non-polar solvents: 10-min synthesis and 2D self-assembly," *Langmuir,* vol. 26, no. 10, pp. 7410-7417, 2010.

[210]. Q. Ling, Z. Gu, and K. Gao, "Smart design of a long-period fiber grating refractive index sensor based on dual-peak resonance near the phase-matching turning point," *Applied optics,* vol. 57, no. 10, pp. 2693-2697, 2018.

[211]. S. Bandyopadhyay, N. Basumallick, S. Bysakh, T. K. Dey, P. Biswas, and S. Bandyopadhyay, "Design of turn around point long period fiber grating sensor with Au-nanoparticle self monolayer," *Optics & Laser Technology,* vol. 102, pp. 254-261, 2018.

[212]. S. Safarzadeh, A. L. Bila, and O. Torsæter, "Experimental Investigation of the Effect of Silica Nanoparticles on Interfacial Tension and Wettability during Low Salinity Water Flooding: A Micromodel Study," 2022.

[213]. S. Korposh, S.-W. Lee, S. W. James, and R. P. Tatam, "Refractive index sensitivity of fibre-optic long period gratings coated with SiO2 nanoparticle

mesoporous thin films," *Measurement Science and Technology,* vol. 22, no. 7, p. 075208, 2011.

[214]. P. Wu, L. Liu, S. P. Morgan, R. Correia, and S. Korposh, "Label-Free Detection of Antibodies Using Functionalised Long Period Grating Optical Fibre Sensors," *Results in Optics,* vol. 5, p. 100172, 2021.

[215]. M. Takahashi *et al.*, "Simultaneous detection of immunoglobulin A (IgA) and IgM antibodies against hepatitis E virus (HEV) is highly specific for diagnosis of acute HEV infection," *Journal of clinical microbiology,* vol. 43, no. 1, pp. 49-56, 2005.

[216]. Z. Li *et al.*, "Development and clinical application of a rapid IgM-IgG combined antibody test for SARS-CoV-2 infection diagnosis," *Journal of medical virology,* vol. 92, no. 9, pp. 1518-1524, 2020.

[217]. M. Xue *et al.*, "Predictive effects of IgA and IgG combination to assess pulmonary exudation progression in COVID-19 patients," *Journal of Medical Virology,* vol. 93, no. 3, pp. 1443-1448, 2021.

[218]. L.-C. Chen *et al.*, "Improving the reproducibility, accuracy, and stability of an electrochemical biosensor platform for point-of-care use," *Biosensors and Bioelectronics,* vol. 155, p. 112111, 2020.

[219]. J. Chastain and R. C. King Jr, "Handbook of X-ray photoelectron spectroscopy," *Perkin-Elmer Corporation,* vol. 40, p. 221, 1992.

[220]. C. Trono, F. Baldini, M. Brenci, F. Chiavaioli, and M. Mugnaini, "Flow cell for strain-and temperature-compensated refractive index measurements by means of cascaded optical fibre long period and Bragg gratings," *Measurement Science and Technology,* vol. 22, no. 7, p. 075204, 2011.

[221]. S. Soma, "Multiple Myeloma With a Rare Presentation at Preserved Uninvolved Immunoglobulins," *Cureus,* vol. 14, no. 5, 2022.

[222]. T. X. O’connell, T. J. Horita, and B. Kasravi, "Understanding and interpreting serum protein electrophoresis," *American family physician,* vol. 71, no. 1, pp. 105-112, 2005.

[223]. R. Lakshminarayanan, Y. Li, K. Janatpour, L. Beckett, and I. Jialal, "Detection by immunofixation of M proteins in hypogammaglobulinemic patients with normal serum protein electrophoresis results," *American journal of clinical pathology,* vol. 127, no. 5, pp. 746-751, 2007.

[224]. G. Csako, "Immunofixation electrophoresis for identification of proteins and specific antibodies," *Protein Electrophoresis: Methods and Protocols,* pp. 147-171, 2012.

[225]. P. Wu, L. Liu, S. P. Morgan, R. Correia, and S. Korposh, "Long Period Grating Mach–Zehnder Interferometer Based Immunosensor with Temperature and Bulk Refractive Index Compensation," *Biosensors,* vol. 12, no. 12, p. 1099, 2022.

[226]. F. Esposito, A. Srivastava, L. Sansone, M. Giordano, S. Campopiano, and A. Iadicicco, "Label-free biosensors based on long period fiber gratings: A review," *IEEE Sensors Journal,* vol. 21, no. 11, pp. 12692-12705, 2020.

[227]. C. Trono, F. Baldini, M. Brenci, F. Chiavaioli, and M. Mugnaini, "Flow cell for strain-and temperature-compensated refractive index measurements by means of cascaded optical fibre long period and Bragg gratings," *Measurement Science and Technology,* vol. 22, no. 7, p. 075204, 2011.

[228]. F. Liu, X. Zhang, K. Li, T. Guo, A. Ianoul, and J. Albert, "Discrimination of bulk and surface refractive index change in plasmonic sensors with narrow bandwidth resonance combs," *ACS sensors,* vol. 6, no. 8, pp. 3013-3023, 2021.

[229]. M. Janik, M. Koba, K. Król, P. Mikulic, W. J. Bock, and M. Śmietana, "Combined long-period fiber grating and microcavity in-line Mach–Zehnder interferometer for refractive index measurements with limited cross-sensitivity," *Sensors,* vol. 20, no. 8, p. 2431, 2020.

[230]. Q. Yao *et al.*, "Simultaneous measurement of refractive index and temperature based on a core-offset Mach–Zehnder interferometer combined with a fiber Bragg grating," *Sensors and Actuators A: Physical,* vol. 209, pp. 73-77, 2014.

[231]. D. A. C. Enríquez, A. R. da Cruz, and M. T. M. R. Giraldi, "Hybrid FBG–LPG sensor for surrounding refractive index and temperature simultaneous discrimination," *Optics & Laser Technology,* vol. 44, no. 4, pp. 981-986, 2012.

[232]. S. W. James, S. Korposh, S.-W. Lee, and R. P. Tatam, "A long period grating-based chemical sensor insensitive to the influence of interfering parameters," *Optics express,* vol. 22, no. 7, pp. 8012-8023, 2014.

[233]. H. C. A. S. G. Vasconcelos, J. M. M. M. de Almeida, C. M. T. Saraiva, P. A. da Silva Jorge, and L. C. C. Coelho, "Mach–Zehnder interferometers based on long period fiber grating coated with titanium dioxide for refractive index sensing," *Journal of Lightwave Technology,* vol. 37, no. 18, pp. 4584-4589, 2019.

[234]. T. Hao and K. S. Chiang, "Graphene-based ammonia-gas sensor using in-fiber Mach-Zehnder interferometer," *IEEE Photonics Technology Letters,* vol. 29, no. 23, pp. 2035-2038, 2017.

[235]. J. Wu *et al.*, "Lab on optical fiber: surface nano-functionalization for real-time monitoring of VOC adsorption/desorption in metal-organic frameworks," *Nanophotonics,* vol. 10, no. 10, pp. 2705-2716, 2021.

[236]. S. Kaushik, U. Tiwari, N. Nilima, S. Prashar, B. Das, and R. K. Sinha, "Label-free detection of Escherichia coli bacteria by cascaded chirped long period gratings immunosensor," *Review of Scientific Instruments,* vol. 90, no. 2, 2019.

[237]. X. Hu, H. Si, and H. Shen, "Spectral characteristics and space division multiplexing scheme of long period fiber grating pair," *Optik,* vol. 227, p. 166117, 2021.

[238]. Y. Liu, J. Williams, L. Zhang, and I. Bennion, "Phase shifted and cascaded long-period fiber gratings," *Optics communications,* vol. 164, no. 1-3, pp. 27-31, 1999.

[239]. N. S. Greenspan, D. A. Dacek, and L. Cooper, "Fc region-dependence of IgG3 anti-streptococcal group A carbohydrate antibody functional affinity. I. The effect of temperature," *Journal of immunology (Baltimore, Md.: 1950),* vol. 141, no. 12, pp. 4276-4282, 1988.

[240]. J. Y. Lichtenberg, Y. Ling, and S. Kim, "Non-specific adsorption reduction methods in biosensing," *Sensors,* vol. 19, no. 11, p. 2488, 2019.

[241]. Y.-J. Lu *et al.*, "Nanoplasmonic structure of a polycarbonate substrate integrated with parallel microchannels for label-free multiplex detection," *Polymers,* vol. 13, no. 19, p. 3294, 2021.

[242]. Y. Yue, H. Ding, and C. Chen, "Label-free optical antibody testing kit based on a self-assembled whispering-gallery-mode microsphere," *Journal of Biophotonics,* vol. 14, no. 3, p. e202000338, 2021.

[243]. C. Preininger, A. Mencaglia, and F. Baldini, "Polymer-coated optical fibres for application in a direct evanescent wave immunoassay," *Analytica chimica acta,* vol. 403, no. 1-2, pp. 67-76, 2000.

[244]. E. Desimoni and B. Brunetti, "X-ray photoelectron spectroscopic characterization of chemically modified electrodes used as chemical sensors and biosensors: a review," *Materials,* vol. 3, no. 2, pp. 70-117, 2015.

[245]. M. J. Pelletier, "Quantitative analysis using Raman spectrometry," *Applied spectroscopy,* vol. 57, no. 1, pp. 20A-42A, 2003.

[246]. C. J. Strachan, T. Rades, K. C. Gordon, and J. Rantanen, "Raman spectroscopy for quantitative analysis of pharmaceutical solids," *Journal of pharmacy and pharmacology,* vol. 59, no. 2, pp. 179-192, 2007.

[247]. A. G. Shard, "Practical guides for x-ray photoelectron spectroscopy: Quantitative XPS," *Journal of Vacuum Science & Technology A,* vol. 38, no. 4, 2020.

[248]. S. Müller, Y. de Hazan, and D. Penner, "Effect of temperature, humidity and aminoalkoxysilane additive on the low temperature curing of polyorganosilazane coatings studied by IR spectroscopy, gravimetric and evolved gas analysis," *Progress in Organic Coatings,* vol. 97, pp. 133-145, 2016.

[249]. J.-O. Gaudron, F. Surre, T. Sun, and K. Grattan, "Long period grating-based optical fibre sensor for the underwater detection of acoustic waves," *Sensors and Actuators A: Physical,* vol. 201, pp. 289-293, 2013.

[250]. V. Moradi, M. Akbari, and P. Wild, "A fluorescence-based pH sensor with microfluidic mixing and fiber optic detection for wide range pH measurements," *Sensors and Actuators A: Physical,* vol. 297, p. 111507, 2019.

[251]. H. Chen, K. Liu, Z. Li, and P. Wang, "Point of care testing for infectious diseases," *Clinica chimica acta,* vol. 493, pp. 138-147, 2019.

[252]. N. Azizipour, R. Avazpour, D. H. Rosenzweig, M. Sawan, and A. Ajji, "Evolution of biochip technology: A review from lab-on-a-chip to organ-on-a-chip," *Micromachines,* vol. 11, no. 6, p. 599, 2020.

[253]. S. Baratchi *et al.*, "Immunology on chip: Promises and opportunities," *Biotechnology advances,* vol. 32, no. 2, pp. 333-346, 2014.

[254]. M. R. Kosorok and E. B. Laber, "Precision medicine," *Annual review of statistics and its application,* vol. 6, no. 1, pp. 263-286, 2019.

[255]. M. Gray *et al.*, "Implantable biosensors and their contribution to the future of precision medicine," *The Veterinary Journal,* vol. 239, pp. 21-29, 2018.

[256]. A.-M. Šimundić, "Measures of diagnostic accuracy: basic definitions," *ejifcc,* vol. 19, no. 4, p. 203, 2009.

Appendix

A. Methods to calculate FWHM of dips and peaks

As shown in Figure 1, point B(670nm, 0.44) is a dip in the transmission spectrum and C(727nm, 0.84) is a peak. To calculate the FWHM of dip B, the nearest points on both sides of B where the transmission's changing rate is zero need to be found. They are A(628nm, 0.68) and C(727, 0.84). Since the distance between A and B is shorter than the distance between B and C in vertical direction, the average of the transmission at A and B is calculated, which is $\frac{0.68+0.44}{2} = 0.56$. P1(650nm, 0.56) and P2(693nm, 0.56) are the closest points to B on left-hand side and right-hand side respectively with transmission of 0.56. The separation between P1 and P2 is the FWHM of dip B, which is 43nm. Similarly, the two points on either side of peak C where the transmission's changing rate is 0 are B(670nm, 0.44) and D(770nm, 0.6). The distance C and D is shorter than the distance between C and B in vertical direction. Therefore, the average of the transmissions at point C and D are calculated, which is $\frac{0.84+0.6}{2} = 0.72$. The two points where the transmissions are 0.72 locating on either side of point C are P3(707nm, 0.72) and P4(750nm, 0.72). The separation between P3 and P4 is the FWHM of peak C, which is 43nm. It is worth mentioning that the unit on y-axis should have a linear scale. If the unit

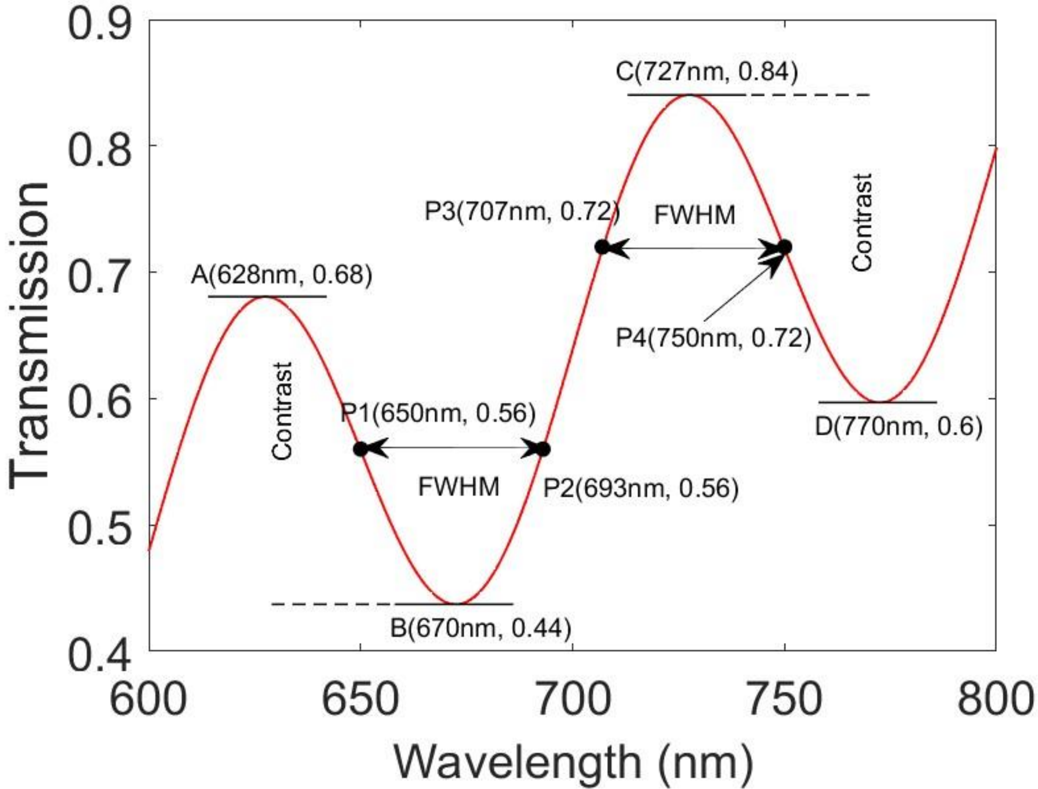

Figure 1. The FWHMs of a dip and a peak

B. Images of sub-5nm AuNPs taken with filed-emission scanning electron microscope

The image of sub-5nm AuNPs in shown in Figure 2, which is taken with field-emission scanning electron microscope. It is sourced from. The AuNPs are fabricated with the protocol explained in Chapter 4, which is also from. The sizes of the particles are smaller than 5nm.

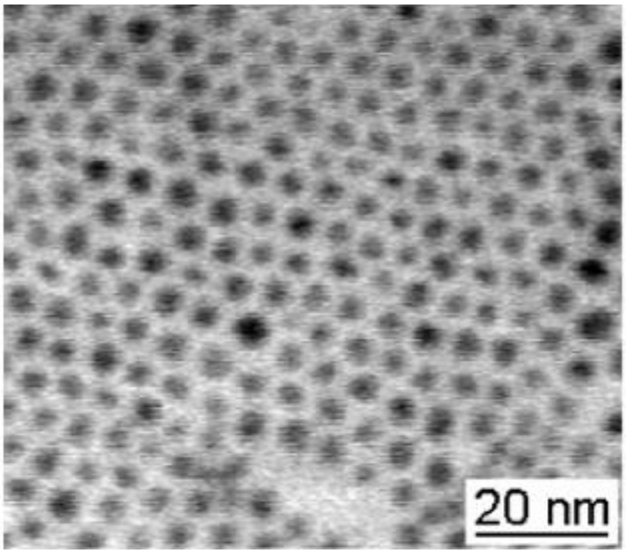

Figure 2. The image of sub-5nm AuNPs taken with field-emission scanning electron microscope sourced from

C. SEM samples

Optical fibre is fixed on glass slide for imaging the surface (Figure 3(a)), or on a vertical holder for imaging the cross-section (Figure 3(b)). 10nm-thick iridium film is deposited on the samples.

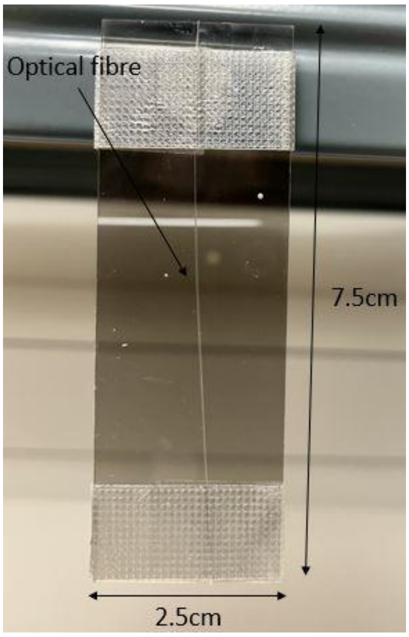

a

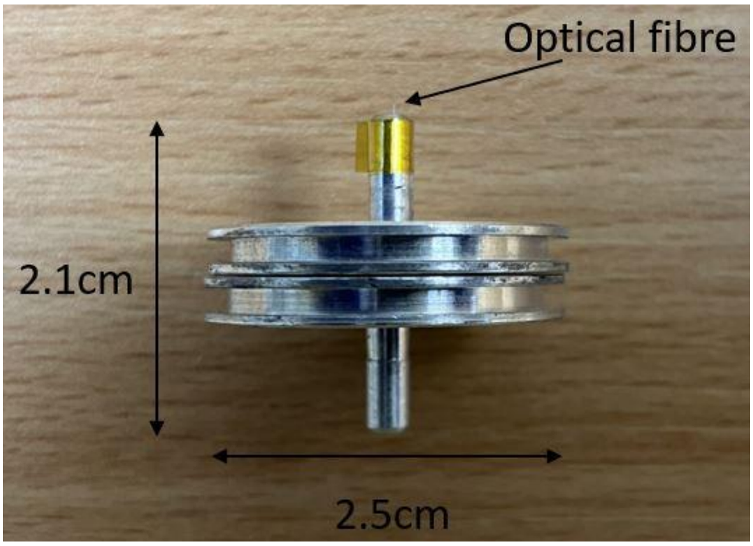

b

Figure 3. The SEM samples. (a) optical fibre is fixed on a glass slide with tape for imaging the surface; (b) optical fibre fixed on a vertical holder for imaging the cross-section.

D The processing on raw spectral

All the spectral data is acquired with Ocean Insight HR4000 spectrometer and SpectraSuite software. The raw spectra show light intensity. To get LPG's transmission spectra, an estimation on the emission spectrum is done based on the measured spectra. The detailed steps are listed below:

1. Loading the raw spectrum (Figure 4(a)), the two attenuation bands are easy to be recognized.
2. Denoising the raw data with moving average filter. The length of window is 10 data points (Equation Ap-1).

$$y_i = \frac{1}{10}\sum_{p=i-5}^{i+4} x_p \ (if\ i-5>0\ and\ i+4<N) \qquad \text{Ap-1(1)}$$

$$y_i = \frac{1}{10}\sum_{p=0}^{i+4} x_p \ (if\ i-5<0\ ) \qquad \text{Ap-1(2)}$$

$$y_i = \frac{1}{10}\sum_{p=i-5}^{N} x_p \ (if\ i+4>N\ ) \qquad \text{Ap-1(3)}$$

Where x is the raw date; y is the data after filtering; i indicates the position of an element in a vector, which is positive integer; N is the length of a vector, which is a positive integer.

The filtered spectrum is shown in Figure 4(b). The points on the edge of the LPG's attenuation bands (Point A, B, C, and D) can be found by visual inspection.

3. The emission intensity over LPG's attenuation bands is estimated with the data at point A, B, C, and D by a linear function. For example, the emission intensity over the region between A and B is estimated by:

$$I(e) = I(A) + \frac{I(B) - I(A)}{W(B) - W(A)} \times (W(e) - W(A)) \qquad \text{Ap-2}$$

Where *I(A)* is the intensity at point (A); *I(B)* is the intensity at point (B); *W(A)* is wavelength of point A; *W(B)* is wavelength of point B; *W(e)* is the wavelength where the intensity is estimated; *I(e)* is the estimated intensity. The estimated emission intensity is shown in (Figure 4(c), blue curve).

4. Divide the raw spectrum Figure 4(a) by the estimated emission spectrum, the estimated transmission spectrum is achieved Figure 4(d).

The raw intensity spectra and estimated transmission spectra of a bare LPG with different external RI are shown in Figure 4(e) and Figure 4(f) respectively. The power of incident light decreases during measurement, which lead to the decrease of raw spectral baseline (The intensity between 730nm and 740nm in Figure 4(e)). As we see, the main features of an LPG's spectrum are maintained during the signal processing such as the shape and wavelength of the attenuation bands. The sidelobes beside the main attenuation bands are removed. It doesn't affect the analysing and understanding on the performance of an LPG.

To track the wavelength shift of the attenuation bands, the minimum intensity within a certain wavelength window is found based on the raw spectrum. For example, to track the wavelength of the band located between 740nm and 800nm, the point with minimum intensity in the 740nm to 800nm window is found in the raw spectrum. The estimated transmission spectra are not used for getting the wavelength information to avoid any potential interference caused by the data processing algorithm.

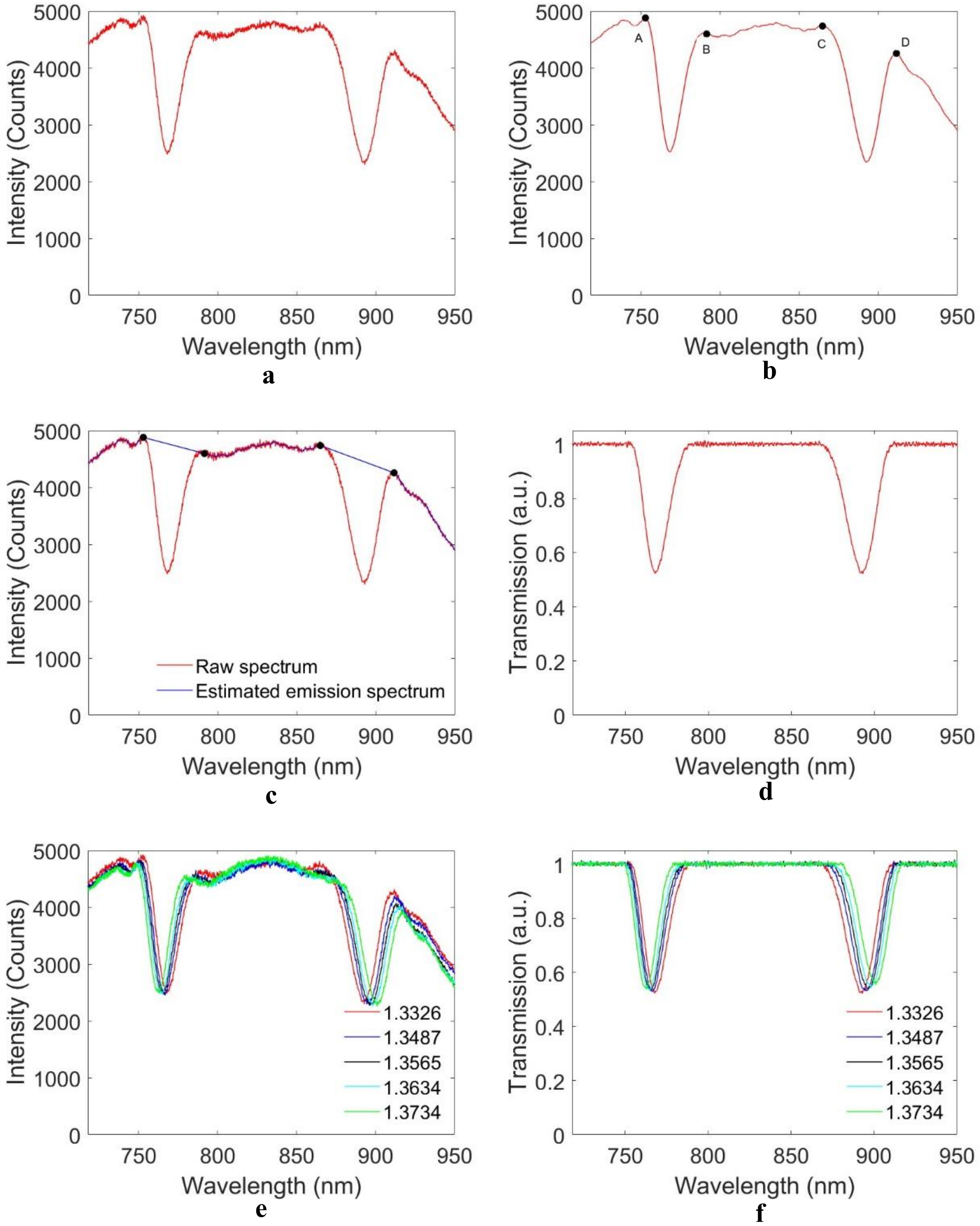

Figure 4. The processing of the raw spectral data. (a) Raw intensity data; (b) Denoising the raw data using a moving-mean filter with a window size of 5; (c) A comparison of the raw measured spectrum and estimated emission spectrum; (d) The transmission spectrum calculated with raw measured spectrum and estimated emission spectrum; (e) The raw measured spectra of an LPG in different external RI; (f) The calculated transmission spectra of an LPG in different external RI.

E. The stability test on an LPG

A stability test on LPG is performed by immersing LPG into DI water 5 times. The wavelength during each immersion is compared. The wavelength shift caused by laboratory temperature fluctuation is less than 0.03nm.

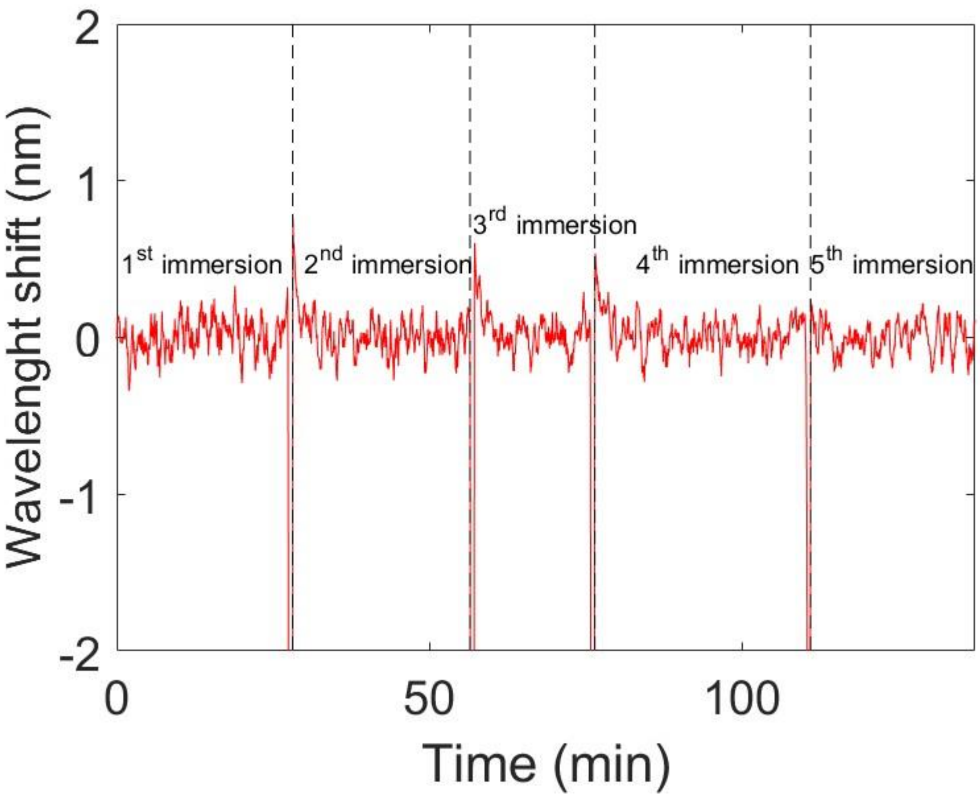

Figure 5. The stability test on an LPG

F. The selectivity of IgG sensors fabricated with bio-receptors of different concentrations

Figure 6 shows the selectivity tests on the IgG sensors fabricated with bio-receptors of different concentrations. The sensors are fabricated with the same methods as the IgG sensor in Chapter 5. Two layers of (PAH/SiNPs) and sub-5nm AuNPs are deposited on the surface. Bio-receptors is immobilized with 11-MUA/EDC/NHS cross-linker. The selectivity test is done with 80µg/ml IgM and 80µg/ml IgG. The selectivity test of the IgG sensor fabricated with 100µg/ml anti-IgG is shown in Figure 6(a). The selectivity is 1.25. The selectivity of IgG sensor fabricated with 500µg/ml anti-IgG is 6.18, which is shown in Figure 6(b). The selectivity is a lot lower than the selectivity of IgG sensor fabricated with 1mg/ml anti-IgG, which is 18.48 (Chapter 5). It is most likely there isn't enough anti-IgG immobilized on the LPG.

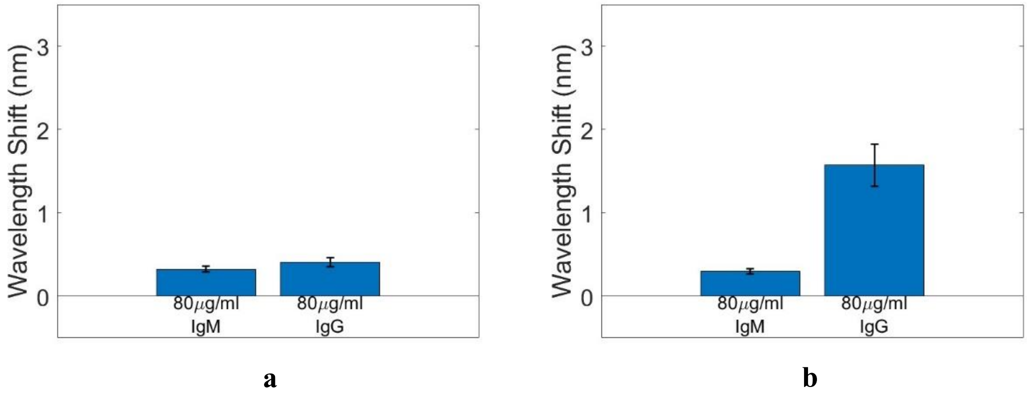

Figure 6. The selectivity tests on different IgG sensors. (a) The selectivity test on an IgG sensor fabricated with 100µg/ml anti-IgG; (b) The selectivity test on an IgG sensor fabricated with 500µg/ml anti-IgG.

G. The ELISA tests on different bio-receptors

The anti-IgM has a little cross-sensitivity to human IgA (HuIgA, Figure 7(a)). The anti-IgG has cross-sensitivity to human IgM (HuIgM, Figure 7(b)).

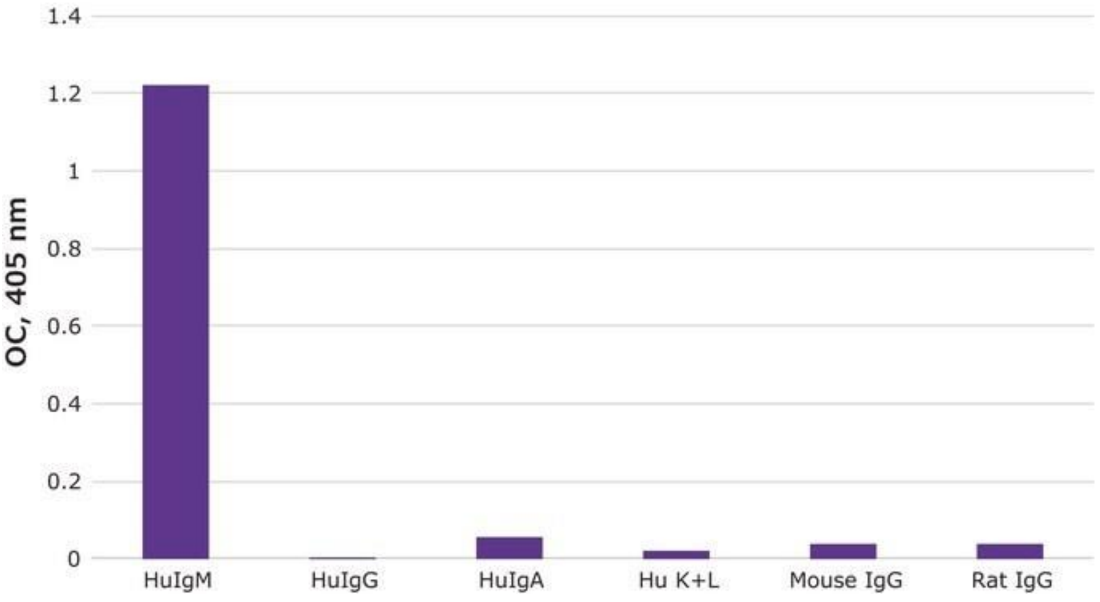

a

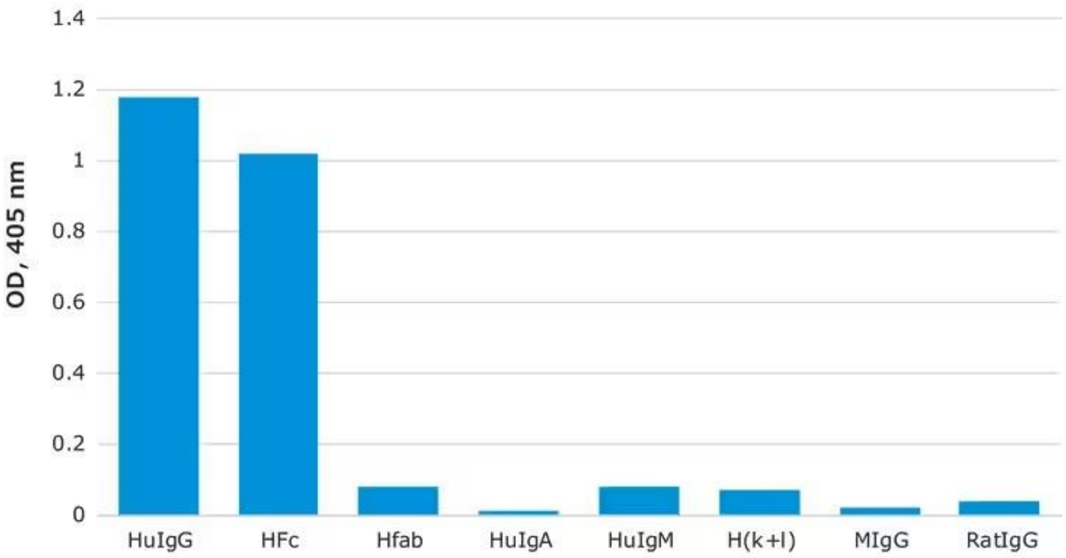

b

Figure 7. The ELISA tests on bio-receptors. (a) ELISA test on anti-IgM sourced from https://www.sigmaaldrich.com/GB/en/product/sigma/i2386; (b) ELISA test on anti-IgG sourced from https://www.sigmaaldrich.com/GB/en/product/sigma/i2136

H. The selectivity of IgG sensors fabricated with Glutaraldehyde cross-linker

Figure 8(a) shows the real-time wavelength shift during the incubation in the solution with an anti-IgG concentration of 1mg/ml. The immobilization of anti-IgG on the surface of an LPG gets saturated after approximately 100 minutes. The responses of the sensor with one hour incubation period to 80µg/ml IgM and 80µg/ml IgG are shown in Figure 8(b). The selectivity is 1.8. Anti-IgG can bind to IgM (Figure 7(b)). IgM can also get immobilized on the LPG through unreacted Glutaraldehyde. The responses of the sensor with two hours incubation period to 80µg/ml IgM and 80µg/ml IgG are shown in Figure 8(c). The selectivity is 19.4. The small response to IgM is most likely because anti-IgG can bind to IgM (Figure 2(b)).

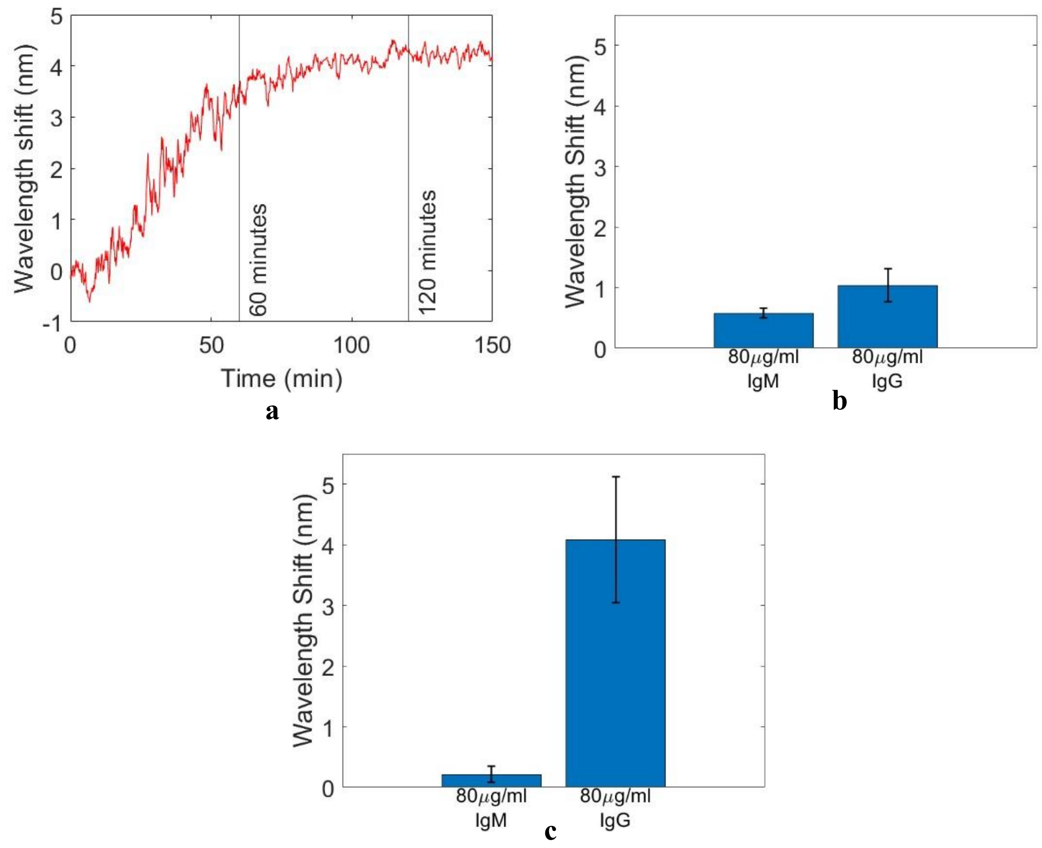

Figure 8. The selectivity of IgG sensors fabricated with Glutaraldehyde cross-linker. (a). The real-time wavelength shift during the incubation in solution with an anti-IgG concentration of 1mg/ml; (b) The selectivity of the sensor with an incubation time of one hour; (c) The selectivity of the sensor with an incubation period of two hours.

I. A comparison among the wavelength shifts of different dips in the transmission spectrum of an LPGMZI

There are four dips that have transmission lower than 0.4 (Figure 9(a)). When the whole LPGMZI is immersed, the wavelength shifts of the four dips are shown in Figure 9(b). Dip 2 has the most comparable wavelength to envelope. The calibration curves between the wavelength shifts of the four dips and refractive index (RI) are shown in Figure 9(c). When the temperature changes homogeneously over the whole LPGMZI, the four dips shift at different rates (Figure 9(d)). Dip 2 has the most comparable shifting rate with the envelope. The calibration curves between the wavelength shifts of the four dips and temperature are shown in Figure 9(e).

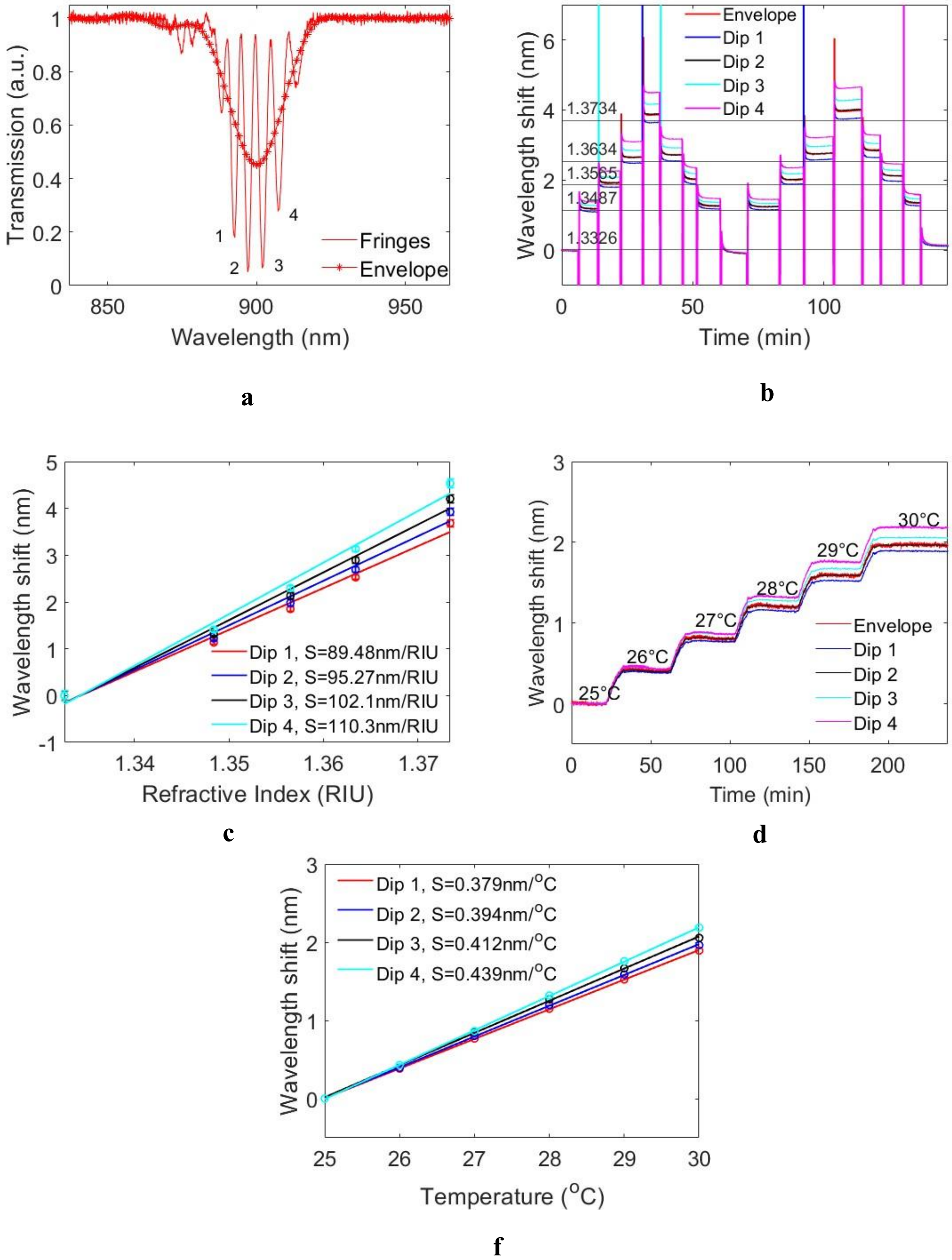

Figure 9. The comparison between the changes of different dips in the transmission spectrum of an LPGMZI. (a) The transmission spectrum and envelope, with four dips with transmission lower than 0.4; (b) The real-time wavelength shifts of the four dips during the external RI measurement with the whole LPGMZI immersed; (c) The calibration curves between the wavelength shifts of the four dips and external RI; (d) The real-time wavelength shifts of the four dips during temperature measurement; (e) The calibration curves between the wavelength shifts of four dips and temperature.

J. An analysis of the relationship between the phase shift of an LPGMZI's fringes and change of temperature

Recalling Equation (7-3):

$$\Phi = \frac{2\pi L}{\Lambda} \tag{7-3}$$

Where L is the length of connecting section; Λ is grating period; Φ is the phase of fringes. L and Λ change with temperature due to thermal expansion. Therefore, the changing rate of phase with temperature is:

$$\frac{d\Phi}{dT} = 2\pi \frac{d(\frac{L}{\Lambda})}{dT} = 2\pi \frac{\frac{dL}{dT}\Lambda - L\frac{d\Lambda}{dT}}{\Lambda^2} \tag{Ap-3}$$

The changes of L and Λ with temperature are:

$$dL = \alpha L(dT) \tag{Ap-4}$$

$$d\Lambda = \alpha \Lambda(dT) \tag{Ap-5}$$

Where α is the thermal-expansion coefficient of the optical fibre. Substituting dL and $d\Lambda$ by Equation (11-2) and Equation (11-3) respectively:

$$\frac{d\Phi}{dT} = 2\pi \frac{\frac{\alpha L(dT)}{dT}\Lambda - L\frac{\alpha \Lambda d(T)}{dT}}{\Lambda^2} = 0$$

Therefore, the phase of fringes doesn't change with temperature.

K. The signal change of an IgM sensor based on LPGMZI when it is entirely immersed in the solution

The connecting section of an LPGMZI is functionalized with anti-IgM, while the two LPGs are left bare. The whole LPGMZI is immersed in Tris buffer and solution with 80μg/ml IgM. The signal wavelength shifts of envelope and fringe are shown in Figure 10. The envelope shifts because of the non-specific binding between IgM and bare LPGs. The fringe shifts more than the envelope as the connecting section is functionalized with anti-IgM.

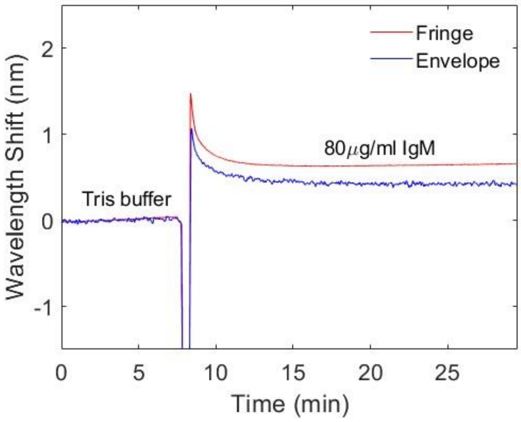

Figure 10. The signal change of an IgM based on LPGMZI when it is entirely immersed in solution.

L. Measuring Immunoglobulin G with a Sensor Based on Reflection-Mode LPG

An Immunoglobulin G (IgG) sensor is designed based on a reflection-mode LPG. A normal LPG is spliced to a single-mode optical-fibre coupler. A silver tip is deposited on the distal end of the LPG. This structure has the potential to be developed as a probe-type sensor. The IgG sensor developed in this work can detect IgG in 1% human serum with an LoD of 8.4μg/ml, and the selectivity of the sensor is over 50.

1. Introduction

LPGs are versatile platforms to design bio-/chemical sensors [2]. It is straightforward to fabricate sensors based on transmission-mode LPGs by depositing functional materials on their surface. Comparing with transmission-mode LPGs, reflection-mode LPGs are more flexible due to their probe-type configurations. To collect the reflected light, an LPG is usually connected to an optical-fibre coupler or optical circulator, and a reflective mirror is deposited on the other end of the LPG [3], [4]. Silver (Ag) [3], gold (Au) [5], and aluminium (Al) [6] are widely used materials for the reflective mirror. When depositing the mirror on the tip, it can form an interference pattern in the detected spectrum due to the interference between core mode and cladding mode when they are reflected to the LPG [3][4]. It can increase the complexity of signal processing. There are two approaches to remove the interference pattern: i) make the distance between the LPG and reflective mirror long such that the cladding mode is absorbed during transmission [7]; ii) extend the metal film on the side surface of optical fibre, the cladding mode can be absorbed by the metal film [7]. From the reviewing of literatures, the methods used for film deposition includes silver mirror reaction [8], sputtering coating [5], and electroless plating [9].

Same as transmission-mode LPGs, reflection-mode LPGs detect the change of external refractive index (RI) [10]. Many sensors are designed by depositing functional materials on the surface of reflection-mode LPGs such as humidity sensors and biosensors [5][11]. Immersion coating and dip coating techniques are applied to deposit the functional materials. For example, an humidity sensor is fabricated by depositing poly(allylamine hydrochloride, PAH) and silica nanoparticles on the LPG with immersion coating [5][11]; sensor to detect human Thyroglobulin (Tg) for cancer monitoring is developed by immobilizing anti-human Tg on a reflection-mode LPG with dip coating [11].

In this chapter, an IgG sensor is fabricated based on a reflection-mode LPG. It is tested in 1% human serum. Whole human serum is diluted in PBS buffer by 100-fold, which is a protocol widely used in clinical laboratories. The sensor responds to IgG with an LoD of 8.4µg/ml and has selectivity of 53 against Bovine serum albumin (BSA). It demonstrates the feasibility of fabricating reflection-mode LPG and designing sensor based on it to measure human IgG in real serum sample.

2. Materials and Methodology

All the chemicals and biological samples used in this work are purchased from Merck, UK. They are 3-Aminopropyltriethoxysline (APTES), PBS phosphate buffered saline, sodium chloride, sulfuric acid, peroxide solution (H_2O_2), ethanol, glutaric dialdehyde solution (Glutaraldehyde, 50% in H_2O), IgG from human serum, anti-human IgG antibody produced in goat (anti-IgG), serum minus IgG human, bovine serum albumin (BSA), silver nitrite ($AgNO_3$), and Glucose ($C_6H_{12}O_6$) are purchased from Merck, UK. Ammonia solution (NH_4OH, 35%) is purchased from Fisher Scientific.

A 3cm long LPG is fabricated in photosensitive fibre (PS750, Fibrecore, UK) with a 266nm wavelength laser and 105µm amplitude mask. The proximal end of the LPG is spliced onto a single-mode optic-fibre coupler (50:50, Thorlabs, UK) with a fusion splicer (FSM-100P, Fujikura, Japan) as shown in Figure 11.

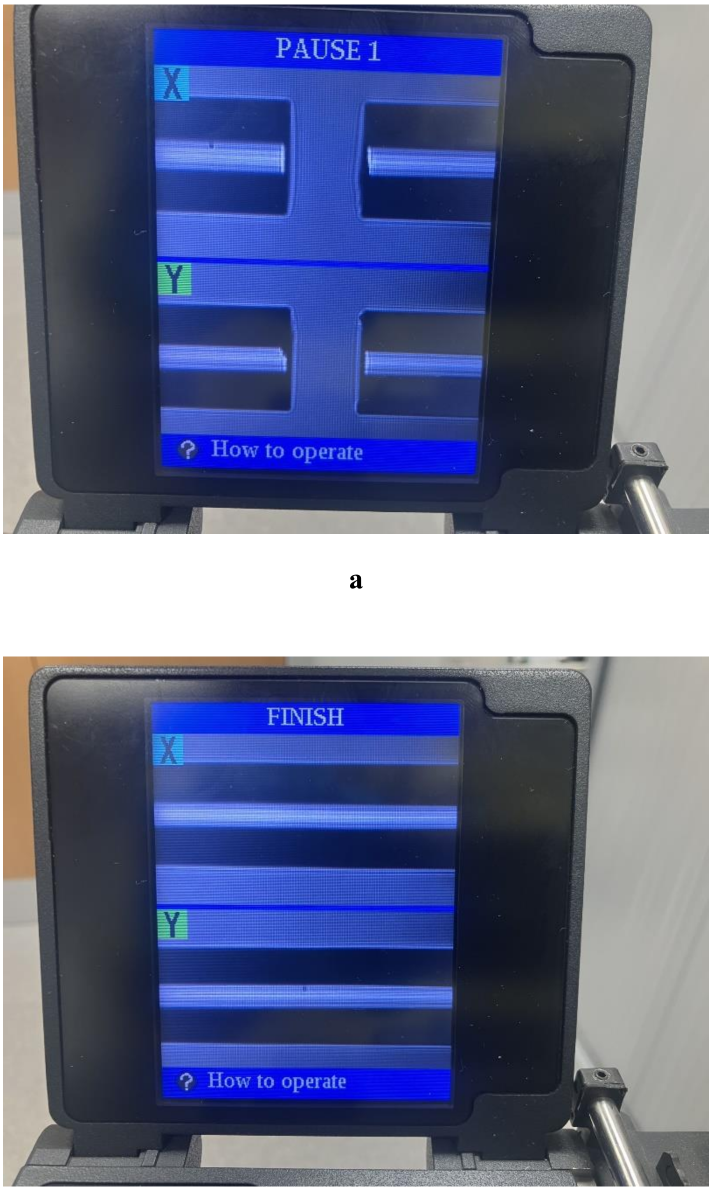

Figure 11. The splicing of two optical fibre. (a) Before splicing; (b) After splicing

A silver layer is deposited on the distal end of the LPG using silver mirror reaction. The separation between the LPG and the silver film is 15cm. The distance is intentionally made a bit longer to make sure interference pattern doesn't show in the measured spectrum and the LPG doesn't contact the solution when depositing the silver film. The silver mirror reaction is used to deposit the film:

$$3AgNO_3 + 2NaOH \rightarrow AgO_2 \downarrow + 2NaNO_3 + H_2O$$

$$Ag_2O + 4NH_3 + H_2O \rightarrow 2Ag(NH_3)_2OH$$

$$C_6H_{12}O_6 + 2Ag(NH_3)_2OH \rightarrow C_5H_{11}O_5COONH_4 + 3NH_3 + 2Ag \downarrow + H_2O$$

The whole protocol is:

1. Set 640μL of S1 in a vial with 1.5mL volume.
2. Add 440μL of S2 to the vial. Precipitation appears.
3. Add 40μL of ammonia solution (35%) to the vial. Precipitation disappears.
4. Add 64μL S3 to the vial and immerse the fibre tip into the solution and wait for approximately 15 minutes.

The deposition of silver film is shown in Figure 12.

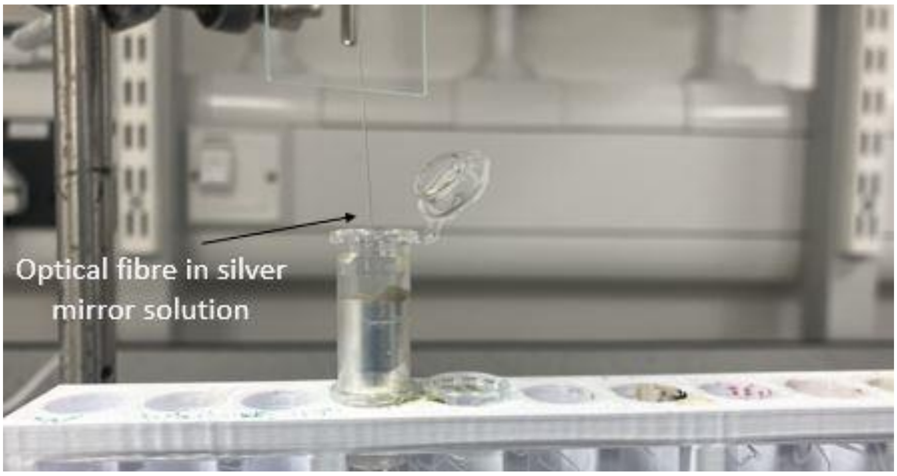

Figure 12. The deposition of silver film on the tip of optical fibre

The whole reflection-mode LPG system configuration is shown in Figure 13.

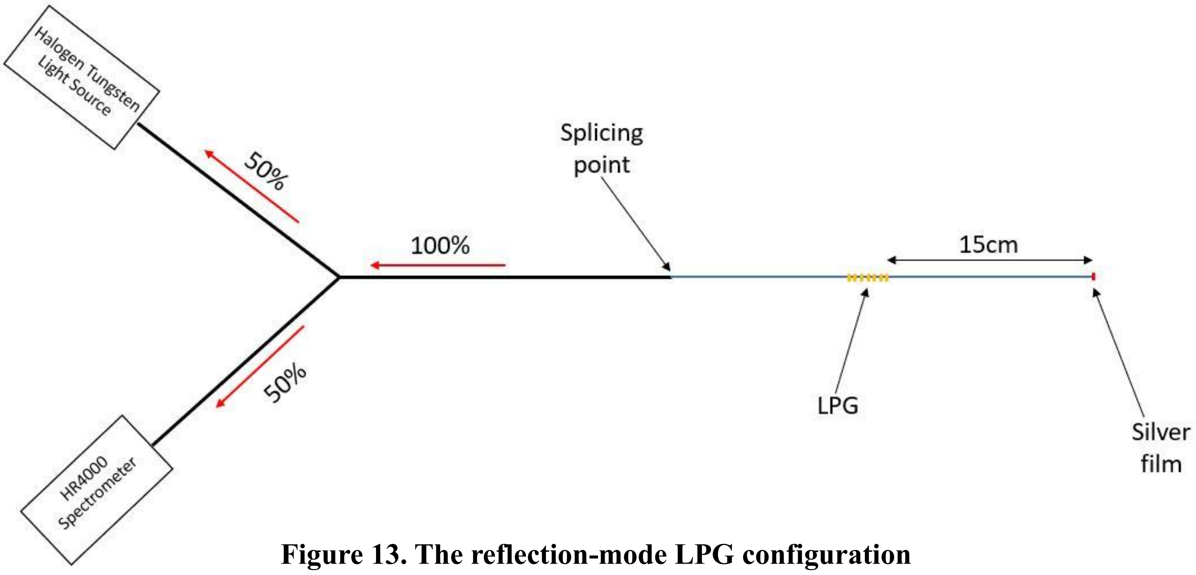

Figure 13. The reflection-mode LPG configuration

To fabricate an IgG sensor, the reflection-mode LPG is functionalized by immobilizing anti-IgG on the surface with Glutaraldehyde cross-linker as described in Section 3.2.3. The IgG samples are prepared with the following steps:

1. Dissolve 16mg IgG into1mL human serum (without IgG) and leave it in fridge (~5°C) for at least 72 hours (Solution 1).
2. Mix 1mL human serum (without IgG) and 99mL PBS buffer to obtain the base solution (Solution 2).
3. Mix 10µL solution 1 and 990µL PBS buffer to obtain 1% human serum with 160µg/ml IgG (Solution 3).
4. Mix solution 3 and solution 2 by different ratios to obtain 1% human serum with different IgG concentrations: 10µg/ml, 20µg/ml, 40µg/ml, 80µg/ml, 120µg/ml, and 160µg/ml.

The surface-functionalized LPG is placed in a Teflon fibre bath holder. The prepared 1% human serum with different IgG concentrations is pipetted into the fibre bath holder. After waiting for a period of at least 20 minutes, the old solution is pumped out, and new solution with a higher IgG concentration is pipetted into the fibre bath.

3. Results

3.1 The measurement of external RI

The measured spectra of transmission-mode LPG and reflection-mode LPG are shown in Figure 14(a). The attenuation bands of reflection-mode LPG are deeper than that of a transmission-mode LPG, while their wavelengths almost don’t change. The measurement spectra of reflection-mode LPG under different external RI are shown in Figure 14(b). The two bands move oppositely when external RI increases, with the separation between them increasing. The real-time wavelength shift is shown in Figure 14(c). The measured spectra of transmission-mode LPG are shown in Figure 14(d). Similar to the reflection-mode LPG, the two bands in the spectra move oppositely when external RI increases, with the separation between them increasing. The real-time wavelength shift is shown in Figure 14(e). The calibration curves are shown in Figure 14(f). The reflection-mode LPG has sensitivity to the change of external of 300nm/RIU (R^2=99.67%). The transmission-mode LPG has sensitivity of 295.7nm/RIU (R^2=99.65%).

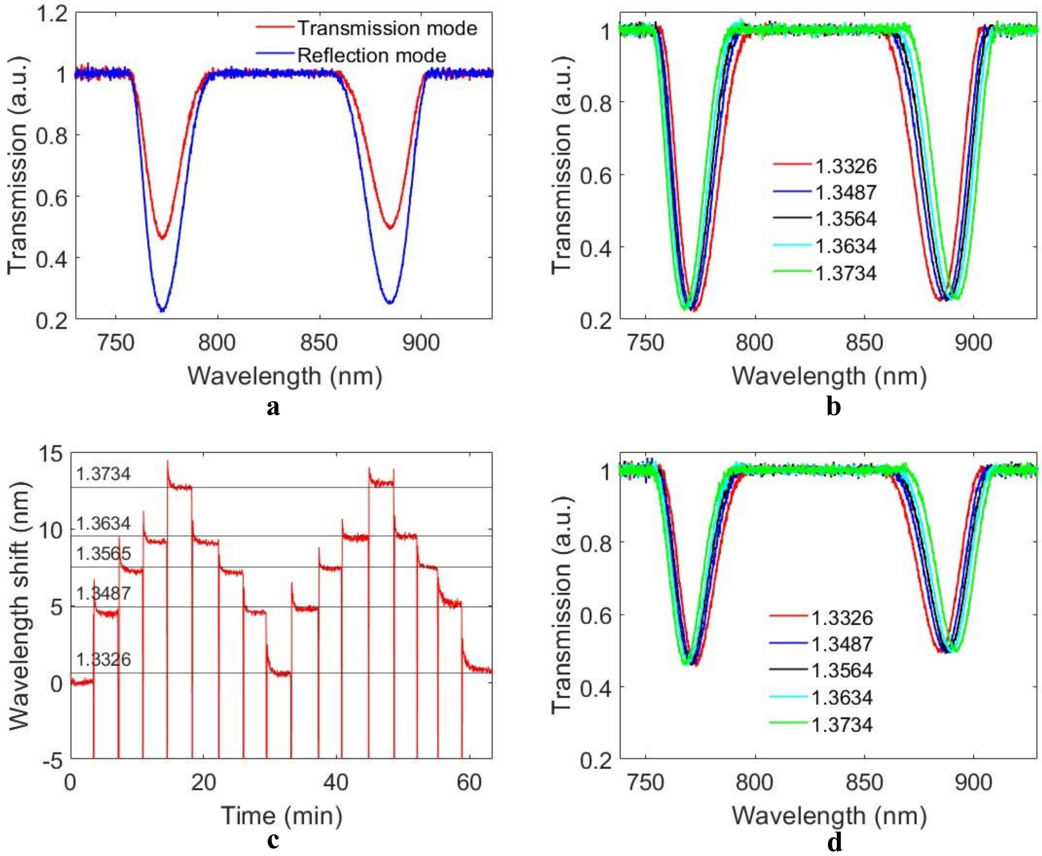

a b

c d

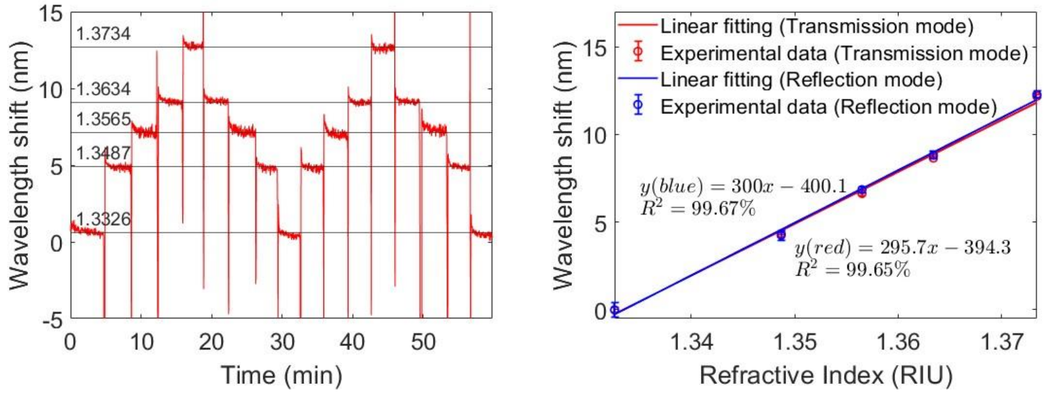

e **f**

Figure 14. Measuring external RI using transmission-mode and reflection-mode LPGs. (a) A comparison of the measured spectra of transmission-mode LPG and reflection-mode LPG; (b) The spectra of reflection-mode LPG under different external RIs; (c) The real-time wavelength shift during the measurement of external RI (reflection-mode); (d) The spectra of transmission-mode LPG under different external RI; (e) The real-time wavelength shift during the measurement of external RI (transmission-mode); (f) The calibration curves

3.2 The measurement of IgG

The measured spectra of the reflection-mode LPG during surface functionalization are shown in Figure 15(a). The attenuation bands move oppositely and the separation between them increases with increasing IgG concentration (Figure 15(b)). The band near 770nm shifts to a shorter wavelength (Figure 15(c)) and the band near 890nm shift to a longer wavelength (Figure 15(d)). The real-time wavelength shift is shown in Figure 15(e). The signal becomes stable within 20 minutes. The calibration between wavelength shift and IgG concentration is performed with exponential fitting (Figure 15(f)). The error bar is the standard deviation of data acquired in multiple independent measurements. A coefficient of determination (R^2) of 98.68% is achieved. The linear range of the sensor is between 0 and 80µg/ml (R^2=91.33) The LoD of the sensor is 15.39µg/ml, which is calculated with Equation (5-1). The sensor's response to 20µg/ml IgG is 56 times higher than its response to 20µg/ml BSA (Figure 15(g)). The RSD of the sensor is 32.7%

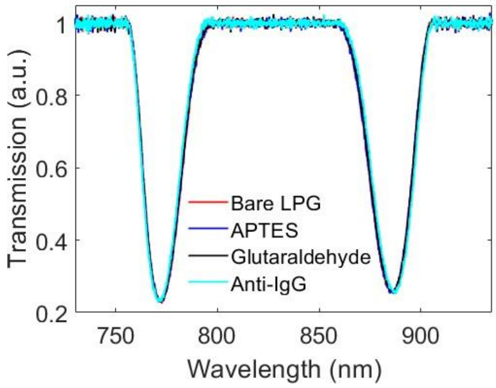
Transmission (a.u.)
Wavelength (nm)
0.2
0.4
0.6
0.8
1
750
800
850
900
Bare LPG
APTES
Glutaraldehyde
Anti-IgG

a

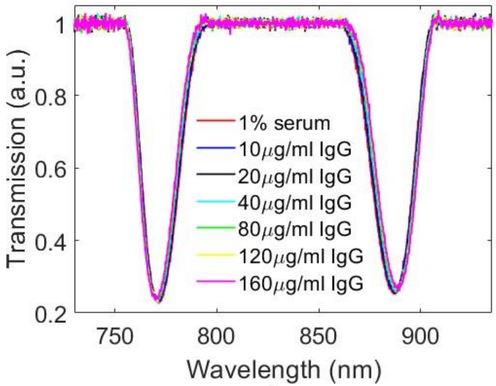
Transmission (a.u.)
Wavelength (nm)
0.2
0.4
0.6
0.8
1
750
800
850
900
1% serum
10μg/ml IgG
20μg/ml IgG
40μg/ml IgG
80μg/ml IgG
120μg/ml IgG
160μg/ml IgG

b

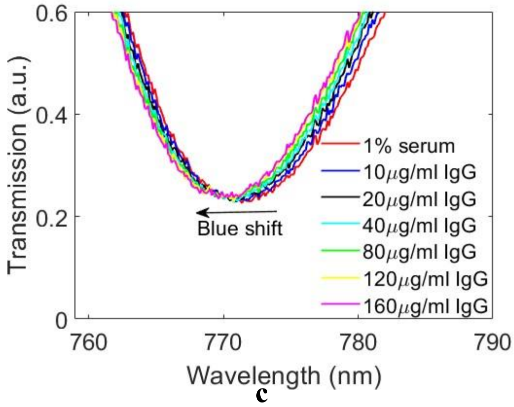
Transmission (a.u.)
Wavelength (nm)
0
0.2
0.4
0.6
760
770
780
790
Blue shift
1% serum
10μg/ml IgG
20μg/ml IgG
40μg/ml IgG
80μg/ml IgG
120μg/ml IgG
160μg/ml IgG

c

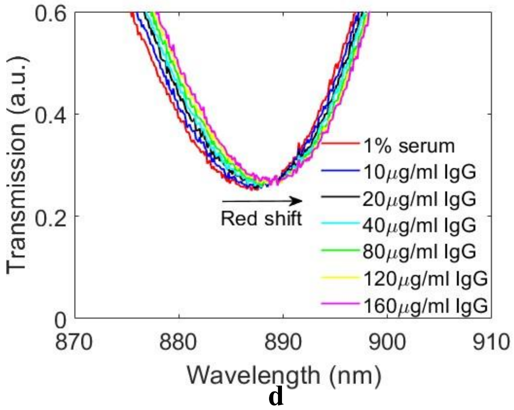
Transmission (a.u.)
Wavelength (nm)
0
0.2
0.4
0.6
870
880
890
900
910
Red shift
1% serum
10μg/ml IgG
20μg/ml IgG
40μg/ml IgG
80μg/ml IgG
120μg/ml IgG
160μg/ml IgG

d

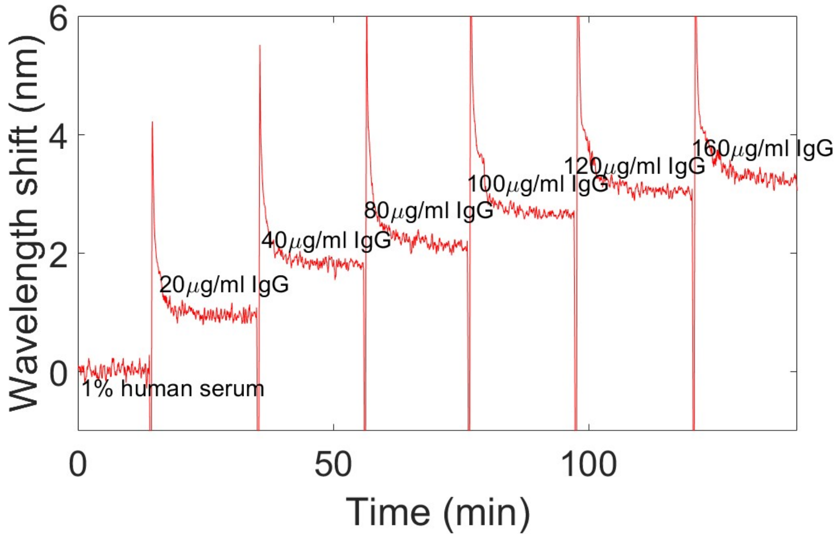
Wavelength shift (nm)
Time (min)
0
2
4
6
0
50
100
1% human serum
20μg/ml IgG
40μg/ml IgG
80μg/ml IgG
100μg/ml IgG
120μg/ml IgG
160μg/ml IgG

e

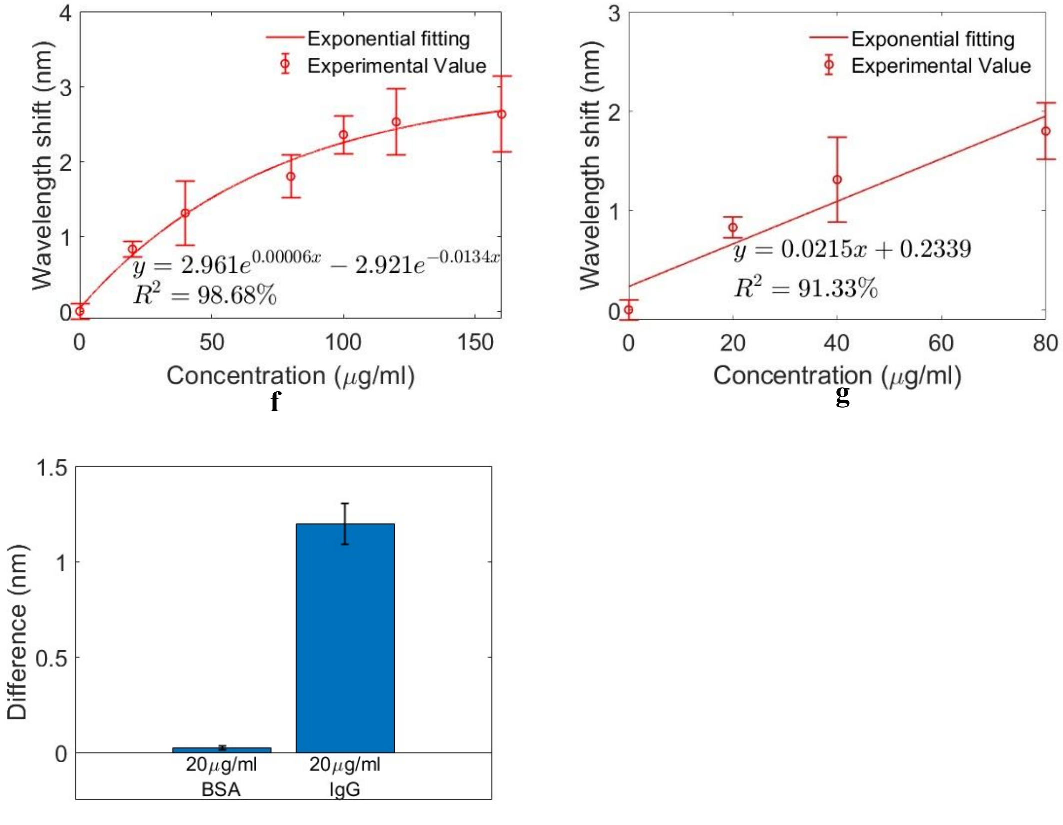

f

g

h

Figure 15. The IgG sensor based on the reflection-mode LPG. (a) The measured spectra during surface functionalization of reflection-mode LPG; (b) The measured spectra of reflection-mode LPG in 1% human serum with different IgG concentrations; (c) The blue shift of the attenuation band near 770nm; (d) The red shift of the attenuation band near 890nm; (e) The real-time wavelength shift during the measurement of IgG; (f) The calibration curve; (g) The linear fitting curve between 0 and 80µg/ml; (h) A comparison of the sensor's response to 20µg/ml IgG and response to 20µg/ml BSA.

4. Discussion

The reflection-mode LPG has deeper attenuation bands than the transmission-mode LPG as the light is attenuated twice by the LPG in reflection-mode LPG while it's only attenuated once in transmission-mode LPG. The IgG sensor based on reflection-mode LPG can measure IgG in human serum with an LoD of 15.39µg/ml. It is over twice of the LoD of IgG sensor described in Chapter 5 (7.38µg/ml). There are three factors that affect the sensor: i) the LPG used in Chapter 5 works closer to the PMC, which results in higher sensitivity; ii) functional matrix of PAH/SiNPs/AuNPs is deposited on the LPG in Chapter 5, which improves the sensitivity; iii) the small molecules in serum accelerate the aggregation of IgG [12]. Changing the sensor type from transmission mode to reflection mode doesn't affect the sensitivity (transmission-mode LPG: 295.7nm/RIU, reflection-mode LPG: 300nm/RIU). The small difference is most likely caused by the inevitable experimental error. In clinical measurement, the serum sample is usually diluted in PBS buffer nearly 100-fold. The IgG concentration in human serum ranges from 8mg/ml to 16mg/ml. After the dilution by 100 folds, the concentration ranges from 80µg/ml to 160µg/ml. The results in this work demonstrate the feasibility of using this sensor in clinic. The sensor's response to IgG is over 50 times higher than the response to BSA. It shows the sensor has immunity to interfering substances. The linear range of the sensor is from 0 to 80µg/ml, and the RSD is 32.7%.

5. Conclusion

An IgG sensor is fabricated based on a reflection-mode LPG in this Appendix. Reflection-mode LPG has deeper attenuation bands than transmission-mode LPG. The responses of reflection-mode LPG and transmission-mode LPG have the same sensitivity. The IgG sensor fabricated based on a reflection-mode LPG can detect IgG in 1% human serum with an LoD of 8.4µg/ml, which is sufficient to be used in clinic. This work shows the feasibility of designing an IgG sensor based on reflection-mode LPGs. The reflection-mode LPG has the potential to be made into a flexible probe-type sensor. There are a few challenges faced to implement it. The separation between the silver film and LPG needs to be made shorter to make the sensing area suitable for being inserted into a sample. However, a shorter separation can make the reflected cladding mode interfere with core mode as it might not be fully dissipated before propagating back through the LPG which affects the measured spectrum. An LPG is sensitive to bending, therefore, the LPG needs a support such as a metal rod whose shape isn't affected by mechanical fluctuations. Also, it is necessary to ensure the functionalized surface is well protected during the fabrication.

6. References

[1]. M. N. Martin, J. I. Basham, P. Chando, and S.-K. Eah, "Charged gold nanoparticles in non-polar solvents: 10-min synthesis and 2D self-assembly," *Langmuir,* vol. 26, no. 10, pp. 7410-7417, 2010.

[2]. F. Esposito, "Chemical sensors based on long period fiber gratings: A review," *Results in Optics,* vol. 5, p. 100196, 2021.

[3]. L. Alwis, T. Sun, and K. V. Grattan, "Analysis of polyimide-coated optical fiber long-period grating-based relative humidity sensor," *IEEE Sensors Journal,* vol. 13, no. 2, pp. 767-771, 2012.

[4]. P. L. Swart, "Long-period grating Michelson refractometric sensor," *Measurement Science and Technology,* vol. 15, no. 8, p. 1576, 2004.

[5]. J. Hromadka *et al.*, "Simultaneous in situ temperature and relative humidity monitoring in mechanical ventilators using an array of functionalised optical fibre long period grating sensors," *Sensors and Actuators B: Chemical,* vol. 286, pp. 306-314, 2019.

[6]. M. Jiang, A. P. Zhang, Y.-C. Wang, H.-Y. Tam, and S. He, "Fabrication of a compact reflective long-period grating sensor with a cladding-mode-selective fiber end-face mirror," *Optics express,* vol. 17, no. 20, pp. 17976-17982, 2009.

[7]. L. Qi *et al.*, "Highly reflective long period fiber grating sensor and its application in refractive index sensing," *Sensors and Actuators B: Chemical,* vol. 193, pp. 185-189, 2014.

[8]. D. W. Kim, Y. Zhang, K. L. Cooper, and A. Wang, "In-fiber reflection mode interferometer based on a long-period grating for external refractive-index measurement," *Applied Optics,* vol. 44, no. 26, pp. 5368-5373, 2005.

[9]. T. K. Dey, P. Biswas, N. Basumallick, and S. Bandyopadhyay, "Long-Period Fiber Grating Probe: An Improved Design Suitable for Biosensing," *IEEE Sensors Journal,* vol. 23, no. 7, pp. 6886-6891, 2023.

[10]. S. Rana, N. Kandadai, and H. Subbaraman, "Experimental validation of a reflective long period grating design methodology," *Results in Optics,* vol. 7, p. 100224, 2022.

[11]. G. Quero *et al.*, "High Sensitive Long Period Fiber Grating Biosensor for Cancer Biomarker Detection," in *HEALTHINF*, 2016, pp. 561-569.

[12]. S. Sreenivasan, S. S. Patil, and A. S. Rathore, "Does Aggregation of Therapeutic IgGs in PBS Offer a True Picture of What Happens in Models Derived from Human Body Fluids?," *Journal of Pharmaceutical Sciences,* 2023.